

THE UNIVERSITY of ADELAIDE

In Silico, *Ex Vivo*, and *In Vivo* approaches for Modelling Tibial Plateau Fractures

Kieran James Bennett

Bachelor of Engineering (Mechanical and Aerospace) (Honours)

A thesis in fulfilment of the degree of Doctor of Philosophy

Adelaide Medical School, The University of Adelaide

Submitted on 31 March 2022

Contents

In Silico, Ex Vivo, and *In Vivo* approaches for Modelling Tibial Plateau Fractures 1

Publications Arising from Candidature xiv

Peer reviewed journal publications included in thesis xiv

Additional publications prepared for publication or currently under review included in this thesis xiv

Publications not included in thesis but completed during candidature xiv

Thesis Abstract xvi

Declaration xvii

Acknowledgements xviii

Chapter 1: Introduction 1

1.1 Musculoskeletal Modelling 3

1.2 Finite Element and Experimental Modelling 3

1.3 Summary 4

1.1 Thesis Aims and Structure 5

Chapter 2: Literature Review 7

2.1 Estimating Knee Joint Loading 7

2.1.1 Inverse Dynamics Approaches 8

2.1.2 Forward Dynamics Approaches 10

2.1.3 Applicability of Musculoskeletal Modelling to Tibial Plateau Fractures 12

2.1.4 Summary 13

2.2 *In* Silico and *Ex Vivo* Models of Tibial Plateau Fractures 13

2.2.1 Finite Element Models of Tibial Plateau Fractures 14

2.2.2 Experimental Models of Tibial Plateau Fractures 19

2.2.3 Strain Response of Tibial Plateau Fractures due to Loading 24

2.2.4 Summary 25

2.3 Patient Recovery from Tibial Plateau Fractures 26

2.4 Summary 27

Chapter 3: EMG-informed neuromusculoskeletal models accurately predict knee loading measured using instrumented implants 30

Statement of authorship 31

Abstract 34
3.1 Introduction 35
3.2 Methods 37
3.2.1 Data 37
3.2.2 Preprocessing and EMG 37
3.2.3 Musculoskeletal Models 38
3.2.4 Muscle Recruitment Models 39
3.2.5 Data Analysis 42
3.3 Results 42
3.4 Discussion 54
3.5 Conclusion 59
3.6 Acknowledgement 59
Chapter 4: Digital Volume Correlation and Finite Element Analysis of the Human Tibial Plateau under Loading 60
Statement of Authorship 61
Abstract 64
Statement of Significance 64
Keywords 64
4.1 Introduction 65
4.2 Materials and Methods 66
4.2.1 Specimens 66
4.2.2 Specimen Preparation 66
4.2.3 Ex vivo Experiment 66
4.2.4 Volumes of Interest selection 70
4.2.5 Digital Volume Correlation (DVC) 72
4.2.6 Finite Element Models 72
4.2.7 Comparison of Methods 73
4.3 Results 74
4.3.1 Micro-CT Images 74
4.3.2 Digital Volume Correlation 76
4.3.4 Finite Element Analysis 77
4.3.5 Comparison Between Methods 79
4.4 Discussion 81
4.5 Conclusions 83

4.6 Funding 83
4.7 Acknowledgements 84

Chapter 5: Ex vivo Assessment of Surgically Repaired Tibial Plateau Fracture Displacement Under Axial Load Using Large-Volume Micro-CT 85
Statement of Authorship 86
Abstract 89
Keywords 89
5.1 Introduction 90
5.2 Methods 91
5.2.1 Specimens 94
5.2.2 Specimen fracture and fracture treatment 94
5.2.3 Loading 96
5.2.4 Micro-CT imaging 96
5.2.5 Analysis 97
5.3 Results 102
5.4 Discussion 107
5.5 Acknowledgements 111

Chapter 6: Postoperative lower limb joint kinematics following tibial plateau fracture: a 2-year longitudinal study 112
Statement of authorship 113
Abstract 116
6.1 Introduction 117
6.2 Methods 118
6.2.1 Patients and protocol 118
6.2.2 Motion capture experiment 119
6.2.3 Joint kinematic measurement 120
6.2.4 Statistical analysis 120
6.3 Results 123
6.3.1 Participants and reference 123
6.3.2 Joint kinematics 123
6.3.4 Objective and self-reported activities of daily living 126
6.4 Discussion 127
6.5 Conclusion 129
6.6 Acknowledgements 130

Chapter 7: Discussion and Conclusion 131
7.1 Key findings and implications of work for tibial plateau fracture research 132
7.1.1 Estimates of knee joint loading are improved when augmenting an EMG-informed approach with statistical processes 132
7.1.2 The internal 3D strains within the tibial plateau under peak walking loads are within the physiological range 133
7.1.3 With ideal surgical fixation, tibial plateau fractures can withstand peak walking loads with minimal displacement 134
7.1.4 People who have undergone surgery to repair a tibial plateau fracture recover their joint kinematics within the first six postoperative months 136
7.2 Limitations 137
7.3 Recommendations for future research 140
7.3.1 Investigation into the long-term functional deficit in tibial plateau fracture patients 140
7.3.2 Digital patient models 140
7.4 Conclusion 143
References 144
Appendices 164
Appendix A – Chapter Supplementary Material 164
Chapter 3 Supplementary Material 164
Chapter 4 Supplementary Material 175
Chapter 6 Supplementary Material 179
Appendix B – Ethical Approval Statements 186
Chapter 4, 5 Ethics: The University of Adelaide HREC reference number 34423 186
Chapter 6 Ethics: CALHN reference number R20160312 189
Chapter 6 Ethics: The University of Adelaide HREC reference number 33506 191

Figures

Figure 1 Lateral split fracture (left) and lateral split fracture with depression (right). Modified from Schatzker, McBroom and Bruce (1979). 2

Figure 2 Thesis structure and linkage between individual studies 6

Figure 3 Generic forward dynamics block diagram, showing the transfer from either estimated or experimental muscle excitations through to joint moments. In a closed loop implementation, the error between simulated and experimental joint moments are included (dashed box). 11

Figure 4 Maximum lateral fragment displacement vs. total applied load (filled circles) for the three studies with a lateral split. A linear trend (Displacement = 0.0007×Load-0.0081 mm) has been fitted to each data point. Note: Belaid et al. (2018) also includes a depression. 15

Figure 5 Fragmental displacements vs. load applied to the fragment for experimental and FE models of fractures involving a split. Lines of best fit have been added to the results from *Cross et al. (2013) and Vendeuvre et al. (2018), and the FE model from Chen, P et al. (2017). *Cross et al. (2013) only report the total load applied to the tibial plateau, and not the load applied directly to the fragment. The data presented for Vendeuvre et al. (2018) is fixation using a bone tamp.....19

Figure 6 Box plots showing the RMSE for each of the objective functions tested for CEINMS (summarized in Supplementary Material) with the selected calibration function highlighted. Red pluses are trials which were statistical outlier for that objective function. 45

Figure 7 Knee loads from the instrumented prostheses (eTibia, black), overlaid with the solutions from CEINMS (red), SO (blue) and the stochastic method (gray) for individual over ground walking trials.....46

Figure 8 Directional components of joint loading for the challenge 5 dataset from the instrumented prostheses (eTibia, black), overlaid with the solutions from SO (blue),

CEINMS (red), and the stochastic method (grey) for individual over ground walking trials. Each row represents a single trial, and for each direction, anterior, inferior, and lateral are positive.....47

Figure 9 Directional components of joint loading for the challenge 6 dataset from the instrumented prostheses (eTibia, black), overlaid with the solutions from SO (blue), CEINMS (red), and the stochastic method (grey) for individual over ground walking trials. Each row represents a single trial, and for each direction, anterior, inferior, and lateral are positive.....48

Figure 10 SnPM results comparing the eTibia measurement to CEINMS (column one), the eTibia measurement to SO (column 2), and SO to CEINMS (column three). Significance is set at α=0.125 and all suprathreshold clusters have p=0.125. 49

Figure 11 RMSE mean and standard deviation in estimation of total knee joint loading for SO, CEINMS, and the best fit stochastic solutions. Colors indicate separate trials. 50

Figure 12 Muscle forces (N) contributing to joint loading for SO (mean±SD), CEINMS (mean±SD), the stochastic method (range) for challenge 4. The muscles presented are: Semiten = semitendinosus; Semimem = semimembranosus; Sar = Sartorius; Grac = gracilis; BFSH = biceps femoris short head; BFLH = biceps femoris long head; LG = lateral gastrocnemius; MG = medial gastrocnemius; RF = rectus femoris; VL = vastus lateralis; VI = vastus intermedialis; VM = vastus medialis; and TFL = tensor fascia latae. 51

Figure 13 Muscle forces (N) contributing to joint loading for SO (mean±SD), CEINMS (mean±SD), the stochastic method (range) for challenge 5. The muscles presented are: Semiten = semitendinosus; Semimem = semimembranosus; Sar = Sartorius; Grac = gracilis; BFSH = biceps femoris short head; BFLH = biceps femoris long head; LG = lateral gastrocnemius; MG = medial gastrocnemius; RF = rectus femoris; VL = vastus lateralis; VI = vastus intermedialis; VM = vastus medialis; and TFL = tensor fascia latae. 52

Figure 14 Muscle forces (N) contributing to joint loading for SO (mean±SD), CEINMS (mean±SD), the stochastic method (range) for challenge 6. The muscles presented are: Semiten = semitendinosus; Semimem = semimembranosus; Sar = Sartorius; Grac = gracilis; BFSH = biceps femoris short head; BFLH = biceps femoris long head; LG = lateral gastrocnemius; MG = medial gastrocnemius; RF = rectus femoris; VL = vastus lateralis; VI = vastus intermedialis; VM = vastus medialis; and TFL = tensor fascia latae. 53

Figure 15 (left) The experimental loading rig (left) set up within the micro-CT scanner (right) showing (A) the hand crank mechanism, (B) the low friction x-y table, (C) the angle adjustment plate, (D) the load cell, (E) the load cell amplifier, (F) the X-ray source, and (G) the rotation stage within the micro-CT scanner. (right) Shadow projection showing the tibia and femur in the preloaded state within the loading stag 69

Figure 16 (A) Surface mesh of specimen 1, with the location of the four VOIs used in the study (AL anterior-lateral, PL posterior-lateral, AM anterior-medial, PM posterior-medial). The ellipses which were used to determine the position of each VOI are presented. (B) The ellipses which were used to apply external boundary conditions in the FE models derived from the clinical CT scans. 71

Figure 17 Coronal micro-CT images of specimen one: (A) preload, (B) loaded conditions, and (C) overlaid with green representing the preload, magenta representing loaded, and white representing the bone present in both images; and of specimen two: (D) preload, (E) loaded conditions, and (F) overlaid with green representing the preload, magenta representing loaded, and white representing bone which is present in both images.....75

Figure 18 DVC results: Von-Mises equivalent strains calculated in the four volumes of interest (VOI) for each specimen (AL anterior-lateral, AM anterior-medial, PL posterior-lateral, PM posterior-medial), where each VOI is composed of 203 sub-volumes (29 (7x7 circle) x 7 subvolumes). Median and interquartile ranges (boxes), along with outliers (1.5 x interquartile range, red crosses) are presented alongside their frequency distributions. 76

Figure 19 FE results: Von-Mises equivalent strains within each volume of interest (AL anterior-lateral, AM anterior-medial, PL posterior-lateral, PM posterior-medial). Median and interquartile ranges (boxes), along with outliers (1.5 x interquartile range, red crosses) are presented alongside their frequency distributions. 77

Figure 20 FE results: von-Mises Equivalent strains within specimen one and two. Values are presented as strain. 78

Figure 21 Von Mises strain distributions calculated using FE and DVC within the four VOIs for each specimen. S1 – specimen one; S2 – specimen two; DVC – digital volume correlation. 80

Figure 22 (A) The loading rig setup within the large-volume micro-CT scanner with the field of view highlighted (red square), (B) an X-ray projection of the specimen within the field of view, (C) the loading history of three cumulative bodyweights (BW) distributed with a target 60:40 medial:lateral proportion applied to specimen two via the femoral condyles (data shown after the second pre-load scan), as measured by the load cell. 93

Figure 23 (A) Left tibia, anterior view, CT 3D reconstruction of the clinical fracture case which presented to our medical centre, (B) subsequent virtual planning of the fracture on specimen one, (C) cutting guide planning on the specimen one model, (D) cutting guide fit on specimen one, (E) anterior view, photograph of the fractured specimen two with separated lateral fragment, (F) of the fractured specimen two after fixation with plate and screws, with the meniscus reattached. The 3D printed specimen holder is visible at the bottom (black colour). 95

Figure 24 (A) Transverse plane micro-CT cross section of specimen one, showing the position of each coronal slice used for correlation (red lines). (B) Coronal slice of specimen two overlaid with the correlation grid (white lines), and the regions of interest (ROIs) selected for analysis (red shaded areas). Only the ROIs which contained bone and no external tissue or gaps were used for analysis. The gray-level histogram was adjusted to enhance visualisation of the bone in the figure. The original, unadjusted images were used for correlation analysis. In each image, the

metalwork (enhanced due to the histogram adjustment) can be seen, along with the trabecular bone and the fracture surfaces. M: medial, L: lateral.....100

Figure 25 Buttress plate fixation used to fix the Type I fractures in this study (left) and an example of the buttress plate and subchondral screw fixation used to fix the Type II fractures, showing the tantalum beads used for DL-RSA in the clinical cohort (right). 101

Figure 26 Micro-CT coronal cross-section images (46 μm/pixel), 20 mm from the anterior edge, of (A) specimen one under preload, (B) under 3BW load; of (C) specimen two under preload, (D) under 3BW load. The gray-level histogram was adjusted to enhance visualisation of the bone in the figure. The original, unadjusted images were used for correlation analysis. In each image, the metalwork (enhanced due to the histogram adjustment) can be seen, along with the trabecular bone and the fracture surfaces. M: medial, L: lateral.....103

Figure 27 Fragment (red shaded region) and intact tibia (white shaded region) displacements from every slice of (A) specimen one, and (B) specimen two overlaid onto the coronal micro-CT reconstructions at 20 mm from the anterior edge. The vectors displayed are from all ten slices analysed, resulting in some appearing within the gaps in the bone. Displacement vectors were multiplied by a factor of five for emphasis.....104

Figure 28 Fragment (red) and intact tibia (black) craniocaudal (left) and mediolateral (right) displacements for specimen one (top) and specimen two (bottom) at each image correlation pair depth from the anterior edge of the plateau under a 3 BW load. The mean and standard deviation fragment motion is plotted to show the overall motion relative to the intact tibia. 105

Figure 29 Displacements at the lateral edge of the fracture fragment (red) and at the fracture site (blue) in the craniocaudal and mediolateral directions for specimen one (left) and specimen two (right). While specimen one did not show significant differences between the lateral edge and the fracture site, specimen two showed significant differences between them.....106

Figure 30 Example of level one statistical parametric mapping analysis estimating the within subject effects. (1) The joint angles for a single participant across the entire gait cycle are determined. (2) The joint angles at each point across the gait cycle (shown here are (A) 25% and (B) 75%) are projected across the number of weeks postoperative the measurement was taken. The linear regression model is used to determine the change in joint angle at this point of the gait cycle across the number of weeks postoperative. (3) The slope of the regression (β) is calculated across the entire gait cycle with positive values showing a positive correlation with time, and negative values showing negative correlation with time. (3) Is the within subject effect of time on joint kinematics. 122

Figure 31 (A) Group mean and standard deviation hip (1), knee (2) and ankle (3) angles at each time point measured. (B) Mean changes in joint kinematics across the gait cycle over time (β) for all participants. (C) The unpaired t-test statistic SPM{t}. The critical threshold at the hip, $t^* = 3.091$ was exceeded at the supra-threshold cluster between 17% and 64% with $p < 0.001$, indicating more hip flexion as the participants recover. At the knee, the critical threshold $t^* = 3.275$ was exceeded at the supra-threshold cluster between 66% and 84% with $p = 0.003$, indicating more knee flexion during mid stance as participants recover. The ankle critical threshold $t^* = 3.264$ was not exceeded at any point along the gait cycle. 124

Figure 32 The Pearson correlation between the hip, knee, and ankle joint ROM and self-reported ADLs. The line of best fit, and 95% confidence interval for the line of best fit are also presented in red. 126

Figure 33 Fragmental displacements vs. load applied to the fragment for experimental and FE models of fractures involving a split with the results obtained from Chapter 5. Lines of best fit have been added to the results from Cross et al. (2013) and Vendeuvre et al. (2018), and the FE model from Chen, P et al. (2017). *Cross et al. (2013) only report the total load applied to the tibial plateau, and not the load applied directly to the fragment. 135

Figure 34 Interfacing between patients and digital patient modelling showing the recursive surgical planning and patient rehabilitation approaches. 142

Figure 35 Normalized EMG signals recorded for Challenge 4 with their reasons for signals being excluded. Each line is an individual measurement. 165

Figure 36 Normalized EMG signals recorded for Challenge 5 with their reasons for signals being excluded. Each line is an individual measurement. 165

Figure 37 Normalized EMG signals recorded for Challenge 6 with their reasons for signals being excluded. Each line is an individual measurement. 166

Figure 38 Knee load traces for all trials for both the eTibia and the CEINMS model calibrated with function 2. 168

Figure 39 Knee load traces for all trials for both the eTibia and the CEINMS model calibrated with function 5. 169

Figure 40 Knee load traces for all trials for both the eTibia and the CEINMS model calibrated with function 8. 169

Figure 41 Joint moments normalized to body weight calculated using inverse dynamics (black), and the resultant joint moments from the muscle forces in CEINMS (red) and SO (blue).....170

Figure 42 RMSE and R^2 between the inverse dynamics solution and the CEINMS and SO solutions. 171

Figure 43 Standard deviation of gluteal muscle forces across stance for Challenge 4. 172

Figure 44 Standard deviation of gluteal muscle forces across stance for Challenge 5. 173

Figure 45 Standard deviation of gluteal muscle forces across stance for Challenge 4. 174

Figure 46. Load cell measurement during the loading experiment for specimens 1 (S1) and 2 (S2). The force in the Z direction has been normalized. 175

Figure 47 MAER, SDER, and Correlation coefficient for all tested sub volume edge lengths for each specimen and each VOI for the unfiltered image sets. S1 = specimen 1, S2 = specimen 2. 177

Figure 48 MAER, SDER, and Correlation coefficient for all tested sub volume edge lengths for each specimen and each VOI for the median filtered image sets. S1 = specimen 1, S2 = specimen 2. 178

Figure 49 Mean and standard deviation of the hip, knee and ankle angles at each time point measured with healthy reference standard deviation superimposed. 179

Figure 50 Mean and standard deviation of the hip angles by Schatzker fracture type at each time point measured with healthy reference standard deviation superimposed. 180

Figure 51 Mean and standard deviation of the knee angles by Schatzker fracture type at each time point measured with healthy reference standard deviation superimposed. 181

Figure 52 Mean and standard deviation of the ankle angles by Schatzker fracture type at each time point measured with healthy reference standard deviation superimposed. 182

Figure 53 Mean and standard deviation of the hip angles by time to radiological evidence of fracture union at each time point measured. 183

Figure 54 Mean and standard deviation of the knee angles by time to radiological evidence of fracture union at each time point measured. 184

Figure 55 Mean and standard deviation of the ankle angles by time to radiological evidence of fracture union at each time point measured. 185

Tables

Table 1 Summary of TPF FE models in the literature. 17

Table 2 Summary of TPF FE models in the literature (continued). 18

Table 3 Summary of experimental models of tibial plateau fractures. 22

Table 4 Summary of experimental models of tibial plateau fractures (continued). 23

Table 5 Joint kinematics reported for TPF patients in the literature 27

Table 6 Muscles informed by EMG in the EMG-informed and stochastic models for each challenge. 38

Table 7 Musculotendon units in the gait2392 model driven by EMG signals. 40

Table 8 Median strains from the DVC and FE analyses for each VOI. The z-value and p-value from the two-sided Wilcoxon sum rank tests. Statistically significant differences in the median are signified with an asterisk (*) 81

Table 9 Accuracy and precision errors in quantifying assumed zero displacements by using image correlation (subvox.vision) (HajiRassouliha et al. 2018) for each specimen in both the mediolateral and craniocaudal directions. 102

Table 10 External load measured during the DL-RSA study (Solomon et al. 2011) and the corresponding displacement measured for each patient in the cohort, in both the craniocaudal (C-C) and mediolateral (M-L) directions. For comparison, the two specimens tested in this study are also presented as S1 and S2. E indicates externally measured, while I indicates internally measured load 107

Table 11 Summary of each calibration function tested 167

Table 12. Sub volume edge length used for each of the multi-pass tests in DVC. The used sequence is in bold. 176

Publications Arising from Candidature

Peer reviewed journal publications included in thesis

Bennett, K. J., Millar, S. C., Fraysse, F., Arnold, J. B., Atkins, G. J., Solomon, L. B., Martelli, S., & Thewlis, D. (2021). Postoperative lower limb joint kinematics following tibial plateau fracture: a 2-year longitudinal study. *Gait & Posture, 83,* 20-25.

Bennett, K. J., Pizzolato C., Martelli, S., Bahl, J.S., Sivakumar A., Atkins, G.J., Solomon, L.B., & Thewlis, D. (2021). EMG-informed neuromusculoskeletal models accurately predict knee loading measured using instrumented implants. *IEEE Transactions on Biomedical Engineering*.

Additional publications prepared for publication or currently under review included in this thesis

Bennett, K.J., Rapagna, S., Wearne, L., Martelli, S., Atkins, G.J., Solomon, L.B., Perilli, E., & Thewlis, D. (2022). Digital Volume Correlation and Finite Element Analysis of the Human Tibial Plateau under Loading. Prepared for submission to *Acta Biomaterialia*.

Bennett, K.J., Callary, S., Atkins, G.J., Martelli, S., Perilli, E., Solomon, L.B., & Thewlis, D. (2022). In vitro Assessment of Surgically Repaired Tibial Plateau Fracture Displacement Under Axial Load Using Large Volume Micro-CT. Submitted to *Journal of Biomechanics*.

The work in these publications have also been presented at conferences. Associated conference presentations are noted in their corresponding chapters.

Publications not included in thesis but completed during candidature

Sivakumar, A., **Bennett, K. J.,** Rickman, M., & Thewlis, D. (2022). An instrumented walker in three-dimensional gait analysis: Improving musculoskeletal estimates in the lower limb mobility impaired. *Gait & posture*, *93*, 142-145.

Millar, S. C., **Bennett, K.,** Fraysse, F., Arnold, J. B., Solomon, L. B., & Thewlis, D. (2020). Longitudinal changes in lower limb joint loading up to two years following tibial plateau fracture. *Gait & posture*, *78*, 72-79.

(Under Review) Millar, S.C. **Bennett, K. J.,** Rickman, M., & Thewlis, D. (2022). Kinematic changes during a 6-minute walk test in people with knee osteoarthritis. Submitted to *Gait and Posture*.

Thesis Abstract

Tibial plateau fractures are associated with reduced lower limb function and poor patient reported outcomes. Allowing earlier postoperative weight bearing in could improve these outcomes. The central aim of this thesis was to ***improve upon methods for modelling the local mechanical environment in surgically repaired tibial plateau fractures to further understand the mechanics associated with fracture recovery, and to investigate long-term patient responses to immediate postoperative weight bearing***. To achieve this, a combination of *in silico*, *ex vivo*, and *in vivo* studies were undertaken. Neuromusculoskeletal methods for estimating knee joint loads were improved and validated using data from instrumented knee replacements. These methods could be applied to tibial plateau fracture patients to better estimate the load applied to their fractures when walking immediately postoperative. Micro-CT imaging during concurrent mechanical loading methods were developed for determining the internal mechanical environment of the proximal tibia. Using these methods, the internal strains calculated using digital volume correlation were compared to subject specific finite element models of the same tibias. The strains within the proximal tibia were within the expected physiological region (200-3000 $\mu\epsilon$) and showed similar median strains to the FE models (error less than 35%). The experimental methods developed were applied to split tibial plateau fractures, showing that, under three bodyweights of load, there is little fracture fragment displacement (<0.3 mm) measured using image correlation. These results suggest that, with adequate mechanical fixation, it is unlikely that simple split fracture fragments would significantly displace from loads applied during basic activities of daily living. Two-year longitudinal patient responses to immediate postoperative weight bearing identified that patients showed similar joint kinematics to immediate postoperative weight bearing when compared to TPF patients who were not prescribed weight bearing. The work presented in this thesis enables further computational and cohort studies of TPF mechanics to assess the safety of postoperative weight bearing.

Declaration

I certify that this work contains no material which has been accepted for the award of any other degree or diploma in my name in any university or other tertiary institution and, to the best of my knowledge and belief, contains no material previously published or written by another person, except where due reference has been made in the text. In addition, I certify that no part of this work will, in the future, be used in a submission in my name for any other degree or diploma in any university or other tertiary institution without the prior approval of the University of Adelaide and where applicable, any partner institution responsible for the joint award of this degree.

The author acknowledges that copyright of published works contained within this thesis resides with the copyright holder(s) of those works.
I give permission for the digital version of my thesis to be made available on the web, via the University's digital research repository, the Library Search and also through web search engines, unless permission has been granted by the University to restrict access for a period of time.

I acknowledge the support I have received for my research through the provision of an Australian Government Research Training Program Scholarship.

Kieran James Bennett

31/03/2022

Acknowledgements

Thank you to my supervisors, Associate Professor Dominic Thewlis, Associate Professor Saulo Martelli, Professor Gerald Atkins and Professor Bogdan Solomon for your supervision and guidance through my PhD journey.

Thank you also to everyone who has supported me on this journey. The real ones know who they are. Regardless of how big or small your contribution was, it made me who I am now, and I am forever grateful.

Mum, Dad, and Adriane, thank you for everything that you have done for me and for being there throughout this entire process. I hope to, one day, return as much love, kindness, and support you have provided me throughout my entire life, education, and most recently, my PhD.

Chapter 1: Introduction

Tibial plateau fractures (TPFs) affect the articular surface of the knee, reducing lower limb function and result in poor patient reported outcomes (Gaston, Will & Keating 2005; Thewlis et al. 2017). They account for 1% of bone fractures, and their incidence follows a bimodal age curve, affecting both men and women in approximately equal proportions (Court-Brown & Caesar 2006). The gold standard for surgical repair of TPFs is open reduction and internal fixation (ORIF) (Prat-Fabregat & Camacho-Carrasco 2016). The primary goals of ORIF are restoration of the articular surface and maintenance of mechanical alignment of the leg (Joshua et al. 2016). Poor surface restoration and maintenance of alignment have been associated with post-traumatic osteoarthritis (Parkkinen et al. 2014), which affects up to 44% of patients who have undergone ORIF for TPF (Honkonen, S. E. 1995).

Maintaining long-term (months to years after ORIF) articular surface congruency is a key consideration in postoperative management (Parkkinen et al. 2014), with a period of non-weight bearing typically prescribed to allow for adequate fracture union before mechanical loading is applied (Arnold, J et al. 2017). There is, however, no consensus on the length of postoperative non-weight bearing required (Arnold, J et al. 2017). TPFs vary significantly, ranging from simple split fractures to bicondylar fractures, and fractures involving dissociation of the metaphysis and diaphysis, all requiring individualised fixation and postoperative management (Schatzker, McBroom & Bruce 1979). For mechanically simpler fractures (split fractures (Schatzker Type I) and split fractures with associated depression (Schatzker Type II), Figure 1), the fracture-fixation construct may be sufficiently stiff to withstand immediate postoperative weight bearing with minimal fragment displacement. Split and split depression fractures account for roughly 50% of TPFs (Millar et al. 2021), and preliminary studies have shown that immediate pain-tolerated weight bearing following ORIF does not lead to fracture displacement (Solomon et al. 2011; Thewlis et al. 2015).

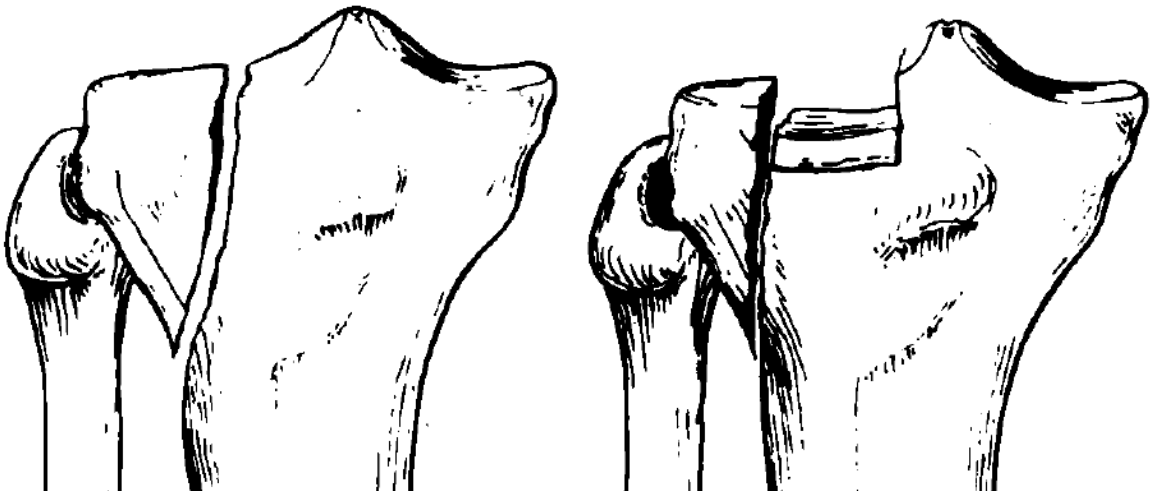

Figure 1 Lateral split fracture (left) and lateral split fracture with depression (right). Modified from Schatzker, McBroom and Bruce (1979).

Fracture fragment displacements relative to the intact segment of the tibia can be measured using 3D radiostereometric analysis, which tracks the motion of assumed rigid bodies (bone fragments) from beads implanted during ORIF (Callary et al. 2013; Solomon et al. 2011). This has provided information on the motion of bone fragments under static loading, but static displacements do not represent the day-to-day motions from dynamic loading, which are the typical mechanical environment present in TPF recovery.

Computational modelling *could* allow for understanding the internal mechanical environment of TPFs when immediate postoperative weight bearing is allowed. One approach, the approach taken in this thesis, is to use a combination of musculoskeletal and finite element (FE) modelling to model the fracture fragment mechanics due to normal daily activity. Musculoskeletal modelling allows for estimation of the contributions of muscles to motion, which account for most of the load at the knee during walking (Bergmann et al. 2014; Kutzner et al. 2010; Shelburne, Torry & Pandy 2006). The effect of these loads on internal fragment deformation, and fragmental motion withstood by the fracture-fixation construct could then be calculated through FE modelling.

1.1 Musculoskeletal Modelling

There is little consensus on the most appropriate musculoskeletal modelling methods for estimating dynamic loading at the knee, with a series of methods evaluated against *in vivo* measurements of knee loads (Fregly et al. 2012; Kinney et al. 2013). This is in part due to the infinite variability in muscle control strategies which can be employed to complete the same task (Loeb 2012; Park & Durand 2008). TPFs further complicate this issue through potential abnormal neuromusculoskeletal control due to trauma and subsequent lower limb surgery, reducing the effectiveness of some more common muscle recruitment modelling methods employing optimization techniques (Anderson & Pandy 2001; Crowninshield & Brand 1981; Loeb 2012). Therefore, further research is required into the most appropriate methods for estimating knee joint loading which can account for the variability in muscular control.

1.2 Finite Element and Experimental Modelling

Three-dimensional Finite element (FE) models of surgically repaired TPFs are still in their infancy, with most approaches aiming to compare the performance of different fixation techniques on simulated fragment displacements and internal stresses (Belaid et al. 2018; Carrera et al. 2016; Chen, F et al. 2018). A major limitation of these models is a lack of experimental validation. Experimental studies measuring external displacements of TPFs which are like these FE models have been undertaken and may be used to inform validation procedures (Cross et al. 2013; Parker et al. 1999; Vendeuvre et al. 2018). These studies, however, are limited to external measures of displacement and so the internal mechanical response of TPFs to external load is still not known. Characterising the internal mechanical response would allow for measurements of fracture fragment depression and the motion of bone at the fracture site when load is applied. These internal mechanical responses could be quantified using large volume micro-computed tomography (micro-CT) imaging combined with concurrent mechanical testing but the methods to undertake such a study need to be developed.

1.3 Summary

Computational models of TPFs could enable further understanding of the effect of immediate postoperative weight bearing on long-term articular surface congruency, associated risk of further complications, and used to inform postoperative care. Currently, there are limitations for both knee modelling in general, and specifically for modelling TPFs which need to be addressed before using computational models for investigating TPF mechanics.

1.1 Thesis Aims and Structure

The central aim of this thesis was to ***improve upon methods for modelling the local mechanical environment in surgically repaired tibial plateau fractures to further understand the mechanics associated with fracture recovery, and to investigate long-term patient responses to immediate postoperative weight bearing***

Specifically, this thesis aimed to:

1. Improve upon methods for estimating knee joint loading using neuromusculoskeletal modelling approaches. **(Chapter 3)**
2. Develop experimental methods for characterising the internal response of the tibial plateau to external joint loading using micro-CT imaging modalities, and to compare measured internal strains to those calculated using finite element models. **(Chapter 4)**

   Calculate internal fragmental displacements of tibial plateau fracture fragments due to external loading using micro-CT imaging. **(Chapter 5)**
3. Investigate patient recovery and outcomes from tibial plateau fracture when immediate postoperative weight bearing is prescribed. **(Chapter 6)**

To achieve these aims, a series of four studies either published, currently under review, or prepared for submission were conducted (Figure 2). These experimental chapters and papers are accompanied by a traditional review of literature and a discussion of the implications of the work. In Chapters 3 – 5, methods for modelling the local environment of the tibial plateau, and TPFs are improved upon. Specifically, in Chapter 3, different methods for estimating knee joint loads using neuromusculoskeletal models are investigated which can be applied to TPF patients. In Chapter 4, the experimental methods for investigating the internal mechanical response of the tibial plateau are developed, and then applied to TPFs in Chapter 5. To investigate long term patient responses to immediate postoperative weight bearing, Chapter 6 explores functional patient responses to understand how weight bearing currently affects patient outcomes.

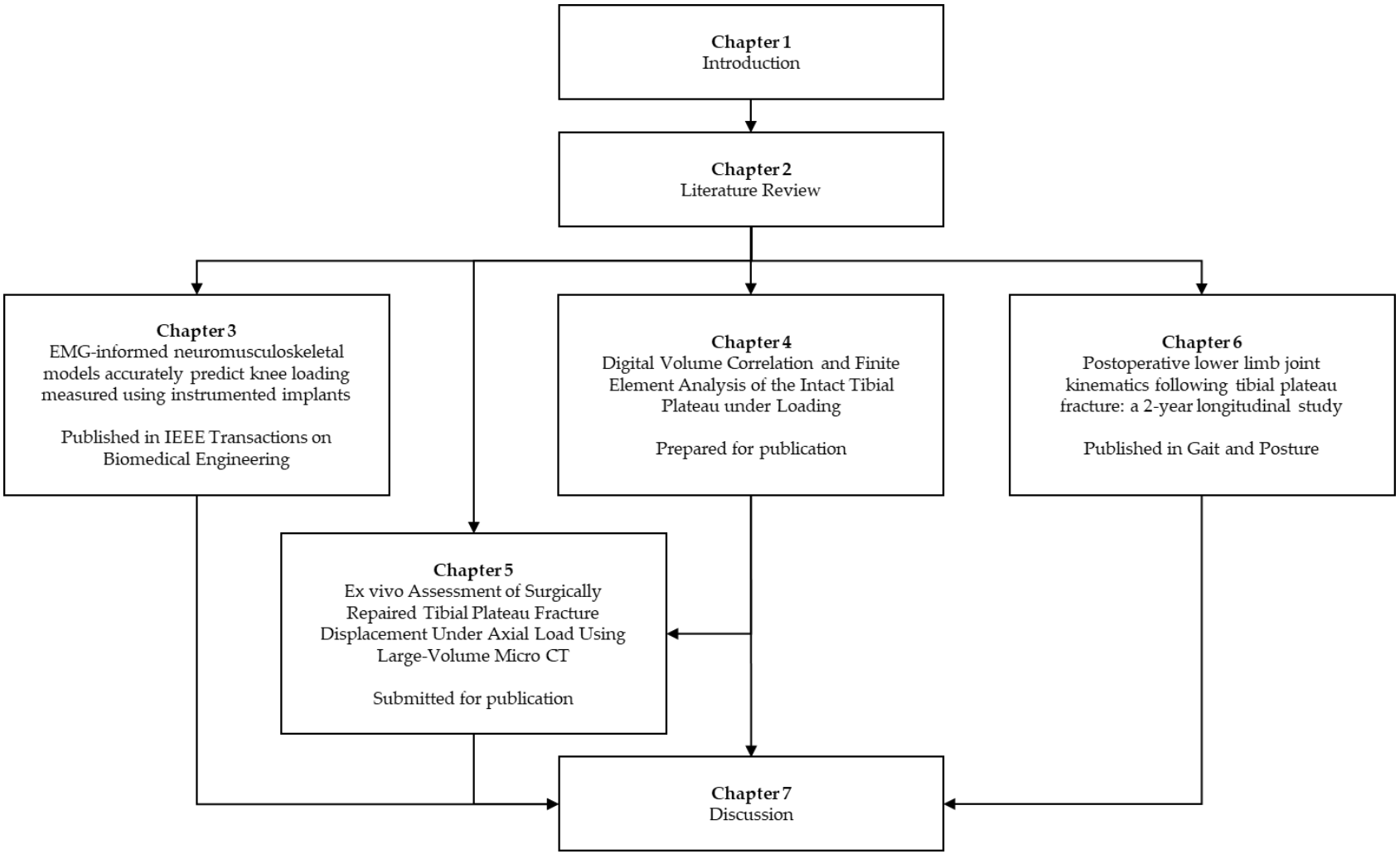

Figure 2 Thesis structure and linkage between individual studies

Chapter 2: Literature Review

The loads applied to TPFs during walking, and their effect on internal fragmental mechanics could be estimated using musculoskeletal modelling and a combination of FE and experimental modelling. This chapter will provide an in-depth review of these modelling approaches, both generally and in the context of TPFs, followed by discussion of methods for assessing patient function.

2.1 Estimating Knee Joint Loading

External measurements of force, for example, ground reaction forces from force platforms, cannot entirely describe the internal knee joint forces; simulation studies suggest that muscles account for roughly two-thirds of knee load (Shelburne, Torry & Pandy 2006). Devices to measure the medial and lateral contact forces during knee replacements during passive flexion are available to surgeons to balance ligament stiffnesses (Wilharm et al. 2013; Zhao, R, Liu & Tian 2021), but these can only be used intraoperatively. Instrumented knee replacements have provided a wealth of data in direct measurements of joint loads during different activities (Bergmann et al. 2014; Fregly et al. 2012; Kinney et al. 2013; Kutzner et al. 2010; Taylor, WR et al. 2017; Zhao, D, Banks, D'Lima, et al. 2007), however, ORIF is typically preferred for TPFs over replacement (Scott et al. 2015; Softness, Murray & Evans 2017). For TPFs, these direct measurement techniques cannot to be used. Therefore, indirect methods for estimating the forces acting at the knee are currently the only reasonable solution. Musculoskeletal modelling is currently the only approach to estimating internal joint loads (Holder et al. 2020).

Musculoskeletal modelling is built upon a rigid multi-body dynamics process. The musculoskeletal system is simplified to a series of rigid segments (bones) and joints, in combination with a set of actuators (muscles). Each segment is prescribed dimensional, mass, and inertial quantities based on either measured or cadaveric data, which are used to calculate joint kinematics (angles) and dynamics (moments or torques) (Delp et al. 2007). Although the joints of the musculoskeletal system are

typically complex multi-degree-of-freedom joints involving both sliding and rotating elements, they are typically simplified to constrain the motion of segments (Carbone et al. 2015; Damsgaard et al. 2006; Rajagopal et al. 2016).

Muscles actuators are used in musculoskeletal modelling to either balance external joint moments, or to generate them, termed inverse and forward dynamics approaches. The joint moment due to muscle actuation is the cross product between the joint-distance vector and the muscle force vector, which are typically defined using cadaveric measurements (Ackland, Lin & Pandy 2012; Hoy, Zajac & Gordon 1990; Killen, B. A. et al. 2020). Muscles models can be implemented as ideal force actuators, or thermodynamics-based formulations, like the Hill muscle model (Buchanan et al. 2004; Delp et al. 2007; Hill 1938). The Hill muscle model is conceptualised as a contractile element in parallel with passive muscle elements, all in series with passive tendon elements (1) (Hill 1938; Millard et al. 2013; Zajac 1989).

$$f^{M*} = f_0^M \left(a\, f^L\left(\tilde{l}^M\right) f^V(\tilde{v}^M) + f^{PE}\left(\tilde{l}^M\right) \right) \quad (1)$$

In this Hill muscle model, f^{M*} is the force which the muscle generates, f_0^M is the maximum isometric force of the muscle, a is the muscle activation, $f^L\left(\tilde{l}^M\right)$ is the active force-length relationship at the muscle length $\tilde{l}^M$, $f^V(\tilde{v}^M)$ is the active force-velocity relationship at muscle velocity $\tilde{v}^M$, and $f^{PE}\left(\tilde{l}^M\right)$ is the passive force-length relationship (Millard et al. 2013; Thelen 2003). The maximum isometric force is typically determined by assuming a maximum muscle stress, ranging from 0.35 to 1.37 MPa (Buchanan 1995; Buchanan et al. 2004), multiplied by the physiological cross section area, the largest cross section of the muscle that runs perpendicular to the muscle fibre (Gans 1982). Both $\tilde{l}^M$ and $\tilde{v}^M$ are the length and velocity of the muscle relative to the ideal muscle length and velocity, which are specific to each muscle (Moissenet, Modenese & Dumas 2017; Ward et al. 2009; Winby, Lloyd & Kirk 2008).

2.1.1 Inverse Dynamics Approaches

In inverse dynamic approaches, muscle forces are estimated to balance the external joint moments. These methods use the external moments and muscle properties as

inputs and solve for muscle forces – typically undertaken by minimising an *a priori* cost function using an optimisation process (Loeb 2012; Patriarco et al. 1981). These cost functions aim to minimise a physiological constraint (Loeb 2012), for example energetic cost (Umberger, Gerritsen & Martin 2003), muscle activation squared (Anderson & Pandy 2001; Crowninshield & Brand 1981), or muscle forces (Buchanan & Shreeve 1996; Damsgaard et al. 2006), among many other formulations. The muscle activation patterns estimated from these methods can show poor agreement with measured electromyogram (EMG, measures of muscle activation potential) signals depending on the objective function, musculoskeletal geometry, and task, and are therefore limited in their accuracy of estimation (Crowninshield & Brand 1981; Damsgaard et al. 2006; Martelli et al. 2015).

A subset of inverse models called probabilistic models can be used to estimate the errors associated with modelling the musculoskeletal system, as well as generating a range of plausible muscle combinations to drive motion. Monte-Carlo simulations are a common method of generating these probabilistic models in the literature (Ackland, Lin & Pandy 2012; Martelli et al. 2015; Myers et al. 2015; Navacchia et al. 2016; van Veen, Mazza & Viceconti 2020). Myers et al. (2015) and Navacchia et al. (2016) used Monte-Carlo simulations to investigate the changes in muscle force predictions using an optimizer by modelling the uncertainty in measured joint positions, limb alignment, inertial parameters, as well as muscle paths and parameters. In these two studies, confidence intervals for knee joint loads were calculated, and it was found that body segment parameters and muscle maximum isometric force affected estimates of joint loading the most. Using a similar approach, Ackland, Lin and Pandy (2012) found that by modelling muscle parameters as probabilistic variables, changes in tendon slack length generally resulted in the largest changes in muscle function, but these changes are muscle specific.

Martelli et al. (2015) and van Veen, Mazza and Viceconti (2020) modelled the muscle forces required to balance external moments as probabilistic variables, holding the muscle and segment properties investigated by previous studies as constant. Using a static optimization solution as a base, van Veen, Mazza and Viceconti (2020) found

that by altering possible muscle forces by ±10% of activation, the *in vivo* measured joint loading was a solution of the model employed, however, the muscle forces which were required to generate this motion did not capture the measured EMG activations of muscles. Martelli et al. (2015) aimed to generate a probabilistic model of muscle recruitment, where EMG signals were used as model inputs and scaled to the maximum force generated using a static optimization approach. The joint loads which were calculated using this approach could not be validated as there were no measured joint loads for the individual modelled. This probabilistic approach may allow for estimation of a range of joint loadings which encompass measured joint loads, however, this has currently not been undertaken. A range of joint loads is useful for investigating potential joint loading, however, if the research question aims to determine a single joint loading, then this probabilistic approach requires additional refinement.

2.1.2 Forward Dynamics Approaches

In forwards dynamics approaches, musculoskeletal model muscles are driven using muscle activations as an input, which simulates joint dynamics and kinematics (Figure 3). Optimization approaches to forwards dynamics approaches have more recently been explored in the field of optimal control (De Groote & Falisse 2021; Dembia et al. 2020), however, this is out of the scope of this thesis. Instead, forwards dynamics approaches using EMG-informed modelling are investigated.

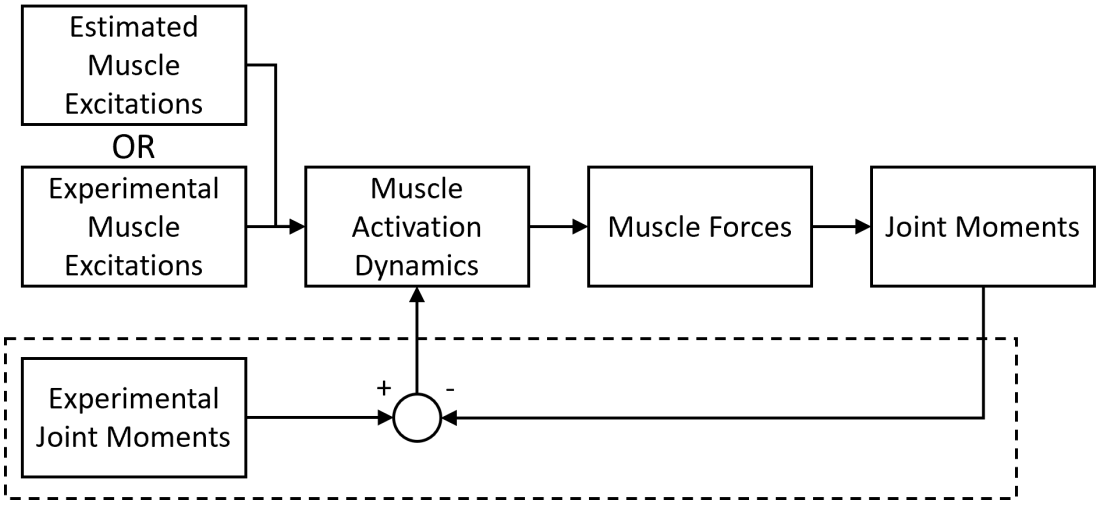

Figure 3 Generic forward dynamics block diagram, showing the transfer from either estimated or experimental muscle excitations through to joint moments. In a closed loop implementation, the error between simulated and experimental joint moments are included (dashed box).

The general methods for estimating muscle forces from EMG signals were summarised by Buchanan et al. (2004). There are two main implementations of EMG informed modelling: open- and closed-loop (Figure 3). In the open-loop implementation, the EMG signals are converted into muscle activations via a nonlinear relationship and used to calculate joint moments with no feedback applied (Pizzolato et al. 2015). This results in EMG-informed forwards dynamics model, however, the dynamics modelled are not always consistent with measurement.

Closed-loop implementations are used to ensure accurate tracking of joint dynamics and kinematics by propagating the error between predicted and measured kinematics and dynamics into the control loop (Figure 3). This could be regarded as a forwards-driven-inverse approach, and has been employed in the literature to model joint dynamics from EMG measurements (Buchanan et al. 2005; Cholewicki & McGill 1994; Cholewicki, McGill & Norman 1995; Lloyd & Besier 2003; Manal & Buchanan 2013; Neptune & McGowan 2011; Sartori et al. 2012). These models either: were only for a single joint, unable to model biarticular muscles (Cholewicki & McGill 1994), or only modelled muscles for which an EMG measurement was taken, limiting their investigations to only superficial muscles. To overcome this limitation, Sartori, Farina

and Lloyd (2014) developed a hybrid EMG-informed neuromusculoskeletal model, similar to that proposed by Cholewicki, McGill and Norman (1995), combining the EMG-informed models of Lloyd and Besier (2003) and Sartori et al. (2012) with the static optimisation method used by Anderson and Pandy (2001). This method allows for these forwards-driven-inverse approaches where not all muscles are informed by EMG signals. While this approach allows for modelling both muscles with and without EMG measurements, it requires subject specific calibration to model the nonlinear relationship between EMG signal and muscle activation.

2.1.3 Applicability of Musculoskeletal Modelling to Tibial Plateau Fractures

To date, there is only one study which has investigated joint loading using musculoskeletal models for TPF patients (Thewlis et al. 2015). This study used an inverse dynamics approach, aiming to minimize the total muscle stresses throughout the lower limbs. Because no EMG data was collected along with 3D gait data, no comparison between model predicted and physically measured neuromusculoskeletal control could be made. It is unlikely that the models would reproduce experimentally recorded muscle activations due to a combination of traumatic neuromusculoskeletal control alterations, and the optimality assumption of the musculoskeletal methods applied.

Traumatic lower limb injury (like TPFs) and subsequent surgery can also affect musculature and neuromusculoskeletal control (Pietrosimone, McLeod & Lepley 2012). Several studies, summarised by Hart et al. (2010), have demonstrated reduced quadricep strength following knee injury up to nine years post injury. Joint effusion models, where fluid is injected into the knee capsule, have demonstrated reduced quadricep muscle activity, and increases in hamstring (Torry et al. 2000) and soleus muscle activity during walking and stimulation tasks (Hopkins et al. 2000). While this reduced quadricep activation and strength are well reported in the literature for knee injuries, no study has investigated the effect of TPF on musculature and neuromusculoskeletal control. It is unlikely that these changes in neuromusculoskeletal control could be modelled using an optimisation-based

method. However, through collecting EMG data and employing a forwards-driven-inverse approach, patient specific neuromusculoskeletal control can be modelled, leading to improved estimates of joint loads for TPF patients.

2.1.4 Summary

Musculoskeletal modelling allows for estimation of muscle contributions to motion, resulting in knee joint loads, and can be applied to TPF patients. Currently, optimization methods which have employed are likely insufficient to model the specific pathologies and neuromusculoskeletal control seen in patients postoperatively. In looking to minimise the amount of work required by patients, augmenting a forwards-driven-inverse approach with probabilistic models may allow for a range of physiologically plausible joint loads to be calculated. A range of joint loads would be useful for estimating possible loads which are not captured as part of a 3D gait analysis session. Such a modelling framework, however, has not been developed and it is not known if the ranges of joint loads would include the true joint loads. Once the knee joint loads applied to TPFs during walking are known, they can be applied to FE models as boundary conditions.

2.2 *In* Silico and *Ex Vivo* Models of Tibial Plateau Fractures

In silico and *ex vivo* models allow for numerical and experimental analysis of TPFs. *In silico* models using FE analysis allow for numerical estimation of bone mechanics (Huiskes & Chao 1983; Taylor, M & Prendergast 2015). These models are formulated using geometry, typically obtained from medical imaging (Dall'Ara, E. et al. 2012; Pahr & Zysset 2009), with material properties defined either from these images (Helgason et al. 2008; Keyak, Lee & Skinner 1994; Morgan, Bayraktar & Keaveny 2003; Taddei, F. et al. 2006), or using aggregate bone properties (Goldstein et al. 1983; Goulet et al. 1994; Guo 2001; Rho 1996; Snyder & Schneider 1991). Following geometric and material definitions, an estimation of the loads expected to act upon the tibial plateau during normal activities are applied as boundary conditions (Gray et al. 2008; Taddei, F et al. 2006) and the model is solved to calculate strains, deformations, and stresses

across the proximal tibia. Models of TPFs in the literature have reported deformations and stresses, however, strains provide mechanical stimulus for bone adaptation, discussed in Chapter 2.2.3.

Ex vivo models assess TPF stability through controlled experimental processes. Fracture models are generated, and loaded externally to replicate the total loading applied to the tibial plateau (Cristofolini et al. 2010). These models have been limited to external measurement of displacements, deformations, and strains, and the internal mechanics present have not been measured.

2.2.1 Finite Element Models of Tibial Plateau Fractures

In FE modelling, mechanical structures (like bone) are discretised into small elements to allow for numerical analysis of structures too complex for analytic models (Huiskes & Chao 1983). It has been used in biomechanics for 50 years, with the first model of skeletal tissue developed in 1972 (Huiskes & Chao 1983). Since this model, increases in computational power have allowed for more complex models. Complex FE models of TPFs can produce reasonable estimates of bone mechanics.

Finite element models of TPFs have investigated the effect of different fixation technique on simulated internal stresses and fracture fragment displacement (Table 1-2). Comparing these studies, the peak fragmental displacements were similar (Figure 4). Under a 400 N total load (75 N applied to the fragment), Carrera et al. (2016) calculated a 0.03 mm maximum fragmental motion. Chen, P et al. (2017) reports a 0.38 mm displacement under a total of 1500 N load (600 N applied to the fragment), and Belaid et al. (2018), who included a depression with the lateral split, report a 0.278 mm caudal displacement under a total of 1764 N (794 N applied to the fragment). Fitting a linear model to these results, it could be implied that to create a 2 mm depression would require 3000 N applied directly to the fragments. Each of these three models vary significantly in their modelling assumptions made, specifically in defining bone material properties, fixation geometry and friction, and friction between bone at the fracture site.

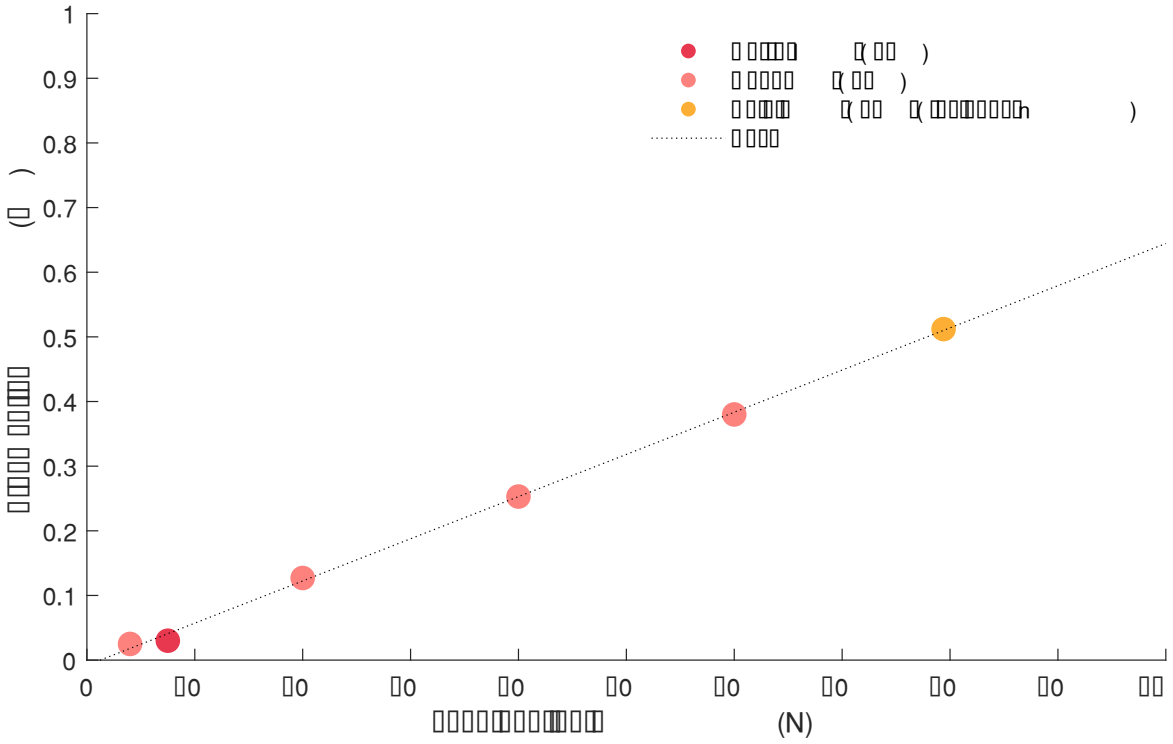

Figure 4 Maximum lateral fragment displacement vs. total applied load (filled circles) for the three studies with a lateral split. A linear trend (Displacement = 0.0007×Load-0.0081 mm) has been fitted to each data point. Note: Belaid et al. (2018) also includes a depression.

Although there is significant heterogeneity within the tibial plateau (Goldstein 1987; Goldstein et al. 1983), it is not captured in some FE models. Carrera et al. (2016) assumed a homogeneous, isotropic, linear elastic material model. Similarly, Belaid et al. (2018) employed a homogeneous, linear elastic model, but also incorporated some orthotropic properties. By varying the elastic modulus and Poisson's ratio of bone depending on anatomic direction, the authors accounted for general internal bone alignment (Cristofolini 2015). However, because the alignment of bone varies depending on anatomic position, the true material axes likely differs from the anatomic axes (Taddei, F. et al. 2006). Chen, P et al. (2017) assigned heterogeneous, linear elastic properties to bone by correlating bone elastic modulus with the apparent density of the bone from CT scans. Although it is not presented which apparent density – elastic modulus correlation was used, it is likely that the elastic modulus – bone density relationship used was determined by either Keyak, Lee and Skinner

(1994) or Morgan, Bayraktar and Keaveny (2003), both relationships showing good agreement with experiments (R^2=0.84 for both). By including subject specific material properties from CT scans (Helgason et al. 2008), FE models of fractures may better model the internal deformations of bone.

For these lateral split fracture models, the fixation screw geometries were simplified to cylinders which, while this simplification is valid for investigating global mechanics, may not be appropriate for modelling localised mechanics (MacLeod, Pankaj & Simpson 2012). Further, all studies assumed the bone-metal interface would be a rigid contact, although studies investigating the friction coefficient for cancellous bone and titanium, report static friction coefficients between 0.3-1.3 (Carter & Hayes 1977; Damm, Morlock & Bishop 2015; Rancourt et al. 1990). The friction coefficient for cancellous bone and metal likely varies based on the density and internal structure of the bone, and so it is difficult to assign a single coefficient for the entire interface. However, for modelling immediate postoperative bone, the assumption that the bone and screw are bonded is likely insufficient and could be resulting in underestimates of fragment displacement under load.

The friction between interfacing bone also varied significantly between studies. Little is known about interfragmental friction, likely due to the variability in bone structures. One study investigating bone-bone friction reported that the frictional coefficient depended not only on the method of cutting, but also the type of bone measured, with rougher surfaces on softer bones producing higher frictional coefficients (Shockey, von Fraunhofer & Seligson 1985). This study, however, was for the cortical bone whereas the tibial plateau is mostly cancellous.

Common to all FE models of TPF is a lack of direct experimental validation. Each study reports the model results with reference to the literature, however it is difficult to directly compare these studies to the literature because the same tibiae are not modelled (Carrera et al. 2016). Regardless, the FE studies all aimed to compare different methods of fracture fixation and reported displacements and surgical considerations consistent with the literature.

Table 1 Summary of TPF FE models in the literature.

Study	Carrera et al. (2016)	Chen, P et al. (2017)	Belaid et al. (2018)
Study Purpose	To assess whether early weight bearing would be possible following two fixation methods, cannulated screws, and a locking plate.	Demonstrate general characteristics of two fixations under axial loads.	Assess cement fixation on a case study of a 24-year-old female; study the mechanical effects and stress distribution in the trabecular bone following fixation.
TPF Type	Lateral split	(1) Lateral split, (2) anterior split and (3) posterior split	Split depression
Material Models	Homogeneous Linear Elastic Isotropic	Heterogeneous Linear Elastic	Homogeneous Elastic Orthotropic
Tibia Elastic Modulus	Cortical: 13 GPa Cancellous: 126 MPa	40.5 MPa to 16790.91 MPa	Cortical: E_3 = 12.847 GPa E_2 = 7.098 GPa E_1 = 6.498 GPa Cancellous: E_3 = 370.6 MPa $E_1 = E_2$ = 123.4 MPa
Poisson's Ratio	0.3	0.3	0.3
Source of Material Properties	Cortical: Guo (2001) Cancellous: Goldstein et al. (1983)	None Presented	Cortical: Snyder and Schneider (1991) Cancellous: Rho (1996)

Table 2 Summary of TPF FE models in the literature (continued).

Study	Carrera et al. (2016)	Chen, P et al. (2017)	Belaid et al. (2018)
Bone-Metal Frictional	Rigid contact	Rigid contact	Rigid contact
Bone-Bone Frictional	Frictionless, finite sliding model	$\mu_S = 0.4$	Not presented
External Boundary Conditions	No discussion of distal tibia boundary condition 400 N axial loading using a frictionless local contact problem between the matched distal femur and the tibial plateau.	Distal tibia constrained to zero displacement. Loading applied in contact patches of approximate dimensions of femur with axial forces of 100, 500, 1000, and 1500 N, with 60% of the load applied to the medial condyle.	Lower surface of tibia constrained to zero displacement. Three bodyweights loading on the plateau, split 55-45% between the medial and lateral condyles.
Source of External Boundary Conditions	Simulated an 80 kg person in bipedal stance.	Loading distribution is originally from Morrison (1970) based on the location of centre of pressure.	Loading distribution is from Zhao, D, Banks, Mitchell, et al. (2007), similar to Fang et al. (2013). Loads are from Taylor, WR et al. (2004) who report an average peak tibiofemoral loading of 3.1×BW.
Outcome Measures	Fragment displacements, shear stresses in bone and principal stresses in fixation.	Fragment displacements, principal and shear stresses in bone and fixation.	Fragment displacements, principal and shear stresses in bone and fixation.

2.2.2 Experimental Models of Tibial Plateau Fractures

Ex vivo experimental models of TPFs have measured the effects of surgical technique, fixation devices, and varying external conditions on the displacement of fracture fragments. The displacement of fractures involving a split due to load (Figure 5) show varying fracture-fixation stiffness. Earlier experimental models (Karunakar et al. 2002; Koval et al. 1996; Parker et al. 1999) reported relatively low stiffnesses, with fracture fragments displacing 2 mm with less than 400 N applied to the fragment. Koval et al. (1996) and Parker et al. (1999) both investigated the use of only screws to repair the fragment, while Karunakar et al. (2002) and later studies employed plate fixation devices, showing increased fracture-fixation stiffness.

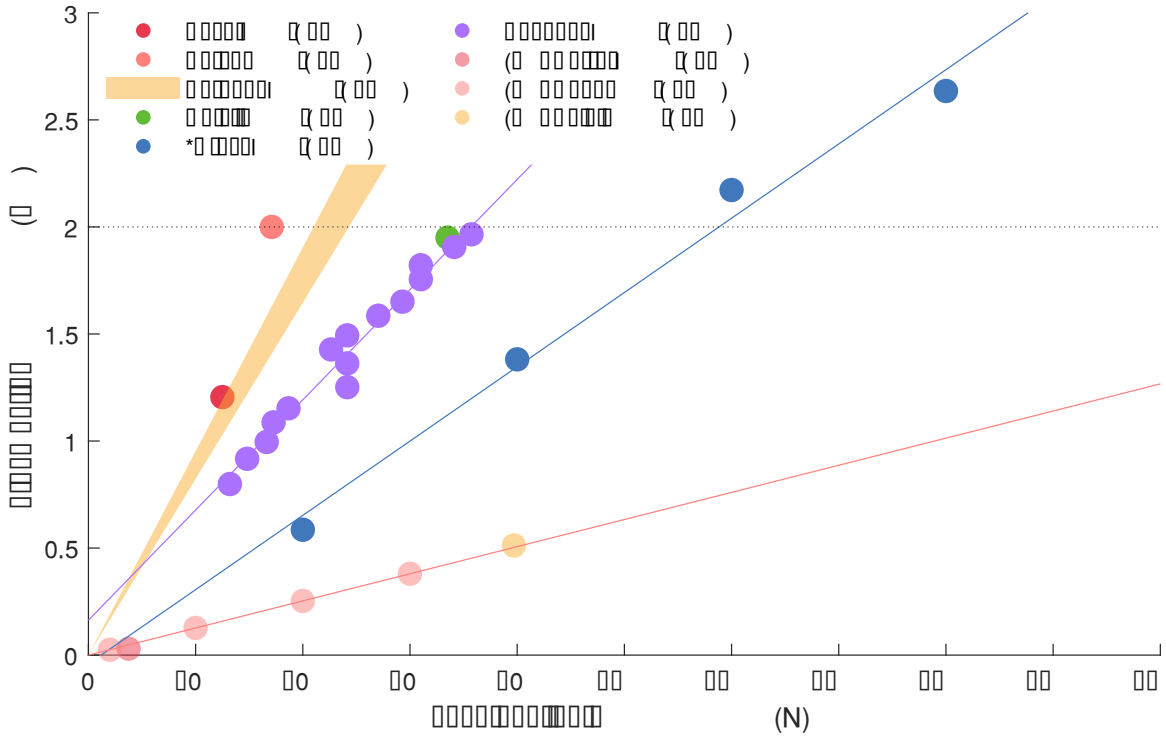

Figure 5 Fragmental displacements vs. load applied to the fragment for experimental and FE models of fractures involving a split. Lines of best fit have been added to the results from *Cross et al. (2013) and Vendeuvre et al. (2018), and the FE model from Chen, P et al. (2017). *Cross et al. (2013) only report the total load applied to the tibial plateau, and not the load applied directly to the fragment. The data presented for Vendeuvre et al. (2018) is fixation using a bone tamp.

The results reported by Cross et al. (2013) and Vendeuvre et al. (2018) suggest that fragment displacement increases linearly with load (Figure 5). A linear fragment displacement was reproduced in the FE study of Carrera et al. (2016), albeit with higher fracture-fixation stiffness.

Differences in fragment displacements measured using plate fixation (Cross et al. 2013; Karunakar et al. 2002; Ratcliff et al. 2007; Vendeuvre et al. 2018) may be attributed to variations in bone quality, screw-bone contact points, and fixation positioning among other factors. For example, additional bone density has been related to a greater screw insertion torque (Ab-Lazid et al. 2014) which results in improved screw stability (Ab-Lazid et al. 2014; Cleek, Reynolds & Hearn 2007; Ryken et al. 1995) and an overall stiffer fixation. Details of both the specimens used, and the resultant fixations would allow for further understanding of the effects of individual differences on fracture fragment stiffness.

To compare different fixation methods, experimental models in literature require methods for simulating near-identical fractures in multiple specimens (Table 3-4). To generate split fractures in the literature, studies have typically used a reciprocating saw (Cross et al. 2013; Egol et al. 2004; Gösling et al. 2004; Koval et al. 1996). However, TPFs *in vivo* propagate through bone via stress concentration sites for low energy fractures (Piekarski 1970), or through composite-like pullout for high energy fractures (Zimmermann, Busse & Ritchie 2015). It is unlikely that generating a fracture from pure impact would generate repeatable fractures in different bones due to varying internal structures, but by drilling holes along the desired fracture path, Karunakar et al. (2002) and Cross et al. (2013) were able to simulate reproducible fractures created using impacts. Both methods have limitations when comparing the simulated fractures to *in vivo* fractures, however, they both present alternative methods for simulating TPFs to assess different methods for fixation.

In most studies, fragment displacement and load applied are measured by the material testing machine (Table 3-4), meaning the fragment displacement reported is the displacement of the method of load application. Some studies have employed

optical and electromagnetic tracking systems to measure fragment displacement which provides direct measurement of the fragments, however, this requires the assumption that the fragment moves as a rigid body (Cross et al. 2013; Parker et al. 1999; Vendeuvre et al. 2018). It is currently not known if TPF fragments displace rigidly or deform with external load due to the resolution of measurements taken, meaning this rigid assumption may not be valid.

Table 3 Summary of experimental models of tibial plateau fractures.

Study	TPF Type	Study Purpose	Load Applied	Fracture Simulation	Measurement
Brown et al. (1988)	Split Depression	Measurement of contact stress due to articular step	1200 N	Jeweller's slotting blade 25% from lateral to medial edge 10° to tibia long axis	Contact stress on tibial plateau using high resolution digital image scans of Fuji-film stain patterns
Koval et al. (1996)	Postereomedial Split	Comparison of three screw and plate configuration s	250 N, 10,000 cycles	Thin blade reciprocal saw 1.5-2 cm lateral fragment In line with the lateral edge of the tibial shaft	Load-displacement determined from data acquisition system
Parker et al. (1999)	Split	Comparison of three screw configurations	Displacement controlled loading applied until a 2 mm displacement was measured	Autopsy saw Most medial portion of the lateral plateau to the inferolateral aspect of the tibial metaphysis 20° to tibia long axis	Measured fragment displacement using a non-contact video system
Karunakar et al. (2002)	Split Depression	Comparison of three fixation methods	Stiffness tested	Three vertical holes drilled on anterior and posterior sides of lateral tibial plateau Unicondylar shaped indenter dropped from 1 m	Angular Displacement Transducer used to measure medial and lateral condylar tilt

Table 4 Summary of experimental models of tibial plateau fractures (continued).

Study	TPF Type	Study Purpose	Load Applied	Fracture Simulation	Measurement
Cross et al. (2013)	Split Depression	Comparison of three screw fixation methods	400, 800, 1200, 1600 N applied five times per tibia. (Load applied to whole tibia, not just the fragment)	Three vertical holes drilled on anterior and posterior sides of lateral tibial plateau Unicondylar shaped indenter dropped from 1 m	Fragment displacement measured using an electromagnetic motion tracking system.
Vendeuvre et al. (2018)	Split	Comparison of bone tamp and balloon reduction methods	Displacement controlled loading applied until failure	Blade attached to compression machine Lateral third of plateau sliced	Fracture displacement and stiffness measured using a combination of a stereoscopic marker-based tracking method and the load cell device.

2.2.3 Strain Response of Tibial Plateau Fractures due to Loading

The FE and experimental studies presented have only investigated fragmental displacements and bone stresses of TPFs due to external loading. None have reported the strain responses of TPFs due to loading. Bone strains provide stimulus for bone growth and healing (Frost 1987, 1998; Sandberg & Aspenberg 2016; Wolff 1892). There is evidence that, through strain-based stimulus, internal bone structures align with regular loading to optimise the ratio of strength to mass (Cristofolini 2015). The internal strain response of TPFs to external loading has not previously been measured, and FE models which have been used to imply these strains have only been validated using superficial measurements of strain (Cristofolini et al. 2010).

Measuring bone strains is a non-trivial task due to the porous, moist, and rough surface properties (Roberts, VL 1966). Strain gauges, digital image correlation (DIC), and digital volume correlation (DVC) are the most common methods for measuring bone strains (Grassi & Isaksson 2015). Strain gauges produce precise measurements and are considered the reference standard in determining bone strains (Grassi & Isaksson 2015), however, they have low resolution (measuring strains only where they are applied) and may increase the stiffness of the bone by up to 15% (Perry 1986). DIC overcomes the resolution limitation of strain gauges by calculating whole surface strains from correlated images of bone specimens (Grassi & Isaksson 2015; Palanca, Tozzi & Cristofolini 2015). Depending on the experimental setup and image postprocessing, DIC can result in high accuracy, precision, and resolution strain fields of bone but are limited to planar measurements.

Digital volume correlation is currently the only method for calculating internal 3D bone strains (Roberts, BC, Perilli & Reynolds 2014). First used to calculate internal strains for bone by Bay et al. (1999) using micro-CT, DVC has previously been used for estimating internal strains due to external load in excised trabecular bone cores, in vertebrae and the proximal femur, mostly by researchers from the University of Sheffield (Comini et al. 2019; Dall'Ara, Enrico et al. 2017; Gillard et al. 2014; Liu & Morgan 2007; Martelli et al. 2021; Palanca et al. 2017; Palanca et al. 2016; Rapagna et

al. 2019; Roberts, BC, Perilli & Reynolds 2014). If applied to the tibial plateau, and TPFs, DVC could be used to calculate the internal strain to external loading. This would allow for whole field strain and deformation measurement, allowing the rigid body assumption of *in vivo* RSA studies and experimental studies of TPFs to be evaluated.

2.2.4 Summary

In silico models of TPF are currently limited by a lack of experimental validation. Discussed by Carrera et al. (2016), direct validation is difficult because the tibiae modelled computationally and experimentally are not consistent. With medical imaging, experimental models could be replicated *in silico* and used to validate FE modelling methods. These FE models have reported significantly stiffer fracture fragment/fixation stiffnesses when compared to experimental models, and it is difficult to determine why without a validation process.

The experimental models of TPFs have presented the external fragmental motion of TPFs under load. The variation of specimens, fixations, and experimental processes makes it difficult to directly compare the external displacements reported. Some general observations can be made, like using a plate fixation appears to be superior to screws alone for creating a stiff fragment/fixation construct, but the small amount of data on the specimens themselves limits generalisability of these results. The external displacements of TPF fragments also do not provide knowledge of what is occurring at the fracture site within the trabecular bone, only what is occurring at the cortical shell. The trabecular bone region is where most of the bone healing is occurring, and there is currently no knowledge of the internal mechanical environment.

While FE and experimental models of TPFs do not currently agree on the external displacements of TPF fragments, no study has reported the strains of the tibial plateau, the major stimulus for bone mass regulation. Knowledge of the internal strains both within the tibial plateau, and present in TPFs, would allow for a more complete definition of the mechanical response of bone to load and to fractures. The only

method to determine these internal strains is through DVC using micro-CT imaging, but the methods for this have not been developed for the tibial plateau.

2.3 Patient Recovery from Tibial Plateau Fractures

In vivo studies of postoperative weight bearing suggest that the fracture-fixation constructs are stable when adequately repaired surgically (Callary et al. 2013; Solomon et al. 2011; Solomon et al. 2010; Thewlis et al. 2015; Thewlis et al. 2017). Immediate postoperative weight bearing as tolerated by pain induces, on average, 0.31 mm of fragmental displacement two weeks post-surgery, measured using RSA (Solomon et al. 2011). These measurements, however, have only been taken under static loading conditions, and may not be representative of the dynamic mechanical environment present in postoperative weight bearing.

TPF patients have historically shown poor outcomes compared to a healthy population when measured subjectively (Elsoe et al. 2015; Timmers et al. 2014). The same has been reported for cohorts prescribed postoperative weight bearing (Thewlis et al. 2017). These outcomes have been reported using the Knee Injury and Osteoarthritis Outcome Score (KOOS) (Roos & Toksvig-Larsen 2003), which has been shown in TKR cohorts to not represent actual function (Bolink, Grimm & Heyligers 2015; Stevens-Lapsley, Schenkman & Dayton 2011). Stevens-Lapsley, Schenkman and Dayton (2011) suggested that for TKR cohorts, the KOOS provides more of an indication of pain than of function. Therefore, improved methods for assessing patient outcomes relative to other patients are required. Despite not representing actual function, longitudinal studies of TPF reporting subjective outcomes have demonstrated that the postoperative weight bearing recommendation followed has little effect on perceived changes in function.

TPF patients who were not instructed to weight bear have shown functional deficits (Table 5), with decreased knee range of motion (ROM) at the knee during walking (Deleanu et al. 2015; Fändriks et al. 2021), however, it is not known if the same deficit is seen in patients prescribed weight bearing. The methods employed in these previous studies may not be sufficient for entirely describing the kinematics of TPF

patients. Deleanu et al. (2015) employed a method employing ultrasonic triplets attached to the thigh and foot of TPF patients using proprietary software, meaning there is no shank measurement to determine knee angle directly. Fändriks et al. (2021) use a camera-based system with 20 retroreflective markers placed on bony landmarks to define the lower limbs. The marker setup employed is similar to the Davis et al. (1991) setup, which has limitations in knee axis alignment (Stief 2018). Despite these limitations, if the reported functional deficit is still seen within a weight bearing cohort, it may indicate that there is additional postoperative care required to allow patients to return to their normal lives.

Table 5 Joint kinematics reported for TPF patients in the literature

Study	Time Postoperative	Maximum Knee Flexion (°)	Ankle Dorsiflexion (°)
(Deleanu et al. 2015)	Six months	58	
	One year	66	
(Fändriks et al. 2021)	Three months	35-64	11-28
	Reference	50-69	3-22

When no weight bearing is prescribed, poor patient reported outcomes and reduced joint flexions have been reported. For patients prescribed immediate postoperative weight bearing, there is evidence that their patient reported outcomes are similar when no weight bearing is prescribed. It is not currently known if, when weight bearing is allowed, if there also exists a deficit in joint flexions.

2.4 Summary

In looking to improve the methods for modelling the local mechanical environment in surgically repaired tibial plateau fractures, and investigate long term patient responses to postoperative weight bearing, there are some key gaps in the literature which need to be addressed. These are: (1) the methods applied to estimate neuromusculoskeletal function to estimate knee joint loading are likely insufficient for modelling TPF patient joint loading; (2) There is little agreement between computational and experimental models of TPF mechanics, requiring further investigation and model validation studies to understand the effect of modelling

parameters on predicted fragment motion; and (3) to address the effect of postoperative weight bearing on TPF patients, and how it affects postoperative outcomes.

The methods for generating physiologically plausible knee joint loads using neuromusculoskeletal modelling approaches require further development before being applied to TPF patients. This may be achieved through EMG-informed approaches, but augmenting them with probabilistic models could enhance their predictive capacities, reducing the amount of effort required from patients. Such a method first needs to be evaluated against experimentally measured joint loads before being applied to fracture patients.

Finite element and experimental models of TPF mechanics currently do not agree on the stiffness of fracture-fixation constructs when external load is applied. FE models are currently limited by their validation, where no study has included a form of validation or sensitivity study to understand and inform on the effect of modelling decisions on fragment displacements. Validation data can come from *ex vivo* models, however, the measurement resolution of these studies is limited to only external measurements of displacement due to external load. To improve the measurement resolution, new techniques for determining TPF fragment displacements due to external load need to be developed. Micro-CT imaging with concurrent mechanical testing may allow for higher resolution, internal displacements to be determined, furthering our understanding of fracture fragment mechanics. This has been explored for other parts of the musculoskeletal system, however, the internal mechanics of the tibial plateau and of TPFs has not been measured.

Patient recovery is a key factor in prescribing postoperative weight bearing. There are some methods for qualitatively assessing postoperative function like surveys, however, these do not agree with objectively measured functional outcomes in knee replacement cohorts. Currently, it is not known whether this is the same for TPF patients. As patients begin to bear weight, there is a risk that their repaired fracture fragments may migrate to unsafe levels, losing the reduction achieved at surgery. The

previously discussed *ex vivo* and *in silico* models of TPF currently do not have the resolution and accuracy required to allow for clinical decisions of postoperative weight bearing. This can be attributed to the low fracture-fixation stiffness seen in *ex vivo* models contrasted with the significantly stiffer fracture-fixation constructs seen in *in silico* models.

These key deficiencies in the literature led to the aim to ***improve upon methods for modelling the local mechanical environment in surgically repaired tibial plateau fractures, to further understand the mechanics involved in fracture recovery, and investigate long term patient responses to immediate postoperative weight bearing***. Through this thesis, these deficiencies will start to be addressed to better understand and model the local mechanical environment of TPFs when postoperative weight bearing is prescribed.

Chapter 3: EMG-informed neuromusculoskeletal models accurately predict knee loading measured using instrumented implants

This chapter has undergone peer review and is published in Gait and Posture:

Bennett, K. J., Pizzolato, C., Martelli, S., Bahl, J.S., Sivakumar, A., Atkins, G., Solomon, L., Thewlis, D. (2022). EMG-informed neuromusculoskeletal models accurately predict knee loading measured using instrumented implants. IEEE Transactions on Biomedical Engineering, 1. http://doi.org/10.1109/TBME.2022.3141067.

This chapter was exempt from ethical approval as it used a publicly available dataset.

Conference presentations associated with this chapter:

Bennett, K.J., Pizzolato C., Martelli, S., Bahl, J.S., Sivakumar A., Atkins, G.J., Solomon, L.B., & Thewlis, D. (2021). Estimations of Knee Joint Loading Using Generalized Methods and Muscle Recruitment Strategies (Poster). *In XVIII Congress of the International Society of Biomechanics Proceedings*. Stockholm, Sweden.

Bennett, K. J., Pizzolato C., Martelli, S., Bahl, J.S., Sivakumar A., Atkins, G.J., Solomon, L.B., & Thewlis, D. (2021). Variations in knee joint loading can be effectively modelled by exploring the uncertainty of muscle recruitment. In *The 12th Australasian Biomechanics Conference*. Online.

Chapter 3: EMG-informed neuromusculoskeletal models accurately predict knee loading measured using instrumented implants

Statement of authorship

Title of Paper	EMG-informed neuromusculoskeletal models accurately predict knee loading measured using instrumented implants
Publication Status	☑ Published ☐ Accepted for Publication ☐ Submitted for Publication ☐ Unpublished and Unsubmitted work written in manuscript style
Publication Details	K. J. Bennett et al., "EMG-informed neuromusculoskeletal models accurately predict knee loading measured using instrumented implants," in IEEE Transactions on Biomedical Engineering, doi: 10.1109/TBME.2022.3141067.

Principal Author

Name of Principal Author (Candidate)	Kieran James Bennett		
Contribution to the Paper	Conception, Knowledge, Analysis, Drafting		
Overall percentage (%)	75%		
Certification:	This paper reports on original research I conducted during the period of my Higher Degree by Research candidature and is not subject to any obligations or contractual agreements with a third party that would constrain its inclusion in this thesis. I am the primary author of this paper.		
Signature		Date	27/03/2022

Chapter 3: EMG-informed neuromusculoskeletal models accurately predict knee loading measured using instrumented implants

Co-Author Contributions

By signing the Statement of Authorship, each author certifies that:

i. the candidate's stated contribution to the publication is accurate (as detailed above);

ii. permission is granted for the candidate in include the publication in the thesis; and

iii. the sum of all co-author contributions is equal to 100% less the candidate's stated contribution.

Name of Co-Author	Claudio Pizzolato		
Contribution to the Paper	Knowledge, Analysis, Drafting		
Signature		Date	23/03/2022

Name of Co-Author	Saulo Martelli		
Contribution to the Paper	Conception, Knowledge, Analysis, Drafting		
Signature		Date	23/03/2022

Name of Co-Author	Jasvir Bahl		
Contribution to the Paper	Knowledge, Drafting		
Signature		Date	24/03/2022

Name of Co-Author	Arjun Sivakumar		
Contribution to the Paper	Knowledge, Drafting		
Signature		Date	23/03/2022

Chapter 3: EMG-informed neuromusculoskeletal models accurately predict knee loading measured using instrumented implants

Name of Co-Author	Gerald Atkins		
Contribution to the Paper	Knowledge, Drafting		
Signature		Date	29/03/2022

Name of Co-Author	L. Bogdan Solomon		
Contribution to the Paper	Knowledge, Drafting		
Signature		Date	23/03/2022

Name of Co-Author	Dominic Thewlis		
Contribution to the Paper	Conception, Knowledge, Analysis, Drafting		
Signature		Date	28/03/2022

Chapter 3: EMG-informed neuromusculoskeletal models accurately predict knee loading measured using instrumented implants

Abstract

Objective: Using a musculoskeletal modelling framework, we aimed to (1) estimate knee joint loading using static optimization (SO); (2) explore different calibration functions in electromyogram (EMG)-informed models used in estimating knee load; and (3) determine, when using an EMG-informed stochastic method, if the measured joint loadings are solutions to the muscle redundancy problem when investigating only the uncertainty in muscle forces.

Methods: Musculoskeletal models for three individuals with instrumented knee replacements were generated. Muscle forces were calculated using SO, EMG-informed, and EMG-informed stochastic methods. Measured knee joint loads from the prostheses were compared to the SO and EMG-informed solutions. Root mean square error (RMSE) in joint load estimation was calculated, and the muscle force ranges were compared.

Results: The RMSE ranged between 192-674 N, 152-487 N, and 7-108 N for the SO, the calibrated EMG-informed solution, and the best fit stochastic result, respectively. The stochastic method produced solution spaces encompassing the measured joint loading up to 98% of stance.

Conclusion: Uncertainty in muscle forces can account for total knee loading and it is recommended that, where possible, EMG measurements should be included to estimate knee joint loading.

Significance: This work shows that the inclusion of EMG-informed modelling allows for better estimation of knee joint loading when compared to SO.

Chapter 3: EMG-informed neuromusculoskeletal models accurately predict knee loading measured using instrumented implants

3.1 Introduction

Determining the internal loads acting on the knee joint is central to characterising its local mechanical environment during activity, and understanding how the environment alters with injury, disease and treatment (Saxby et al. 2020). However, measuring joint loads is only possible through instrumented joint replacements (Fregly et al. 2012; Taylor, WR et al. 2017), thus limiting knowledge of joint loading to a small cohort of people worldwide. Musculoskeletal modelling can be used to estimate joint loads using experimental data, including kinematics, foot-ground reaction forces, and electromyograms (EMG). This modelling framework estimates the muscle forces required to ensure joint equilibrium during motion (Anderson & Pandy 2001; Buchanan et al. 2004; Killen, Bryce A. et al. 2020).

The human musculoskeletal system is highly redundant, meaning there are more muscles than mechanical degrees of freedom. This implies that there is an infinite number of muscle activation solutions to produce the same observed motion (Loeb 2012; Martelli et al. 2013; Martelli et al. 2011). Several methods have been described to estimate muscle forces, including: static optimization (SO), which assumes that the nervous systems use an *a priori* optimal strategy for the control of muscles (Anderson & Pandy 2001; Crowninshield & Brand 1981; Delp et al. 2007); EMG-informed methods, which constrain the muscle activation using the experimentally measured muscle electrical activity in selected superficial muscles (Hoang et al. 2019; Lloyd & Besier 2003; Pizzolato et al. 2015); and stochastic methods, which generate a spectrum of muscle forces and joint loadings consistent with the model employed and uncertainties associated with model parameters (Martelli et al. 2015; Martelli et al. 2013).

EMG-informed methods can model individual muscle activation (Gerus et al. 2013; Hoang et al. 2019; Kian et al. 2019; Lloyd & Buchanan 1996; Manal & Buchanan 2013), accounting for co-contractions (Hoang et al. 2019), but require parameter calibration due to the nonlinear relationships between EMG measures and muscle function (Buchanan et al. 2004; Lloyd & Besier 2003). In calibration, physiological

neuromuscular parameters are adjusted to minimize an objective function. Several objective functions have previously been implemented to generate physiologically plausible joint contact forces (contact forces similar to those measured *in vivo*) (Davico et al. 2020; Hoang et al. 2019), and validated for one individual but their generalizability has not been evaluated (Gerus et al. 2013). It is currently unclear if there exists an optimal calibration function which could be used for multiple subjects to model muscle combinations while yielding accurate estimation of joint loading.

Stochastic methods can explore the variability in muscle contributions to motion by sampling the space of muscle forces satisfying joint equilibrium within prescribed force constraints (Martelli et al. 2015; van Veen, Mazza & Viceconti 2020). For example, the uncertainty in muscle forces (due to a lack of known muscle forces) can be modelled by constraining them to within their physiological boundaries (i.e., between zero and their peak force). Uncertainty in measured parameters (i.e., EMG measurements, body position, and ground reaction forces) can also be investigated in this framework to statistically model movement. Van Veen and co-workers demonstrated that there exists a muscle coordination which generates the measured knee load in the model of one volunteer while walking (van Veen, Mazza & Viceconti 2020). However, there were discrepancies between stochastic perturbations of a SO solution, the measured knee load, and the related muscle coordination. It is not currently known if, using an EMG-informed stochastic approach, modelling the uncertainty in muscle forces can be used to generate knee loading solution spaces which encompass measured joint loads.

The aims of this study were to: (1) estimate knee loading using SO; (2) explore different calibration functions in EMG-informed models used in estimating knee load; and (3) determine, when using an EMG-informed stochastic method, if the measured joint loadings are solutions to the muscle redundancy problem when investigating only the uncertainty in muscle forces. We hypothesize that (1) using a single optimization function to calibrate EMG-informed models, accurate estimates of joint loading can be obtained for multiple individuals and (2) the knee load will be contained within the

range of solutions in the stochastic solution. All estimations of knee load, including their directional components, will be compared to the loads measured *in vivo*.

3.2 Methods

3.2.1 Data

Data were obtained from the Grand Challenge Competition to Predict *In Vivo* Knee Loads (Fregly et al. 2012), specifically, those for challenges four, five, and six. These were chosen due to their file format (challenges three onwards present data in .c3d) and volume of walking data available (challenge three had four useable trials, while challenges four and five had five useable trials, and challenge six had six useable trials). Each challenge includes a comprehensive dataset from a single participant with an instrumented knee replacement. The participants in challenges five and six both had the second generation of the eTibia implant, which measured directional loading as individual components. The mass of each participant was 70 kg, 75 kg, and 66.7 kg for challenges 4, 5, and 6 respectively.

3.2.2 Preprocessing and EMG

The marker trajectories, ground reaction forces, and EMG data from one static trial and five over ground walking gait trials were used for each of the three participants. Marker trajectories and ground reaction forces were low pass filtered with a cutoff frequency of 8 Hz, and EMG signals were band-pass filtered to 30-300 Hz (Buchanan et al. 2004), full wave rectified, low pass filtered with a cutoff frequency of 6Hz, and subsequently amplitude normalized to the maximum value across all trials (Buchanan et al. 2004; Mantoan et al. 2015). All filtering was completed using 2nd order zero lag Butterworth filters.

Between 10 and 11 EMG signals were used for each challenge (Table 6, processed signals in Supplementary Material). EMG signals were not used if the muscles were weak (model maximum isometric force less than 500 N. i.e. tensor fascia latae, and

sartorius), if the signal was too noisy (as determined by a single operator via visual inspection, considering the raw EMG signals), or if the inclusion of the measurements produced spurious results in the EMG-informed solution (e.g. soleus in challenges 4 and 5 were estimated to activate to over 50% because it was the most 'efficient' muscle to drive the ankle plantarflexion).

Table 6 Muscles informed by EMG in the EMG-informed and stochastic models for each challenge.

	Challenge		
Muscle	4	5	6
Vastus lateralis	✓	✓	✓
Vastus medialis	✓	✓	Noise
Tibialis anterior	✓	✓	✓
Biceps femoris long head	✓	✓	Noise
Semimembranosus	✓	✓	✓
Lateral gastrocnemius	✓	✓	✓
Medial gastrocnemius	✓	✓	✓
Gluteus maximus	✓	Noise	✓
Gluteus medius	Noise	Noise	Noise
Adductor magnus	✓	✓	✓
Rectus femoris	✓	✓	✓
Peroneus longus	✓	✓	✓
Soleus	Produced Spurious Results		✓

3.2.3 Musculoskeletal Models

The OpenSim lower limb model (Gait2392) (Delp et al. 2007) was used as a base to tailor individual musculoskeletal models. This model has 23 degrees of freedom (DOF) and 92 musculotendon units (MTUs) (Delp et al. 2007). The model was scaled to the mass and anthropometry of each participant using static trial marker data. The Musculoskeletal Atlas Project (MAPClient) was used to perform principal component morphing of the MAPClient pelvis, femur, and shank to the experimental markers in the static trial, whereby scale factors for the three segments were calculated as the distance between corresponding marker pairs on the two models (Zhang, Sorby, et al.

2014). The trunk and feet were linearly scaled, as statistical shape models for these segments are not currently implemented in the MAPClient (Zhang, Malcolm, et al. 2014). Segment masses were determined using the mass distributions from de Leva (1996), with additional mass added to the calcaneus segment, based on the shoe worn (approximately 0.3 kg). The muscle and tendon geometry were unchanged from the gait2392 model; however, their lengths were optimized based on cadaveric specimens (Winby, Lloyd & Kirk 2008) using the implementation from Modenese et al. (2016). Muscle maximum isometric forces were then scaled to the participant's height and mass, using the relationships from Handsfield et al. (2014), with a maximum muscle stress of 0.61 MPa (Buchanan et al. 2004).

Using OpenSim (Version 3.3) (Delp et al. 2007), the inverse kinematics tool reconstructed the model motion from marker data (Delp et al. 2007). External joint moments were calculated using the recursive Newton-Euler method in the inverse dynamics tool, and muscle moment arms, lengths, and velocities were calculated using the muscle analysis tool (Delp et al. 2007).

3.2.4 Muscle Recruitment Models

Three methods to determine muscle recruitment were implemented: (1) SO; (2) EMG-informed modelling, and (3) an EMG-informed stochastic method. For the EMG-informed and stochastic methods, the gait2392 model was reduced to only the implanted side.

3.2.4.1 Static Optimization

Muscle contributions were calculated to balance the external moments (τ) (2) by minimizing muscle activation squared (a_m) in the objective function (3) using the static optimization tool in OpenSim (Delp et al. 2007). Muscle activations were related to joint moments using the Hill type muscle model $f(F_m^0, l_m, v_m)$ multiplied by their lever arms ($r_{m,j}$) (Hill 1938). The activation was constrained for each muscle (m) to between zero and one (Anderson & Pandy 2001). The force-length-velocity relationships were

used, and reserve actuators were included with an optimal moment of 1 Nm. Joint loads were calculated using the joint reaction analysis tool.

$$\sum_{m=1}^{n}[a_m f(F_m^0, l_m, v_m)]r_{m,j} = \tau_j \quad (2)$$

$$f_{obj} = \sum_{m=1}^{n}(a_m)^2 \quad (3)$$

3.2.4.2 Calibrated EMG-Informed Neuromusculoskeletal Modelling Toolbox

The EMG signals were mapped to their corresponding model MTUs (Table 7) (Sartori et al. 2012). To do this, the non-linear relationships between EMG signals and MTU activations (C1, C2, and shape factor from the work of Lloyd and Besier (2003), and a parameter to scale the EMG signal) were modified using the Calibrated EMG-Informed Neuromusculoskeletal Modelling Toolbox (CEINMS) calibration step (Buchanan et al. 2004; Pizzolato et al. 2015). In this step, muscle parameters are adjusted such that a user defined objective function is minimized. The generic composite objective function (4) was applied. In this, f_{obj} is the objective function, w_n is the weighting coefficient for the function (f_n) and k_n is the exponent.

Table 7 Musculotendon units in the gait2392 model driven by EMG signals.

EMG Signal	Gait 2392 MTU
Vastus lateralis	vas_lat
Vastus medialis	vas_med
Tibialis anterior	tib_ant
Biceps femoris long head	bifemlh
Semimembranosus	semimem, semiten
Lateral gastrocnemius	lat_gas
Medial gastrocnemius	med_gas
Gluteus maximus	glut_max (1,2,3)
Adductor magnus	add_mag (1,2,3)
Rectus femoris	rec_fem
Peroneus longus	per_long
Soleus	soleus

$$f_{obj} = w_1 f_1^{k_1} + w_2 f_2^{k_1} + \cdots + w_n f_n^{k_n} \quad (4)$$

Based on the work from Gerus et al. (Gerus et al. 2013) and Hoang et al. (Hoang et al. 2019), it was necessary to include model-estimated joint loading (the sum of external joint forces and internal muscle forces) in the calibration step to minimize total muscle forces, and hence joint loads. Therefore, the objective functions investigated in this study minimized a combination of peak joint loading (F_{joint}^{peak}) and normalized error in the external moments from the filtered moments (τ), and the CEINMS estimated moments ($\hat{\tau}$) (5). Twenty-four different combinations of weightings and exponents were tested to determine a function which minimized root mean square error (RMSE) between the *in vivo* measured and estimated joint loading for all trials (functions in Supplementary Material).

$$f_{obj} = w_1 NRMSE(\tau, \hat{\tau})^{k_1} + w_2 {F_{hip}^{peak}}^{k_2} + w_3 {F_{knee}^{peak}}^{k_3} + w_4 {F_{ankle}^{peak}}^{k_4} \quad (5)$$

Joint moments from inverse dynamics were filtered using a low-pass 2nd order zero-lag Butterworth filter with cut off frequency 8 Hz. This was done to minimize the effect of any discontinuities resulting from the initial force platform strike on the CEINMS solution. Muscle forces for each trial were estimated by driving four degrees of freedom (hip flexion, adduction; knee flexion; ankle flexion) in EMG-assisted mode (Sartori, Farina & Lloyd 2014). For each subject, the first two trials were used for calibration, and subsequent three for analysis. Joint loads were calculated using the inbuilt CEINMS joint reaction solver.

3.2.4.3 EMG-informed Stochastic Modelling

The solution space of the equilibrium equation at the joints (6) was formulated using the muscle lever arms ($\bar{B}$) and the external joint moments ($\bar{\tau}$) from muscle analysis and inverse dynamics. The muscle forces ($\bar{F}$) were then sampled using the Markov-Chain Monte-Carlo method implemented in Metabolica (Martelli et al. 2015). The constraints on the muscle forces were set up in two steps. First step: muscles were bound between

zero and one half of the peak muscle force, determined using the force-length-velocity Hill-type muscle model from Thelen (2003). Second step: muscles that were driven in the EMG-informed approach were constrained between zero and one standard deviation above the mean muscle force estimated from CEINMS. The solution space of the equilibrium equation at the joints was sampled using one million iterations per frame and constraining external moment error to 1 Nm. Joint loads were calculated by multiplying the direction vectors of each muscle by their force and adding that to the body forces calculated using the joint reaction tool in OpenSim.

$$\bar{B} \times \bar{F} = \bar{\tau} \tag{6}$$

3.2.5 Data Analysis

Joint loadings were normalized to 101 data points across stance phase and RMSE calculated between measured and modelled knee joint loadings for both SO and EMG-informed methods. Statistical analyses were performed using non-parametric paired one-dimensional t-tests using statistical non-parametric mapping (SnPM) in spm1d with significance set at α=0.125 ($1/2^{nTrials}$) (Pataky 2012; Pataky, TC, Vanrenterghem, J & Robinson, MA 2015). The directional loading for each method was also presented for qualitative assessment. To investigate the variation in muscle control, the range muscle forces for each method were qualitatively compared.

3.3 Results

Objective function number eight (7) resulted in the lowest mean RMSE among all objective functions evaluated while also not showing any force discontinuities (summary of RMSE shown in Figure 6, Joint loadings for the three best calibration functions shown in Supplementary Material). This function compromised between minimizing the moment error and maximum model predicted joint loads. This reduced the total loading at each joint at the expense of some moment balancing (comparison of joint moments in Supplementary Material).

$$f_{obj} = \text{NRMSE}(\tau, \hat{\tau})^2 + 0.05 \cdot \left(\max\left(F_{hip}\right) + \max(F_{knee}) + \max(F_{ankle})\right) \quad (7)$$

For challenges four and five (Figure 7), SO, on average, overestimated the second peak loading by 717 N (0.95 BW range: -55-1432 N, -0.09-1.95 BW) whereas the EMG-informed solutions overestimated the initial loading by, on average, 560 N (0.8 BW, range -259-1202 N, -0.38-1.6 BW) but produced a lower error for the second peak loads (mean absolute error 216 N, 0.31 BW, range 93-328 N, 0.13-0.5 BW). The stochastic solution space encompassed the measured loading for 76% (challenge 6, Trial 3) to 98% (challenge 5, Trials 1, 3) of stance phase. R^2 for the SO and CEINMS approaches ranged from 0.25-0.77 and 0.1-0.82 respectively.

Comparing the directional components of the total knee loading (only available for challenges 5 and 6) for SO and CEINMS (Figure 8-9), the superior-inferior components were best estimated by the models. Considering the peak superior-inferior loading, the SO solution shows error in challenge 5 (1324-1438 N, 1.8-1.96 BW), and a comparably smaller error in challenge 6 (2-495 N, 0-0.76 BW). For both methods, the anterior posterior (RMSE SO: 170-250 N, 0.26-0.34 BW, CEINMS: 267-386 N, 0.41-0.52 BW) and medial-lateral (RMSE SO: 52-89 N, 0.08-0.14 BW, CEINMS: 65-112 N, 0.09-0.17 BW) loads were not well estimated. Considering the solution space of possible joint loading scenarios from the stochastic method, only the superior-inferior loading was entirely within the solution space for all trials.

The SnPM analysis of the knee loads (Figure 10) showed a series of very short supra-threshold clusters where the maximum detectable significance (0.125) was exceeded. None of these clusters, however, were longer than 1% of stance phase. Across the nine trials, the mean RMSE (Figure 11) for SO was 422 N (0.61 BW, range 192-674 N, 0.29-0.9 BW) and for CEINMS was 342 N (0.5 BW, range 152-487 N, 0.22-0.65 BW).

To assess the plausibility of muscle recruitment patterns, we compared the estimated forces of each of the muscles which contribute to knee loading for each method to each other (Figure 12-14). In all three challenge datasets, the SO solution estimated the

medial gastrocnemius force to be 2.75-3.6 times more than the CEINMS solutions. Using the stochastic method, for challenges 4 and 5, where the vastus medialis was constrained to EMG measures, there were no solutions where the rectus femoris activated to one half of its maximum possible force (shown by the stochastic solution space (gray) not reaching the maximum force constraint in the stochastic approach).

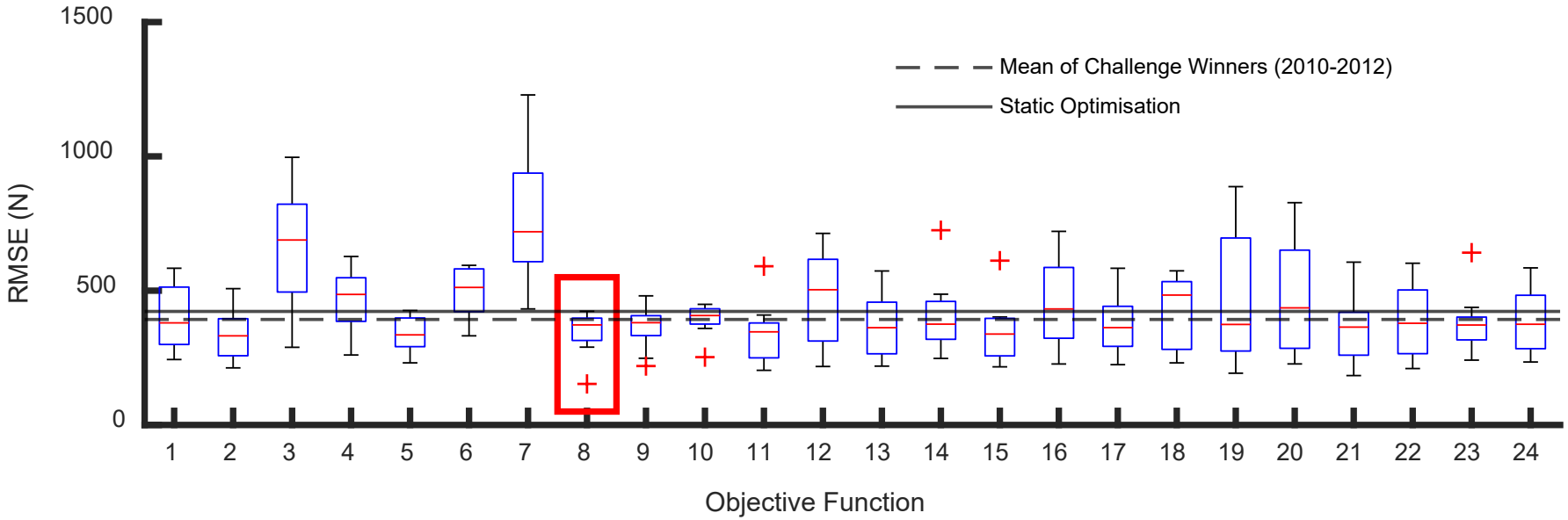

Figure 6 Box plots showing the RMSE for each of the objective functions tested for CEINMS (summarized in Supplementary Material) with the selected calibration function highlighted. Red pluses are trials which were statistical outlier for that objective function.

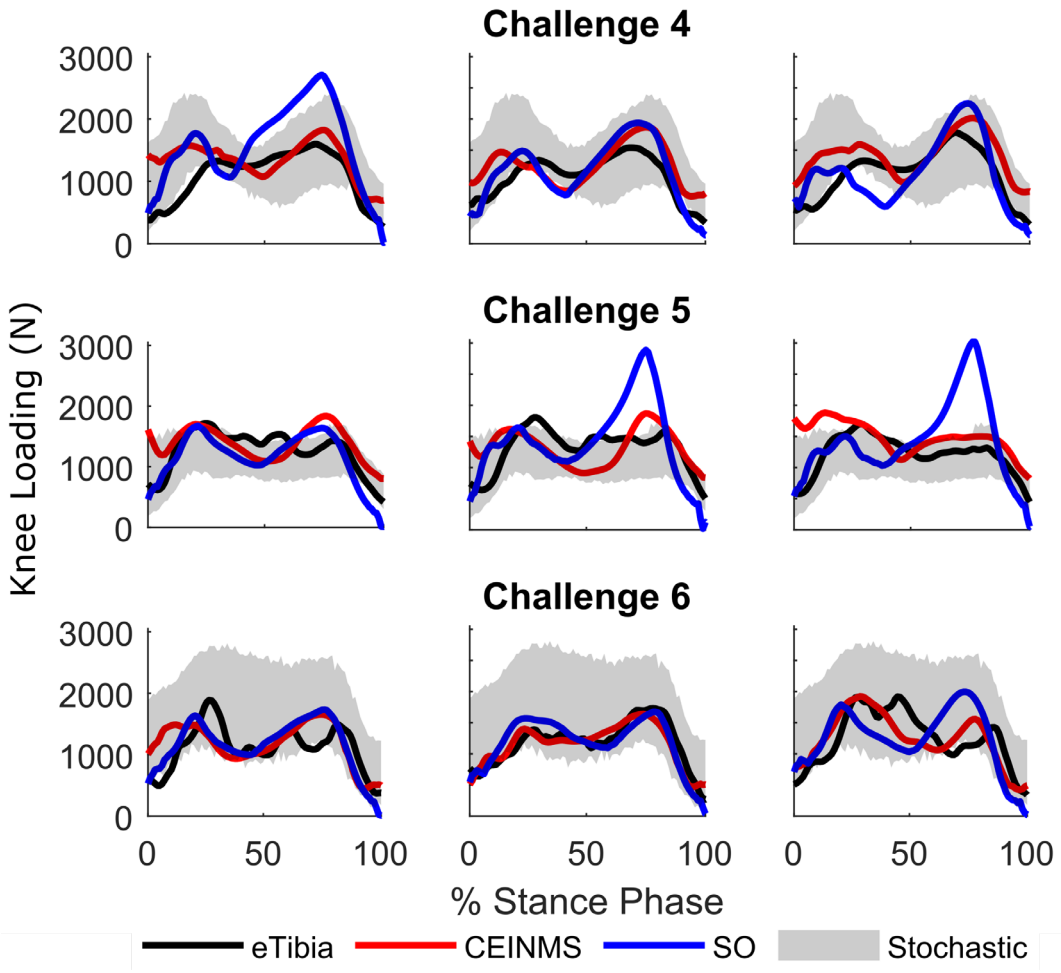

Figure 7 Knee loads from the instrumented prostheses (eTibia, black), overlaid with the solutions from CEINMS (red), SO (blue) and the stochastic method (gray) for individual over ground walking trials.

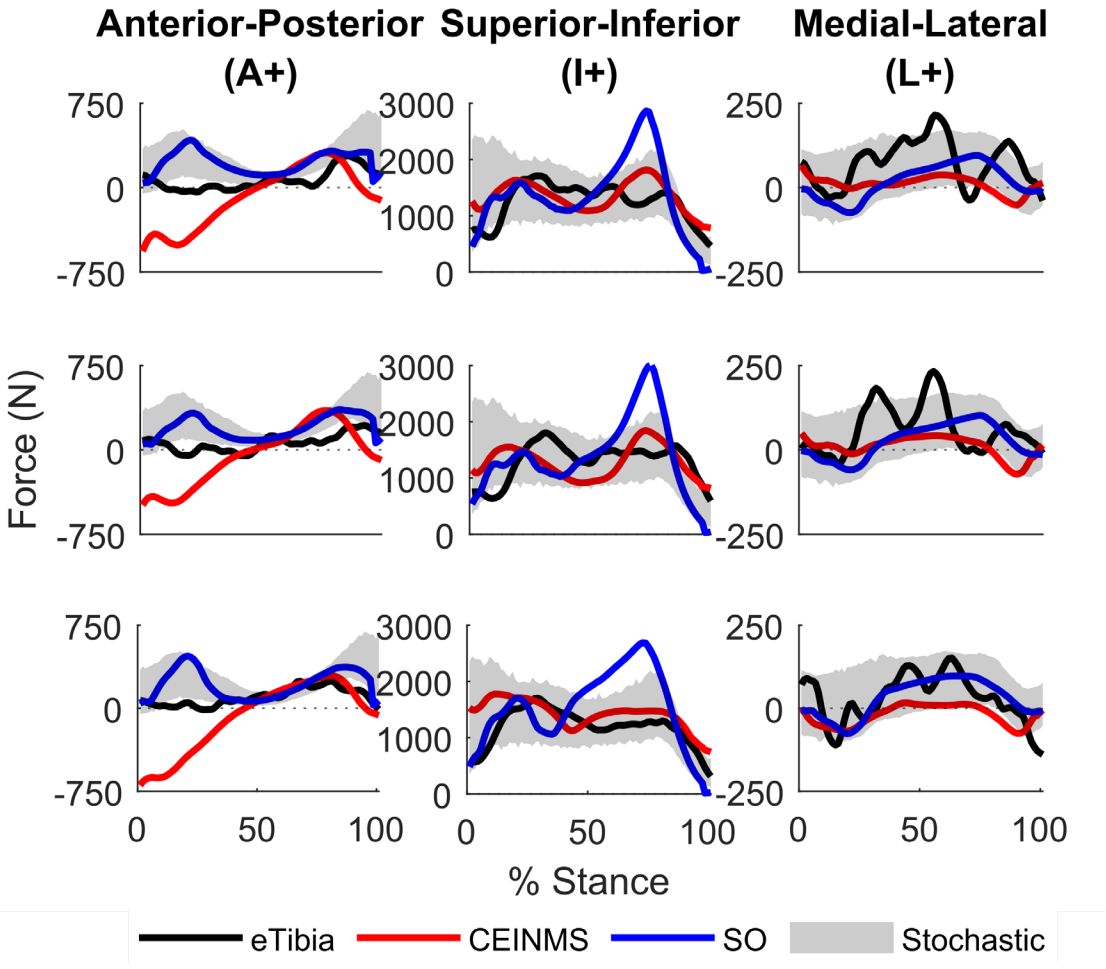

Figure 8 Directional components of joint loading for the challenge 5 dataset from the instrumented prostheses (eTibia, black), overlaid with the solutions from SO (blue), CEINMS (red), and the stochastic method (grey) for individual over ground walking trials. Each row represents a single trial, and for each direction, anterior, inferior, and lateral are positive.

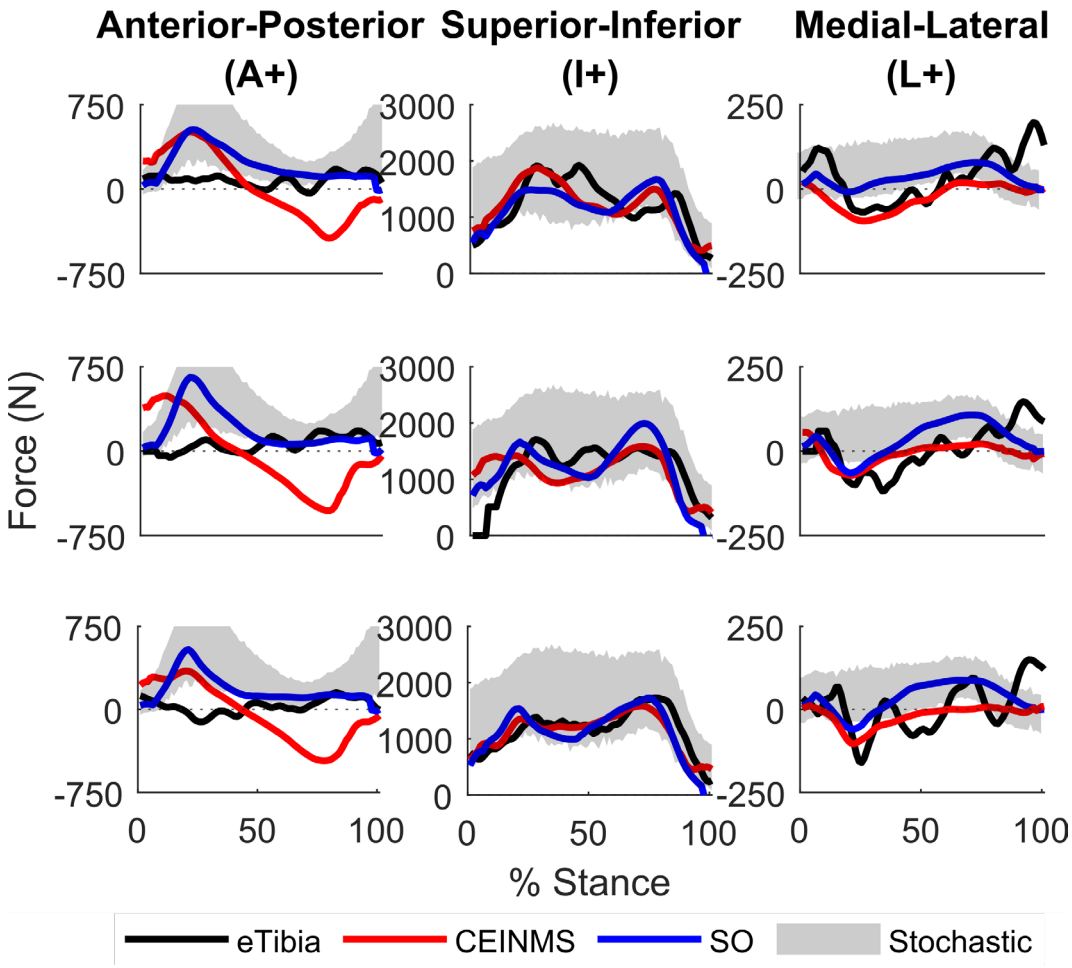

Figure 9 Directional components of joint loading for the challenge 6 dataset from the instrumented prostheses (eTibia, black), overlaid with the solutions from SO (blue), CEINMS (red), and the stochastic method (grey) for individual over ground walking trials. Each row represents a single trial, and for each direction, anterior, inferior, and lateral are positive

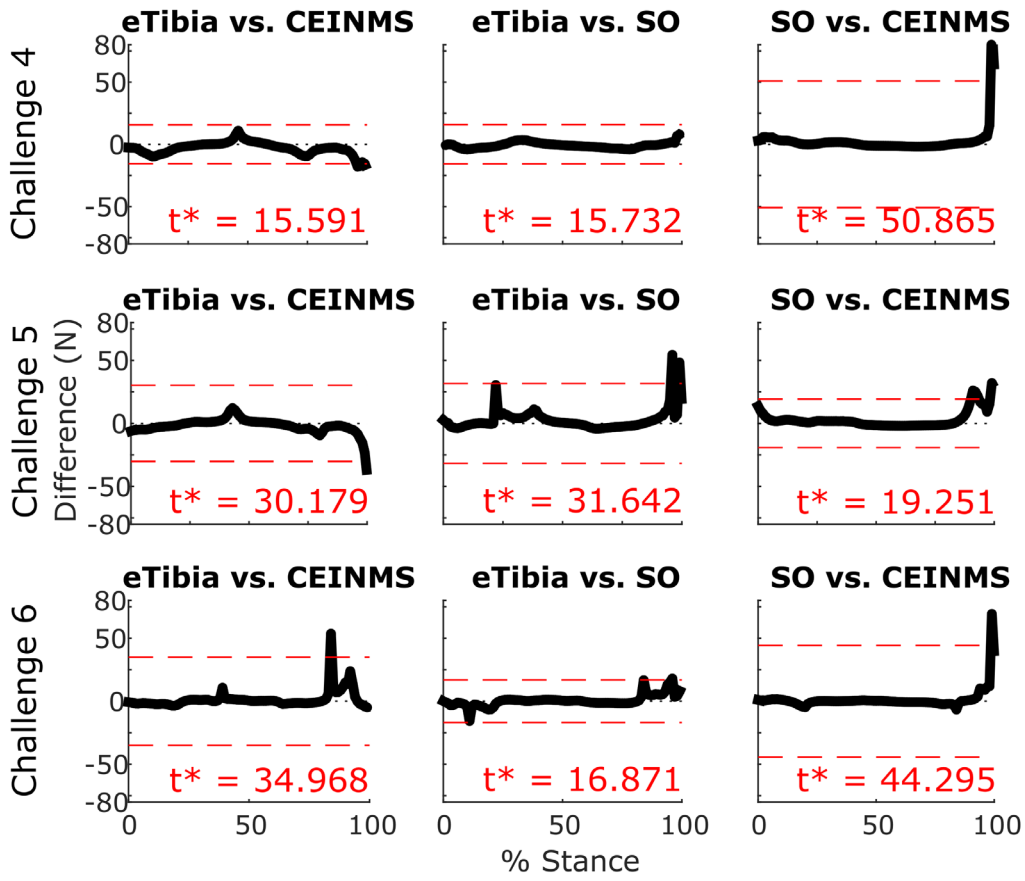

Figure 10 SnPM results comparing the eTibia measurement to CEINMS (column one), the eTibia measurement to SO (column 2), and SO to CEINMS (column three). Significance is set at α=0.125 and all suprathreshold clusters have p=0.125.

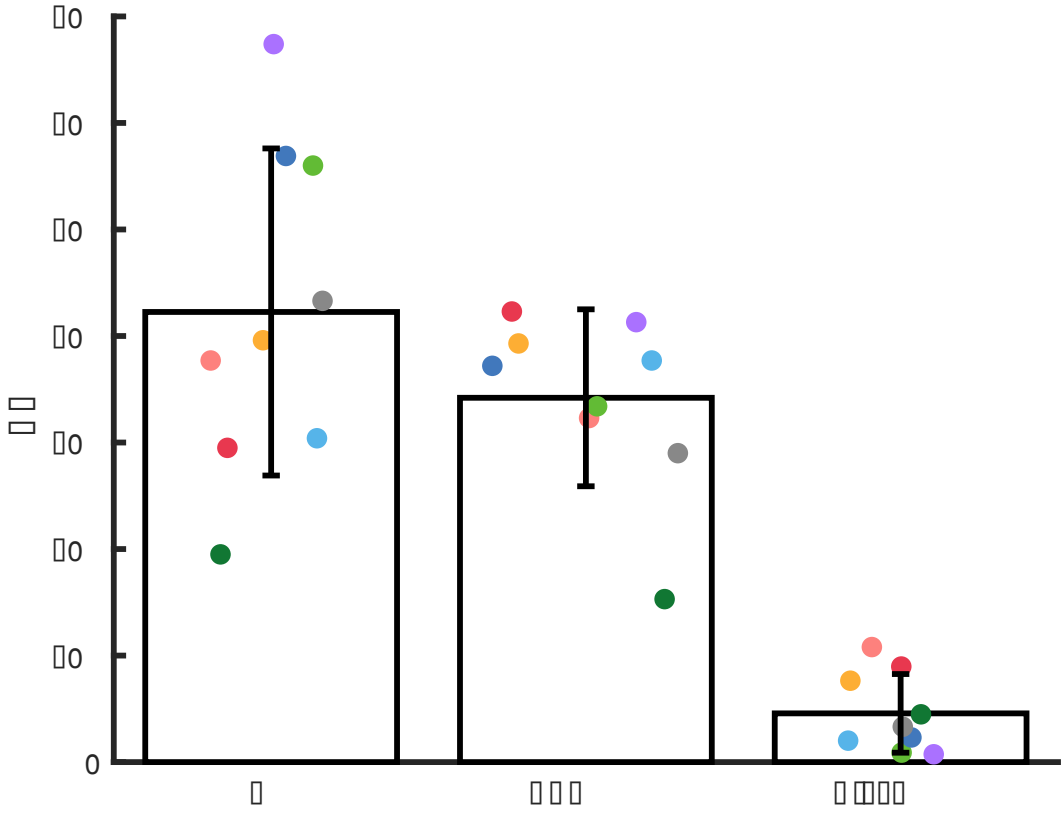

Figure 11 RMSE mean and standard deviation in estimation of total knee joint loading for SO, CEINMS, and the best fit stochastic solutions. Colors indicate separate trials.

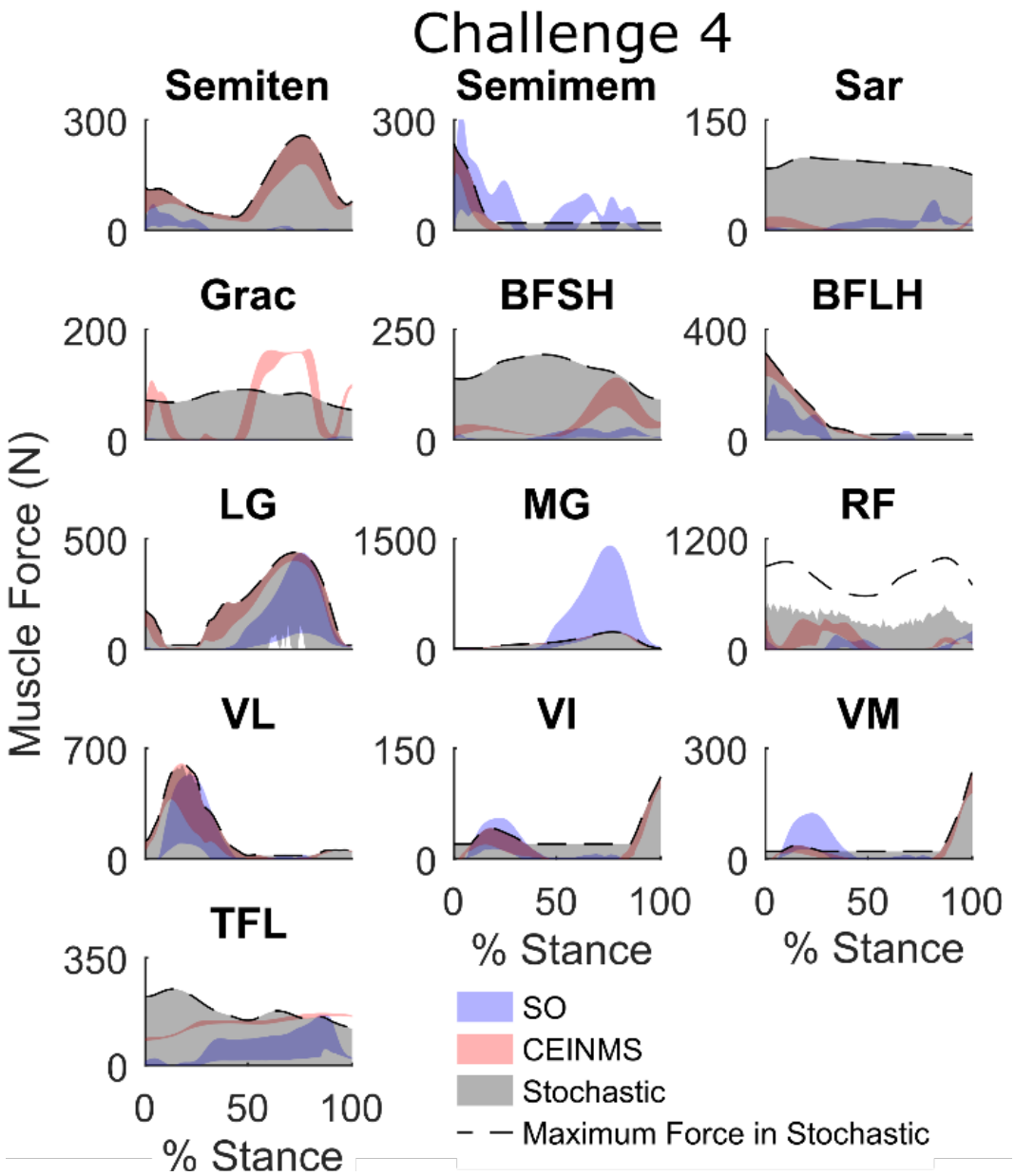

Figure 12 Muscle forces (N) contributing to joint loading for SO (mean±SD), CEINMS (mean±SD), the stochastic method (range) for challenge 4. The muscles presented are: Semiten = semitendinosus; Semimem = semimembranosus; Sar = Sartorius; Grac = gracilis; BFSH = biceps femoris short head; BFLH = biceps femoris long head; LG = lateral gastrocnemius; MG = medial gastrocnemius; RF = rectus femoris; VL = vastus lateralis; VI = vastus intermedialis; VM = vastus medialis; and TFL = tensor fascia latae.

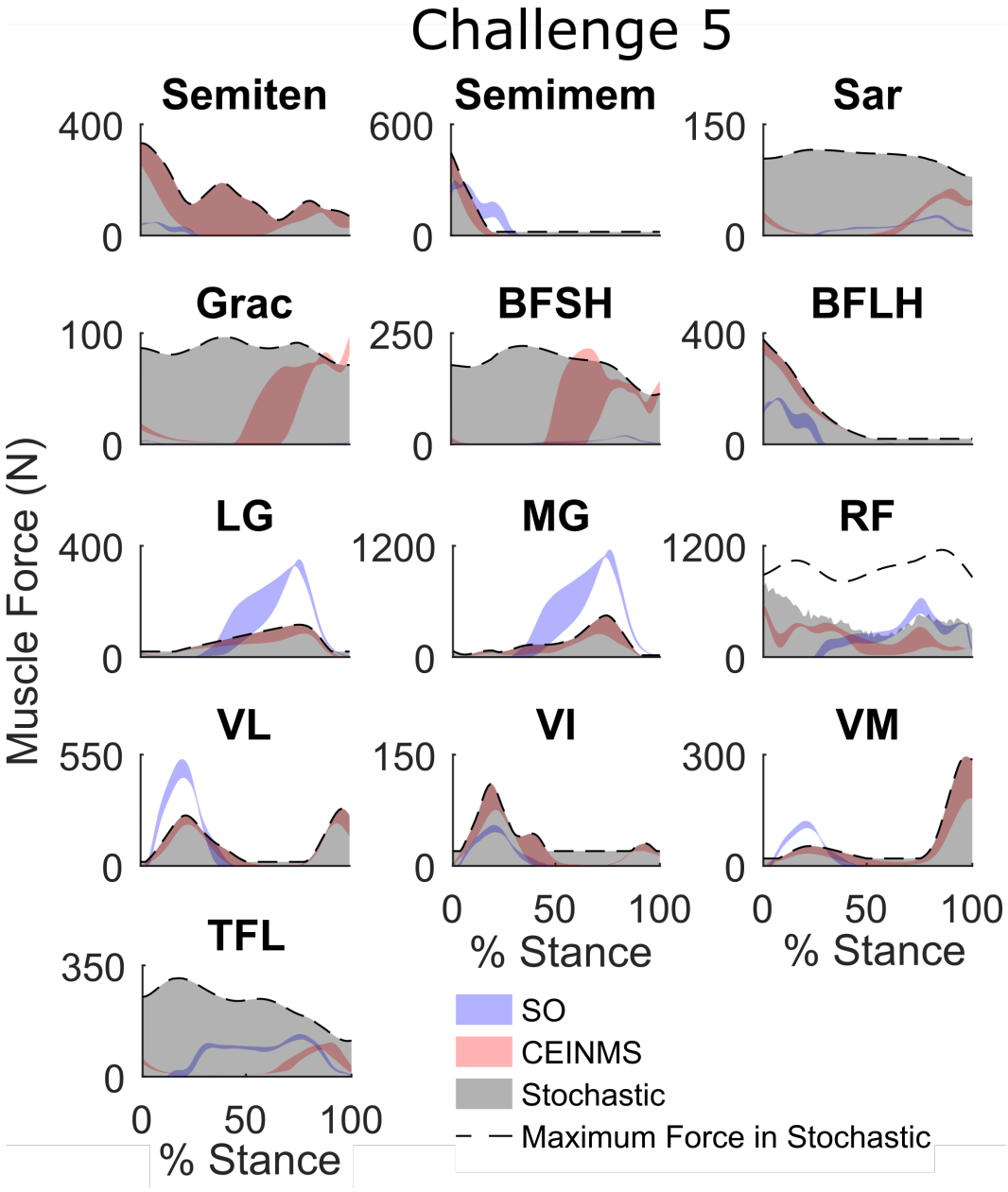

Figure 13 Muscle forces (N) contributing to joint loading for SO (mean±SD), CEINMS (mean±SD), the stochastic method (range) for challenge 5. The muscles presented are: Semiten = semitendinosus; Semimem = semimembranosus; Sar = Sartorius; Grac = gracilis; BFSH = biceps femoris short head; BFLH = biceps femoris long head; LG = lateral gastrocnemius; MG = medial gastrocnemius; RF = rectus femoris; VL = vastus lateralis; VI = vastus intermedialis; VM = vastus medialis; and TFL = tensor fascia latae.

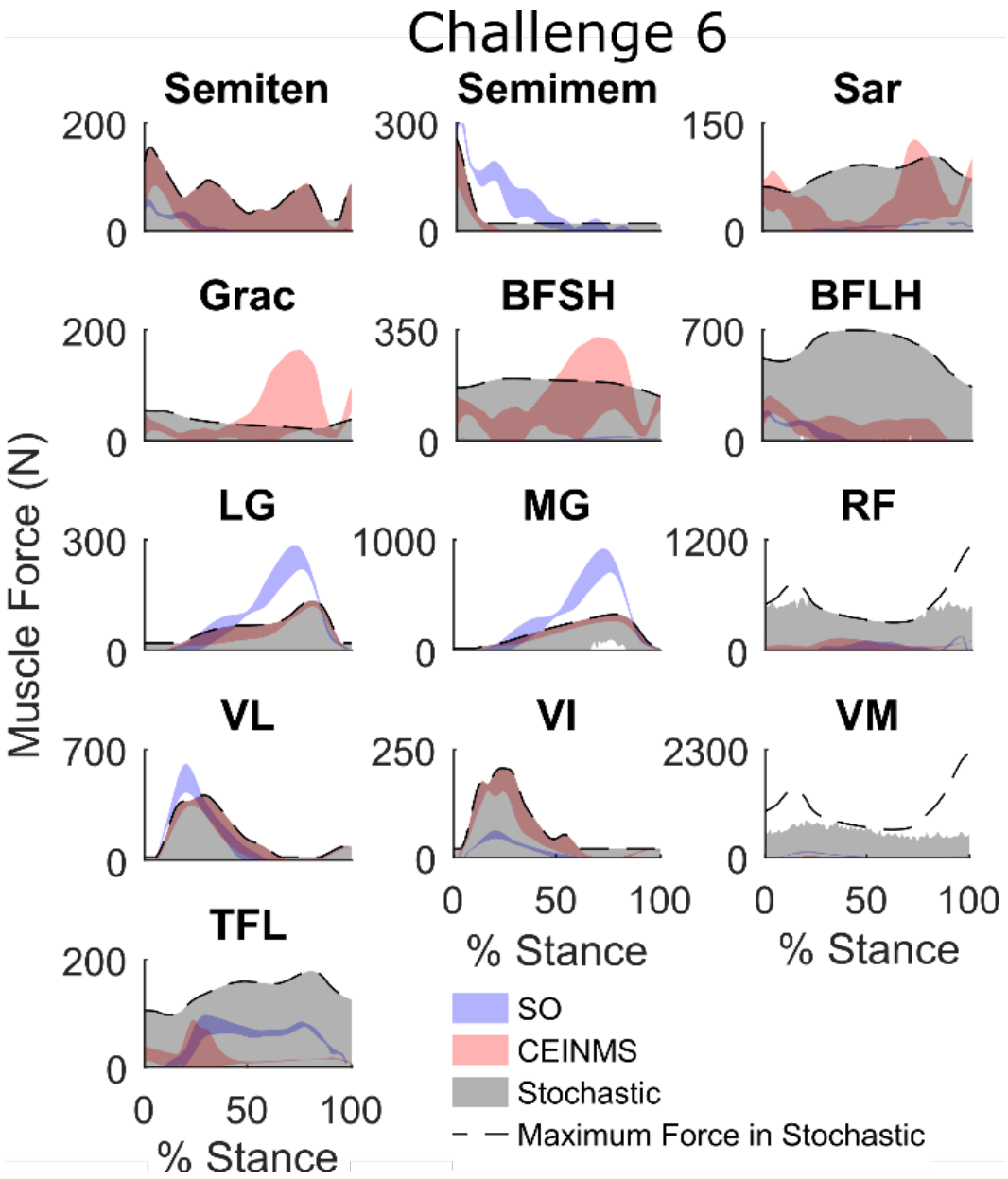

Figure 14 Muscle forces (N) contributing to joint loading for SO (mean±SD), CEINMS (mean±SD), the stochastic method (range) for challenge 6. The muscles presented are: Semiten = semitendinosus; Semimem = semimembranosus; Sar = Sartorius; Grac = gracilis; BFSH = biceps femoris short head; BFLH = biceps femoris long head; LG = lateral gastrocnemius; MG = medial gastrocnemius; RF = rectus femoris; VL = vastus lateralis; VI = vastus intermedialis; VM = vastus medialis; and TFL = tensor fascia latae.

Each method required varying levels of computational resources. SO solutions required seconds to minutes to solve on a desktop PC, whereas the CEINMS calibration step required 25.8 hours with 201,750 evaluations per calibration. All models were calibrated (3 subjects × 24 objective functions) simultaneously in 110.5 hours on a desktop HPC (Intel Xeon E52630v4 2.20 GHz, 20 cores). Following calibration, trials were solved in less than one minute each. The stochastic method was implemented on the Phoenix HPC, where eight cores were used to calculate muscle combinations in parallel, requiring 2.5 hours to solve for 93 frames and generating up to 30 GB of solutions per trial.

3.4 Discussion

This study found that the use of EMG information increases the accuracy of knee loading prediction. A single objective function was identified for calibration of EMG-informed models, which resulted in improved estimates of knee loading when compared to SO. Using an EMG-informed stochastic method, the variation in total knee loading was estimated by investigating the uncertainty in muscle forces.

We identified an optimal objective function for calibrating model neuromuscular parameters to use in EMG-informed modelling. Incorporation of the model estimated load for the joint of interest in calibration has previously been shown to improve estimates of loading at the knee (Gerus et al. 2013) and the hip (Hoang et al. 2019). Here, we found that by minimizing a combination of the model predicted hip, knee, and ankle loading resulted in the best estimate of knee loading when compared to measured data. The resulting calibrated model, used in combination with an EMG-assisted method, also outperformed SO for multiple individuals, in terms of knee joint contact force prediction accuracy.

Determining the error associated with musculoskeletal simulations was made possible through direct comparison with measured joint loads. Using SO, the second peak loading was overestimated. This was more pronounced in the data from

challenge 5, where a peak error of 1432 N (1.95 BW) was obtained in one trial. This overestimation was consistent with previous studies reporting on similar datasets (Imani Nejad et al. 2020; Knarr & Higginson 2015). It is likely that the optimization task preferentially activated the medial gastrocnemius to plantar flex the ankle due to its maximum isometric force. The result of preferentially activating the medial gastrocnemius is an increase in second peak loading at the knee. The EMG-informed approach predicted, on average, more accurate knee contact forces when compared to SO. There was some error in joint loading during initial contact, but estimates of second peak loading were closer to the loads measured.

The directional components of the loads for both SO and CEINMS were different to those measured in both the A-P and M-L directions. The results of the stochastic method show that the directional components of joint load could not be estimated based only on the variations in muscle forces. Previous studies using multiple DOF knees have shown good estimates of M-L and A-P loading (Esrafilian et al. 2021; Hast & Piazza 2013). While a single DOF planar knee, as used here, is sufficient to obtain estimates of total load, it is unable to accurately estimate the directional components of loading.

The muscle forces generated in the CEINMS solution are different to those from the SO solution. While some larger muscles (vastus and gastrocnemii) show similar activation patterns, weaker muscles show distinctly different activation patterns (biceps femoris, gracilis, sartorius) to generate the same external moments. When comparing muscles which were driven using EMG, the CEINMS solutions used less medial gastrocnemius activation, and instead used other, smaller muscles to drive motion. The stochastic method shows that, using the CEINMS solutions to constrain driven muscle solutions, the constraints on the muscles used for knee flexion (semiten, semimem, biceps femoris, gastrocnemii) limited the maximum knee extensor muscle forces (vastus, rectus femoris) through maintenance of external moment balance.

This study showed, through application, that an EMG-informed stochastic method of muscle recruitment employed can be applied to multiple individuals to generate knee

loading solution spaces encompassing measured joint loads, extending the work of Martelli et al. (2015) and van Veen, Mazza and Viceconti (2020). The use of the stochastic method in this study allowed for further interrogation of muscle recruitment strategies. Based on this interrogation, we hypothesize that more physiological motion constraints of the knee joint may improve prediction of the knee force components, especially in the A-P direction. The stochastic approach allows for investigation into the range of possible muscle recruitment, providing a solution space of joint loadings rather than a single value. This is both a strength, and a weakness of the approach, where multiple muscle control strategies can be accounted for, however, a single, time continuous control solution cannot be easily determined. This method may be further perturbed to include selective muscle weakness, or to account for error in data collection procedures by modelling the measured parameters as stochastic parameters surrounding the recorded value.

Using statistical shape models to scale musculoskeletal anatomy reduces error in anatomical definitions by up to 82% (Bahl et al. 2019), and in kinematic reconstruction when compared to linear scaling (R^2 range from 0.724-0.997 for linear scaling, and 0.994-1.000 for statistical shape scaling) (Bakke & Besier 2020). A limitation of this study is that the scaled musculoskeletal anatomy was not compared to medical imaging to further assess the accuracy of the models. The statistical methods employed do not account for geometric variance of knee, which has a large effect on reconstructed tibiofemoral motion and subsequent measures of muscle function (Martelli et al. 2020). This geometric variance also includes differences in muscle insertion locations, directions, and moment arms, which we were unable to account for using statistical shape modelling. These data all require medical imaging, which is available for the Grand Challenge datasets at the knee, but is not typically available for people undergoing gait analysis.

This study was limited by the amount of available data. Constraining this investigation to only static and over ground walking trials meant only five or six trials were available for each challenge. Further, in challenges 4 and 5, some recordings were

cropped to within 55 frames before the initial heel strike. To process EMG data and run CEINMS, 75 frames of data are required. Therefore, to run CEINMS, additional frames were added to the beginning of the trials by taking the first n frames of data, reflecting them, and appending them to the beginning of the trial. Due to the initial feed-forward control implemented in CEINMS, there were higher estimations of joint loading at the start of trials, as the external dynamics were partially from a foot contact event before the true foot contact event, requiring muscles to be active.

We used two walking trials from each participant for calibrating the CEINMS models and did not include them in the final analysis as they may have biased the results. This resulted in three trials for comparison for each participant, which is insufficient for using statistical parametric mapping. Even when using statistical non-parametric mapping, the smallest significance (p value) that can be detected is $1/2^{ntrials}$, which for three trials is 0.125. Additionally, including a wide repertoire of motor tasks for the NMS model calibration improved estimated of joint contact forces at the shoulder, compared to calibration that used a single task (Kian et al. 2021). It is plausible that these same observations could extend to the knee joint, and that including motor tasks other than walking in the calibration might further improve estimates of knee contact forces.

There was an inconsistency between the hip adduction moments generated in the CEINMS solution and those calculated using inverse dynamics. The gluteus medius typically drives the hip adduction moment, but because the available EMG data was noisy, we decided to exclude it from the simulation. The gluteus maximus (which was driven using EMG) was employed to drive hip motion, but was unable to balance both the flexion the adduction, resulting in the inconsistency identified (a comparison between the gluteal muscle forces in each method is in supplementary material). This was observed across all calibration functions, suggesting that, when using an EMG informed approach, it is important to capture the activation of the gluteus medius muscles.

Further, by not driving 'weak' muscles in CEINMS, knee stabilisers, like the tensor fascia latae, which also play a role in hip abduction, are not employed in the optimisation component. This is due to their low maximum isometric force and hence high optimisation cost but can result in poor balancing of the external joint moment which was seen in this study.

When using the stochastic modelling method, we assumed that the muscle forces which were not driven using EMG in CEINMS could only produce half of their maximum possible force. This biased the solution space towards lower estimated joint loads. While this did reduce the solution space to include the measured joint loading, it meant that other solutions were not able to be considered in the sampling.

The comparison between the CEINMS and both the SO and stochastic modelling approach is limited by the DOFs driven and balanced in the model. For both SO and the stochastic modelling approach, all DOFs were driven, and muscle forces completely balanced the external moments. Because the hip adduction was not balanced in the CEINMS solution, and the hip rotation was not considered, this biases the CEINMS solution towards lower overall knee loads because fewer constraints are placed on the model.

The SO implementation used in this study used the sum of the activations squared as a cost function (Anderson & Pandy, 2001). This is a relatively simple cost function when compared to other implementations which have also minimised joint loading error (van Veen, Mazza & Viceconti 2020), or energetic cost (Umberger, Gerritsen & Martin 2003). It is, however, the most commonly used cost function in the literature.

Finally, as this study only investigated the methods for three individuals, it would be useful to further study the use of the generated CEINMS calibration function on more participants to assess its efficacy in estimating knee joint loading. The availability of additional open access datasets, such as the Grand Challenge (Fregly et al. 2012) and the CAMS knee project (Taylor, WR et al. 2017), might allow for future additional validation of these methods for estimating knee joint loading.

3.5 Conclusion

The inclusion of subject-specific muscle activation measures using surface EMG improved estimates of knee joint loading when compared to static optimization. There were deficiencies in estimating the directional components of loading, however the stochastic method employed showed that this is not due to errors in muscle recruitment modelling. Our results show that uncertainty in muscle forces can account for total loading and it is recommended that, where possible, EMG measurements should be included to estimate knee joint loading.

3.6 Acknowledgement

This work was supported with supercomputing resources provided by the Phoenix HPC service at the University of Adelaide.

Chapter 4: Digital Volume Correlation and Finite Element Analysis of the Human Tibial Plateau under Loading

This chapter has been prepared for Acta Biomaterialia, where there is a recommendation of 20 double spaced pages.

Bennett, K.J., Rapagna, S., Wearne, L., Martelli, S., Atkins, G.J., Solomon, L.B., Perilli, E., & Thewlis, D. (2022). Digital Volume Correlation and Finite Element Analysis of the Human Tibial Plateau under Loading.

This study was granted ethical approval by the University of Adelaide HREC: reference number 34423

Conference presentations associated with this chapter:

Bennett, K.J., Rapagna, S., Wearne, L., Martelli, S., Atkins, G.J., Solomon, L.B., Perilli, E., & Thewlis, D. (2021). Preliminary Micro-CT Imaging of the Human Tibial Plateau Under Load. In *XXVIII Congress of the International Society of Biomechanics Proceedings*. Stockholm, Sweden.

Bennett, K.J., Rapagna, S., Wearne, L., Martelli, S., Atkins, G.J., Solomon, L.B., Perilli, E., & Thewlis, D. (2021). The mechanical Response of Trabecular Bone Within the Tibial Plateau due to External Joint Loading. In *ANZORS 26th Annual Scientific Meeting*. Online.

Bennett, K.J., Rapagna, S., Wearne, L., Martelli, S., Atkins, G.J., Solomon, L.B., Perilli, E., & Thewlis, D. (2021). Internal microstructural deformation of the tibial plateau under loading. In *The 12th Australasian Biomechanics Conference*. Online.

Chapter 4: Digital Volume Correlation and Finite Element Analysis of the Human Tibial Plateau under Loading

Statement of Authorship

Title of Paper	Digital Volume Correlation and Finite Element Analysis of the Human Tibial Plateau under Loading
Publication Status	☐ Published ☐ Accepted for Publication ☐ Submitted for Publication ☑ Unpublished and Unsubmitted work written in manuscript style
Publication Details	Prepared for submission to Acta Biomaterialia.

Principal Author

Name of Principal Author (Candidate)	Kieran James Bennett		
Contribution to the Paper	Conception, Acquiring data, Knowledge, Analysis, Drafting		
Overall percentage (%)	75%		
Certification:	This paper reports on original research I conducted during the period of my Higher Degree by Research candidature and is not subject to any obligations or contractual agreements with a third party that would constrain its inclusion in this thesis. I am the primary author of this paper.		
Signature		Date	27/03/2022

Co-Author Contributions

By signing the Statement of Authorship, each author certifies that:

iv. the candidate's stated contribution to the publication is accurate (as detailed above);

v. permission is granted for the candidate in include the publication in the thesis; and

vi. the sum of all co-author contributions is equal to 100% less the candidate's stated contribution.

Name of Co-Author	Lauren Wearne		
Contribution to the Paper	Acquiring data, Knowledge, Analysis, Drafting		
Signature		Date	18/03/2022

Name of Co-Author	Sophie Rapagna		
Contribution to the Paper	Acquiring data, Knowledge, Analysis, Drafting		
Signature		Date	18/03/2022

Name of Co-Author	Gerald Atkins		
Contribution to the Paper	Conception, Knowledge, Drafting		
Signature		Date	29/03/2022

Name of Co-Author	L. Bogdan Solomon		
Contribution to the Paper	Conception, Knowledge, Drafting		
Signature		Date	23/02/2022

Name of Co-Author	Saulo Martelli		
Contribution to the Paper	Conception, Knowledge, Analysis, Drafting		
Signature		Date	23/03/2022

Name of Co-Author	Egon Perilli		
Contribution to the Paper	Conception, Acquiring data, Knowledge, Analysis, Drafting		
Signature		Date	18/03/2022

Name of Co-Author	Dominic Thewlis		
Contribution to the Paper	Conception, Acquiring data, Knowledge, Analysis, Drafting		
Signature		Date	28/03/2022

Chapter 4: Digital Volume Correlation and Finite Element Analysis of the Human Tibial Plateau under Loading

Abstract

The internal mechanical response of the proximal tibia to load has been limited to those implied from finite element (FE) models. Digital volume correlation (DVC), using micro-CT images, can be used to estimate the internal strains within the proximal tibia due to external load and compared to subject-specific FE models to address their validity. The aims of this study were to (1) to characterise the strain response of regions within the human proximal tibia while under physiological tibiofemoral load using DVC of micro-CT datasets, and (2) to compare these strains to a subject specific FE methodology derived from clinical CT scans of the same knees. To meet these aims, two proximal tibias were loaded to three bodyweights inside a large volume micro-CT scanner. Scans were obtained at a 46 μm isotropic voxel size and analysed using DVC. Subject-specific FE models from clinical CT scans were generated for each specimen, and the loads applied in the experiment were applied to the models. For the two specimens, the median internal strains from DVC were 1529 and 1392 με. Subject specific FE models showed general agreement with the DVC, resulting in mean strain errors of 33% and 7%.

Statement of Significance

This is the first study to report internal strains using DVC of the tibial plateau due to externally applied physiological tibiofemoral forces. Subject-specific FE models of the proximal tibia generated using clinical CT scans can predict the mean strains calculated from DVC with reasonable error.

Keywords

Micro computed tomography; internal bone strains; bone finite element modelling;

Chapter 4: Digital Volume Correlation and Finite Element Analysis of the Human Tibial Plateau under Loading

4.1 Introduction

Investigating the internal mechanical response of bone due to joint loading is important for understanding the effect of load on bone formation, resorption, and homeostasis (Frost 1987; Wolff 1892). The tibial plateau is one of the major weight bearing surfaces within the skeletal system, with the proximal tibia demonstrating heterogeneity within its internal bone structure (Goldstein 1987; Morgan, Bayraktar & Keaveny 2003; Pope & Outwater 1974). There is evidence that bone is optimized to withstand regular loading while being structurally efficient (Cristofolini 2015), but the internal response of the proximal tibia to activities of daily living are limited to those implied from finite element (FE) models, validated using surface strain measurements (Cristofolini et al. 2010).

Knowledge of internal bone strains can be used to validate the internal mechanics modelled in finite element models (Taylor, M & Prendergast 2015). Digital volume correlation (DVC), using micro-CT images, has been used for estimating internal strains in excised trabecular bone cores (Comini et al. 2019; Dall'Ara, Enrico et al. 2017; Gillard et al. 2014; Liu & Morgan 2007; Palanca et al. 2017; Roberts, BC, Perilli & Reynolds 2014), in vertebrae (Palanca et al. 2016) and the femur (Martelli et al. 2021; Rapagna et al. 2019). However, to the best of the author's knowledge, there have been no studies presenting the internal 3D strains within the human proximal tibia due to external loading. Using the knowledge of internal 3D strains, FE models could be improved to better model the tibial plateau, and to further understand specific contribution of biomechanics to bone physiology.

The aims of this study were (1) to characterise the strain response of regions within the human proximal tibia while under a three body-weight equivalent tibiofemoral load using digital volume correlation of micro-CT datasets, and (2) to compare these strains to a subject specific FE methodology derived from clinical CT scans of the same knees. It was hypothesised that (1) as there is a physiological load applied, the internal strains would be within the physiological ranges for bone homeostasis suggested in the literature (Frost 1987); and (2) FE models, which use bone geometry and material

properties derived from clinical imaging, can be used to predict internal strains similar to those calculated using DVC from an identical *ex vivo* experiment using micro-CT imaging.

4.2 Materials and Methods

4.2.1 Specimens

Two fresh-frozen cadaveric left knees were sourced (Science Care, Inc.). Specimen 1 was of a 74-year-old male who weighed 51.7 kg at time of death, and specimen 2 was of an 80-year-old male who weighed 40.8 kg at time of death. Ethical approval was granted by The University of Adelaide Human Research Ethics Committee (H-2020-076, 15th May 2020).

4.2.2 Specimen Preparation

Specimens were stored at -20°C. Each specimen underwent a clinical CT scan prior to the *ex vivo* experiment (SIEMENS SOMATOM Force, 0.6 mm isotropic voxel size). The knees were thawed, and all soft tissue and ligaments were removed except for the articular cartilage and menisci, which were left intact. 3D printed jigs were then fitted and screwed to the distal tibia and proximal femur for positioning based on the natural knee position and bone geometry from the CT scans and subsequently refrozen at -20°C.

4.2.3 Ex vivo Experiment

Specimens were thawed and hydrated in phosphate buffered saline (PBS) solution for 24 hours prior to the *ex vivo* experiment. The specimens were then wrapped in PBS-soaked paper to maintain hydration during loading and micro-CT scanning.

Using the 3D printed potting jigs, the specimens were mounted in aluminium potting cups to a previously developed custom-made loading stage (Martelli & Perilli 2018). This aluminium stage was modified to adjust the loading direction, to allow a second

cup to mount the tibia, and the cylinder wall thickness was reduced from 3 mm to 2 mm (Figure 15). Axial load (1540 N for specimen 1 and 1270 N for specimen 2), with a targeted 60:40 medial:lateral ratio, was applied to each specimen (Fregly et al. 2012; Kinney et al. 2013). This load is approximately three body-weights (BW) of the respective donor, which is similar to reported values of maximum total loading (and medial:lateral ratios) at the knee during level walking through instrumented knee prostheses (Fregly et al. 2012; Kinney et al. 2013). This load was applied in four stages (2×1 BW, 2×0.5 BW), with 10 minutes of relaxation between each stage, using the hand crank mechanism while monitoring the load cell measurements (6DOF K6D68 load cell continuously measuring at 10 Hz, ME-measurement systems GmbH, Hennigsdorf, GE). Before applying any physiological load, two repeated micro-CT scans under a preload of 50 N (the smallest stable load which could be applied) were performed, to undertake a DVC zero-strain error analysis. Then, after physiological load application, a micro-CT scan was obtained for determining the internal strains using DVC under load.

Micro-CT imaging was performed using a Nikon XT H 225 ST large-volume micro-CT scanner (Nikon Metrology, UK). Scans were contained the proximal tibia and distal femur in the field of view. Scans (projection images 2028×2028 pixels in size, corresponding to 93 x 93 mm field of view, width x height) were acquired at a source peak voltage 215 kVp, current 195 μA (42 W) using a 0.5 mm tin filter, at a 46 μm isotropic pixel size using a 0.18° rotation step over 360°, with 2s exposure time (2x binning). The total acquisition time was 66 minutes per scan.

Axial cross-section images were reconstructed using CTPro3D software (Nikon Metrology) and saved as 8-bit bitmap images. For each scan, a stack of up to 1870 consecutive cross sections of 2028 x 2028 pixels was reconstructed (46 μm voxel size), resulting in a height of up to 86 mm and producing a reconstructed dataset of 7.2 GB dataset per scan. Reconstructions were 3D rigidly co-registered to the first unloaded scan of that specimen in a distal region where it was expected there was little deformation, near the jig, using DataViewer software (Version 1.5.2.4, SkyScan

Bruker). Images were then filtered using a 3D circular (radius of 1 px) median filter in CTAn software (version 1.15.4.0+, SkyScan Bruker).

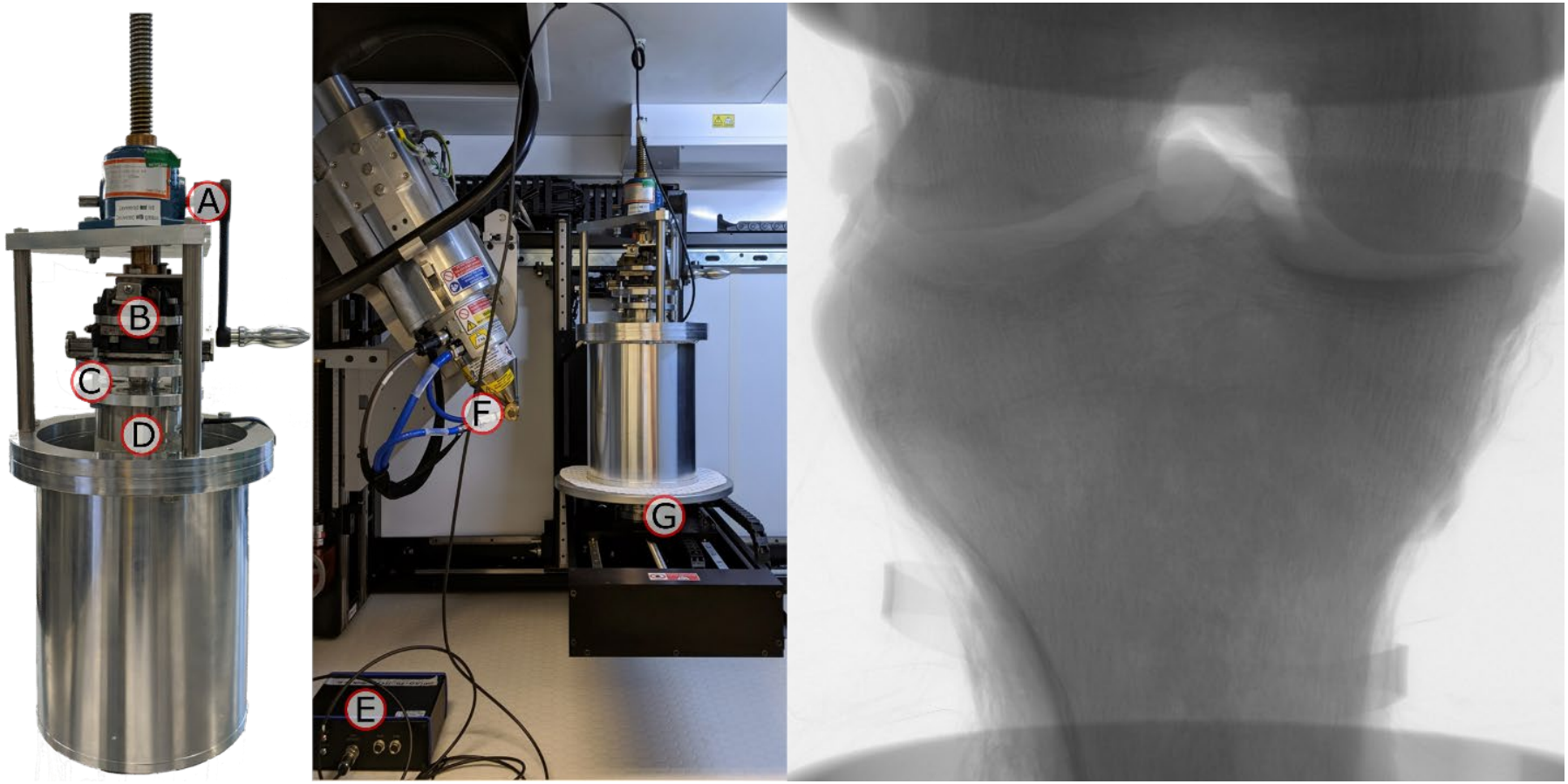

Figure 15 (left) The experimental loading rig (left) set up within the micro-CT scanner (right) showing (A) the hand crank mechanism, (B) the low friction x-y table, (C) the angle adjustment plate, (D) the load cell, (E) the load cell amplifier, (F) the X-ray source, and (G) the rotation stage within the micro-CT scanner. (right) Shadow projection showing the tibia and femur in the preloaded state within the loading stag

4.2.4 Volumes of Interest selection

Four cylindrical volumes of interest (VOIs) were used for strain analysis based on regions of low and high loading indicated in the literature (Figure 16A) (Adouni & Shirazi-Adl 2014; Roberts, BC, Solomon, et al. 2017; Roberts, BC, Thewlis, et al. 2017). Each VOI was centred within the anterior or posterior halves of the medial and lateral condyles, which were defined by elliptical regions (Roberts, BC, Solomon, et al. 2017; Roberts, BC et al. 2018): anterior-lateral (AL), anterior-medial (AM), posterior-lateral (PL) and posterior-medial (PM). The four cylindrical VOIs extended from 5 mm to 15mm below the lowest point of the tibial bony condylar surface above each VOI. We chose to analyse starting from 5 mm below the bony condylar surface to minimise boundary effects. The cylindrical VOIs contained only trabecular bone and were of diameter 10 mm and 10 mm height, satisfying the continuum assumption of trabecular bone (Harrigan et al. 1988; Tassani & Perilli 2013). The VOIs were selected on the micro-CT images using CTAn (version 1.15.4.0+, SkyScan Bruker), and for the FE models using Matlab (Matlab, R2019b, Mathworks).

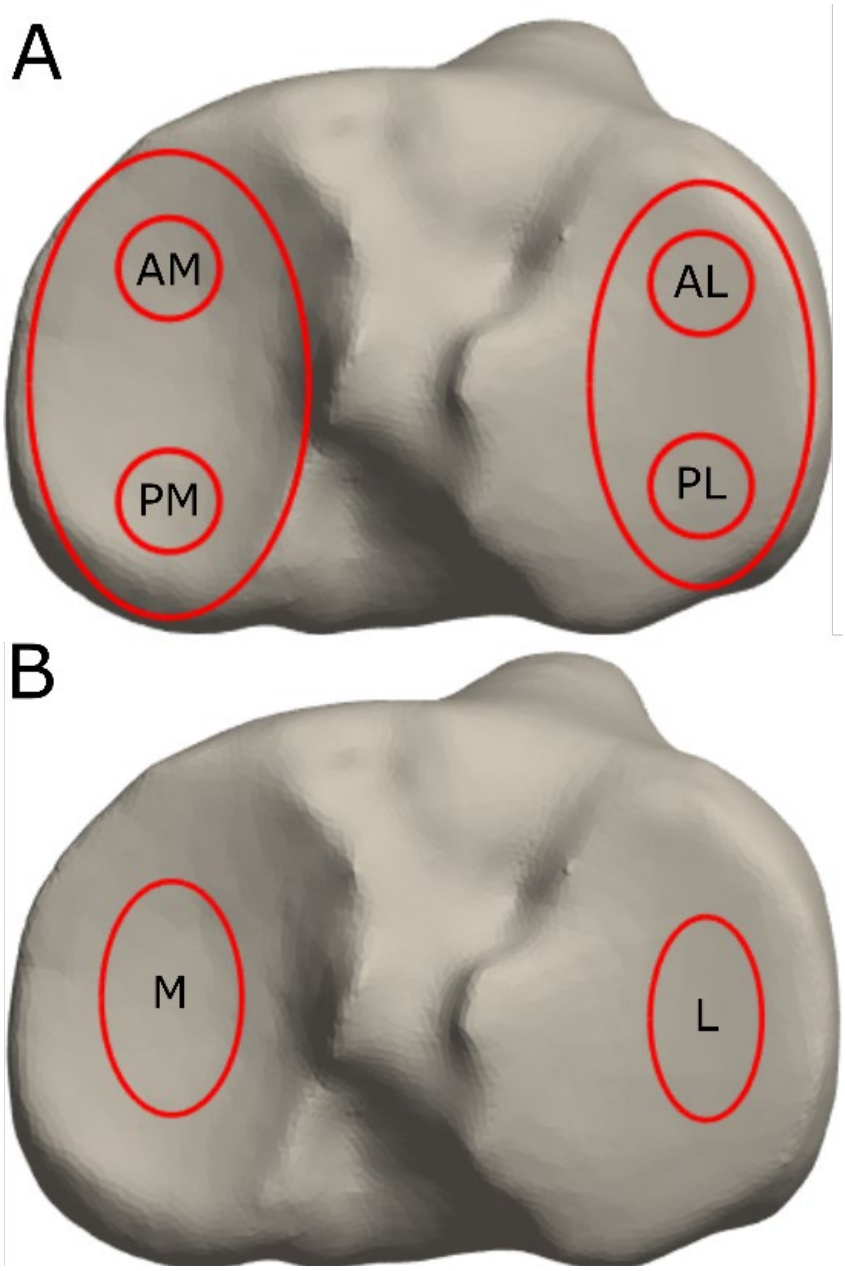

Figure 16 (A) Surface mesh of specimen 1, with the location of the four VOIs used in the study (AL anterior-lateral, PL posterior-lateral, AM anterior-medial, PM posterior-medial). The ellipses which were used to determine the position of each VOI are presented. (B) The ellipses which were used to apply external boundary conditions in the FE models derived from the clinical CT scans.

4.2.5 Digital Volume Correlation (DVC)

For DVC analysis in the four VOIs of interest, the full image micro-CT datasets were cropped to cubes of 30 mm (652 pixels) side length, each centred on the corresponding VOI using CTAn (version 1.15.4.0+, SkyScan Bruker). DVC was implemented via the commercially available program DaVis (Version 8.3.1, LaVision, Germany) on a workstation computer (Windows 8.1, 64-bit Intel Xeon E5-2630, 2.60 GHz, 128 GB memory). Direct correlation was employed, with a five step multipass sequence and no overlap between subvolumes (Palanca et al. 2015). Four different multipass subvolume edge length progressions were performed to determine an appropriate grid size, which compromises between accuracy, precision, and resolution. To do this, a zero-strain analysis was undertaken to calculate the accuracy, precision, and correlation coefficient within each VOI. Accuracy and precision were estimated using the mean absolute error (MAER) and standard deviation of the error (SDER) (Liu & Morgan 2007; Rapagna et al. 2019; Tozzi et al. 2017).

A 34 voxel subvolume edge length was used for the loaded analysis. Directional strains were calculated to populate the 3D strain matrix. From the extracted strain fields, principal strains were calculated as the eigenvalues of the strain matrix, and from these the von-Mises equivalent strain was calculated. This was completed using Matlab (Matlab, R2019b, Mathworks).

4.2.6 Finite Element Models

The clinical CT scans were segmented using the advanced segmentation tool in MIMICS (Version 22.0, Materialise), smoothed and meshed using 3-MATIC (Version 14.0, Materialise). The volume mesh was created out of quadratic tetrahedral elements, with a target maximum edge length of 2 mm and mean 1 mm. The resultant mesh had a characteristic length with mean 0.77 mm and standard deviation 0.16 mm (766,511 and 801,005 elements for specimens one and two respectively). The material properties of each element were calculated from the CT scans. CT numbers were

converted to bone ash density by assigning bone marrow (determined by selecting a pixel region where there is no calcium within the tibial shaft) a density of 0 g/cm^3 and cortical bone 1.2 g/cm^3. Ash density was then related to apparent density (ρ) by multiplying it by 1.54 (Schileo et al. 2008) and subsequently converted to elastic modulus (E) using (8) (Morgan, Bayraktar & Keaveny 2003). Two hundred materials were defined ranging from 50 MPa (0.05 g·cm^{-3}) to 22 GPa (1.2 g·cm^{-3}). Elastic moduli that were outside of this range were assigned the modulus of the closest boundary. All Poisson's ratios were set to ν = 0.3.

$$E = 15520\rho^{1.93}\ (MPa) \tag{8}$$

All models were constrained to zero displacement and rotation in all directions distally, 100 mm from the peak intercondylar eminence. The resultant medial and lateral forces determined from the load cell measurement during the experiment were applied to the condyles in the same ellipses used to select the four VOIs, but with major and minor axes half the length (Figure 16B). A preconditioned conjugate gradient solver was used in the static structural workflow of ANSYS Workbench (v18.2). The equivalent von-Mises strains were exported. FE models were solved on a workstation computer (Windows 10, 64-bit Intel Core i7-6700, 3.40 GHz, 64 GB memory). Four cores and 4581 MB of memory were used, and each solution was computed within 10 minutes.

4.2.7 Comparison of Methods

Strains calculated using the DVC analysis and the FE models were checked for normality using a series of Kolmogorov-Smirnov tests. As the null hypothesis was rejected for the tests of distribution for all strain distributions calculated, non-parametric tests were undertaken. To compare the strain distributions between the subject-specific FE models and the DVC from the *ex vivo* experiment, Wilcoxon rank sum tests were conducted for each specimen in both matched VOIs and when pooling

all strains. Significance was set to $\alpha = 0.05$ and all tests were completed using Matlab (Matlab, R2019b, Mathworks).

4.3 Results

4.3.1 Micro-CT Images

The micro-CT images (Figure 17) showed the trabecular bone structure and the narrowing of the joint space to accommodate loading (loading profiles in Supplementary Material).

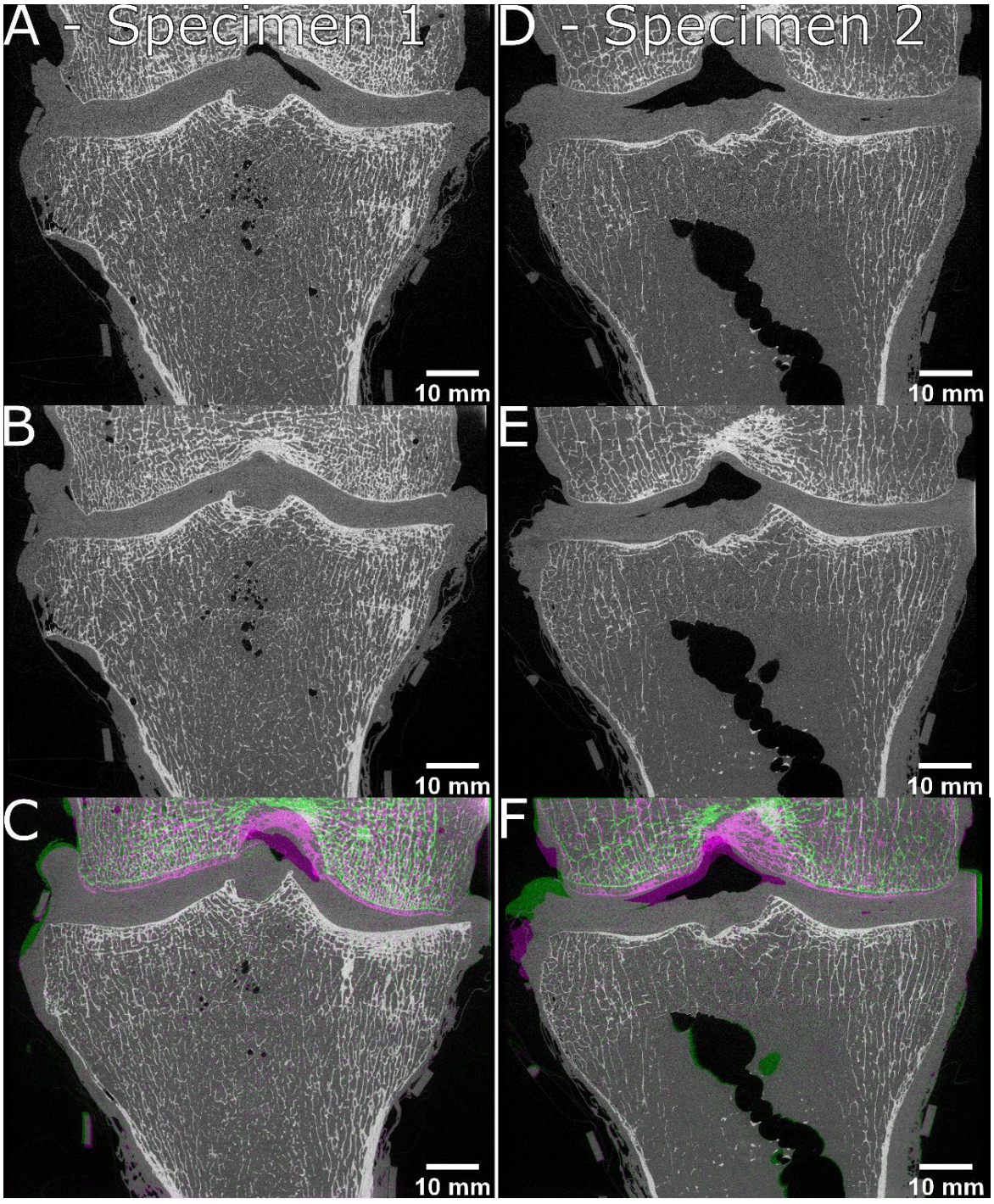

Figure 17 Coronal micro-CT images of specimen one: (A) preload, (B) loaded conditions, and (C) overlaid with green representing the preload, magenta representing loaded, and white representing the bone present in both images; and of specimen two: (D) preload, (E) loaded conditions, and (F) overlaid with green representing the preload, magenta representing loaded, and white representing bone which is present in both images.

4.3.2 Digital Volume Correlation

From the zero-strain analysis (Supplementary material), the chosen final subvolume side length (34 voxels (1.56 mm) side) resulted in MAER of 285 με (range: 239-337 με), a SDER of 94 με (range: 78-112 με) and a mean correlation coefficient of 0.87 (range: 0.83-0.92). This subvolume side length provided a good compromise between resolution, accuracy, and precision. The loaded DVC analysis undertaken using the same final subvolume size (Figure 18) showed in each VOI the median von-Mises strains ranging from 1222 με (S1 AL) to 2220 με (S1 PM).

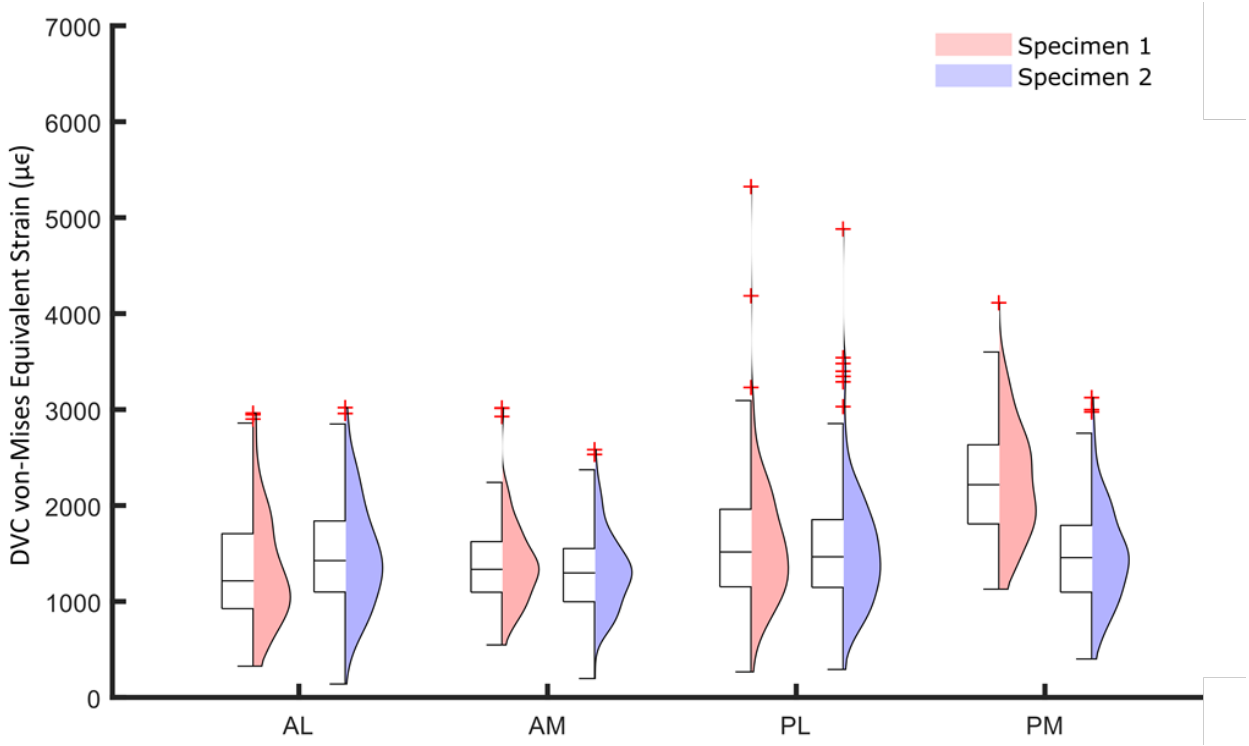

Figure 18 DVC results: Von-Mises equivalent strains calculated in the four volumes of interest (VOI) for each specimen (AL anterior-lateral, AM anterior-medial, PL posterior-lateral, PM posterior-medial), where each VOI is composed of 203 sub-volumes (29 (7x7 circle) x 7 subvolumes). Median and interquartile ranges (boxes), along with outliers (1.5 x interquartile range, red crosses) are presented alongside their frequency distributions.

4.3.4 Finite Element Analysis

The median von-Mises strains in the four VOIs (Figure 19) ranged from 681 με (S1 AM) με to 2067 με (S2 PM). The highest strains were in the PM region (Figure 20), directly below the ellipse which defined the loading region.

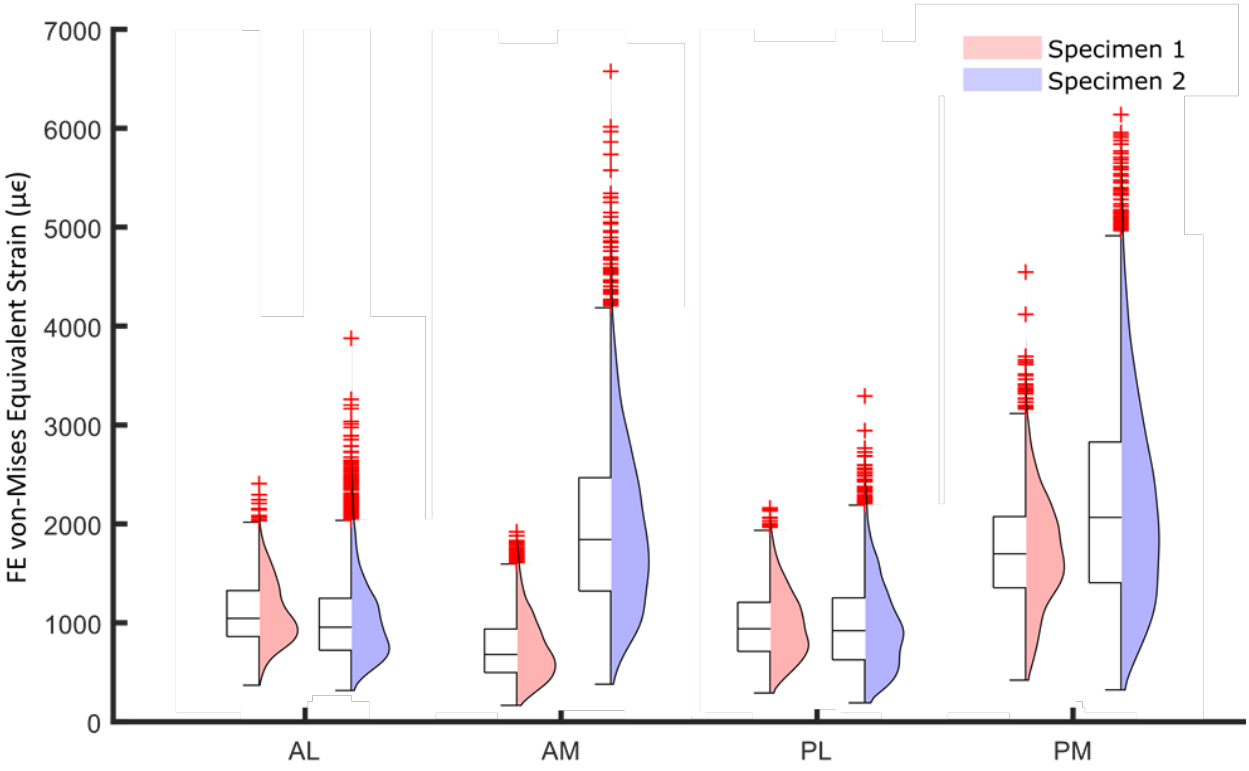

Figure 19 FE results: Von-Mises equivalent strains within each volume of interest (AL anterior-lateral, AM anterior-medial, PL posterior-lateral, PM posterior-medial). Median and interquartile ranges (boxes), along with outliers (1.5 x interquartile range, red crosses) are presented alongside their frequency distributions.

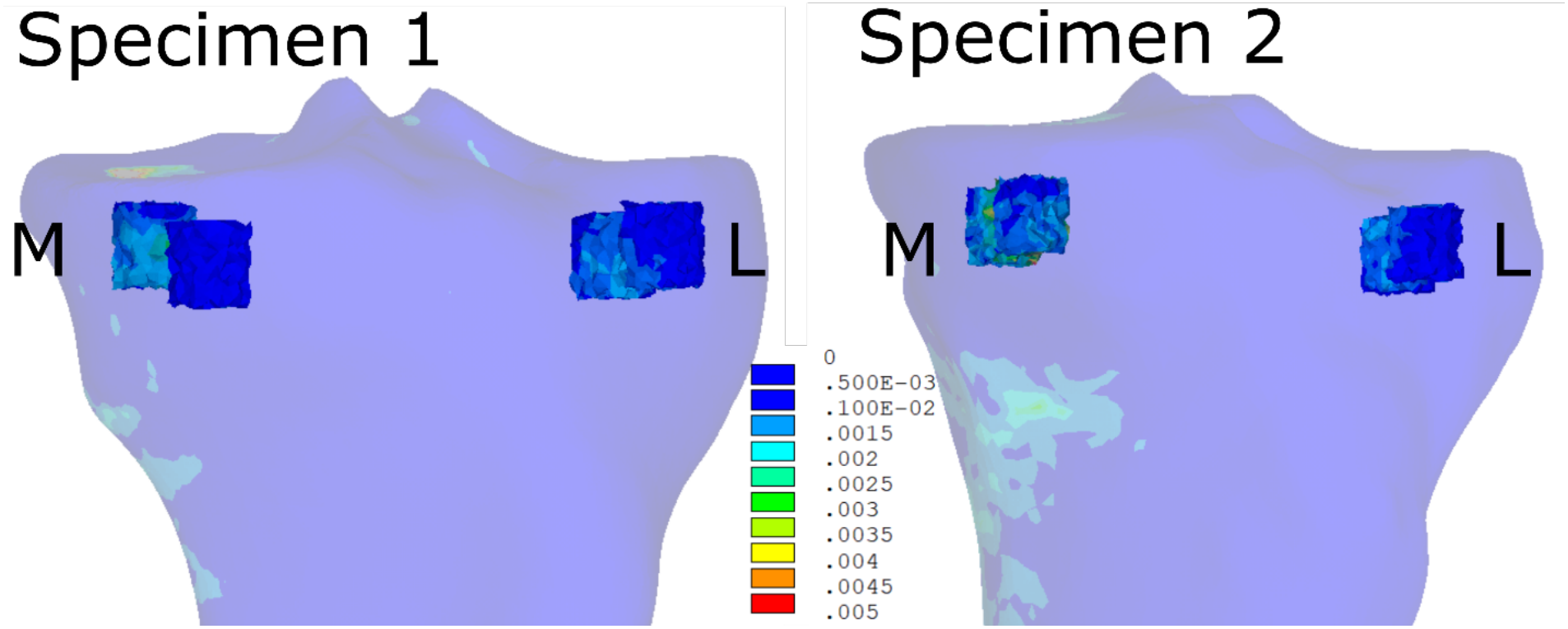

Figure 20 FE results: von-Mises Equivalent strains within specimen one and two. Values are presented as strain.

4.3.5 Comparison Between Methods

For both specimens, the distributions of strains across all regions were similar in appearance, but significantly different (Figure 21, Table 8). For specimen one, strain in the AM VOI was significantly underestimated using FE when compared to the DVC results (Table 8). For specimen two, the strains in the PL VOI were overestimated and the strains in the PM VOI was underestimated when compared to the DVC results (Table 8).

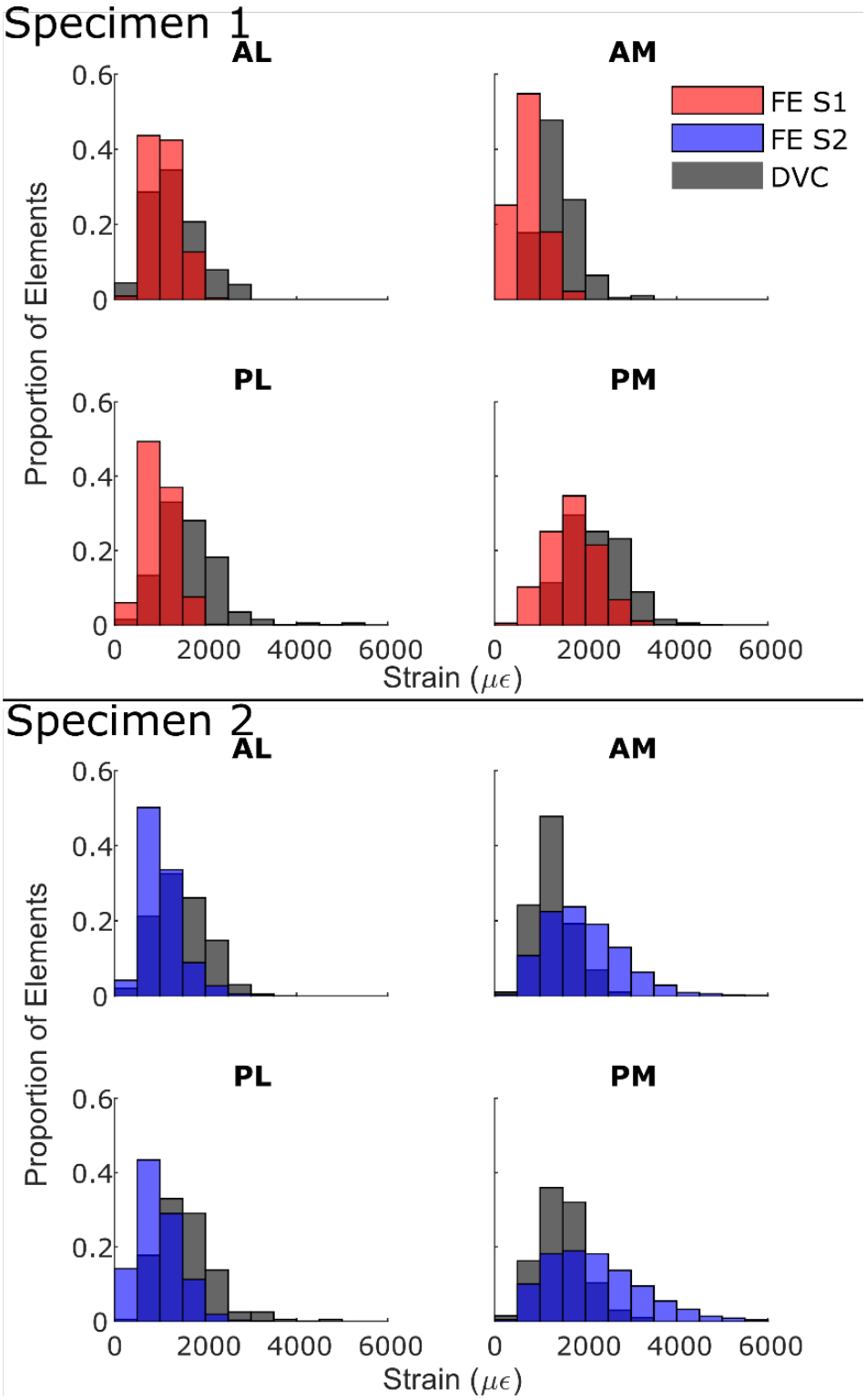

Figure 21 Von Mises strain distributions calculated using FE and DVC within the four VOIs for each specimen. S1 – specimen one; S2 – specimen two; DVC – digital volume correlation.

Table 8 Median strains from the DVC and FE analyses for each VOI. The z-value and p-value from the two-sided Wilcoxon sum rank tests. Statistically significant differences in the median are signified with an asterisk (*).

	Region	DVC	FE	p-value
S1	AL	1222	1043	<0.01*
	AM	1338	681	<0.01*
	PL	1524	942	<0.01*
	PM	2220	1695	<0.01*
	Pooled	1529	1030	<0.01*
S2	AL	1427	954	<0.01*
	AM	1298	1842	<0.01*
	PL	1473	921	<0.01*
	PM	1463	2067	<0.01*
	Pooled	1392	1289	0.01

4.4 Discussion

In this study, we aimed to characterise the strain response of regions within the proximal tibia due to tibiofemoral loading using micro-CT analysis and DVC, and to compare these strains to subject-specific finite element models of the same tibias. Micro-CT images of the human knee in unloaded and physiologically loaded conditions were obtained at 46 μm isotropic voxel size and a DVC analysis was performed. In four selected volumes of interest in the proximal tibia (from virtual coring), the median strains calculated from the DVC analysis were 1529 με and 1392 με for specimens one and two respectively. For the second aim, when pooling the four VOIs, there were statistically significant differences in the median strains calculated using DVC and FE. The difference in median strains were 499 με (specimen 1) and 103 με (specimen 2).

By applying a three-bodyweight axial load with a 60:40 M:L ratio, both the experimental stains obtained by DVC, and computational strains obtained from the FE models were within the expected range for maintaining bone homeostasis (200-300 με to 2000-3000 με) (Frost 1987). This result both meets the first hypothesis of

this study, and support the argument that bone is structurally optimised for regular loading (Cristofolini 2015). The distributions of strains in the DVC analysis were smaller than the FE analysis, in part due to the fewer points of strain evaluation (203 DVC subvolumes per VOI vs up to 4635 FE elements per VOI).

Our second hypothesis was that the internal strains from these FE models would be similar to the DVC calculated strains. Although there were statistically significant differences using the Wilcoxon rank sum test, considering the pooled data, the percentage error in mean strains for the FE models was 30% and 5% for specimens one and two respectively. Comparing the VOI strains, the largest errors were all less than 50%, and were greatest in the AM VOI for specimen one and the AM and PM VOIs for specimen two.

The largest source of error in FE models of bone is in the definition of boundary conditions (Taddei, F. et al. 2006). The loads applied to the FE models in this study were in ellipses centred on the medial and lateral condyles rather than the exact points of load application in the experiment due to difficulties in accurately identifying load application sites from micro-CT images. These models could be improved by obtaining a pressure field across the tibial plateau *ex vivo*, or by applying a probabilistic approach to applying the loading condition.

In this study, the values for DVC strain accuracy, precision and mean correlation coefficient obtained (285 με, 94 με and 0.87, respectively) fall within those suggested in the literature for analysis of bone. Errors of an order of magnitude lower than the expected strain (e.g., in the order of 200 με, in the case of physiological loading) (Dall'Ara, Enrico et al. 2017) and correlation coefficients above 0.9 (Liu & Morgan 2007) are indicated as most suitable.

This study was limited by the samples used. Only two specimens were used, both from elderly males who were in the lowest percentile for weight amongst American men (CDC NHANES 2015-2016 examination data). While this is not representative of a healthy person, it does provide a point of reference for internal 3D trabecular strains

within the tibial plateau under physiological loading. The internal von-Mises strains in four VOIs were compared for this analysis, rather than across the entire tibial plateau. This allowed for the general strain distributions to be analysed in regions of high and low loading (Adouni & Shirazi-Adl 2014; Roberts, BC et al. 2018; Roberts, BC, Thewlis, et al. 2017), but does not indicate the directions of principal strains, or strain distributions across the entire plateau.

Each micro-CT scan was completed within 66 minutes. While there is an effect of rate dependency on yield strain, there is little rate dependency on bone elastic response to compressive loading (Hansen et al. 2008; Martelli & Costi 2021). While there was some stress relaxation, we minimised motion while scanning by allowing 10 minutes of relaxation at multiple points during the loading profile, and began scanning after stable loads were measured using the load cell.

4.5 Conclusions

Using a combination of large-volume micro-CT imaging and DVC, the mean internal strain within the human tibial plateau due to physiological loading was 1566 με, which is within the expected physiological range for bone homeostasis. This is the first study to report internal strains using DVC of the proximal tibia due to externally applied physiological tibiofemoral forces. There are some deficiencies in subject-specific finite element modelling procedures resulting in median strain errors up to 657 με when using DVC as the reference. The median strains calculated within the four volumes of interest are within the same range of the DVC analysis, which provides confidence that the FE models are representing the gross strain present in the proximal tibia due to external load but were not accurate enough to predict the direct strains measured using DVC.

4.6 Funding

This research program is supported by an Australian Government Research Training Program (RTP) Scholarship. A/Prof Thewlis receives fellowship funding from the

NHMRC (CDF ID: 1126229). A/Prof Perilli and A/Prof Martelli receive funding from the ARC (ID: LE180100136, and IDs: DP180103146; FT180100338; IC190100020 respectively).

4.7 Acknowledgements

Thank you to Michael Russo and Francesca Bucci for their assistance in preparing specimens, and Thomas Grace, Rami Al-Dirini and Dermot O'Rourke for their support and discussions surrounding the generation of finite element models used in this study. The authors thank Flinders Microscopy and Micro Analysis for providing access to the micro-CT system.

Chapter 5: Ex vivo Assessment of Surgically Repaired Tibial Plateau Fracture Displacement Under Axial Load Using Large-Volume Micro-CT

This chapter is currently under peer review with the Journal of Biomechanics and was submitted on 26/03/2022.

Bennett, K.J., Callary, S.A., Atkins, G.J., Martelli, S., Perilli, E., Solomon, L.B., & Thewlis, D. (2022). Ex vivo Assessment of Surgically Repaired Tibial Plateau Fracture Displacement Under Axial Load Using Large-Volume Micro CT. Submitted to Journal of Biomechanics.

This study was granted ethical approval by the University of Adelaide HREC: reference number 34423

Chapter 5: Ex vivo Assessment of Surgically Repaired Tibial Plateau Fracture Displacement Under Axial Load Using Large-Volume Micro CT

Statement of Authorship

Title of Paper	Ex vivo Assessment of Surgically Repaired Tibial Plateau Fracture Displacement Under Axial Load Using Large-Volume Micro-CT
Publication Status	☐ Published ☐ Accepted for Publication ☑ Submitted for Publication ☐ Unpublished and Unsubmitted work written in manuscript style
Publication Details	Submitted to Journal of Biomechanics.

Principal Author

Name of Principal Author (Candidate)	Kieran James Bennett		
Contribution to the Paper	Conception, Acquiring data, Knowledge, Analysis, Drafting		
Overall percentage (%)	80%		
Certification:	This paper reports on original research I conducted during the period of my Higher Degree by Research candidature and is not subject to any obligations or contractual agreements with a third party that would constrain its inclusion in this thesis. I am the primary author of this paper.		
Signature		Date	27/03/2022

Chapter 5: Ex vivo Assessment of Surgically Repaired Tibial Plateau Fracture Displacement Under Axial Load Using Large-Volume Micro CT

Co-Author Contributions

By signing the Statement of Authorship, each author certifies that:

vii. the candidate's stated contribution to the publication is accurate (as detailed above);

viii. permission is granted for the candidate in include the publication in the thesis; and

ix. the sum of all co-author contributions is equal to 100% less the candidate's stated contribution.

Name of Co-Author	Stuart Callary		
Contribution to the Paper	Knowledge, Analysis, Drafting		
Signature		Date	23/3/2022

Name of Co-Author	Gerald Atkins		
Contribution to the Paper	Conception, Knowledge, Drafting		
Signature		Date	29/03/2022

Name of Co-Author	Saulo Martelli		
Contribution to the Paper	Conception, Knowledge, Analysis, Drafting		
Signature		Date	

Chapter 5: Ex vivo Assessment of Surgically Repaired Tibial Plateau Fracture Displacement Under Axial Load Using Large-Volume Micro CT

Name of Co-Author	Egon Perilli		
Contribution to the Paper	Conception, Acquiring data, Knowledge, Analysis, Drafting		
Signature		Date	22/03/2022

Name of Co-Author	L. Bogdan Solomon		
Contribution to the Paper	Conception, Knowledge, Analysis, Drafting		
Signature		Date	23/3/2022

Name of Co-Author	Dominic Thewlis		
Contribution to the Paper	Conception, Acquiring data, Knowledge, Analysis, Drafting		
Signature		Date	28/03/2022

Chapter 5: Ex vivo Assessment of Surgically Repaired Tibial Plateau Fracture Displacement Under Axial Load Using Large-Volume Micro CT

Abstract

Postoperative weight bearing has the potential to generate fragmental motion of surgically repaired tibial plateau fractures (TPFs), which may contribute to loss of fracture reduction. The effect of loading on the internal distribution of fragmentary displacements is currently unknown. The aim of this study was to determine the internal displacements of surgically repaired split TPFs due to a three-bodyweight load, using large-volume micro-CT imaging and image correlation. Fractures were generated and surgically repaired for two cadaveric specimens. Load was applied to the specimens inside a large-volume micro-CT system and scanned at 0.046 mm isotropic voxel size. Pre- and post-loading images were paired, co-registered, and internal fragmentary displacements quantified. Internal fragmental displacements of the cadaveric bones were compared to *in vivo* displacements measured in the lateral split fragments of TPFs in a clinical cohort of patients who had similar surgical repair and were prescribed pain tolerated postoperative weight bearing. The split fragments of cadaveric specimens displaced, on average, less than 0.3 mm, consistent with *in vivo* measurements. Specimen one rotated around the mediolateral axis, while specimen two displaced consistently caudally. Specimen two also had varying displacements along the mediolateral axis where, at the fracture site, the fragment displaced caudally and laterally, while the most lateral edge of the tibial plateau displaced caudally and medially. The methods applied in this study can be used to measure internal fragmental motion within other TPFs.

Keywords

Micro-Computed Tomography; Tibial Plateau Fracture; Digital Image Correlation; Internal Fragmentary Displacements

Chapter 5: Ex vivo Assessment of Surgically Repaired Tibial Plateau Fracture Displacement Under Axial Load Using Large-Volume Micro CT

5.1 Introduction

Postoperative weight bearing instructions following surgical management of tibial plateau fractures (TPFs) are currently controversial (Bennett et al. 2021). Many patients with TPFs have sub-optimal outcomes, with relatively poor quality of life (Thewlis et al. 2017), and a high incidence of knee osteoarthritis (Parkkinen et al. 2014). The onset of knee osteoarthritis after a TPF has mostly been attributed to poor fracture reduction at time of surgery, or loss of reduction over time (Parkkinen et al. 2014). Cohort studies have shown that internal fixation in selected cases of TPF can allow immediate weight bearing without significant loss of fracture reduction (Solomon et al. 2011; Thewlis et al. 2015). Despite this, one of the concerns following TPF repair is that the motion produced through weight bearing may be sufficient to cause a loss of the reduction achieved during surgery (Thewlis et al. 2015).

In vivo studies of TPF fragment displacement have historically been limited to measurements on plain radiographs over time (Honkonen, Seppo E. 1994; Thewlis et al. 2017). The associated inaccuracy of measurements of fracture fragment migration on plain radiographs is related to multiple factors, including the different leg position during each examination affecting its projection on the radiographic cassette, as well as its magnification. Radiostereometric analysis (RSA), uses small tantalum markers implanted intra-operatively within fracture fragments to allow calibrated measurement of fracture fragment migration over time, and fragment displacement under load, termed differentially loaded RSA (DL-RSA) (Callary et al. 2013; Solomon et al. 2011). This is done through measuring the three-dimensional motion of fracture fragments assumed rigid and localized using the tantalum markers (Solomon et al. 2010). DL-RSA studies of TPFs found that there is a degree of fracture fragment migration in the first year postoperative not detected using plain x-rays, which can be greater than 1.5 mm (Solomon et al. 2011).

Ex vivo studies of TPFs have shown fracture fragment displacements greater than 1 mm with less than 350 N of load applied to the fragment (Karunakar et al. 2002; Koval et al. 1996; Parker et al. 1999; Ratcliff et al. 2007; Vendeuvre et al. 2018). These

studies, however, have only measured the displacement of fragments on the cortical surface (external) under load following fixation, meaning the internal fracture fragment displacement (within the trabecular bone, and the relative motion of the fragment at the fracture site) under load is currently unknown. Further, the amount of fragment motion at or near the fracture site can only be implied based on external measurements of bone, and the internal motion is not currently known. Measuring the fragment motion at the fracture site would allow for further understanding of the effect of joint loading and its associated micromotion on fracture healing.

Large-volume micro-computed tomography (micro-CT) imaging combined with concurrent mechanical testing enables visualisation and quantification of internal deformation under load of long bone segments, at spatial resolution in the micro-meter range (Martelli et al. 2021; Martelli & Perilli 2018). Applied to a surgically repaired TPFs, this method could be used to visualise and quantify the internal displacements of fragments under load, overcoming some of the experimental limitations of previous studies.

The first aim of this study was to determine the internal displacements of surgically repaired TPFs due to a three-bodyweight external axial loading across the tibial plateau, using large- volume micro-CT imaging and image correlation techniques. The secondary aim was to compare these *ex vivo* fragmental displacements to the similar lateral split TPF fragment migration reported by Solomon et al. (2011) *in vivo*, using DL-RSA. It was hypothesized that fracture fragment displacements would be less than 2 mm, the current clinical definition for the threshold of loss of fracture reduction (Parkkinen et al. 2014).

5.2 Methods

To measure the internal displacements of surgically repaired TPFs, Type I (simple split) fractures were simulated in two cadaveric specimens, repaired surgically, and scanned in a large-volume micro-CT scanner with 65 N of preload (the smallest stable load which could be applied, Figure 22A and Figure 22B). The proximal tibia was then

loaded axially, via the distal femur, to a total of three body-weights and re-scanned (Figure 22B and Figure 22C). By correlating the coronal cross-sections of the unloaded and loaded datasets, the internal displacements of the fracture fragments were calculated

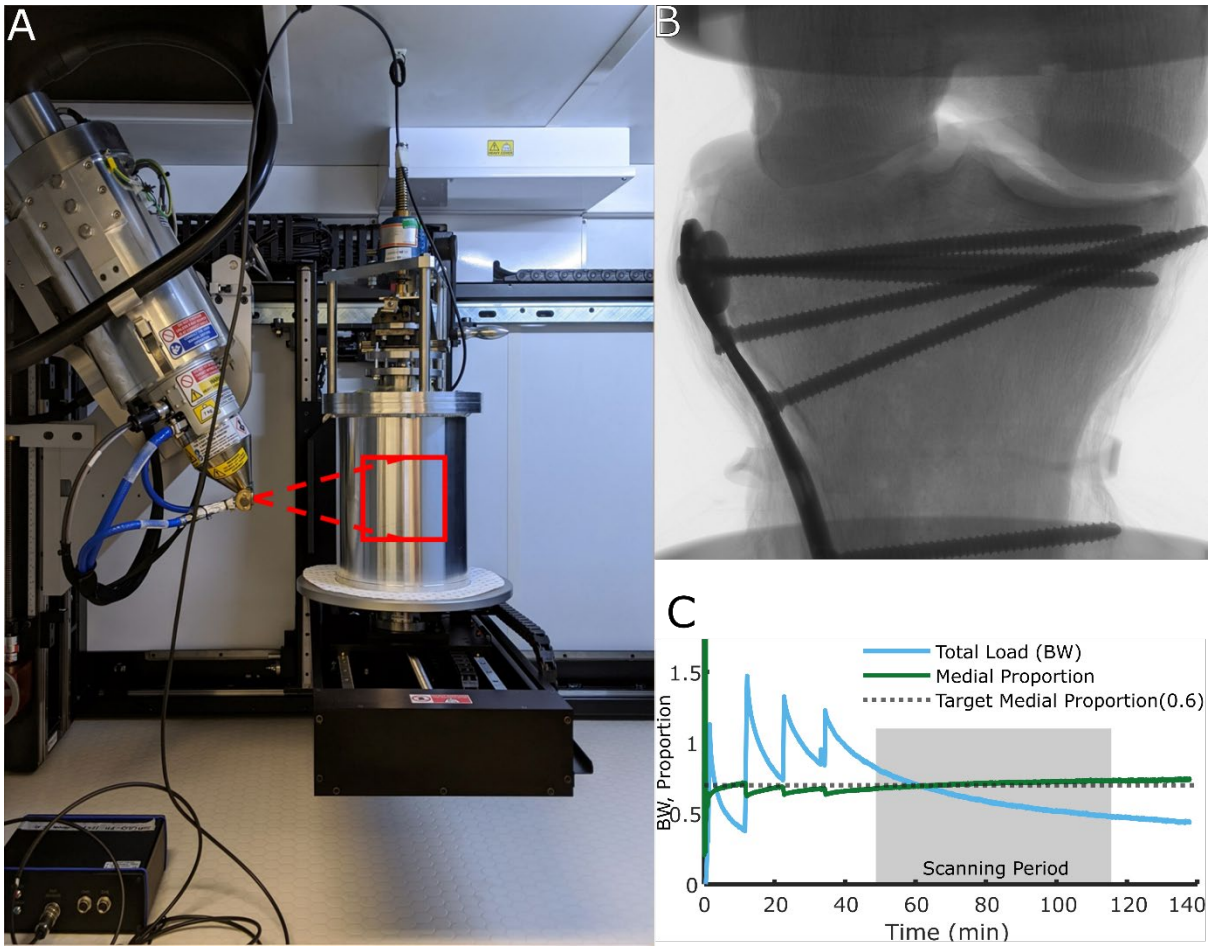

Figure 22 (A) The loading rig setup within the large-volume micro-CT scanner with the field of view highlighted (red square), (B) an X-ray projection of the specimen within the field of view, (C) the loading history of three cumulative bodyweights (BW) distributed with a target 60:40 medial:lateral proportion applied to specimen two via the femoral condyles (data shown after the second pre-load scan), as measured by the load cell.

5.2.1 Specimens

Two fresh-frozen cadaveric specimens were sourced (Science Care, Inc.) for use in this study. Both specimens were left tibia from elderly males with body masses of 51.7 kg and 40.8 kg at time of death (74 and 80 years old respectively). The study protocol was approved by The University of Adelaide Human Research Ethics Committee (H-2020-076, 15th May 2020). Each specimen was scanned using a standard clinical CT scanner prior to experiment (SIEMENS SOMATOM Force, 0.6 mm isotropic voxel size). Samples were stored at -20°C and thawed to remove all soft tissue except for cartilage and menisci. During this time, 3D printed jigs were fitted to the distal tibia and proximal femur for positioning and attachment to the loading device used later during the experiments, prior to re-freezing at -20°C.

5.2.2 Specimen fracture and fracture treatment

Fractures were produced based upon a clinical case of a Schatzker Type I fracture (Schatzker, McBroom & Bruce 1979) (Figure 23A). This fracture, representative of a case which presented to our medical centre, was a lateral split fracture with no depression, beginning within the intercondylar eminence, angled 75° to the mediolateral axis on the sagittal plane, and 85° to the mediolateral axis on the transverse plane. Fractures were planned virtually (Figure 23B) using MIMICS software (Version 22.0, Materialise). A specimen-specific cutting guide (Figure 23C) was 3D-printed, which fitted over the anterior lateral plateau (Figure 23D). To produce the simulated fractures, the anterior horn was released, followed by fitting the cutting guide to the plateau (Figure 23E). Fractures were simulated by cutting the plateau using a hacksaw with a fresh thin blade. Following fracture, a single stainless-steel locking plate (Smith & Nephew Peri-Loc VLP, 4-hole, 68 mm) with five stainless-steel locking screws was used to repair the proximal tibia, and the meniscus was repaired back, preserving it (Figure 23F). The fracture and repair were completed by an experienced orthopaedic surgeon directly before testing.

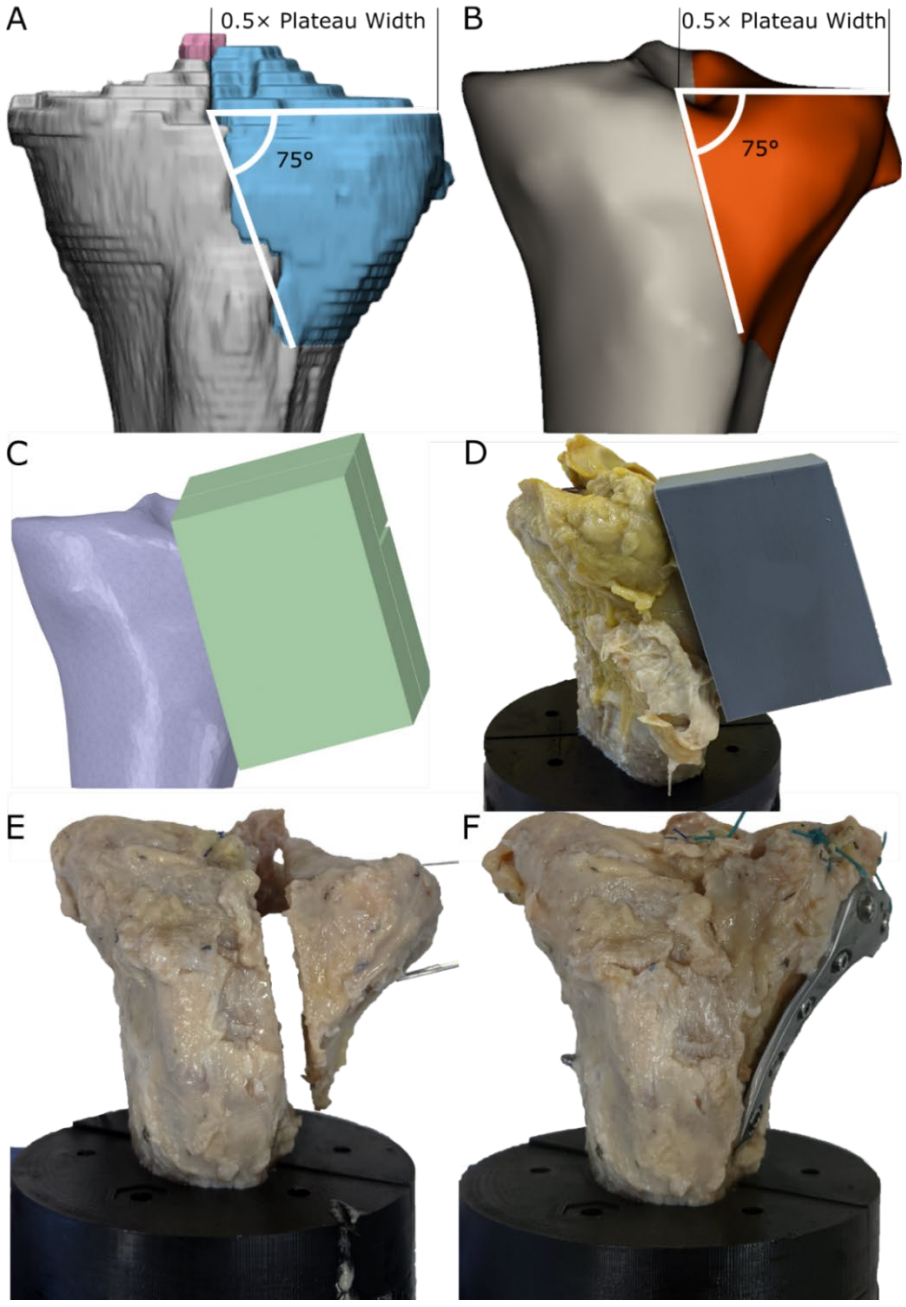

Figure 23 (A) Left tibia, anterior view, CT 3D reconstruction of the clinical fracture case which presented to our medical centre, (B) subsequent virtual planning of the fracture on specimen one, (C) cutting guide planning on the specimen one model, (D) cutting guide fit on specimen one, (E) anterior view, photograph of the fractured specimen two with separated lateral fragment, (F) of the fractured specimen two after fixation with plate and screws, with the meniscus reattached. The 3D printed specimen holder is visible at the bottom (black colour).

5.2.3 Loading

Specimens were mounted to a previously developed custom hand-cranked aluminium loading stage (Martelli et al. 2021; Martelli & Perilli 2018) using the 3D printed potting jigs. The loading stage was modified in three ways: (1) to allow adjustments to the angle of the femur; (2) add a second potting cup to mount the tibia; and (3) the cylinder wall was reduced from 3 mm to 2 mm thickness to reduce the x-ray power required. A total load of three body weights (BW) was applied to the specimens. Two-thirds of the load was applied to the medial condyle, determined using the moment around the sagittal axis, the vertical force, and the position of the femoral condyles. The loading was selected as an absolute maximum loading which can be expected during walking, measured using instrumented knee replacements (Fregly et al. 2012). Loading was applied in four steps of 2×1 BW, followed by 2×0.5 BW loads (Figure 22C), resulting in a cumulative load of 3 BW. Following each loading step, 10 minutes of relaxation was allowed before continuing. Loads were recorded continuously at 10 Hz using a six degree of freedom load cell (K6D68, ME-measurement systems GmbH, Hennigsdorf, GE).

5.2.4 Micro-CT imaging

Micro-CT imaging was performed using a Nikon XT H 225 large-volume Micro-CT scanner (Nikon Metrology, UK) (Grace et al. 2021). Scans were first performed with a pre-load of 65 N (two consecutive scans under preload) and then in loaded conditions (one single scan), with the proximal tibia and distal femur contained in the field of view. Scans (projection images 2028×2028 pixels in size, corresponding to 93 x 93 mm field of view, width x height, Figure 22B) were acquired at a peak voltage 215 kVp, current 195 μA (42 W), using a 0.25 mm tin filter, at a 46 μm isotropic pixel size, using a 0.18° rotation step over 360°, with 2 s exposure time and 2× binning. The total acquisition time was 66 minutes (Figure 22C) per scan. During and in-between scans, specimens were wrapped in saline-soaked paper towel and sprayed regularly to

maintain hydration. Both the micro-CT facility and the internals of the scanner were maintained at 22.7°C.

Axial cross-section images were reconstructed using CTPro3D software (Nikon Metrology) and saved as 8-bit bitmap images (256 gray-levels, 0= air, 255=metal). For each specimen, a stack of up to 1870 consecutive cross-sections were reconstructed, resulting in a height of up to 86 mm.

The reconstructed cross-sections were then coregistered to the first unloaded scan within each set (software DataViewer, version 1.5.2.4, SkyScan Bruker)(Martelli & Perilli 2018) in a region of the distal tibia with no metal-work and exported as a coronal image set (Martelli et al. 2021; Rapagna et al. 2019). Images were then filtered using a one-pixel radius 3D circular median filter (software CTAn, version 1.15.4.0+, SkyScan Bruker).

5.2.5 Analysis

Paired coregistered coronal plane images were compared with digital image correlation using a sub-pixel based gradient-correlation technique (subvox.vision) (HajiRassouliha et al. 2018). To estimate the displacement accuracy and precision, the central coronal slices of the two unloaded scans were correlated for each specimen, assuming zero displacement between the scans. The directional accuracy was determined by calculating the mean absolute displacement of sub-regions of interest (sub-ROIs) across the tibial plateau, and precision determined by the standard deviation in the displacement (Wang et al. 2012). Both were calculated in the craniocaudal and mediolateral directions separately.

To determine the internal fragmentary displacements under loading, ten coronal image pairs were correlated for each specimen, equally spaced from each other anterior-posteriorly (100-pixel, 4.6 mm spacing, cross section positions shown in Figure 24A). Images were correlated in a 19 x 19 sub-ROI grid with a 73-pixel (3.36 mm) edge length centred on the image. For the analysis, only the sub-ROIs which

contained bone and no external tissue or internal gaps were selected for analysis (an example of the correlation grid in Figure 24B, with the ROIs used for analysis highlighted in red colour).

The internal fragmental displacement at the fracture site and the lateral edge of each plateau were also compared. For each slice, Cook's distance was calculated and displacements outside of 3×Cook's distance were removed (Cook 1977). The magnitude of displacement was compared using a two sampled t-test with $\alpha = 0.05$ (Matlab, R2019b, The Mathworks Inc., Natick, USA) to determine if there was a statistically significant difference between the displacements measured at the fracture site and the most lateral edge of the plateau.

The closest similar split TPF fragment migration reported in the literature *in vivo* using DL-RSA was reported in type II (split depression) TPFs (Solomon et al. 2011), the data of which was provided for this study. Although these fractures are more complex than the type I (split only) investigated in this study, both the split component and the fixation of the fractures were similar (Figure 25). In the study by Solomon et al. (2011), seven patients were recruited and during surgery, tantalum markers were implanted, including into the split component of the fracture and into the adjacent intact tibial metaphysis. During their follow up appointments, DL-RSA images were taken using biplanar X-ray and a calibration cage (Cage 43; RSA Biomedical, Umea, Sweden). The total load applied to the affected limb was recorded during the DL-RSA examination using a set of scales. All patients were instructed to weight-bear as tolerated by pain immediately following surgery. Only the DL-RSA examinations conducted at the six-week follow up appointment were compared to micro-CT measurements; six weeks was chosen as a compromise between maximum pain-tolerated loading, and minimal fracture healing, allowing for a comparison to the micro-CT experiment as close as possible.

No statistical test was conducted for the secondary aim, to compare the displacements from the micro-CT imaging to the DL-RSA cohort. Instead, the mean displacements in

the mediolateral and craniocaudal directions were qualitatively compared between the two groups under load.

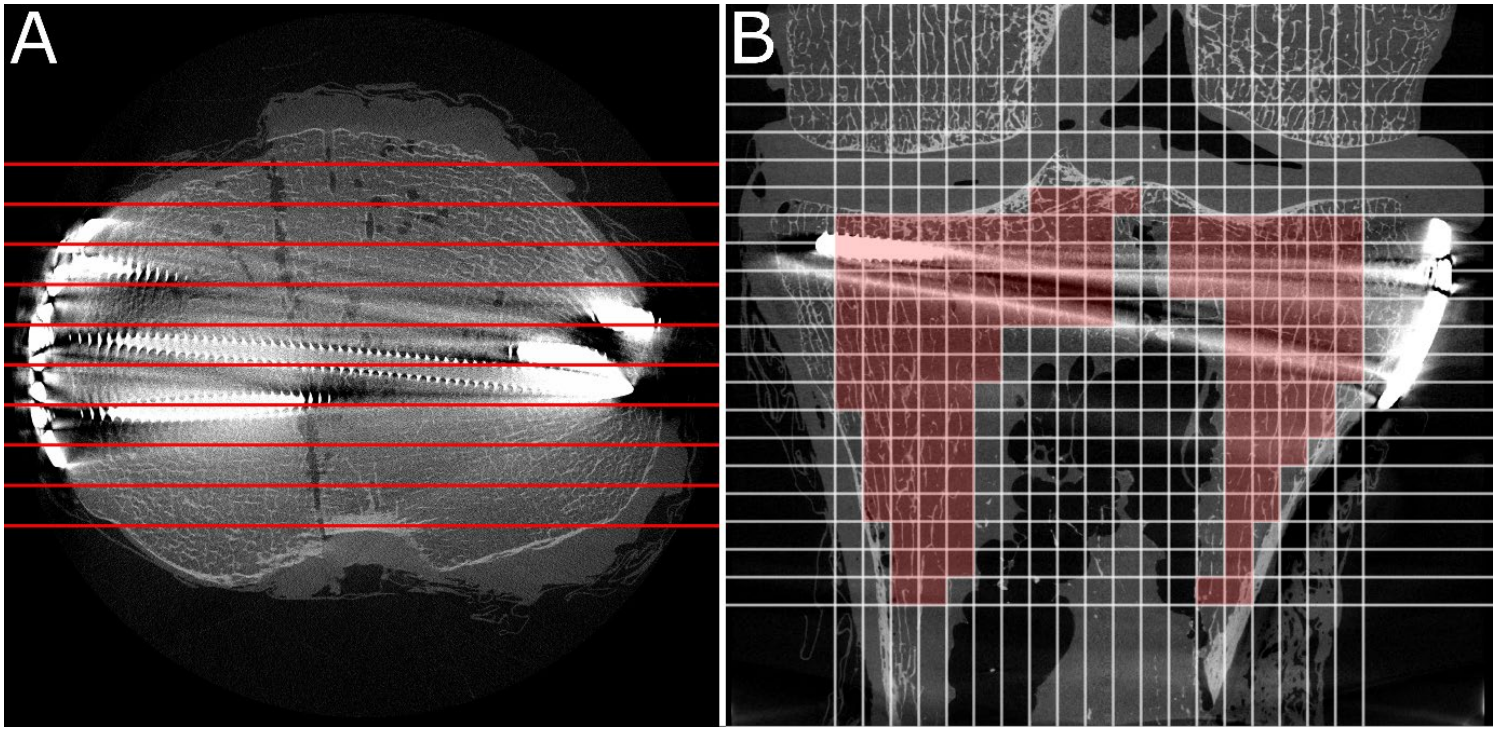

Figure 24 (A) Transverse plane micro-CT cross section of specimen one, showing the position of each coronal slice used for correlation (red lines). (B) Coronal slice of specimen two overlaid with the correlation grid (white lines), and the regions of interest (ROIs) selected for analysis (red shaded areas). Only the ROIs which contained bone and no external tissue or gaps were used for analysis. The gray-level histogram was adjusted to enhance visualisation of the bone in the figure. The original, unadjusted images were used for correlation analysis. In each image, the metalwork (enhanced due to the histogram adjustment) can be seen, along with the trabecular bone and the fracture surfaces. M: medial, L: lateral.

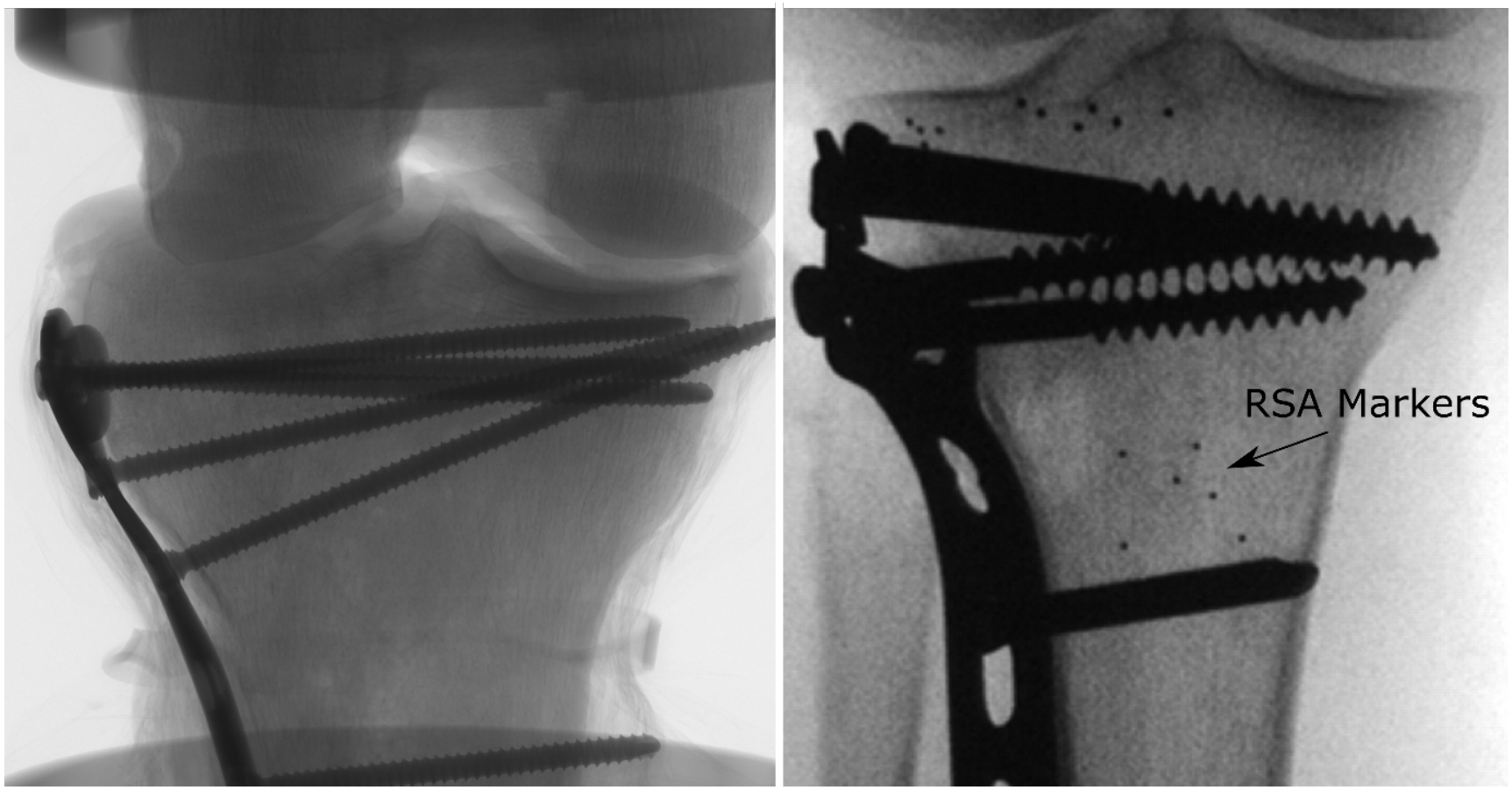

Figure 25 Buttress plate fixation used to fix the Type I fractures in this study (left) and an example of the buttress plate and subchondral screw fixation used to fix the Type II fractures, showing the tantalum beads used for DL-RSA in the clinical cohort (right).

5.3 Results

Micro-CT images of the two fixed TPFs (Figure 26) showed movement of the femur and soft tissue as a result of the applied load. The two fracture angles from the mediolateral axis were 75° and 82° for specimens one and 2 two respectively. The digital image correlation method had accuracy errors below 0.020 mm and precision below 0.012 mm (Table 9), with smaller values in the craniocaudal direction.

Table 9 Accuracy and precision errors in quantifying assumed zero displacements by using image correlation (subvox.vision) (HajiRassouliha et al. 2018) for each specimen in both the mediolateral and craniocaudal directions.

Specimen	Direction	Accuracy (mm)	Precision (mm)
1	Craniocaudal	0.007	0.008
	Mediolateral	0.020	0.012
2	Craniocaudal	0.005	0.005
	Mediolateral	0.008	0.006

Two-dimensional analysis of these images (Figure 27) indicated that the fragment of specimen one displaced -0.292±0.229 mm (mean ± SD) in the craniocaudal direction (cranial positive), and -0.013±0.054 mm in the mediolateral direction (medial positive). The fragment of specimen two displaced -0.234±0.047 mm in the craniocaudal direction (cranial positive), and 0.003±0.040 mm in the mediolateral direction (medial positive, mean ± SD). Considering the displacement vs. depth (Figure 28), the fracture fragment of specimen one (top) overall displaced caudally but also rotated around the sagittal axis, while specimen two (bottom) displaced consistently caudally across the fracture fragment. Specimen one tilted posteriorly under load, resulting in a 0.1 mm cranial displacement at the anterior edge, and a 0.7 mm caudal displacement at the posterior edge, a 0.02° rotation around the sagittal axis.

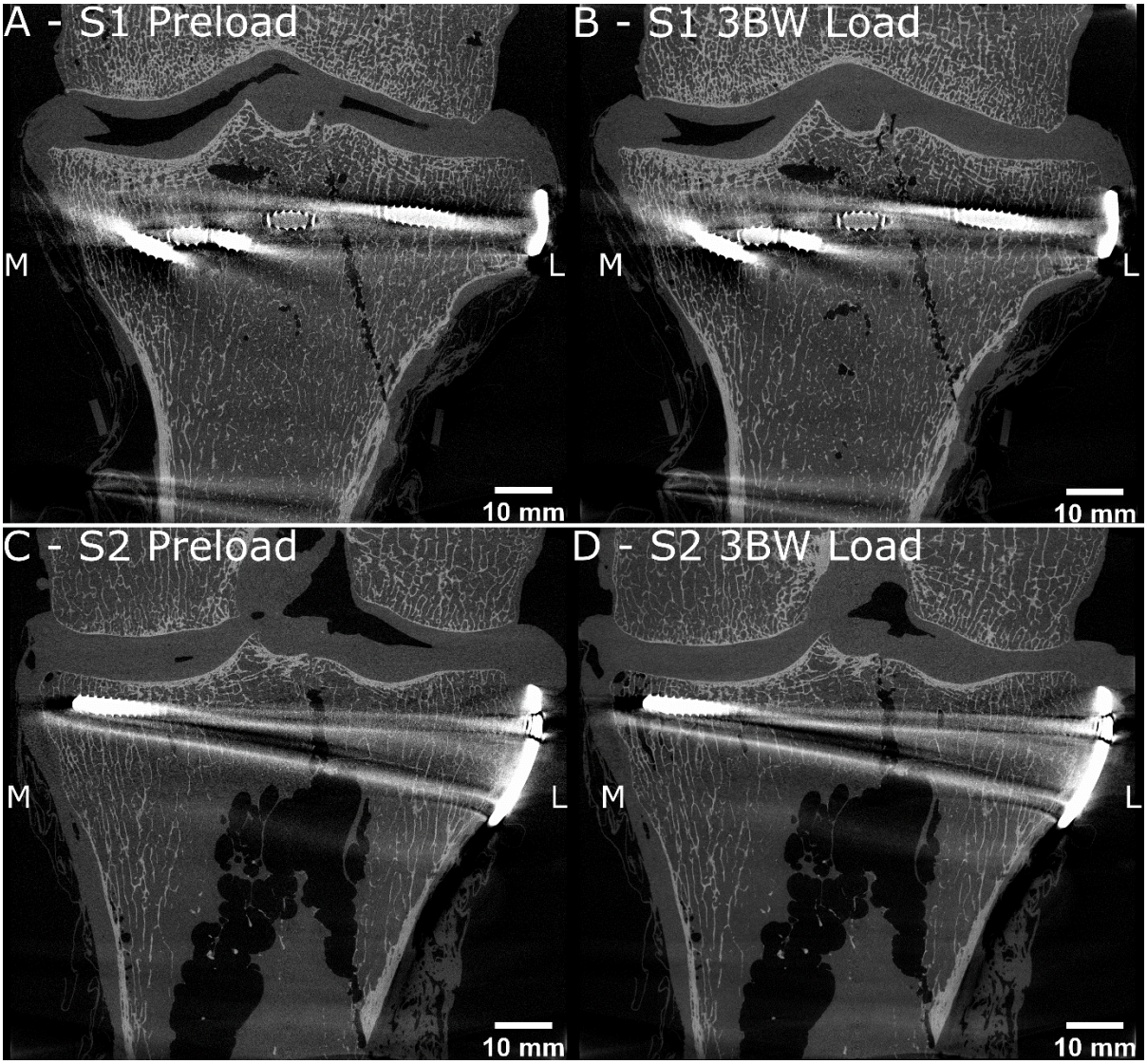

Figure 26 Micro-CT coronal cross-section images (46 μm/pixel), 20 mm from the anterior edge, of (A) specimen one under preload, (B) under 3BW load; of (C) specimen two under preload, (D) under 3BW load. The gray-level histogram was adjusted to enhance visualisation of the bone in the figure. The original, unadjusted images were used for correlation analysis. In each image, the metalwork (enhanced due to the histogram adjustment) can be seen, along with the trabecular bone and the fracture surfaces. M: medial, L: lateral.

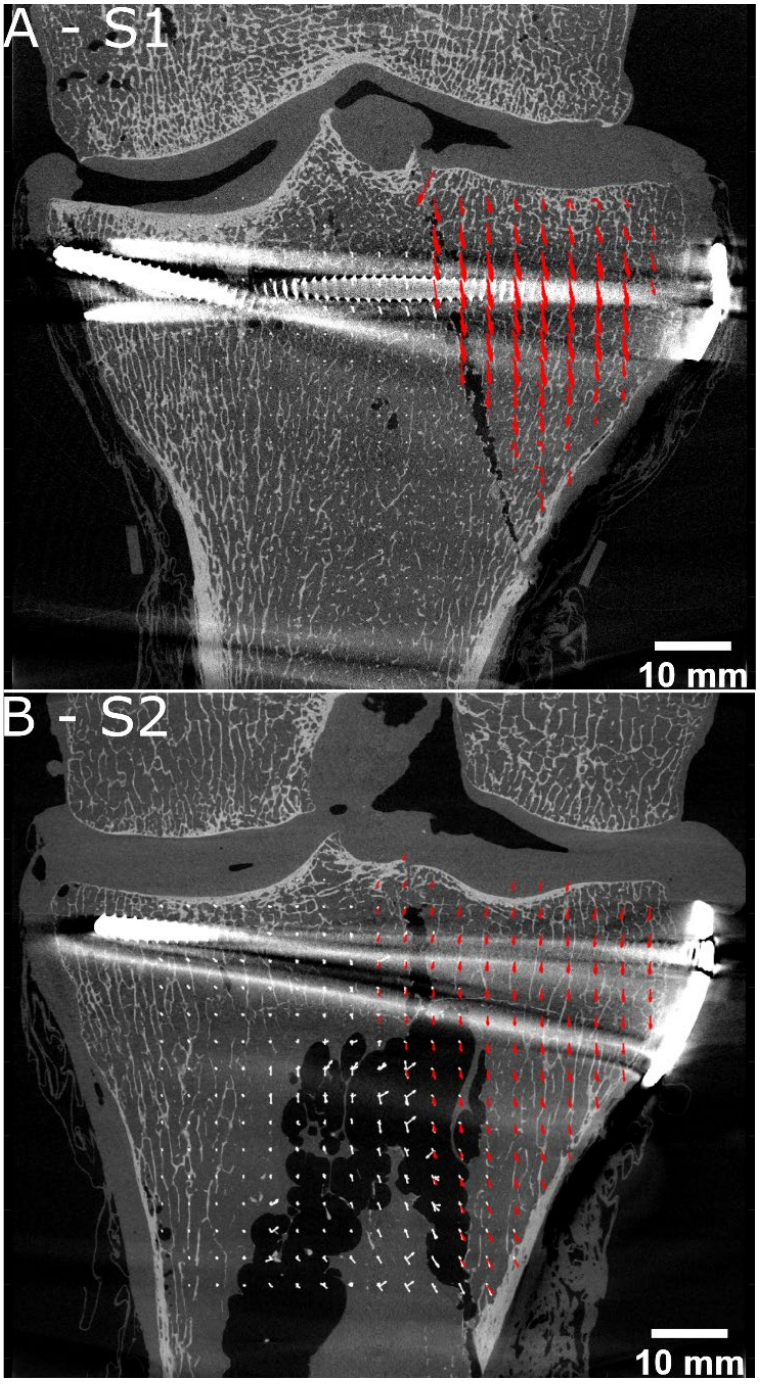

Figure 27 Fragment (red shaded region) and intact tibia (white shaded region) displacements from every slice of (A) specimen one, and (B) specimen two overlaid onto the coronal micro-CT reconstructions at 20 mm from the anterior edge. The vectors displayed are from all ten slices analysed, resulting in some appearing within the gaps in the bone. Displacement vectors were multiplied by a factor of five for emphasis.

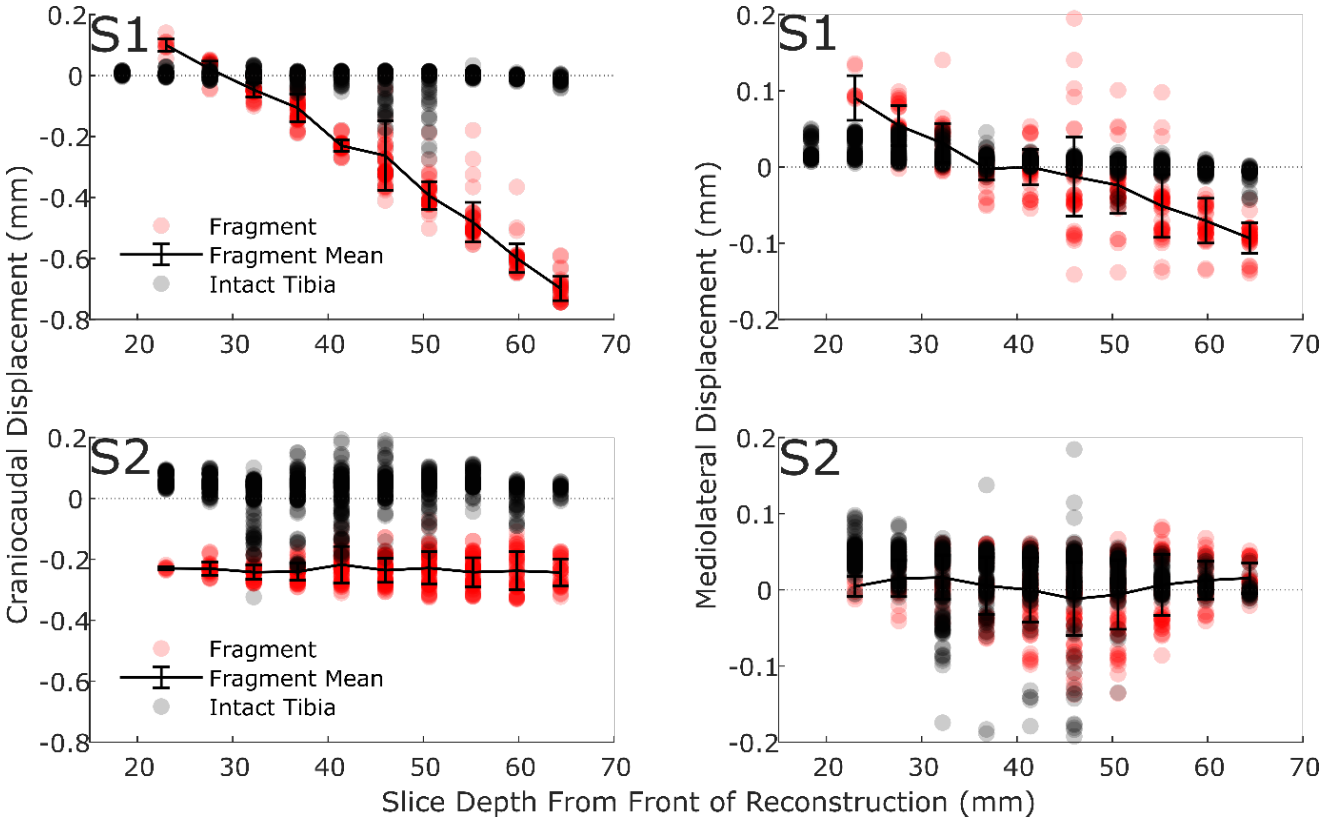

Figure 28 Fragment (red) and intact tibia (black) craniocaudal (left) and mediolateral (right) displacements for specimen one (top) and specimen two (bottom) at each image correlation pair depth from the anterior edge of the plateau under a 3 BW load. The mean and standard deviation fragment motion is plotted to show the overall motion relative to the intact tibia.

For specimen one, there was no significant difference between the displacements measured at the fracture site and the most lateral edge of the plateau (p=0.938, Figure 29, *left*). At the fracture line, the displacements were -0.250 ± 0.242 mm (craniocaudal) and 0.000 ± 0.057 mm (mediolateral), while at the lateral edge, the displacements were 0.254 ± 0.238 mm (craniocaudal) and -0.019 ± 0.064 mm (mediolateral, mean ± SD). However, for specimen two, there was a significant difference in displacement ($p < 0.001$), where the fracture line displacements were -0.212 ± 0.027 mm (craniocaudal) and -0.009 ± 0.045 mm (mediolateral), and at the lateral edge were -0.289 ± 0.024 mm (craniocaudal) and -0.018 ± 0.024 mm (mediolateral, mean ± SD, Figure 29, *right*).

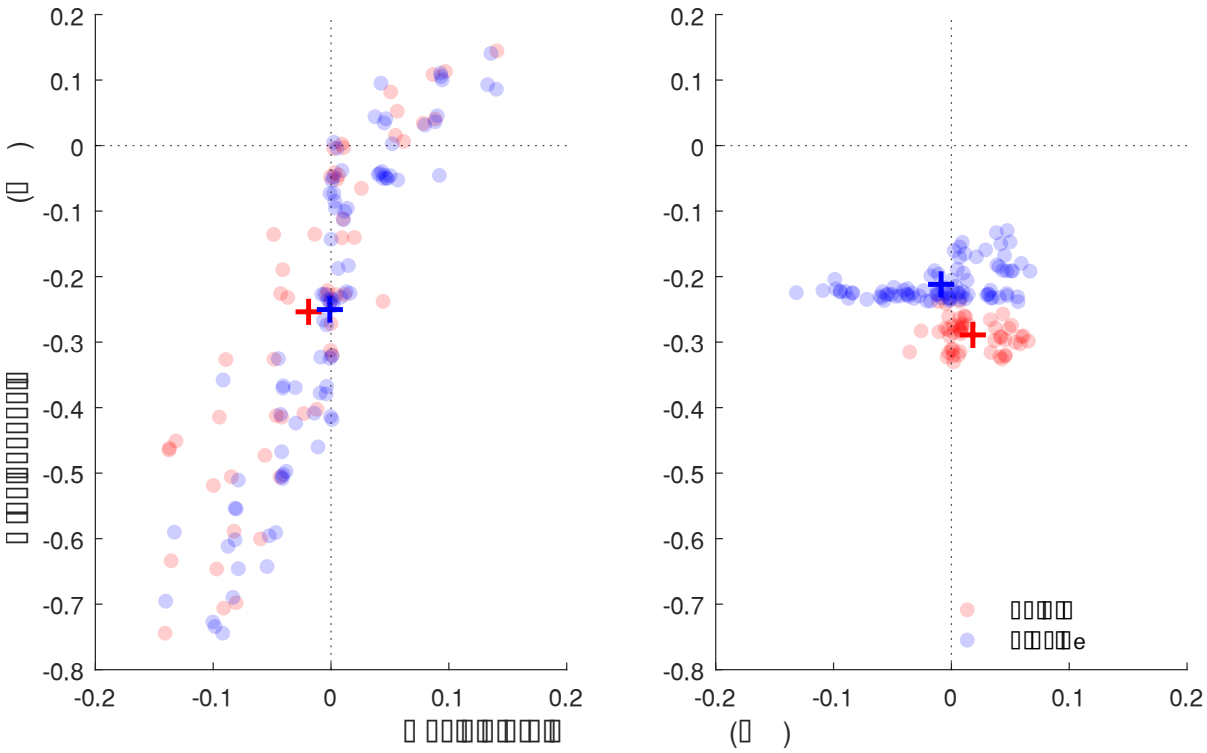

Figure 29 Displacements at the lateral edge of the fracture fragment (red) and at the fracture site (blue) in the craniocaudal and mediolateral directions for specimen one (left) and specimen two (right). While specimen one did not show significant differences between the lateral edge and the fracture site, specimen two showed significant differences between them.

The retrospective analysis of DL-RSA data showed that the clinical split fracture fragments investigated displaced, on average, -0.016 mm in the mediolateral direction, and, -0.166 mm in the craniocaudal direction (medial positive, cranial positive, Table 10). This displacement was measured under loads which were tolerated by pain, and were all less than one BW measured externally (Solomon et al. 2011). The mean fragment displacements from the micro-CT analysis under three BW load were within the same magnitude of DL-RSA displacements.

Table 10 External load measured during the DL-RSA study (Solomon et al. 2011) and the corresponding displacement measured for each patient in the cohort, in both the craniocaudal (C-C) and mediolateral (M-L) directions. For comparison, the two specimens tested in this study are also presented as S1 and S2. E indicates externally measured, while I indicates internally measured load.

Participant ID	Load (BW, kg)	C-C displacement (mm)	M-L displacement (mm)
1	0.48, 30 (E)	-0.091	-0.05
2	0.55, 30 (E)	-0.057	0.141
3	0.86, 60 (E)	-0.097	0.099
4	0.35, 30 (E)	-0.047	0.0306
5	0.75, 75 (E)	-0.575	0.504
6	0.48, 40 (E)	-0.149	0.01
7	0.74, 50 (E)	-0.143	-0.854
Mean (SD)	0.6 (E)	-0.166 (0.185)	-0.016 (0.411)
S1	**3 (I)**	**-0.292**	**-0.013**
S2	**3 (I)**	**-0.234**	**0.003**

5.4 Discussion

In this study, we quantified the internal mechanical displacements of surgically repaired TPFs under external loading using micro-CT and image correlation techniques. Under three bodyweights of load, the total fracture fragment displacements for specimens one and two were on average 0.296 mm and 0.234 mm, respectively. For specimen two, there was a significantly larger total displacement recorded at the lateral plateau edge (0.290 mm) when compared to the fracture line (0.212 mm), representing a 27% difference in displacement. Within the limitations of

this study, the displacements measured using our *ex vivo* technique were of comparable magnitude to the lateral split fragment of a clinical cohort of Type II fractures measured using DL-RSA at six weeks postoperatively (Solomon et al. 2011).

There were differences between the two specimens in the displacements measured at the fracture site and the most lateral edge of the fragments. The fracture fragment of specimen one appeared to move as a rigid body, with the fracture site and lateral edge displacing similar amounts. Specimen two, however, showed the bone at the fracture site moving parallel to the fracture (depicted by red arrows at the fracture site pointing in the caudal-lateral direction, Figure 27B; and the lateral displacement at maximum craniocaudal displacement shown by the blue circles in Figure 28), and the lateral edge moving as if it was a cantilever beam (depicted by red arrows at the lateral edge pointing in the caudal to caudal-medial direction Figure 27B; this is also shown by the red circles in Figure 28). While external measurements would be able to detect some of this motion by tracking multiple points on the cortical bone, they are unable to measure the distribution of internal fragmental displacements, especially at the fracture site.

The results of the retrospective DL-RSA analysis are within the same magnitude of the *ex vivo* micro-CT investigation, and both datasets show that there is very little motion (<1 mm) of the fracture fragment due to external loading. One of the key assumptions of RSA analysis is that the bone fragment moves as a rigid body, and by investigating the differences in displacements at the fracture site and lateral edge from our micro-CT analysis we found that there can be a difference in measured displacement in both magnitude and direction depending on the position within the fragment analysed. This difference, however, was less than 0.1 mm and may be negligible depending on the study design. It is recommended that for future studies involving RSA measurement to also report rotation around the anterior-posterior axis as well as translation to capture this motion.

The fragmental displacements due to external load measured in this study were both less than those previously reported for similar studies investigating fractures

including a split component, which tested specimens either to failure, or to a predetermined displacement (Cross et al. 2013; Karunakar et al. 2002; Koval et al. 1996; Parker et al. 1999; Ratcliff et al. 2007; Vendeuvre et al. 2018). Vendeuvre et al. (2018) reported a mostly linear behaviour up to 5 mm of craniocaudal displacement, which when applied to our findings suggests we would require a 4000 N load directly applied to the fracture fragments (7.9-10 BW) to produce a 2 mm displacement, the threshold for loss of fracture reduction (Parkkinen et al. 2014). Each of these studies utilised different methods and tools for surgical repair, therefore comparison of the findings is likely influenced by a combination of specimen, fixation, surgical variation, and methods for measuring displacement.

There were some limitations to our study and analysis which must be considered when interpreting the results. First, the two cadaveric specimens used in the micro-CT experiment were from elderly donors, whereas the DL-RSA cohort was between 25-58 years of age (Solomon et al. 2011). It would be useful to repeat this analysis with a larger number of specimens obtained from younger donors to determine if the small displacements calculated are still observed. Second, the fractures simulated in our study, while based on a clinical case, were generated using a saw, producing a straight cut. This is not representative of *in vivo* fractures, which propagate through the path of least resistance (Zimmermann, Busse & Ritchie 2015), but it is currently the most common method for generating repeatable models of TPFs in the literature. Third, the fracture for specimen one was produced as planned, however, the fracture of specimen two was 7° more from the mediolateral axis than planned, meaning the load was transferred from the fragment to the tibia in a different direction. This makes it impossible to discern whether the differences observed are due to the fracture geometry, surgical fixation, or bone quality. Fourth, in an *in vivo* fracture, there would also be a degree of comminution which would be different to the layer of bone removed by the saw. Finally, while previous studies in the literature have measured fragment displacement due to external loading in real time, our micro-CT images required a 66-minute scan time.

Further limitations are present when considering the comparison between cadaveric specimens and the clinical cohort from Solomon et al. (2011). For the cadaveric specimens, ideal fixation was able to be achieved because there were no additional surgical considerations required. The fracture types were different (Type I vs. Type II). For this study, we only considered motion of the lateral split fragment which was fixed in both the experiment and the clinical cohort using a buttress plate. The clinical cohort fixations also included extra subchondral screws, however, these were to stabilise the depression rather than the lateral fragment (Figure 25). In the micro-CT experiment, a total of three BW of load was applied to simulate a maximum expected loading during walking, whereas none of the DL-RSA patients could load their leg to one BW measured externally. Due to the contributions of muscles surrounding the knee, the load transferred through the tibial plateau can be double the externally measured load during double legged stance (Kutzner et al. 2010), and so it is difficult to make a comparison between known internal loads (*ex vivo*), and unknown internal loads but known external loads (*in vivo*).

In summary, using the methodology presented in this study, we obtained novel insights into the internal displacements throughout the fracture fragments under load at spatial resolutions in the micro-meter range. We also measured internal non-uniform displacement of the fracture fragments which would not be captured by current *ex vivo* testing methods and DL-RSA measurements. This approach, when combined with further clinical studies, could help improve long-term outcomes for TPF including management of the onset of osteoarthritis, and assist in improving short-to-mid term patient reported quality of life measures. From our study we can suggest that, following adequate mechanical fixation, it is likely that mechanical loading from basic activities of daily living would result in small displacements, less than the current clinical definition (<2mm) for the threshold of loss of fracture reduction.

5.5 Acknowledgements

The authors would like to thank Sophie Rapagna and Lauren Wearne for their support during the micro-CT scanning experiment, and to Smith & Nephew for donating the fixation devices. This research program is supported by an Australian Government Research Training Program (RTP) Scholarship. DT was funded by the NHMRC (ID: 1126229). SM was funded by the Australian Research Council (ARC) (DP180103146; FT180100338; IC190100020). EP received funding for procurement of the large-volume micro-CT scanner from the ARC (LE180100136). The authors thank Flinders Microscopy and Micro Analysis for providing access to the micro-CT system. SC Mary Overton Fellowship was funded by the Royal Adelaide Hospital Research Fund.

Chapter 6: Postoperative lower limb joint kinematics following tibial plateau fracture: a 2-year longitudinal study

This chapter has undergone peer review and is published in Gait and Posture:

Bennett, K. J., Millar, S., Fraysse, F., Arnold, J., Atkins, G., Solomon, L., Martelli S., Thewlis, D. (2021). Postoperative lower limb joint kinematics following tibial plateau fracture: a 2-year longitudinal study. Gait and Posture, 83, 20-25. https://doi.org/10.1016/j.gaitpost.2020.10.005

This study was granted ethical approval by CALHN Research Ethics: reference number: R20160312 and the University of Adelaide HREC: reference number 34423

Conference presentations associated with this chapter:

Bennett, K. J., Millar, S., Fraysse, F., Arnold, J., Solomon, L. B., Martelli, S., & Thewlis, D. (2019). Longitudinal Postoperative Joint Kinematics of Tibial Plateau Fracture Patients. In *ANZORS 25th Annual Scientific Meeting*. Canberra, ACT, Australia.

Bennett, K. J., Millar, S., Fraysse, F., Arnold, J., Solomon, L. B., Martelli, S., & Thewlis, D. (2019). Longitudinal Postoperative Joint Kinematics of Tibial Plateau Fracture Patients. In *XXVII Congress of the International Society of Biomechanics Conference Proceedings*. Calgary, Canada.

Chapter 6: Postoperative lower limb joint kinematics following tibial plateau fracture: a 2-year longitudinal study

Statement of authorship

Title of Paper	Postoperative lower limb joint kinematics following tibial plateau fracture: a 2-year longitudinal study
Publication Status	☑ Published ☐ Submitted for Publication ☐ Accepted for Publication ☐ Unpublished and Unsubmitted w ork w ritten in manuscript style
Publication Details	Bennett, K. J., Millar, S., Fraysse, F., Arnold, J., Atkins, G., Solomon, L., Martelli S., Thewlis, D. (2021). Postoperative lower limb joint kinematics following tibial plateau fracture: a 2-year longitudinal study. Gait and Posture, 83, 20-25.

Principal Author

Name of Principal Author (Candidate)	Kieran James Bennett		
Contribution to the Paper	Conception, Knowledge, Analysis, Drafting		
Overall percentage (%)	75%		
Certification:	This paper reports on original research I conducted during the period of my Higher Degree by Research candidature and is not subject to any obligations or contractual agreements with a third party that would constrain its inclusion in this thesis. I am the primary author of this paper.		
Signature		Date	27/03/2022

Chapter 6: Postoperative lower limb joint kinematics following tibial plateau fracture: a 2-year longitudinal study

Co-Author Contributions

By signing the Statement of Authorship, each author certifies that:

x. the candidate's stated contribution to the publication is accurate (as detailed above);

xi. permission is granted for the candidate in include the publication in the thesis; and

xii. the sum of all co-author contributions is equal to 100% less the candidate's stated contribution.

Name of Co-Author	Stuart Millar		
Contribution to the Paper	Conception, Acquiring data, Knowledge, Analysis, Drafting		
Signature		Date	17/01/2022

Name of Co-Author	Francois Fraysse		
Contribution to the Paper	Acquiring data, Knowledge, Analysis, Drafting		
Signature		Date	23/03/2022

Name of Co-Author	John Arnold		
Contribution to the Paper	Acquiring data, Knowledge, Analysis, Drafting		
Signature		Date	23/03/2022

Name of Co-Author	Gerald Atkins		
Contribution to the Paper	Knowledge, Drafting		
Signature		Date	29/03/2022

Chapter 6: Postoperative lower limb joint kinematics following tibial plateau fracture: a 2-year longitudinal study

Name of Co-Author	L. Bogdan Solomon		
Contribution to the Paper	Acquiring data, Knowledge, Drafting		
Signature		Date	23/02/2022

Name of Co-Author	Saulo Martelli		
Contribution to the Paper	Knowledge, Analysis, Drafting		
Signature		Date	23/02/2022

Name of Co-Author	Dominic Thewlis		
Contribution to the Paper	Conception, Acquiring data, Knowledge, Analysis, Drafting		
Signature		Date	28/03/2022

Chapter 6: Postoperative lower limb joint kinematics following tibial plateau fracture: a 2-year longitudinal study

Abstract

Background: The goal of postoperative tibial plateau fracture (TPF) management is to ensure surgical fixation is maintained while returning patients to normal function as soon as possible, allowing patients to resume their normal activities of daily living. The aim of this study was to investigate longitudinal changes in lower limb joint kinematics following TPF and determine how these kinematics relate to self-reported function.

Methods: Patients presenting with a TPF were recruited (n=18) and undertook gait analysis at six postoperative time points (two weeks, six weeks, three months, six months, one and two years). Lower limb joint kinematics were assessed at each time point based on gait data. Statistical parametric mapping (SPM) was undertaken to investigate the change in joint kinematic traces with time. The Knee Injury and Osteoarthritis Outcome Score (KOOS) was assessed at each time point to obtain self-reported outcomes. A healthy reference was also analysed and used for qualitative comparison of joint kinematics.

Results and Significance: Knee kinematics showed improvements with time, however only minor changes were noted after six weeks at the hip, and six months at the knee and ankle relative to two weeks postoperative. SPM identified significant improvements with time in hip ($p<0.001$) and knee ($p=0.003$) flexion. No significant changes were observed with time at the ankle however, when compared to the healthy reference, participants showed reduced plantarflexion at two years. Lower limb joint ROM showed significant weak to moderate correlation with the activities of daily living (ADL) sub-scale of the KOOS (hip $r=0.442$, knee $r=0.303$, ankle $r=0.367$). The lack of significant changes with time and overall reduced plantarflexion at the ankle potentially reduces propulsive capacity during gait up to two years postoperative. In this study, we see a deficiency in joint kinematics in TPF patients up to two years when compared to a healthy reference, especially at the ankle.

Chapter 6: Postoperative lower limb joint kinematics following tibial plateau fracture: a 2-year longitudinal study

6.1 Introduction

Tibial plateau fractures (TPFs) affect the articular surface of the knee, and account for 1% of bone fractures (Court-Brown & Caesar 2006). Open reduction internal fixation (ORIF) of TPF aims to reduce the articular fracture anatomically as well as restore the mechanical alignment of the knee (Joshua et al. 2016; Prat-Fabregat & Camacho-Carrasco 2016). Postoperative management aims to maintain the reduction achieved at surgery to reduce the long-term risk of arthritis (Honkonen, S. E. 1995). In many centres, this management includes a period of non-weight bearing (Arnold, J et al. 2017). However, this is controversial as several centres have shown that immediate weight bearing after TPF does not lead to fracture displacement (Solomon et al. 2011; Thewlis et al. 2015) and several studies have shown that patients are unable to follow weight bearing instructions (Dabke et al. 2004; Thewlis et al. 2017).

Assuming fracture reduction is maintained, the overall goal of postoperative management is to return patients to normal function as soon as possible minimising the impact of the fracture on activities of daily living (ADLs). These ADLs can be subjectively measured using patient reported outcome measures. Previous work has shown, using the Knee Injury and Osteoarthritis Outcome Score (KOOS) (Roos & Toksvig-Larsen 2003), that TPF patient reported ADLs do not appear to reach the same level as people who have not suffered an injury, but they do improve after surgery up to one year postoperative (Thewlis et al. 2017). There is, however, a lack of objective measurement of ADLs, specifically physical function following injury. Some studies have utilised gait analysis to objectively assess postoperative changes following TPF (Deleanu et al. 2015; Thewlis et al. 2015; Thewlis et al. 2017). Gait analysis can be used to assess joint kinematics, potentially providing an objective measure of physical function and how this function changes with time. Bolink, Grimm and Heyligers (2015) have suggested that, for total knee replacement, that self-reported ADLs and objective measures investigate different components of function, but it is unknown if this is also the case for TPF.

Only one previous study has measured sagittal plane knee joint kinematics of TPF patients during walking (Deleanu et al. 2015), reporting improvements in knee range of motion (ROM) during walking from six to twelve months postoperative. Yet, there are currently no longitudinal data investigating lower limb kinematics which may contribute to understanding how TPF patients return to function following fracture.

The aim of this study was to investigate longitudinal changes, up to two years postoperative, in lower limb kinematics during walking in TPF patients. We hypothesised that TPF patient joint kinematics would improve, both in terms of temporal footprint and magnitude over time. The secondary aim of this investigation was to determine if self-reported ADLs correlate with objective measures of function measured using gait analysis techniques.

6.2 Methods

This was a prospective longitudinal cohort study involving patients who sustained a TPF, treated by ORIF, who were followed at six time-points postoperatively (two weeks, six weeks, three months, six months, one year and two years). All time-points were selected to coincide with standard clinical appointments. Participants were recruited consecutively from a trauma centre at a major metropolitan hospital between December 2012 and October 2016. Ethical approval for the study was granted from the Central Adelaide Local Health Network Human Research Ethics Committee (HREC/16/RAH/74). All participants provided written informed consent.

6.2.1 Patients and protocol

Patients were invited to participate in this study if they were an adult, aged over 18 years, who presented to the hospital with an articular fracture of the proximal tibia requiring ORIF. This included both high energy and fragility fractures. Participants were excluded if polytrauma was present, or any neurological disturbance that would affect their walking gait, if any acute ligament repair or reconstruction was required, if the participant had a BMI > 35 kg/m^2, or if they resided in a remote area and were

unable to attend follow-ups. Fractures were classified using the Schatzker classification (Schatzker, McBroom & Bruce 1979). All participants were instructed to weight bear as tolerated by pain and encouraged unrestricted knee ROM immediately following surgery. For the first six weeks postoperative, patients were encouraged to use crutches and an unlocked hinge brace when ambulating. The brace was removed during motion capture sessions. These motion capture sessions were conducted at each time point and participants were excluded from this analysis if they did not attend at least four motion capture sessions (and in those four sessions they achieved at least three full walking gait cycles following a clean force platform strike), or required revision surgery. Motion data for similarly aged healthy volunteers were used as a reference, but not for quantitative comparisons or statistical analyses. At each clinical follow up, AP x-rays were taken, and participants completed the KOOS to assess their pain, symptoms, ADLs, and quality of life (Roos & Toksvig-Larsen 2003).

6.2.2 Motion capture experiment

Participants were instructed to walk barefoot along a 10 m runway at a self-selected pace as many times as they were able to, or up to 10 successful trials, with a supportive device (walking frame or crutches) if required at two and six weeks postoperative. A 12-camera Vicon MX-F20 system (Vicon, Oxford, UK) was used to record walking trials at 100 Hz. Thirty-eight retro-reflective markers were placed on anatomical landmarks of the pelvis and lower limbs of the participant to define the joints along with four rigid clusters attached to the thighs and shanks (Cappozzo et al. 1995). Two AMTI force platforms (Advanced Mechanical Technology Inc., Watertown, MA) and two Kistler force platforms (Kistler Group, Winterthur, Switzerland) were used to measure ground reaction forces at 2000 Hz synchronously with motion data. Marker trajectories were low-pass filtered using a zero-lag 2nd order Butterworth filter with cut-off frequency of 8 Hz (Koike et al. 2017).

6.2.3 Joint kinematic measurement

Joint kinematics were calculated in OpenSim using a generic lower limb model (Gait2392) (Delp et al. 2007). The model includes three degrees of freedom (DOF) at the hip, one DOF at the knee (flexion-extension), and two DOF at the ankle (flexion-extension, abduction-adduction). The subtalar joint was fixed (subtalar rotation angle = 0°). In this study, we only focus on the sagittal plane kinematics, as changes in coronal and transverse plane kinematics following surgery are likely to be smaller than the known measurement noise in these planes (Baker, Finney & Orr 1999; Benoit et al. 2006, 2007; Piazza & Cavanagh 2000).

The generic model was linearly scaled using static trial marker data using the shape modelling and principal component fit method from Bahl et al. (2019). Scale factors were determined using an atlas-based statistical shape model in MAPClient (Zhang, Sorby, et al. 2014) for each bone segment (Zhang, Malcolm, et al. 2014) ensuring the highest confidence possible between the anatomy in the model and in the participants (Bahl et al. 2019). Inverse kinematics were used to reconstruct the motion of the model from experimental data (Delp et al. 2007) and then the joint angles were calculated as Euler angles according to ISB recommendations (Grood & Suntay 1983; Wu et al. 2002). Joint angles were resampled to 101 data points across each gait cycle. At each time point, a minimum of three and maximum of five joint kinematic traces were used for the statistical analysis and to calculate joint ROMs.

6.2.4 Statistical analysis

Statistical parametric mapping analysis was used to investigate the effect of time postoperative on joint kinematics in a two-level process within (1) and across (2) subjects. The first level (Figure 30) uses the linear regression model (9) at each of the 101 points across the gait cycle to estimate the within subject effect of time on joint angle. The slopes of these curves, β are the within subject effect, or the change in joint kinematics over time (°/week) for the participant.

$$Angle = \beta \times (Weeks\ Postoperative) + a + \epsilon \quad (9)$$

These β curves were calculated for each participant to be used in the analysis across patients, an unpaired 1-D t-test. The null hypothesis was no effect of time on joint kinematics. The 1-D equivalent of the 0-D t statistic, the statistical parametric map, SPM{t}, was calculated across the gait cycle using the whole population data (Pataky, TC, Vanrenterghem, J & Robinson, MA 2015). For this map, the critical threshold t* is calculated with a type 1 error rate $\alpha = 0.05$ using random field theory (Adler & Taylor 2007). t* is the threshold that only 5% of smooth random curves are expected to traverse. If the SPM{t} value crosses t* at any point, the null hypothesis is rejected. Where there are multiple consecutive points crossing t* (called a 'supra-threshold cluster'), the cluster p-value is calculated from random field theory (Adler & Taylor 2007). All of these analyses were implemented using spm1d (Pataky, T, Vanrenterghem, J & Robinson, M 2015).

Two-tailed bivariate Pearson correlations were used to investigate if there is a correlation between each joint ROM and self-reported ADL score from the KOOS. This test was selected to investigate the secondary aim, to determine whether self-reported ADLs correlate with objective measures of ADLs using SPSS 25 with $\alpha = 0.05$ (IBM, New York, USA)

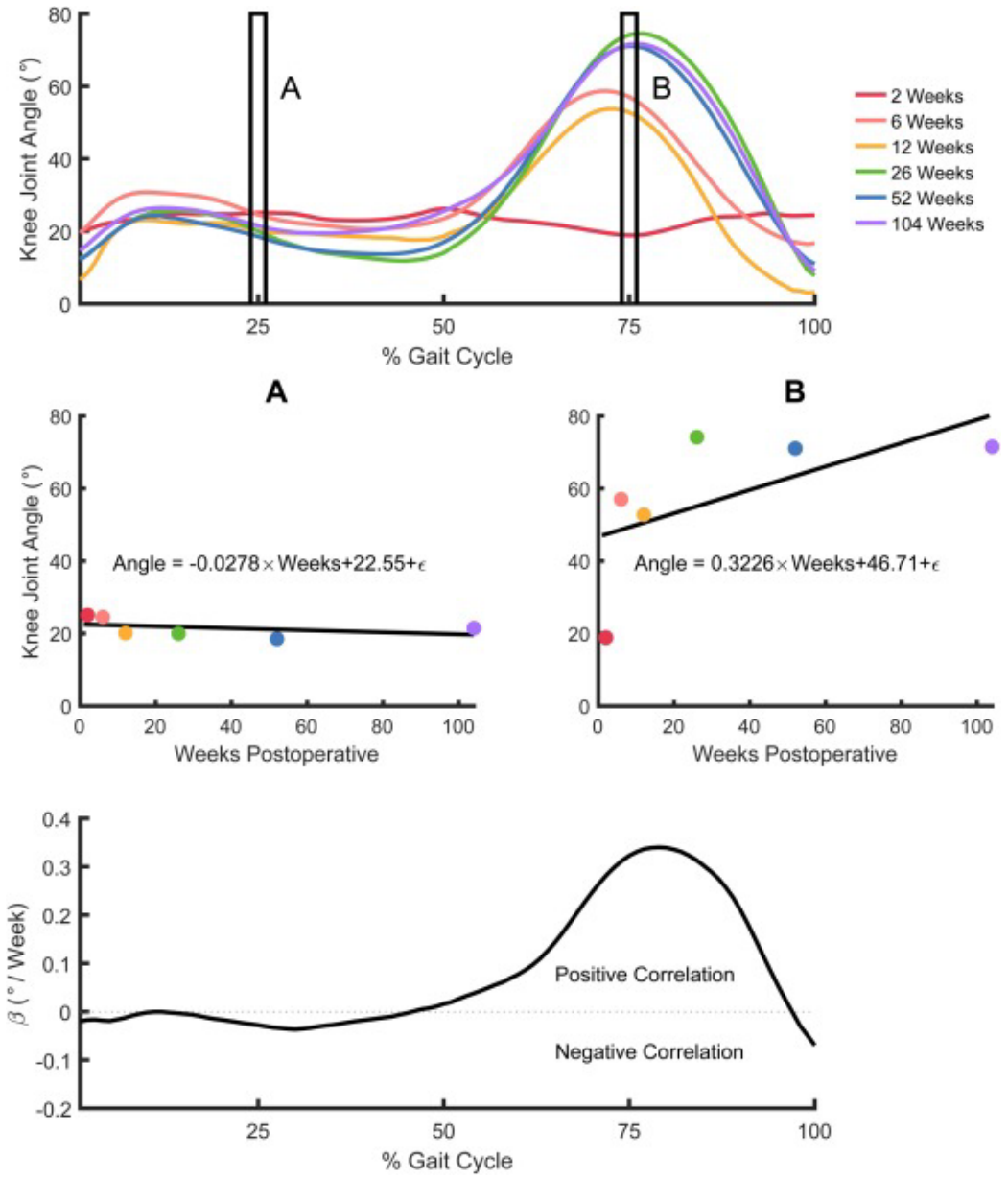

Figure 30 Example of level one statistical parametric mapping analysis estimating the within subject effects. (1) The joint angles for a single participant across the entire gait cycle are determined. (2) The joint angles at each point across the gait cycle (shown here are (A) 25% and (B) 75%) are projected across the number of weeks postoperative the measurement was taken. The linear regression model is used to determine the change in joint angle at this point of the gait cycle across the number of weeks postoperative. (3) The slope of the regression (β) is calculated across the entire gait cycle with positive values showing a positive correlation with time, and negative values showing negative correlation with time. (3) Is the within subject effect of time on joint kinematics.

6.3 Results

6.3.1 Participants and reference

Thirty-seven participants with TPFs were recruited (mean age 52 years, range 27-67 years; 16M/21F) into the study. Nineteen participants were either lost to follow up, did not attend the minimum of four motion capture sessions, or insufficient data were collected at their motion capture sessions, resulting in a total of 18 participants analysed (mean age 51 years, range 27-67 years; 8M/10F). Using the Schatzker classification, these participants' fractures were classified as: Type II n = 9, Type IV n = 6, and Type VI n = 3. Motion data for 15 similarly aged healthy volunteers (age: 35 – 68 years) were used as a reference for qualitative comparison from Kersh et al. (2018) and lab reference data. The healthy reference was then selected based on the study population to have similar age distributions.

6.3.2 Joint kinematics

Mean and standard deviation joint flexion angles at each time point (Figure 31A) show that after six weeks, the hip functions in a normal pattern, whereas the knee and ankle function in a pattern closer to normal after 26 weeks (expanded view of each mean and standard deviation joint flexion angles at each time point, and the joint flexion angles by Schatzker fracture type, and by weeks until radiological evidence of fracture union, in supplementary material). The mean β curves for the population (Figure 31B) show an increase in hip flexion from mid-stance to early swing over time, an increase in knee flexion during swing over time, and increased ankle plantarflexion during terminal stance. Finally, the outcome of the statistical parametric mapping analysis (Figure 31C) identifies supra-threshold clusters for the change in both hip and knee angles over time for the population.

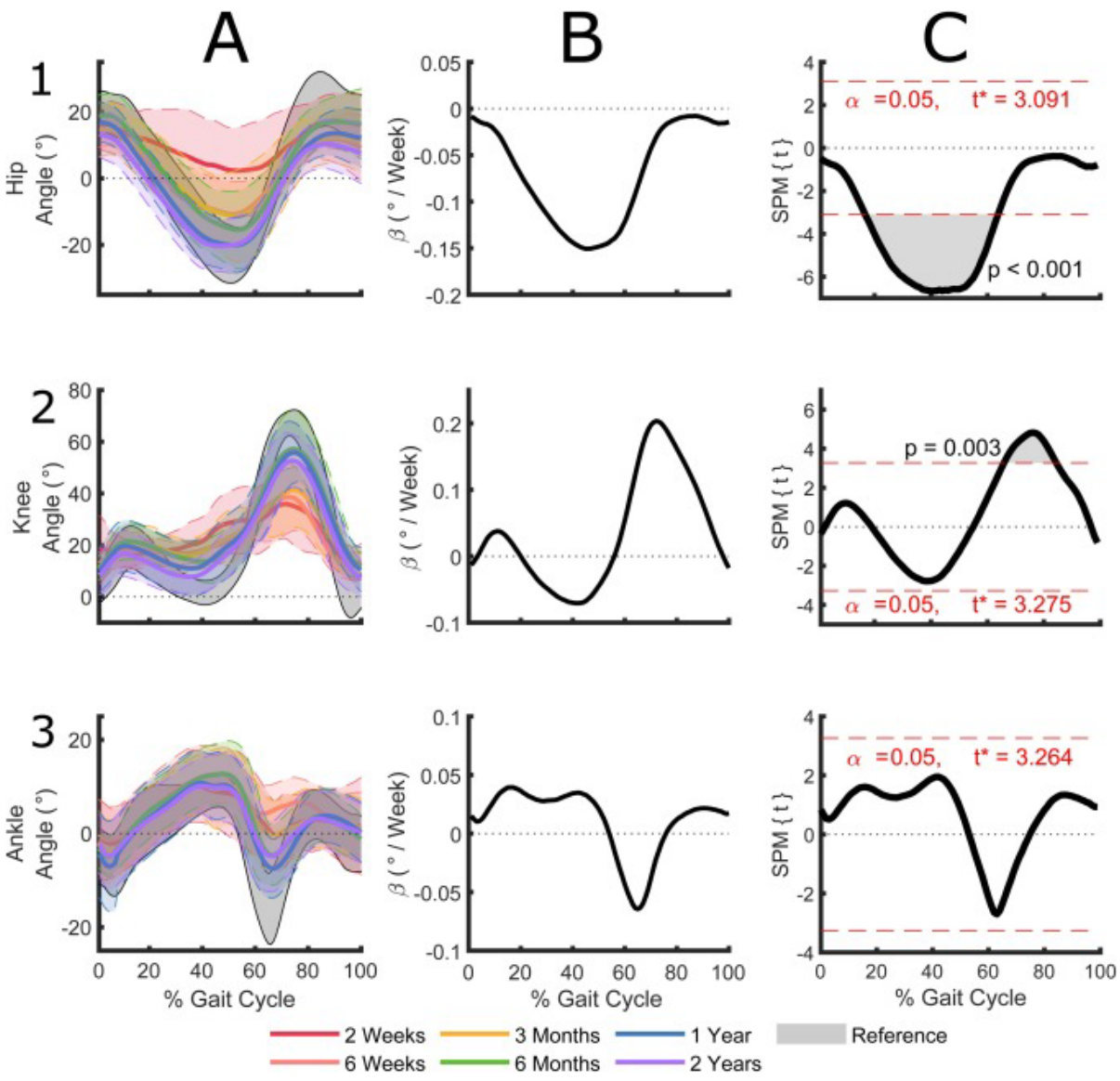

Figure 31 (A) Group mean and standard deviation hip (1), knee (2) and ankle (3) angles at each time point measured. (B) Mean changes in joint kinematics across the gait cycle over time (β) for all participants. (C) The unpaired t-test statistic SPM{t}. The critical threshold at the hip, t* = 3.091 was exceeded at the supra-threshold cluster between 17% and 64% with $p < 0.001$, indicating more hip flexion as the participants recover. At the knee, the critical threshold t* = 3.275 was exceeded at the supra-threshold cluster between 66% and 84% with $p = 0.003$, indicating more knee flexion during mid stance as participants recover. The ankle critical threshold t* = 3.264 was not exceeded at any point along the gait cycle.

The mean hip flexion angles (Figure 31A1) show that there is a large change in maximum hip flexion between two and six weeks (2° to 11°), with further improvements up to two years postoperative (20°). This two-year hip flexion is similar to the healthy reference of 23° of flexion. The SPM analysis (Figure 31C1) identified that there is a significant association between improved hip flexion and time postoperative, identified by the supra-threshold cluster between 17% and 64% which exceeded the critical threshold of 3.091 ($p < 0.001$) (Figure 31C1).

Peak knee flexion showed improvements from two weeks (36°) up to two years (53°) but remained lower than the reference (67°) (Figure 31A2). There is little change across the gait cycle except for one supra-threshold cluster identified between 66% and 84% which exceeded the critical threshold of 3.275 as the knee angle showed significantly increased flexion with time postoperative ($p = 0.003$) (Figure 31C2).

The mean ankle joint flexion angle shows an angle pattern more similar to the healthy reference after 26 weeks compared to before (Figure 31A3). The β curve (Figure 31B3) shows improvement in participant plantarflexion over time, changing from a mean of 0° at two weeks, to 5° at 26 weeks, which remains up to two years but is less than the reference plantarflexion (16°). The SPM analysis (Figure 31C3), however, showed no significant change with time from zero across the gait cycle, indicated by no supra-threshold clusters meeting or exceeding the critical threshold of 3.264.

6.3.4 Objective and self-reported activities of daily living

The Pearson correlations (Figure 32) identified significant, weak to moderate positive correlations between the hip ($r = 0.442$, $p < 0.001$), knee ($r = 0.303$, $p = 0.009$), and ankle ($r = 0.367$, $p = 0.001$) ROM and self-reported ADLs.

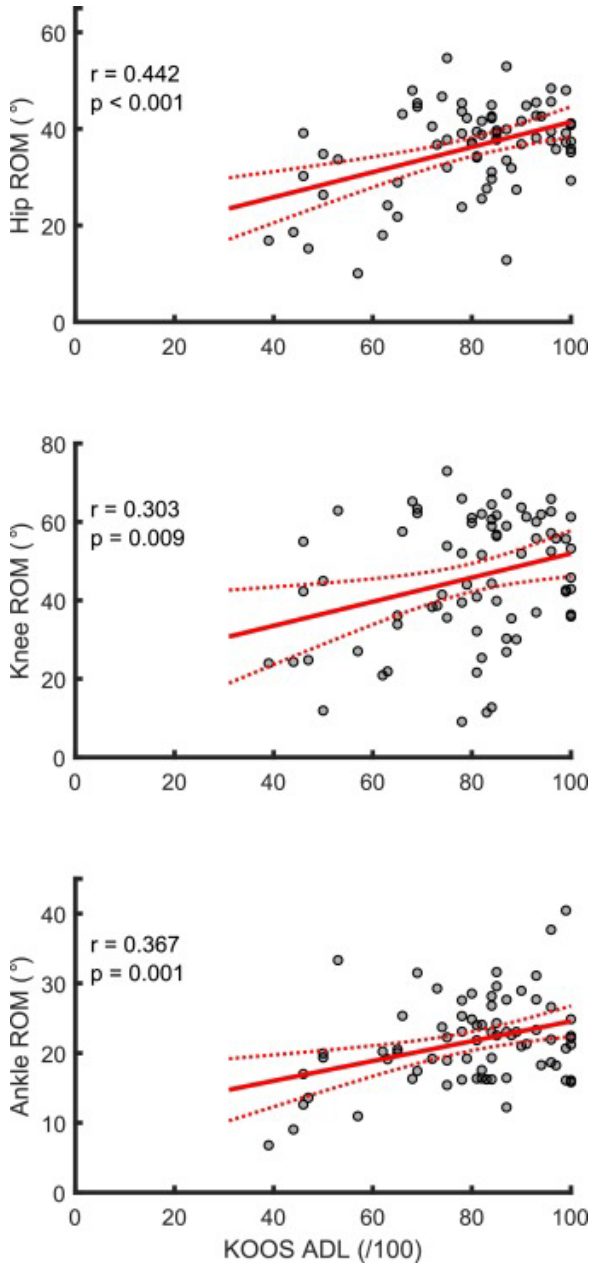

Figure 32 The Pearson correlation between the hip, knee, and ankle joint ROM and self-reported ADLs. The line of best fit, and 95% confidence interval for the line of best fit are also presented in red.

6.4 Discussion

Tibial plateau fractures are complex injuries which typically show poor long-term patient outcomes (Thewlis et al. 2017; Timmers et al. 2014). This study aimed to investigate longitudinal changes in lower limb kinematics and determine whether self-reported ADLs correlate with objective measures of lower limb function. Significant changes in hip and knee joint kinematics over time were observed, however, there were no significant changes in ankle joint kinematics. Lower limb joint ranges of motion showed positive weak to moderate correlations with self-reported ADLs from the KOOS questionnaire.

In assessing lower limb joint kinematics, TPF patients showed similarities in hip function at six weeks postoperative and beyond compared to the reference cohort. However, function at the knee and ankle did not approach the reference cohort until six months postoperative. Results reported here are similar to those of Deleanu et al. (2015) who found comparable sagittal plane knee joint kinematics at six months and one year postoperative, however, these studies remain unique in their application of methods for measuring joint kinematics. Deleanu et al. (2015) use a direct readout of an ultrasound-based measurement system to estimate joint kinematics which, while accurate, requires a physical connection between participant and system with cable length limiting the capture area. Such a limitation is likely to impede participants reaching normal walking cadence and stride length thereby altering lower limb joint kinematics (Francis et al. 2016; McGrath et al. 2019).

The SPM analysis showed positive association between joint kinematics and time postoperative. There was a significant association between time postoperative and improved hip extension during mid stance, terminal stance, and pre-swing. Furthermore, there was a significant association with improved knee flexion during mid swing. However, no significant association was found between time postoperative and ankle plantar or dorsi-flexion. This, coupled with the noted reduction in ankle ROM compared to the reference data, potentially limits propulsive capacity during gait, an effect similar to that of age on walking reported by Arnold, JB

et al. (2014). The reduced propulsion can place increased load on the hip flexors requiring them to act to 'pull' the foot off the ground as opposed to the normal push-off at the ankle joint enabling forward propulsion and ground clearance.

Any long-term deficit in ankle plantarflexion may result in distal-to-proximal work redistribution (Browne & Franz 2019). This has been reported to increase hip flexor work (Zelik & Adamczyk 2016) for propulsion, and may further alter the muscular control and actuation surrounding the knee. Further investigation should be conducted to determine the effect of reduced plantarflexion on the muscular control surrounding the knee along with the effect of these loading patterns on the load and density distribution of the tibial plateau.

The joint ROMs showed weak to moderate correlations with self-reported ADL scores, with the hip range of motion explaining the most (19.5%) variance in self-reported ADL scores. These correlations were similar to the findings of Bolink, Grimm and Heyligers (2015) for TKA, supporting the notion that the patient reported ADLs and objective measures of function are measuring different outcomes. Function assessed through gait analysis and patient reported ADLs provide complementary measures of recovery following TPF, and the use of both in assessing postoperative capabilities is recommended. Stevens-Lapsley, Schenkman and Dayton (2011) suggest that, for TKA, patient reports are more indicative of their pain than actual postoperative function. Because of this, it may be suitable to include some basic functional assessments, like the sit to stand used by Elsoe et al. (2015), to supplement patient reported scores with objective postoperative functional measures.

There were some limitations in this study. Only 48% of participants enrolled in this study were included in this analysis. Eleven participants were lost to follow up, one participant did not attend the minimum number of motion capture sessions, and seven participants were unable to complete the minimum required walking trials and were excluded from the analysis. While not directly comparable, the loss to follow-up in this study was lower than previous studies reporting on clinical outcomes following TPF (<6 months 73.3% loss, 1 year 76.8% loss) (Hoffmann, Sietsema & Jones 2016). As

seven participants were unable to complete the minimum number of walking trials, this biased the results of the study towards patients who were more physically able following surgery.

A further limitation in this analysis was that there were different numbers of participants at each time point. Only seven of the 18 participants attended all analysis sessions. There is no technique to account for missing data in statistical parametric mapping. By systematically removing time points from the seven participants at every time point and recalculating individual β curves, there were only very small changes, except for where the two-week data is missing where the β curves showed much lower changes over time across the walking gait cycle. This likely means we are seeing a reduced effect of time (β) on changes in joint kinematics measured from SPM for the six participants not at the two-week time point and may explain why there are no significant differences seen at the ankle.

The study only investigated changes in the sagittal plane. The musculoskeletal modelling methods used are currently limited in their ability to measure accurate kinematic data in the coronal and transverse plane for the knee (Besier et al. 2003) as they are significantly affected by skin artefact (Benoit et al. 2006, 2007) and cross talk from the sagittal plane (Baker, Finney & Orr 1999; Piazza & Cavanagh 2000). While it would be beneficial to understand the coronal and transverse rotations of TPF patients to determine if there are additional peripheral changes with time, the modelling limitations impact the accuracy with which these data can be reported. Therefore, we opted not to include these measurements.

6.5 Conclusion

The findings of this study suggest that the greatest improvement in walking gait occurred within the first six months postoperative. At two years, patient maximum knee flexion and plantarflexion were less than the healthy reference, indicating a functional deficit is still present. The total ROM at each joint showed positive weak to moderate correlations with patient reported ADL scores. It is therefore suggested that

functional movement testing be undertaken to supplement patient reported outcome measures to better gauge true patient outcomes.

6.6 Acknowledgements

Dr Mark Robinson (Liverpool John Moores University) assisted in the design of the statistical parametric mapping approach used. This research program is supported by an Australian Government Research Training Program (RTP) Scholarship. Dr Arnold and A/Prof Thewlis receive Fellowship funding from the NHMRC (ECF (ID: 1120560) and CDF (ID: 1126229), respectively). Dr Martelli receives funding from the ARC (ID: FT180100338, DP180103146).

Chapter 7: Discussion and Conclusion

The central aim of this thesis was to ***improve upon methods for modelling the local mechanical environment in surgically repaired tibial plateau fractures to further understand the mechanics associated with fracture recovery, and to investigate long-term patient responses to immediate postoperative weight bearing.*** While addressing this aim, three *methodological* contributions to the field of knee mechanics and modelling were produced. These were:

1. Augmenting an EMG-informed neuromusculoskeletal modelling pipeline to include a stochastic process to generate a range of plausible knee joint loads which includes the *in-vivo* measured loading. These methods are well suited to knee pathology, as altered neuromusculoskeletal control can be modelled. **(Chapter 3)**
2. Estimating the internal strains within the tibial plateau due to a physiologically relevant external load using micro-CT imaging and digital volume correlation, and development of the methods associated with capturing this data. This work provides evidence that the internal strains are in the expected physiological range through calculating internal bone strains, which had previously not been undertaken within the tibial plateau. **(Chapter 4)**
3. Comparison of a subject specific finite element methodology for estimating the internal strains within the tibial plateau with experimental measures of strain. This work provides a base for modelling other tibial plateaus, as well as models of fractures including metalwork. **(Chapter 4)**

Further to these *methodological* contributions, four key findings, which will be elaborated upon were obtained.

7.1 Key findings and implications of work for tibial plateau fracture research

The key findings of this thesis are:

1. Estimates of knee joint loading are improved when augmenting an EMG-informed approach with statistical processes. **(Chapter 3)**
2. The internal 3D strains within the tibial plateau under peak walking loads are within the physiological range. **(Chapter 4)**
3. With ideal surgical fixation, tibial plateau fractures can withstand peak walking loads with minimal displacement. **(Chapter 5)**
4. People who have undergone surgery to repair a TPF recover their joint kinematics within the first six postoperative months. **(Chapter 6)**

7.1.1 Estimates of knee joint loading are improved when augmenting an EMG-informed approach with statistical processes

In Chapter 3, an EMG-informed neuromusculoskeletal modelling method was augmented using a stochastic process – the EMG-informed stochastic approach. Using this method, a solution space of possible knee joint loads was generated which included the measured knee loads for three separate individuals. Estimates of joint loading were improved when an EMG-informed approach when compared to optimization tasks (Gerus et al. 2013; Hast & Piazza 2013; Manal & Buchanan 2013; Serrancolí, Kinney & Fregly 2020). This improvement is likely due to the within- and between-task variability, as well as the between-subject variability in muscle recruitment (Scholz & Schöner 1999) which cannot be effectively modelled using optimization techniques (Körding & Wolpert 2006; Martelli et al. 2015; van Veen, Mazza & Viceconti 2020).

By augmenting EMG-informed approaches with a stochastic process, muscles which are not driven by EMG signals can be statistically modelled. This effectively models the variability in muscle recruitment methods. The generation of a probabilistic

solution rather than a single joint load for a single walking trial, means a probabilistic analysis of the range of possible joint loadings can be investigated using only a single walking stride. For TPF patients, a single walking trial – which may be painful – can be analysed to generate a range of possible joint loads. This range could be applied to patient specific computational models for estimating the amount of fragmental motion caused by possible loading, allowing for additional tailoring of, and investigation into postoperative weight bearing management.

7.1.2 The internal 3D strains within the tibial plateau under peak walking loads are within the physiological range

Chapter 4 presents the first measurement of the internal strains within the tibial plateau due to external joint loading. When applying a three-bodyweight load – the maximum expected load applied during walking – to two tibial plateaus, the internal strains calculated using DVC were within the physiological region, between 200-300 and 2000-3000 με (Frost 1987; Wolff 1892). These strains had not previously been measured, and support the argument that bone is structurally optimised for regular loading (Cristofolini 2015). The calculated strains also provide a reference range of internal strains within the tibial plateau for validation of finite element models.

The measured strains were also compared to those calculated using subject specific FE models to determine the predictive power of current FE modelling techniques. The strains calculated from both DVC and FE were similar in almost all volumes of interest compared, with total median differences of 499 με and 103 με. While similar workflows and models exist, the FE models developed are the first to be compared to internal strain measurements. This provides an indication of the expected internal strain errors which are predicted using subject specific finite element modelling.

7.1.3 With ideal surgical fixation, tibial plateau fractures can withstand peak walking loads with minimal displacement

In Chapter 5, the internal fragmental displacements of two TPFs due to external joint loading was calculated using 2D image correlation on micro-CT images. In this work, fracture fragments displaced, on average, less than 0.3 mm when three-bodyweights of load were applied to the entire tibial plateau. When comparing these results to experimental and FE studies in the literature, the displacements obtained in Chapter 5 show significantly stiffer (displacement per load) fracture-fixation constructs when compared to other experimental studies, but similar stiffness to FE studies literature (Figure 33, Figure 5 with the results from Chapter 5).

A three-bodyweight knee joint loading is significantly higher than estimated using musculoskeletal models for TPF patients two weeks postoperative (Thewlis et al. 2015). Withstanding more load than can be applied during pain-tolerated postoperative weight bearing means that the fracture-fragment construct in these ideally repaired TPFs is stiff enough to not significantly displace. Assuming a linear relationship between displacement and load, to produce a 2 mm displacement, which has been associated with an increased risk of posttraumatic osteoarthritis (Parkkinen et al. 2014), would require almost 4000 N to be applied directly to the fragment. This 4000 N, for the two specimens investigated, would mean knee joint loads of 7.9-10 BW, which is greater than peak knee loads measured during stair (3.38 BW) and ramp (3.39 BW) descent (Taylor, WR et al. 2017).

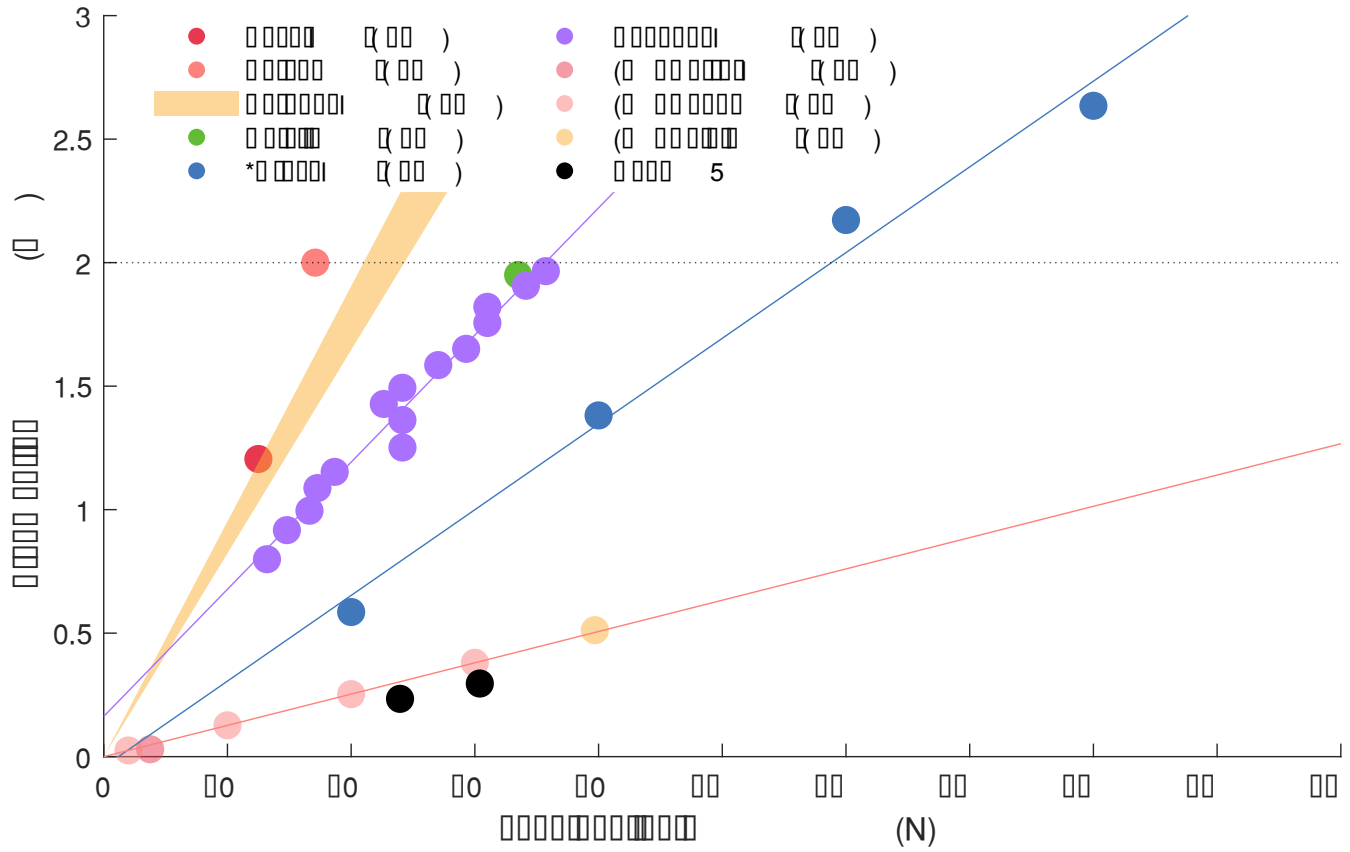

Figure 33 Fragmental displacements vs. load applied to the fragment for experimental and FE models of fractures involving a split with the results obtained from Chapter 5. Lines of best fit have been added to the results from Cross et al. (2013) and Vendeuvre et al. (2018), and the FE model from Chen, P et al. (2017). *Cross et al. (2013) only report the total load applied to the tibial plateau, and not the load applied directly to the fragment.

This study is the first to report the internal displacements within TPFs due to external loading. Previous studies have been limited to external measured of displacement, either through optical tracking of markers on the outside edge of the plateau (Cuéllar et al. 2015; Högel et al. 2013; Parker et al. 1999; Vendeuvre et al. 2018), or direct measurements from the load application system employed (Doht et al. 2012; Koval et al. 1996; Ratcliff et al. 2007). Previous studies have only been able to imply the fracture fragment motion at the fracture site, and the results of Chapter 5 show inconsistent displacement across fracture fragments. In future, this displacement should be estimated using DVC techniques, like in Chapter 4, to quantify the 3D deformation of TPF fragments, and determine the inter-fragmentary strains. Using these strains and deformations, finite element models of TPFs can be validated, and used to investigate the effect of altered loading on fragmental motion *in-silico*.

7.1.4 People who have undergone surgery to repair a tibial plateau fracture recover their joint kinematics within the first six postoperative months

From the longitudinal changes in joint kinematics presented in Chapter 6, we can suggest that most of the recovery in joint motion occurs within the first six months postoperative. For Schatzker II fractures, most of the changes in joint kinematics occurs between two and six weeks postoperative, while for more complex Schatzker IV and VI fractures, most of the joint kinematic recovery occurs between six and twelve weeks postoperative. Given the scope of this thesis, focusing on Schatzker I and II fractures, the joint kinematics recovery adds to the growing evidence that, for mechanically simpler fractures, early weight bearing is well tolerated.

Similar joint kinematics have been reported at both two-to-five months (Fändriks et al. 2021) and six months (Deleanu et al. 2015) postoperatively, but no study had

reported these motions longitudinally, and none up to two years postoperative. The longitudinal study revealed at which stages of recovery TPF patients recovered their joint kinematics, however, the continuing deficit at two years postoperative indicates that there is additional mid-term postoperative management required. It may be hypothesised that these patients will never recover their full range of motion during walking, however, it is unlikely that this could be answered using computational modelling alone. An intervention study assessing different mid-term postoperative management strategies could assist in returning patients to normal long-term function.

7.2 Limitations

The work presented in this thesis represents state-of-the-art computational and experimental modelling for TPFs. There are, however, some limitations in their design and implementation. In each Chapter, specific limitations are discussed in terms of each study objective, including: only comparing the von Mises strains in four volumes of interest when comparing FE models to DVC results **(Chapter 4)**; and calculating only 2D internal fragmentary motions of TPFs **(Chapter 5)**. There are limitations posed by the scope of the research, and in the methods currently available for estimating joint loads. Throughout the thesis, each component is fundamentally limited by the samples, and sample sizes and the sampled populations.

The scope of this thesis was constrained to only mechanically simple TPFs with split components. The significant heterogeneity in TPFs means that this work covers approximately half of the fractures reported clinically. The remaining fractures are significantly more complex in their makeup and associated fixation. By improving upon the modelling capabilities and methodologies for investigating simpler TPFs, this work provides a foundation on which more complex fractures and fixations can be modelled.

The neuromusculoskeletal modelling techniques presented and investigated are some of the few methods available for investigating joint loading which can be used for investigating the mechanical environment in TPFs. Discussed previously, instrumented implants allow for direct measurement of joint loads, but this is not feasible for fracture cohorts. The musculoskeletal modelling techniques investigated required significant fundamental simplifications like defining the knee as a single degree of freedom hinge joint, neglecting the effects of secondary rotations and translations.

TPF patients have serious impairment to joint motion and neuromusculoskeletal control. The neuromusculoskeletal modelling presented in Chapter 3 was investigated using three individuals who had undergone a knee replacement due to osteoarthritis. This presents two significant challenges in (1) generalizing the methods for larger populations, and (2) transferring the methods to TPF patients. To further generalize the methods, they should be assessed on additional data, an example of this data is the CAMS knee dataset, which includes a further six individuals who have undergone a knee replacement (Taylor, WR et al. 2017). While this dataset does not necessarily represent healthy people, it is currently impossible to directly measure the knee loads without these instrumented replacements. To transfer the modelling methods to TPF patients, it would be necessary to develop a method for measuring the loads within the fractures. These estimation techniques are currently the best techniques available for incorporating measurements of muscle EMG into neuromusculoskeletal models to estimate joint loads, and could be improved through the introduction of additional participant data.

The two tibial plateaus investigated in Chapters 4 and 5 are from elderly, male, underweight donors. TPFs occur in a bimodal distribution, with more than half of these fractures occurring in people under 50 years of age, and a 54:46 male to female ratio (Court-Brown & Caesar 2006). The two donors age is representative of only 12.7% of fracture patients (>75 years), and so caution should be taken when interpreting the results of Chapter 6 especially. Despite this, the fragment-fixation construct stiffness calculated provides confidence in modern fixation techniques for minimising

fragment displacement under loading. This age limitation in measuring the internal displacements of tibial plateau fragments could be reduced by repeated experimentation on cadaveric specimens, or through further *in-vivo* radiostereometric analysis, especially given the findings from Chapter 5 where fragmental displacements were of a similar magnitude to radiostereometric analysis measurements.

The patients investigated in Chapter 6 represent only a sub-group of 18 TPF patients who were all operated on at a single trauma centre and prescribed similar postoperative weight bearing (either weight bearing to 20 kg or as tolerated by pain). This limits the between-patient variability as, although their fractures were different and fixations personalised, the results may not be valid for a different trauma centre which uses different techniques and devices to fix these fractures. While we see general agreement in joint kinematic profiles with other cohorts in the literature (Deleanu et al. 2015; Fändriks et al. 2021), determining if postoperative weight bearing provides improved patient outcomes would require a randomised control trial. The experimental and computational techniques developed through this thesis could be used to provide evidence regarding the safety of postoperative weight bearing to support a randomised control trial.

7.3 Recommendations for future research

7.3.1 Investigation into the long-term functional deficit in tibial plateau fracture patients

Highlighted in Chapter 6 was a long-term functional deficit in joint kinematics for TPF patients. From this study alone, it is not clear why this is occurring and further research is required. A combination of musculoskeletal modelling and rehabilitation therapy could be applied to reduce this deficit, and improve functional outcomes for TPF patients. Musculoskeletal modelling could provide some support in planning and assessing rehabilitation protocols on the recovery of TPFs. Forwards driven musculoskeletal models using optimal control theory could be employed to model the effect of different regimes on long-term function. Recently, optimal control theory has been used to investigate the effect of selective muscle weakness like reducing the strength of hip flexors, resulting in Trendelenburg gait (Dembia et al. 2020). This approach could also be used to model the opposite effect, strengthening of selected muscle groups to see their effect on gait. The data obtained and presented in Chapter 6 can be used to tune these forwards driven models to better represent the TPF cohort produce *in-silico* training regime outcome measures.

7.3.2 Digital patient models

Digital patient models have the potential for evaluating different treatments and postoperative management solutions on a computational model before clinical decisions are made (Pappalardo et al. 2019). An example workflow of how digital patient models could improve preoperative planning and subsequent postoperative rehabilitation is in Figure 34. Shown across the top of Figure 34, there is little additional input from the patients to optimise their care using digital modelling.

Following hospital triage, all patients undergo a CT scan to plan surgical approach. Using this CT scan a digital reconstruction of the patients' TPF can be virtually operated upon. A recursive loop of virtual implant positioning, followed by FE models of the fracture with implant, followed by virtual postoperative evaluations can

be conducted to optimise surgical approach and guide postoperative management. Following this recursive approach, recommendations can be provided to surgeons who would then operate on the patient and provide postoperative management recommendations. As more digital patient models are generated and validated using mid- to long-term patient data, surgeon and patient confidence in the models will improve.

At postoperative follow ups, using 3D gait analysis, patient specific musculoskeletal models can be developed. Using these models and stochastic neuromusculoskeletal models, the effect of altering different musculoskeletal parameters of rehabilitation techniques could be modelled to assess their effect on joint loading estimates. Further, a combination of optimal control models and stochastic neuromusculoskeletal models could be applied to undertake virtual intervention trials for patients. The results of these virtual trials could then be used to inform patient postoperative care through optimising rehabilitation approaches based on digital patient modelling.

Data obtained from the postoperative follow-ups can also be used to improve upon the FE models for surgical planning. Further defining the loads which the fractures may be exposed to reduces the likelihood that unexpected loading conditions are experienced by the patient which may result in fixation failure or poor patient outcomes.

The use of digital patient models from surgical planning through to postoperative care may assist in improving patient reported and functional outcomes. An example of using digital patient models for improving patient functional outcomes is modelling the effect of improving plantar flexor mobility and strength. This may assist in recovering the reduced ankle plantarflexion seen in TPF patients in Chapter 6 which may be altering the muscular control surrounding the knee. From a gait analysis session of a patient, a musculoskeletal model can be personalised, with an optimal control algorithm implemented to reproduce the kinematics measured. From this model, muscle parameters like maximum isometric force can be altered and the

control algorithm used to computationally assess the effect of targeted strength training on joint kinematics, leading to improved patient postoperative care.

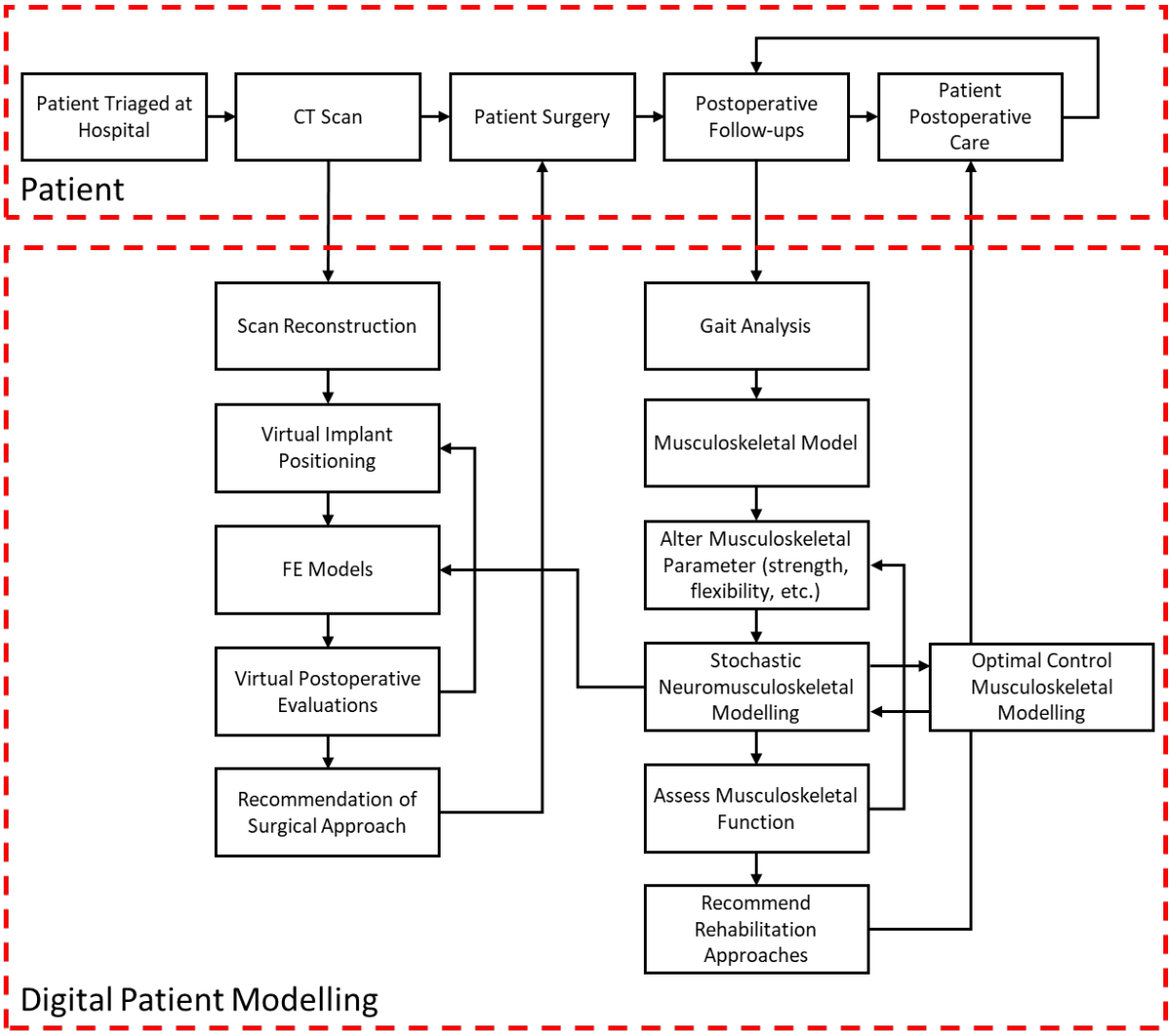

Figure 34 Interfacing between patients and digital patient modelling showing the recursive surgical planning and patient rehabilitation approaches.

7.4 Conclusion

Tibial plateau fractures reduce lower limb function and result in poor patient reported outcomes. Allowing earlier weight bearing in postoperative maintenance of fractures could improve these outcomes. A current limitation in prescribing this earlier weight bearing is in understanding the dynamic mechanical environment present in surgically repaired tibial plateau fractures.

Neuromusculoskeletal modelling approaches for estimating knee joint loading were improved and validated on participants who had received an instrumented knee replacement. Experimental micro-CT techniques for determining the internal mechanical environment of TPFs were developed and applied to split fractures. In developing these methods, it was shown that the internal strains within regions of the tibial plateau are within the expected physiological range (200-3000 με), further strengthening the argument that bone is optimized for regular loading. Subject specific finite element modelling methods were evaluated using this data, showing up to 500 με differences in median strains within the tibial plateau. From applying the micro-CT techniques to fractured and surgically repaired tibial plateau fractures, the amount of internal displacement measured was within the same order of magnitude as both a clinical cohort of similar fractures, and current finite element models of tibial plateau fracture mechanics.

These methods can be used to assess different fracture and fixation techniques on the internal fragmental displacements, furthering our understanding of the internal mechanics present during early weight bearing. Long-term, patients showed similar kinematic responses to immediate postoperative weight bearing when compared to TPF patients who were not prescribed weight bearing. The work presented in this thesis enables further computational studies of TPF mechanics to assess the safety of postoperative weight bearing, aiming to improving patient quality of life following fracture and repair.

References

Ab-Lazid, R, Perilli, E, Ryan, MK, Costi, JJ & Reynolds, KJ 2014, 'Does cancellous screw insertion torque depend on bone mineral density and/or microarchitecture?', *Journal of Biomechanics*, vol. 47, no. 2, 2014/01/22/, pp. 347-353.

Ackland, DC, Lin, Y-C & Pandy, MG 2012, 'Sensitivity of model predictions of muscle function to changes in moment arms and muscle–tendon properties: A Monte-Carlo analysis', *Journal of Biomechanics*, vol. 45, no. 8, 2012/05/11/, pp. 1463-1471.

Adler, RJ & Taylor, JE 2007, *Random Fields and Geometry*, Springer, New York, NY.

Adouni, M & Shirazi-Adl, A 2014, 'Evaluation of knee joint muscle forces and tissue stresses-strains during gait in severe OA versus normal subjects', *Journal of Orthopaedic Research*, vol. 32, no. 1, pp. 69-78.

Anderson, FC & Pandy, MG 2001, 'Static and dynamic optimization solutions for gait are practically equivalent', *Journal of Biomechanics*, vol. 34, no. 2, pp. 153-161.

Arnold, J, Tu, C, Phan, T, Rickman, M, Varghese, V, Thewlis, D & Solomon, L 2017, 'Characteristics of postoperative weight bearing and management protocols for tibial plateau fractures: Findings from a scoping review', *Injury*, vol. 48, no. 12, pp. 2634-2642.

Arnold, JB, Mackintosh, S, Jones, S & Thewlis, D 2014, 'Differences in foot kinematics between young and older adults during walking', *Gait & Posture*, vol. 39, no. 2, pp. 689-694.

Bahl, J, Zhang, J, Killen, B, Taylor, M, Solomon, L, Arnold, J, Lloyd, D, Besier, T & Thewlis, D 2019, 'Statistical shape modelling versus linear scaling: Effects on predictions of hip joint centre location and muscle moment arms in people with hip osteoarthritis', *Journal of Biomechanics*, vol. 85.

Baker, R, Finney, L & Orr, J 1999, 'A new approach to determine the hip rotation profile from clinical gait analysis data', *Human Movement Science*, vol. 18, no. 5, pp. 655-667.

Bakke, D & Besier, T 2020, 'Shape model constrained scaling improves repeatability of gait data', *Journal of Biomechanics*, vol. 107, p. 109838.

Bay, BK, Smith, TS, Fyhrie, DP & Saad, M 1999, 'Digital volume correlation: Three-dimensional strain mapping using X-ray tomography', *Experimental Mechanics*, vol. 39, no. 3, 1999/09/01, pp. 217-226.

Belaid, D, Vendeuvre, T, Bouchoucha, A, Bremand, F, Brèque, C, Rigoard, P & Germaneau, A 2018, 'Utility of cement injection to stabilize split-depression tibial plateau fracture by minimally invasive methods: A finite element analysis', *Clinical Biomechanics*, vol. 56.

Bennett, KJ, Millar, SC, Fraysse, F, Arnold, JB, Atkins, GJ, Solomon, LB, Martelli, S & Thewlis, D 2021, 'Postoperative lower limb joint kinematics following tibial plateau fracture: A 2-year longitudinal study', *Gait & Posture*, vol. 83, 2021/01/01/, pp. 20-25.

Benoit, DL, Ramsey, DK, Lamontagne, M, Xu, L, Wretenberg, P & Renström, P 2006, 'Effect of skin movement artifact on knee kinematics during gait and cutting motions measured in vivo', *Gait & Posture*, vol. 24, no. 2, pp. 152-164.

Benoit, DL, Ramsey, DK, Lamontagne, M, Xu, L, Wretenberg, P & Renström, P 2007, 'In Vivo Knee Kinematics during Gait Reveals New Rotation Profiles and Smaller Translations', *Clinical Orthopaedics and Related Research*, vol. 454, pp. 81-88.

Bergmann, G, Bender, A, Graichen, F, Dymke, J, Rohlmann, A, Trepczynski, A, Heller, MO & Kutzner, I 2014, 'Standardized Loads Acting in Knee Implants', *PLOS ONE*, vol. 9, no. 1, p. e86035.

Besier, TF, Sturnieks, DL, Alderson, JA & Lloyd, DG 2003, 'Repeatability of gait data using a functional hip joint centre and a mean helical knee axis', *Journal of Biomechanics*, vol. 36, no. 8, 2003/08/01/, pp. 1159-1168.

Bolink, SAAN, Grimm, B & Heyligers, IC 2015, 'Patient-reported outcome measures versus inertial performance-based outcome measures: A prospective study in patients undergoing primary total knee arthroplasty', *The Knee*, vol. 22, no. 6, 2015/12/01/, pp. 618-623.

Brown, TD, Anderson, DD, Nepola, JV, Singerman, RJ, Pedersen, DR & Brand, RA 1988, 'Contact stress aberrations following imprecise reduction of simple tibial plateau fractures', *Journal of Orthopaedic Research*, vol. 6, no. 6, pp. 851-862.

Browne, MG & Franz, JR 2019, 'Ankle power biofeedback attenuates the distal-to-proximal redistribution in older adults', *Gait & Posture*, vol. 71, pp. 44-49.

Buchanan, TS 1995, 'Evidence that maximum muscle stress is not a constant: differences in specific tension in elbow flexors and extensors', *Medical Engineering & Physics*, vol. 17, no. 7, pp. 529-536.

Buchanan, TS, Lloyd, DG, Manal, K & Besier, TF 2004, 'Neuromusculoskeletal Modeling: Estimation of Muscle Forces and Joint Moments and Movements From

Measurements of Neural Command', *Journal of applied biomechanics*, vol. 20, no. 4, pp. 367-395.

Buchanan, TS, Lloyd, DG, Manal, K & Besier, TF 2005, 'Estimation of muscle forces and joint moments using a forward-inverse dynamics model', *Medicine & Science in Sports & Exercise*, vol. 37, no. 11, Nov, pp. 1911-1916.

Buchanan, TS & Shreeve, DA 1996, 'An Evaluation of Optimization Techniques for the Prediction of Muscle Activation Patterns During Isometric Tasks', *Journal of Biomechanical Engineering*, vol. 118, no. 4, pp. 565-574.

Callary, SA, Thewlis, D, Rowlands, AV, Findlay, DM & Solomon, LB 2013, 'Collecting a comprehensive evidence base to monitor fracture rehabilitation: A case study', *World Journal of Orthopedics*, vol. 4, no. 4, 10/18, pp. 259-266.

Cappozzo, A, Catani, F, Della Croce, U & Leardini, A 1995, 'Position and orientation in space of bones during movement: anatomical frame definition and determination', *Clinical Biomechanics*, vol. 10, no. 4, pp. 171-178.

Carbone, V, Fluit, R, Pellikaan, P, Van Der Krogt, MM, Janssen, D, Damsgaard, M, Vigneron, L, Feilkas, T, Koopman, HFJM & Verdonschot, N 2015, 'TLEM 2.0 – A comprehensive musculoskeletal geometry dataset for subject-specific modeling of lower extremity', *Journal of Biomechanics*, vol. 48, no. 5, pp. 734-741.

Carrera, I, Gelber, PE, Chary, G, González-Ballester, MA, Monllau, JC & Noailly, J 2016, 'Fixation of a split fracture of the lateral tibial plateau with a locking screw plate instead of cannulated screws would allow early weight bearing: a computational exploration', *International Orthopaedics*, vol. 40, no. 10, 2016/10/01, pp. 2163-2169.

Carter, DR & Hayes, WC 1977, 'The compressive behavior of bone as a two-phase porous structure', *Journal of Bone and Joint Surgery*, vol. 59, no. 7, Oct, pp. 954-962.

Chen, F, Huang, X, Ya, Y, Ma, F, Qian, Z, Shi, J, Guo, S & Yu, B 2018, 'Finite element analysis of intramedullary nailing and double locking plate for treating extra-articular proximal tibial fractures', *Journal of Orthopaedic Surgery and Research*, vol. 13, no. 1, Jan 16, p. 12.

Chen, P, Lu, H, Shen, H, Wang, W, Ni, B & Chen, J 2017, 'Newly designed anterolateral and posterolateral locking anatomic plates for lateral tibial plateau fractures: A finite element study', *Journal of Orthopaedic Surgery and Research*, vol. 12.

Cholewicki, J & McGill, SM 1994, 'EMG assisted optimization: A hybrid approach for estimating muscle forces in an indeterminate biomechanical model', *Journal of Biomechanics*, vol. 27, no. 10, 1994/10/01/, pp. 1287-1289.

Cholewicki, J, McGill, SM & Norman, RW 1995, 'Comparison of muscle forces and joint load from an optimization and EMG assisted lumbar spine model: Towards development of a hybrid approach', *Journal of Biomechanics*, vol. 28, no. 3, pp. 321-331.

Cleek, TM, Reynolds, KJ & Hearn, TC 2007, 'Effect of screw torque level on cortical bone pullout strength', *Journal of Orthopaedic Trauma*, vol. 21, no. 2, pp. 117-123.

Comini, F, Palanca, M, Cristofolini, L & Dall'Ara, E 2019, 'Uncertainties of synchrotron microCT-based digital volume correlation bone strain measurements under simulated deformation', *Journal of Biomechanics*, vol. 86, 03/27, pp. 232-237.

Cook, RD 1977, 'Detection of Influential Observation in Linear Regression', *Technometrics*, vol. 19, no. 1, p. 15.

Court-Brown, CM & Caesar, B 2006, 'Epidemiology of adult fractures: A review', *Injury*, vol. 37, no. 8, pp. 691-697.

Cristofolini, L 2015, 'In vitro evidence of the structural optimization of the human skeletal bones', *Journal of Biomechanics*, vol. 48, no. 5, 2015/03/18/, pp. 787-796.

Cristofolini, L, Schileo, E, Juszczyk, M, Taddei, F, Martelli, S & Viceconti, M 2010, 'Mechanical testing of bones: the positive synergy of finite element models and in vitro experiments', *Philosophical Transactions of the Royal Society A: Mathematical, Physical and Engineering Sciences*, vol. 368, no. 1920, pp. 2725-2763.

Cross, WW, Levy, BA, Morgan, JA, Armitage, BM & Cole, PA 2013, 'Periarticular raft constructs and fracture stability in split-depression tibial plateau fractures', *Injury*, vol. 44, no. 6, 2013/06/01/, pp. 796-801.

Crowninshield, RD & Brand, RA 1981, 'A physiologically based criterion of muscle force prediction in locomotion', *Journal of Biomechanics*, vol. 14, no. 11, pp. 793-801.

Cuéllar, VG, Martinez, D, Immerman, I, Oh, C, Walker, PS & Egol, KA 2015, 'A Biomechanical Study of Posteromedial Tibial Plateau Fracture Stability: Do They All Require Fixation?', *Journal of Orthopaedic Trauma*, vol. 29, no. 7, pp. 325-330.

Dabke, HV, Gupta, SK, Holt, CA, O'Callaghan, P & Dent, CM 2004, 'How Accurate Is Partial Weightbearing?', *Clinical Orthopaedics and Related Research*, vol. 421, pp. 282-286.

Dall'Ara, E, Pahr, D, Varga, P, Kainberger, F & Zysset, P 2012, 'QCT-based finite element models predict human vertebral strength in vitro significantly better than simulated DEXA', *Osteoporosis International*, vol. 23, no. 2, pp. 563-572.

Dall'Ara, E, Peña-Fernández, M, Palanca, M, Giorgi, M, Cristofolini, L & Tozzi, G 2017, 'Precision of Digital Volume Correlation Approaches for Strain Analysis in Bone Imaged with Micro-Computed Tomography at Different Dimensional Levels', *Frontiers in Materials*, vol. 4, no. 31, 2017-November-08.

Damm, NB, Morlock, MM & Bishop, NE 2015, 'Friction coefficient and effective interference at the implant-bone interface', *Journal of Biomechanics*, vol. 48, no. 12, 2015/09/18/, pp. 3517-3521.

Damsgaard, M, Rasmussen, J, Christensen, ST, Surma, E & De Zee, M 2006, 'Analysis of musculoskeletal systems in the AnyBody Modeling System', *Simulation Modelling Practice and Theory*, vol. 14, no. 8, pp. 1100-1111.

Davico, G, Pizzolato, C, Lloyd, DG, Obst, SJ, Walsh, HPJ & Carty, CP 2020, 'Increasing level of neuromusculoskeletal model personalisation to investigate joint contact forces in cerebral palsy: A twin case study', *Clinical Biomechanics*, vol. 72, 2020/02/01/, pp. 141-149.

Davis, RB, Õunpuu, S, Tyburski, D & Gage, JR 1991, 'A gait analysis data collection and reduction technique', *Human Movement Science*, vol. 10, no. 5, 1991/10/01/, pp. 575-587.

De Groote, F & Falisse, A 2021, 'Perspective on musculoskeletal modelling and predictive simulations of human movement to assess the neuromechanics of gait', *Proceedings of the Royal Society B: Biological Sciences*, vol. 288, no. 1946, p. 20202432.

de Leva, P 1996, 'Adjustments to Zatsiorsky-Seluyanov's segment inertia parameters', *Journal of Biomechanics*, vol. 29, no. 9, 1996/09/01/, pp. 1223-1230.

Deleanu, B, Prejbeanu, R, Crisan, D, Predescu, V, Popa, I & Poenaru, DV 2015, 'Gait characteristics before hardware removal in patients operated upon for tibial plateau fractures', *International Orthopaedics*, vol. 39, no. 7, Jul, pp. 1411-1415.

Delp, SL, Anderson, FC, Arnold, AS, Loan, P, Habib, A, John, CT, Guendelman, E & Thelen, DG 2007, 'OpenSim: Open-Source Software to Create and Analyze Dynamic Simulations of Movement', *IEEE Transactions on Biomedical Engineering*, vol. 54, no. 11, pp. 1940-1950.

Dembia, CL, Bianco, NA, Falisse, A, Hicks, JL & Delp, SL 2020, 'OpenSim Moco: Musculoskeletal optimal control', *PLOS Computational Biology*, vol. 16, no. 12, p. e1008493.

Doht, S, Lehnert, T, Frey, S, Fehske, K, Jansen, H, Blunk, T & Meffert, RH 2012, 'Effective combination of bone substitute and screws in the jail technique: a

biomechanical study of tibial depression fractures', *International Orthopaedics*, vol. 36, no. 10, 2012/10/01, pp. 2121-2125.

Egol, KA, Su, E, Tejwani, NC, Sims, SH, Kummer, FJ & Koval, KJ 2004, 'Treatment of Complex Tibial Plateau Fractures Using the Less Invasive Stabilization System Plate: Clinical Experience and a Laboratory Comparison with Double Plating', *Journal of Trauma and Acute Care Surgery*, vol. 57, no. 2, pp. 340-346.

Elsoe, R, Larsen, P, Shekhrajka, N, Ferreira, L, Ostgaard, SE & Rasmussen, S 2015, 'The outcome after lateral tibial plateau fracture treated with percutaneus screw fixation show a tendency towards worse functional outcome compared with a reference population', *European Journal of Trauma and Emergency Surgery*, vol. 42, p. 177–184.

Esrafilian, A, Stenroth, L, Mononen, ME, Tanska, P, Rossom, SV, Lloyd, DG, Jonkers, I & Korhonen, RK 2021, '12 Degrees of Freedom Muscle Force Driven Fibril-Reinforced Poroviscoelastic Finite Element Model of the Knee Joint', *IEEE Transactions on Neural Systems and Rehabilitation Engineering*, vol. 29, pp. 123-133.

Fändriks, A, Tranberg, R, Karlsson, J, Möller, M & Zügner, R 2021, 'Gait biomechanics in patients with intra-articular tibial plateau fractures – gait analysis at three months compared with age- and gender-matched healthy subjects', *BMC Musculoskeletal Disorders*, vol. 22, no. 1.

Fang, J, Gong, H, Kong, L & Zhu, D 2013, 'Simulation on the internal structure of three-dimensional proximal tibia under different mechanical environments', *BioMedical Engineering OnLine*, vol. 12, no. 1, 2013/12/20, p. 130.

Francis, P, Ledingham, J, Clarke, S, Collins, DJ & Jakeman, P 2016, 'A Comparison of Stride Length and Lower Extremity Kinematics during Barefoot and Shod Running in Well Trained Distance Runners', *Journal of sports science & medicine*, vol. 15, no. 3, pp. 417-423.

Fregly, BJ, Besier, TF, Lloyd, DG, Delp, SL, Banks, SA, Pandy, MG & D'Lima, DD 2012, 'Grand challenge competition to predict in vivo knee loads', *Journal of Orthopaedic Research*, vol. 30, no. 4, Apr, pp. 503-513.

Frost, HM 1987, 'Bone "mass" and the "mechanostat": a proposal', *The Anatomical Record*, vol. 219, no. 1, pp. 1-9.

Frost, HM 1998, 'Perspectives: A proposed general model of the “mechanostat” (suggestions from a new skeletal-biologic paradigm)', *The Anatomical Record*, vol. 244, no. 2, pp. 139-147.

Gans, C 1982, 'FIBER ARCHITECTURE AND MUSCLE FUNCTION', *Exercise and Sport Sciences Reviews*, vol. 10, no. 1.

Gaston, P, Will, EM & Keating, JF 2005, 'Recovery of knee function following fracture of the tibial plateau', *The Journal of Bone and Joint Surgery. British volume*, vol. 87-B, no. 9, 2005/09/01, pp. 1233-1236.

Gerus, P, Sartori, M, Besier, TF, Fregly, BJ, Delp, SL, Banks, SA, Pandy, MG, D'Lima, DD & Lloyd, DG 2013, 'Subject-specific knee joint geometry improves predictions of medial tibiofemoral contact forces', *Journal of Biomechanics*, vol. 46, no. 16, 2013/11/15/, pp. 2778-2786.

Gillard, F, Boardman, R, Mavrogordato, M, Hollis, D, Sinclair, I, Pierron, F & Browne, M 2014, 'The application of digital volume correlation (DVC) to study the microstructural behaviour of trabecular bone during compression', *Journal of the Mechanical Behavior of Biomedical Materials*, vol. 29, pp. 480-499.

Goldstein, SA 1987, 'The mechanical properties of trabecular bone: Dependence on anatomic location and function', *Journal of Biomechanics*, vol. 20, no. 11, 1987/01/01/, pp. 1055-1061.

Goldstein, SA, Wilson, DL, Sonstegard, DA & Matthews, LS 1983, 'The mechanical properties of human tibial trabecular bone as a function of metaphyseal location', *Journal of Biomechanics*, vol. 16, no. 12, pp. 965-969.

Gösling, T, Schandelmaier, P, Marti, A, Hufner, T, Partenheimer, A & Krettek, C 2004, 'Less Invasive Stabilization of Complex Tibial Plateau Fractures: A Biomechanical Evaluation of a Unilateral Locked Screw Plate and Double Plating', *Journal of Orthopaedic Trauma*, vol. 18, no. 8, pp. 546-551.

Goulet, RW, Goldstein, SA, Ciarelli, MJ, Kuhn, JL, Brown, MB & Feldkamp, LA 1994, 'The relationship between the structural and orthogonal compressive properties of trabecular bone', *Journal of Biomechanics*, vol. 27, no. 4, Apr, pp. 375-389.

Grace, TM, O'Rourke, D, Robertson, T, Perilli, E, Callary, S, Taylor, M, Atkins, GJ, Solomon, LB & Thewlis, D 2021, 'A semiautomated method to quantitatively assess osteolytic lesion volume and bone mineral density within acetabular regions of interest from CT', *Journal of Orthopaedic Research*.

Grassi, L & Isaksson, H 2015, 'Extracting accurate strain measurements in bone mechanics: A critical review of current methods', *Journal of the Mechanical Behavior of Biomedical Materials*, vol. 50, pp. 43-54.

Gray, HA, Taddei, F, Zavatsky, AB, Cristofolini, L & Gill, HS 2008, 'Experimental Validation of a Finite Element Model of a Human Cadaveric Tibia', *Journal of Biomechanical Engineering*, vol. 130, no. 3, pp. 031016-031019.

Grood, E & Suntay, WJ 1983, 'A Joint Coordinate System for the Clinical Description of Three-Dimensional Motions: Application to the Knee', *Journal of Biomechanical Engineering*, vol. 105.

Guo, XE 2001, 'Mechanical properties of cortical bone and cancellous bone tissue.' In Bone Mechanics Handbook.

HajiRassouliha, A, Taberner, AJ, Nash, MP & Nielsen, PMF 2018, 'Subpixel phase-based image registration using Savitzky–Golay differentiators in gradient-correlation', *Computer Vision and Image Understanding*, vol. 170, 2018/05/01/, pp. 28-39.

Handsfield, GG, Meyer, CH, Hart, JM, Abel, MF & Blemker, SS 2014, 'Relationships of 35 lower limb muscles to height and body mass quantified using MRI', *Journal of Biomechanics*, vol. 47, no. 3, pp. 631-638.

Hansen, U, Zioupos, P, Simpson, R, Currey, JD & Hynd, D 2008, 'The Effect of Strain Rate on the Mechanical Properties of Human Cortical Bone', *Journal of Biomechanical Engineering*, vol. 130, no. 1, p. 011011.

Harrigan, TP, Jasty, M, Mann, RW & Harris, WH 1988, 'Limitations of the continuum assumption in cancellous bone', *Journal of Biomechanics*, vol. 21, no. 4, pp. 269-275.

Hart, JM, Pietrosimone, B, Hertel, J & Ingersoll, CD 2010, 'Quadriceps Activation Following Knee Injuries: A Systematic Review', *Journal of Athletic Training*, vol. 45, no. 1, pp. 87-97.

Hast, MW & Piazza, SJ 2013, 'Dual-Joint Modeling for Estimation of Total Knee Replacement Contact Forces During Locomotion', *Journal of Biomechanical Engineering*, vol. 135, no. 2, p. 021013.

Helgason, B, Perilli, E, Schileo, E, Taddei, F, Brynjólfsson, S & Viceconti, M 2008, 'Mathematical relationships between bone density and mechanical properties: A literature review', *Clinical Biomechanics*, vol. 23, no. 2, pp. 135-146.

Hill, A 1938, 'The Heat of Shortening and the Dynamic Constants of Muscle', *The Royal Society*, vol. 126, no. 843, p. 136-195.

Hoang, HX, Diamond, LE, Lloyd, DG & Pizzolato, C 2019, 'A calibrated EMG-informed neuromusculoskeletal model can appropriately account for muscle co-

contraction in the estimation of hip joint contact forces in people with hip osteoarthritis', *Journal of Biomechanics*, vol. 83, pp. 134-142.

Hoffmann, MF, Sietsema, DL & Jones, CB 2016, 'Lost to follow-up: reasons and outcomes following tibial plateau fractures', *European Journal of Orthopaedic Surgery & Traumatology*, vol. 26, no. 8, pp. 937-942.

Högel, F, Hoffmann, S, Panzer, S, Wimber, J, Bühren, V & Augat, P 2013, 'Biomechanical comparison of intramedullar versus extramedullar stabilization of intra-articular tibial plateau fractures', *Archives of Orthopaedic and Trauma Surgery*, vol. 133, no. 1, 2013/01/01, pp. 59-64.

Holder, J, Trinler, U, Meurer, A & Stief, F 2020, 'A Systematic Review of the Associations Between Inverse Dynamics and Musculoskeletal Modeling to Investigate Joint Loading in a Clinical Environment', *Frontiers in Bioengineering and Biotechnology*, vol. 8.

Honkonen, SE 1994, 'Indications for Surgical Treatment of Tibial Condyle Fractures', *Clinical Orthopaedics and Related Research®*, vol. 302.

Honkonen, SE 1995, 'Degenerative arthritis after tibial plateau fractures', *J Orthop Trauma*, vol. 9, no. 4, pp. 273-277.

Hopkins, JT, Ingersoll, CD, Edwards, JE & Cordova, ML 2000, 'Changes in soleus motoneuron pool excitability after artificial knee joint effusion', *Archives of Physical Medicine and Rehabilitation*, vol. 81, no. 9, 2000/09/01/, pp. 1199-1203.

Hoy, MG, Zajac, FE & Gordon, ME 1990, 'A musculoskeletal model of the human lower extremity: The effect of muscle, tendon, and moment arm on the moment-angle relationship of musculotendon actuators at the hip, knee, and ankle', *Journal of Biomechanics*, vol. 23, no. 2, 1990/01/01/, pp. 157-169.

Huiskes, R & Chao, EYS 1983, 'A survey of finite element analysis in orthopedic biomechanics: The first decade', *Journal of Biomechanics*, vol. 16, no. 6, 1983/01/01/, pp. 385-409.

Imani Nejad, Z, Khalili, K, Hosseini Nasab, SH, Schütz, P, Damm, P, Trepczynski, A, Taylor, WR & Smith, CR 2020, 'The Capacity of Generic Musculoskeletal Simulations to Predict Knee Joint Loading Using the CAMS-Knee Datasets', *Annals of Biomedical Engineering*, vol. 48, no. 4, pp. 1430-1440.

Joshua, CR, Krishna, CV, Joshua, LG & Derek, JD 2016, 'Tibial Plateau Fractures in Elderly Patients', *Geriatric Orthopaedic Surgery & Rehabilitation*, vol. 7, no. 3, pp. 126-134.

Karunakar, MA, Egol, KA, Peindl, R, Harrow, ME, Bosse, MJ & Kellam, JF 2002, 'Split Depression Tibial Plateau Fractures: A Biomechanical Study', *Journal of Orthopaedic Trauma*, vol. 16, no. 3, pp. 172-177.

Kersh, ME, Martelli, S, Zebaze, R, Seeman, E & Pandy, MG 2018, 'Mechanical Loading of the Femoral Neck in Human Locomotion', *Journal of Bone and Mineral Research*, vol. 33, no. 11, pp. 1999-2006.

Keyak, JH, Lee, IY & Skinner, HB 1994, 'Correlations between orthogonal mechanical properties and density of trabecular bone: Use of different densitometric measures', *Journal of Biomedical Materials Research*, vol. 28, no. 11, pp. 1329-1336.

Kian, A, Pizzolato, C, Halaki, M, Ginn, K, Lloyd, D, Reed, D & Ackland, D 2019, 'Static optimization underestimates antagonist muscle activity at the glenohumeral joint: A musculoskeletal modeling study', *Journal of Biomechanics*, vol. 97, 2019/12/03/, p. 109348.

Kian, A, Pizzolato, C, Halaki, M, Ginn, K, Lloyd, D, Reed, D & Ackland, D 2021, 'The effectiveness of emg-driven neuromusculoskeletal model calibration is task dependent', *Journal of Biomechanics*, 2021/08/25/, p. 110698.

Killen, BA, Brito Da Luz, S, Lloyd, DG, Carleton, AD, Zhang, J, Besier, TF & Saxby, DJ 2020, 'Automated creation and tuning of personalised muscle paths for OpenSim musculoskeletal models of the knee joint', *Biomechanics and Modeling in Mechanobiology*.

Killen, BA, Falisse, A, De Groote, F & Jonkers, I 2020, 'In Silico-Enhanced Treatment and Rehabilitation Planning for Patients with Musculoskeletal Disorders: Can Musculoskeletal Modelling and Dynamic Simulations Really Impact Current Clinical Practice?', *Applied Sciences*, vol. 10, no. 20.

Kinney, AL, Besier, TF, D'Lima, DD & Fregly, BJ 2013, 'Update on grand challenge competition to predict in vivo knee loads', *Journal of Biomechanics Eng*, vol. 135, no. 2, Feb, p. 021012.

Knarr, BA & Higginson, JS 2015, 'Practical approach to subject-specific estimation of knee joint contact force', *Journal of Biomechanics*, vol. 48, no. 11, 2015/08/20/, pp. 2897-2902.

Koike, S, Nakaya, S, Mori, H, Ishikawa, T & Willmott, AP 2017, 'Modelling error distribution in the ground reaction force during an induced-acceleration analysis of running in rear-foot strikers', *Journal of Sports Sciences*, pp. 1-12.

Körding, KP & Wolpert, DM 2006, 'Bayesian decision theory in sensorimotor control', *Trends in Cognitive Sciences*, vol. 10, no. 7, 2006/07/01/, pp. 319-326.

Koval, KJ, Polatsch, D, Kummer, FJ, Cheng, D & Zuckerman, JD 1996, 'Split Fractures of the Lateral Tibial Plateau: Evaluation of Three Fixation Methods', *Journal of Orthopaedic Trauma*, vol. 10, no. 5, pp. 304-308.

Kutzner, I, Heinlein, B, Graichen, F, Bender, A, Rohlmann, A, Halder, A, Beier, A & Bergmann, G 2010, 'Loading of the knee joint during activities of daily living measured in vivo in five subjects', *Journal of Biomechanics*, vol. 43, no. 11, Aug 10, pp. 2164-2173.

Liu, L & Morgan, EF 2007, 'Accuracy and precision of digital volume correlation in quantifying displacements and strains in trabecular bone', *Journal of Biomechanics*, vol. 40, no. 15, pp. 3516-3520.

Lloyd, DG & Besier, TF 2003, 'An EMG-driven musculoskeletal model to estimate muscle forces and knee joint moments in vivo', *Journal of Biomechanics*, vol. 36, no. 6, 2003/06/01/, pp. 765-776.

Lloyd, DG & Buchanan, TS 1996, 'A model of load sharing between muscles and soft tissues at the human knee during static tasks', *Journal of Biomechanics Eng*, vol. 118, no. 3, Aug, pp. 367-376.

Loeb, GE 2012, 'Optimal isn't good enough', *Biological Cybernetics*, vol. 106, no. 11-12, pp. 757-765.

MacLeod, AR, Pankaj, P & Simpson, AHRW 2012, 'Does screw–bone interface modelling matter in finite element analyses?', *Journal of Biomechanics*, vol. 45, no. 9, 2012/06/01/, pp. 1712-1716.

Manal, K & Buchanan, TS 2013, 'An Electromyogram-Driven Musculoskeletal Model of the Knee to Predict in Vivo Joint Contact Forces During Normal and Novel Gait Patterns', *Journal of Biomechanical Engineering*, vol. 135, no. 2, p. 021014.

Mantoan, A, Pizzolato, C, Sartori, M, Sawacha, Z, Cobelli, C & Reggiani, M 2015, 'MOtoNMS: A MATLAB toolbox to process motion data for neuromusculoskeletal modeling and simulation', *Source Code for Biology and Medicine*, vol. 10, no. 1, November 16, p. 12.

Martelli, S, Calvetti, D, Somersalo, E & Viceconti, M 2015, 'Stochastic modelling of muscle recruitment during activity', *Interface Focus*, vol. 5, no. 2, pp. 20140094-20140094.

Martelli, S, Calvetti, D, Somersalo, E, Viceconti, M & Taddei, F 2013, 'Computational tools for calculating alternative muscle force patterns during motion: A comparison of possible solutions', *Journal of Biomechanics*, vol. 46, no. 12, pp. 2097-2100.

Martelli, S & Costi, JJ 2021, 'Real-time replication of three-dimensional and time-varying physiological loading cycles for bone and implant testing: A novel protocol demonstrated for the proximal human femur while walking', *Journal of the Mechanical Behavior of Biomedical Materials*, vol. 124, 2021/12/01/, p. 104817.

Martelli, S, Giorgi, M, Dall' Ara, E & Perilli, E 2021, 'Damage tolerance and toughness of elderly human femora', *Acta Biomaterialia*, vol. 123, 2021/03/15/, pp. 167-177.

Martelli, S & Perilli, E 2018, 'Time-elapsed synchrotron-light microstructural imaging of femoral neck fracture', *Journal of the Mechanical Behavior of Biomedical Materials*, vol. 84, pp. 265-272.

Martelli, S, Sancisi, N, Conconi, M, Pandy, MG, Kersh, ME, Parenti-Castelli, V & Reynolds, KJ 2020, 'The relationship between tibiofemoral geometry and musculoskeletal function during normal activity', *Gait & Posture*, vol. 80, 2020/07/01/, pp. 374-382.

Martelli, S, Taddei, F, Cappello, A, Van Sint Jan, S, Leardini, A & Viceconti, M 2011, 'Effect of sub-optimal neuromotor control on the hip joint load during level walking', *Journal of Biomechanics*, vol. 44, no. 9, pp. 1716-1721.

McGrath, RL, Ziegler, ML, Pires-Fernandes, M, Knarr, BA, Higginson, JS & Sergi, F 2019, 'The effect of stride length on lower extremity joint kinetics at various gait speeds', *PLOS ONE*, vol. 14, no. 2, p. e0200862.

Millar, SC, Fraysse, F, Arnold, JB, Thewlis, D & Solomon, LB 2021, '3D modelling of tibial plateau fractures: Variability in fracture location and characteristics across Schatzker fracture types', *Injury*, vol. 52, no. 8, 2021/08/01/, pp. 2415-2424.

Millard, M, Uchida, T, Seth, A & Delp, SL 2013, 'Flexing Computational Muscle: Modeling and Simulation of Musculotendon Dynamics', *Journal of Biomechanical Engineering*, vol. 135, no. 2, p. 021005.

Modenese, L, Ceseracciu, E, Reggiani, M & Lloyd, DG 2016, 'Estimation of musculotendon parameters for scaled and subject specific musculoskeletal models using an optimization technique', *Journal of Biomechanics*, vol. 49, no. 2, 2016/01/25/, pp. 141-148.

Moissenet, F, Modenese, L & Dumas, R 2017, 'Alterations of musculoskeletal models for a more accurate estimation of lower limb joint contact forces during normal gait: A systematic review', *Journal of Biomechanics*, vol. 63, pp. 8-20.

Morgan, EF, Bayraktar, HH & Keaveny, TM 2003, 'Trabecular bone modulus–density relationships depend on anatomic site', *Journal of Biomechanics*, vol. 36, no. 7, pp. 897-904.

Morrison, JB 1970, 'The mechanics of the knee joint in relation to normal walking', *Journal of Biomechanics*, vol. 3, no. 1, Jan, pp. 51-61.

Myers, CA, Laz, PJ, Shelburne, KB & Davidson, BS 2015, 'A Probabilistic Approach to Quantify the Impact of Uncertainty Propagation in Musculoskeletal Simulations', *Annals of Biomedical Engineering*, vol. 43, no. 5, pp. 1098-1111.

Navacchia, A, Myers, CA, Rullkoetter, PJ & Shelburne, KB 2016, 'Prediction of In Vivo Knee Joint Loads Using a Global Probabilistic Analysis', *Journal of Biomechanical Engineering*, vol. 138, no. 3, p. 031002.

Neptune, RR & McGowan, CP 2011, 'Muscle contributions to whole-body sagittal plane angular momentum during walking', *Journal of Biomechanics*, vol. 44, no. 1, 2011/01/04/, pp. 6-12.

Nikon Metrology, I 2020, *XT H 225 for all-purpose X-ray and CT inspection*, viewed December 2020, <https://www.nikonmetrology.com/en-us/product/xt-h-225>.

Pahr, DH & Zysset, PK 2009, 'From high-resolution CT data to finite element models: development of an integrated modular framework', *Computer Methods in Biomechanics and Biomedical Engineering*, vol. 12, no. 1, pp. 45-57.

Palanca, M, Bodey, AJ, Giorgi, M, Viceconti, M, Lacroix, D, Cristofolini, L & Dall'Ara, E 2017, 'Local displacement and strain uncertainties in different bone types by digital volume correlation of synchrotron microtomograms', *Journal of Biomechanics*, vol. 58, pp. 27-36.

Palanca, M, Cristofolini, L, Dall'Ara, E, Curto, M, Innocente, F, Danesi, V & Tozzi, G 2016, 'Digital volume correlation can be used to estimate local strains in natural and augmented vertebrae: An organ-level study', *Journal of Biomechanics*, vol. 49, no. 16, 2016/12/08/, pp. 3882-3890.

Palanca, M, Tozzi, G & Cristofolini, L 2015, 'The use of digital image correlation in the biomechanical area: a review', *International Biomechanics*, vol. 3, no. 1, pp. 1-21.

Palanca, M, Tozzi, G, Cristofolini, L, Viceconti, M & Dall'Ara, E 2015, 'Three-Dimensional Local Measurements of Bone Strain and Displacement: Comparison of Three Digital Volume Correlation Approaches', *Journal of Biomechanical Engineering*, vol. 137, no. 7, p. 071006.

Pappalardo, F, Russo, G, Tshinanu, FM & Viceconti, M 2019, 'In silico clinical trials: concepts and early adoptions', *Briefings in Bioinformatics*, vol. 20, no. 5, pp. 1699-1708.

Park, H & Durand, DM 2008, 'Motion control of musculoskeletal systems with redundancy', *Biological Cybernetics*, vol. 99, no. 6, pp. 503-516.

Parker, PJ, Tepper, KB, Brumback, RJ, Novak, VP & Belkoff, SM 1999, 'Biomechanical comparison of fixation of type-I fractures of the lateral tibial plateau', *The Journal of Bone and Joint Surgery. British volume*, vol. 81-B, no. 3, 1999/05/01, pp. 478-480.

Parkkinen, M, Madanat, R, Mustonen, A, Koskinen, SK, Paavola, M & Lindahl, J 2014, 'Factors predicting the development of early osteoarthritis following lateral tibial plateau fractures: mid-term clinical and radiographic outcomes of 73 operatively treated patients', *Scandinavian Journal of Surgery*, vol. 103, no. 4, pp. 256-262.

Pataky, T, Vanrenterghem, J & Robinson, M 2015, 'Zero- vs. one-dimensional, parametric vs. non-parametric, and confidence interval vs. hypothesis testing procedures in one-dimensional biomechanical trajectory analysis', *Journal of Biomechanics*, vol. 48, 03/13.

Pataky, TC 2012, 'One-dimensional statistical parametric mapping in Python', *Computer Methods in Biomechanics and Biomedical Engineering*, vol. 15, no. 3, pp. 295-301.

Pataky, TC, Vanrenterghem, J & Robinson, MA 2015, 'Zero- vs. one-dimensional, parametric vs. non-parametric, and confidence interval vs. hypothesis testing procedures in one-dimensional biomechanical trajectory analysis', *Journal of Biomechanics*, vol. 48, no. 7, 2015/05/01/, pp. 1277-1285.

Patriarco, AG, Mann, RW, Simon, SR & Mansour, JM 1981, 'An evaluation of the approaches of optimization models in the prediction of muscle forces during human gait', *Journal of Biomechanics*, vol. 14, no. 8, 1981/01/01/, pp. 513-525.

Perry, CC 1986, 'Strain-gage reinforcement effects on orthotropic materials', *Experimental Techniques*, vol. 10, no. 2, pp. 20-24.

Piazza, SJ & Cavanagh, PR 2000, 'Measurement of the screw-home motion of the knee is sensitive to errors in axis alignment', *Journal of Biomechanics*, vol. 33, no. 8, pp. 1029-1034.

Piekarski, K 1970, 'Fracture of Bone', *Journal of Applied Physics*, vol. 41, no. 1, pp. 215-223.

Pietrosimone, BG, McLeod, MM & Lepley, AS 2012, 'A Theoretical Framework for Understanding Neuromuscular Response to Lower Extremity Joint Injury', *Sports Health: A Multidisciplinary Approach*, vol. 4, no. 1, pp. 31-35.

Pizzolato, C, Lloyd, DG, Sartori, M, Ceseracciu, E, Besier, TF, Fregly, BJ & Reggiani, M 2015, 'CEINMS: A toolbox to investigate the influence of different neural control solutions on the prediction of muscle excitation and joint moments during dynamic motor tasks', *Journal of Biomechanics*, vol. 48, no. 14, pp. 3929-3936.

Pope, MH & Outwater, JO 1974, 'Mechanical properties of bone as a function of position and orientation', *Journal of Biomechanics*, vol. 7, no. 1, 1974/01/01/, pp. 61-66.

Prat-Fabregat, S & Camacho-Carrasco, P 2016, 'Treatment strategy for tibial plateau fractures: an update', *EFORT Open Reviews*, vol. 1, no. 5, pp. 225-232.

Rajagopal, A, Dembia, CL, Demers, MS, Delp, DD, Hicks, JL & Delp, SL 2016, 'Full-Body Musculoskeletal Model for Muscle-Driven Simulation of Human Gait', *IEEE Transactions on Biomedical Engineering*, vol. 63, no. 10, pp. 2068-2079.

Rancourt, D, Shirazi-Adl, A, Drouin, G & Paiement, G 1990, 'Friction properties of the interface between porous-surfaced metals and tibial cancellous bone', *Journal of Biomedical Materials Research*, vol. 24, no. 11, pp. 1503-1519.

Rapagna, S, Berahmani, S, Wyers, CE, Van Den Bergh, JPW, Reynolds, KJ, Tozzi, G, Janssen, D & Perilli, E 2019, 'Quantification of human bone microarchitecture damage in press-fit femoral knee implantation using HR-pQCT and digital volume correlation', *Journal of the Mechanical Behavior of Biomedical Materials*, vol. 97, pp. 278-287.

Ratcliff, JR, Werner, FW, Green, JK & Harley, BJ 2007, 'Medial Buttress Versus Lateral Locked Plating in a Cadaver Medial Tibial Plateau Fracture Model', *Journal of Orthopaedic Trauma*, vol. 21, no. 7, pp. 444-448.

Rho, JY 1996, 'An ultrasonic method for measuring the elastic properties of human tibial cortical and cancellous bone', *Ultrasonics*, vol. 34, no. 8, pp. 777-783.

Roberts, BC, Perilli, E & Reynolds, KJ 2014, 'Application of the digital volume correlation technique for the measurement of displacement and strain fields in bone: a literature review', *Journal of Biomechanics*, vol. 47, no. 5, 03/21, pp. 923-934.

Roberts, BC, Solomon, LB, Mercer, G, Reynolds, KJ, Thewlis, D & Perilli, E 2017, 'Joint loading and proximal tibia subchondral trabecular bone microarchitecture differ with walking gait patterns in end-stage knee osteoarthritis', *Osteoarthritis and Cartilage*, vol. 25, no. 10, pp. 1623-1632.

Roberts, BC, Solomon, LB, Mercer, G, Reynolds, KJ, Thewlis, D & Perilli, E 2018, 'Relationships between in vivo dynamic knee joint loading, static alignment and tibial subchondral bone microarchitecture in end-stage knee osteoarthritis', *Osteoarthritis and Cartilage*, vol. 26, no. 4, pp. 547-556.

Roberts, BC, Thewlis, D, Solomon, LB, Mercer, G, Reynolds, KJ & Perilli, E 2017, 'Systematic mapping of the subchondral bone 3D microarchitecture in the human tibial plateau: Variations with joint alignment', *Journal of Orthopaedic Research*, vol. 35, no. 9, pp. 1927-1941.

Roberts, VL 1966, 'Strain-gage techniques in biomechanics', *Experimental Mechanics*, vol. 6, no. 3, pp. 19A-22A.

Roos, EM & Toksvig-Larsen, S 2003, 'Knee injury and Osteoarthritis Outcome Score (KOOS) – validation and comparison to the WOMAC in total knee replacement', *Health and Quality of Life Outcomes*, vol. 1, no. 1, 2003/05/25, p. 17.

Ryken, TC, Clausen, JD, Traynelis, VC & Goel, VK 1995, 'Biomechanical analysis of bone mineral density, insertion technique, screw torque, and holding strength of anterior cervical plate screws', *Journal of Neurosurgery*, vol. 83, no. 2, pp. 324-329.

Sandberg, OH & Aspenberg, P 2016, 'Inter-trabecular bone formation: a specific mechanism for healing of cancellous bone: A narrative review', *Acta Orthopaedica*, vol. 87, no. 5, pp. 459-465.

Sartori, M, Farina, D & Lloyd, DG 2014, 'Hybrid neuromusculoskeletal modeling to best track joint moments using a balance between muscle excitations derived from electromyograms and optimization', *Journal of Biomechanics*, vol. 47, no. 15, 2014/11/28/, pp. 3613-3621.

Sartori, M, Reggiani, M, Farina, D & Lloyd, DG 2012, 'EMG-Driven Forward-Dynamic Estimation of Muscle Force and Joint Moment about Multiple Degrees of Freedom in the Human Lower Extremity', *PLOS ONE*, vol. 7, no. 12, p. e52618.

Saxby, DJ, Killen, BA, Pizzolato, C, Carty, CP, Diamond, LE, Modenese, L, Fernandez, J, Davico, G, Barzan, M, Lenton, G, Da Luz, SB, Suwarganda, E, Devaprakash, D, Korhonen, RK, Alderson, JA, Besier, TF, Barrett, RS & Lloyd, DG 2020, 'Machine learning methods to support personalized neuromusculoskeletal modelling', *Biomechanics and Modeling in Mechanobiology*, vol. 19, no. 4, pp. 1169-1185.

Schatzker, J, McBroom, R & Bruce, D 1979, 'The Tibial Plateau Fracture: The Toronto Experience 1968-1975', *Clinical Orthopaedics & Related Research January/February*, vol. 138, pp. 94-104.

Schileo, E, Dall'Ara, E, Taddei, F, Malandrino, A, Schotkamp, T, Baleani, M & Viceconti, M 2008, 'An accurate estimation of bone density improves the accuracy of subject-specific finite element models', *Journal of Biomechanics*, vol. 41, no. 11, 2008/08/07/, pp. 2483-2491.

Scholz, JP & Schöner, G 1999, 'The uncontrolled manifold concept: identifying control variables for a functional task', *Experimental Brain Research*, vol. 126, no. 3, pp. 289-306.

Scott, CEH, Davidson, E, MacDonald, DJ, White, TO & Keating, JF 2015, 'Total knee arthroplasty following tibial plateau fracture', *Bone Joint Journal*, vol. 97-B, no. 4, 2015/04/01, pp. 532-538.

Serrancolí, G, Kinney, AL & Fregly, BJ 2020, 'Influence of musculoskeletal model parameter values on prediction of accurate knee contact forces during walking', *Medical Engineering & Physics*, vol. 85, 2020/11/01/, pp. 35-47.

Shelburne, KB, Torry, MR & Pandy, MG 2006, 'Contributions of muscles, ligaments, and the ground-reaction force to tibiofemoral joint loading during normal gait', *Journal of Orthopaedic Research*, vol. 24, no. 10, Oct, pp. 1983-1990.

Shockey, JS, von Fraunhofer, JA & Seligson, D 1985, 'A measurement of the coefficient of static friction of human long bones', *Surface Technology*, vol. 25, no. 2, 1985/06/01/, pp. 167-173.

Snyder, SM & Schneider, E 1991, 'Estimation of mechanical properties of cortical bone by computed tomography', *Journal of Orthopaedic Research*, vol. 9, no. 3, 1991/05/01, pp. 422-431.

Softness, KA, Murray, RS & Evans, BG 2017, 'Total knee arthroplasty and fractures of the tibial plateau', *World Journal of Orthopedics*, vol. 8, no. 2, pp. 107-114.

Solomon, L, Callary, S, Stevenson, A, McGee, M, Chehade, M & Howie, D 2011, 'Weight-bearing-induced displacement and migration over time of fracture fragments following split depression fractures of the lateral tibial plateau: A case series with radiostereometric analysis', *Journal of Bone and Joint Surgery - Series B*, vol. 93 B, no. 6, pp. 817-823.

Solomon, L, Stevenson, A, Callary, S, Sullivan, T, Howie, D & Chehade, M 2010, 'The accuracy and precision of radiostereometric analysis in monitoring tibial plateau fractures', *Acta Orthopaedica*, vol. 81, no. 4, pp. 487-494.

Stevens-Lapsley, JE, Schenkman, ML & Dayton, MR 2011, 'Comparison of Self-Reported Knee Injury and Osteoarthritis Outcome Score to Performance Measures in Patients After Total Knee Arthroplasty', *PM&R*, vol. 3, no. 6, pp. 541-549.

Stief, F 2018, 'Variations of Marker Sets and Models for Standard Gait Analysis', In Handbook of Human Motion, pp. 509-526.

Taddei, F, Cristofolini, L, Martelli, S, Gill, H & Viceconti, M 2006, 'Subject-specific finite element models of long bones: An in vitro evaluation of the overall accuracy', *Journal of Biomechanics*, vol. 39, no. 13, pp. 2457-2467.

Taddei, F, Martelli, S, Reggiani, B, Cristofolini, L & Viceconti, M 2006, 'Finite-Element Modeling of Bones From CT Data: Sensitivity to Geometry and Material Uncertainties', *IEEE Transactions on Biomedical Engineering*, vol. 53, no. 11, pp. 2194-2200.

Tassani, S & Perilli, E 2013, 'On local micro-architecture analysis of trabecular bone in three dimensions', *International Orthopaedics*, vol. 37, no. 8, pp. 1645-1646.

Taylor, M & Prendergast, PJ 2015, 'Four decades of finite element analysis of orthopaedic devices: Where are we now and what are the opportunities?', *Journal of Biomechanics*, vol. 48, no. 5, 2015/03/18/, pp. 767-778.

Taylor, WR, Heller, MO, Bergmann, G & Duda, GN 2004, 'Tibio-femoral loading during human gait and stair climbing', *Journal of Orthopaedic Research*, vol. 22, no. 3, 2004/05/01/, pp. 625-632.

Taylor, WR, Schütz, P, Bergmann, G, List, R, Postolka, B, Hitz, M, Dymke, J, Damm, P, Duda, G, Gerber, H, Schwachmeyer, V, Hosseini Nasab, SH, Trepczynski, A & Kutzner, I 2017, 'A comprehensive assessment of the musculoskeletal system: The CAMS-Knee data set', *Journal of Biomechanics*, vol. 65, 2017/12/08/, pp. 32-39.

Thelen, DG 2003, 'Adjustment of Muscle Mechanics Model Parameters to Simulate Dynamic Contractions in Older Adults', *Journal of Biomechanical Engineering*, vol. 125, no. 1, pp. 70-77.

Thewlis, D, Callary, S, Fraysse, F & Solomon, L 2015, 'Peak Loading During Walking is Not Associated With Fracture Migration Following Tibial Plateau Fracture: A Preliminary Case Series', *Journal of Orthopaedic Research*, vol. 33, no. 9, pp. 1398-1406.

Thewlis, D, Fraysse, F, Callary, SA, Verghese, VD, Jones, CF, Findlay, DM, Atkins, GJ, Rickman, M & Solomon, LB 2017, 'Postoperative weight bearing and patient reported outcomes at one year following tibial plateau fractures', *Injury*, vol. 48, no. 7, pp. 1650-1656.

Timmers, TK, van der Ven, DJ, de Vries, LS & van Olden, GD 2014, 'Functional outcome after tibial plateau fracture osteosynthesis: a mean follow-up of 6 years', *Knee*, vol. 21, no. 6, Dec, pp. 1210-1215.

Torry, MR, Decker, MJ, Viola, RW, O'Connor, DD & Richard Steadman, J 2000, 'Intra-articular knee joint effusion induces quadriceps avoidance gait patterns', *Clinical Biomechanics*, vol. 15, no. 3, 2000/03/01/, pp. 147-159.

Tozzi, G, Dall'Ara, E, Palanca, M, Curto, M, Innocente, F & Cristofolini, L 2017, 'Strain uncertainties from two digital volume correlation approaches in prophylactically augmented vertebrae: Local analysis on bone and cement-bone microstructures', *Journal of the Mechanical Behavior of Biomedical Materials*, vol. 67, 2017/03/01/, pp. 117-126.

Umberger, BR, Gerritsen, KGM & Martin, PE 2003, 'A Model of Human Muscle Energy Expenditure', *Computer Methods in Biomechanics and Biomedical Engineering*, vol. 6, no. 2, pp. 99-111.

van Veen, BC, Mazza, C & Viceconti, M 2020, 'The Uncontrolled Manifold Theory Could Explain Part of the Inter-Trial Variability of Knee Contact Force During Level Walking', *IEEE Transactions on Neural Systems and Rehabilitation Engineering*, vol. 28, no. 8, Aug, pp. 1800-1807.

Vendeuvre, T, Grunberg, M, Germaneau, A, Maloubier, F, Faure, JP, Gayet, LE, Rigoard, P & Breque, C 2018, 'Contribution of minimally invasive bone augmentation to primary stabilization of the osteosynthesis of Schatzker type II tibial plateau fractures: Balloon vs bone tamp', *Clinical Biomechanics*, vol. 59, pp. 27-33.

Wang, Y, Lava, P, Coppieters, S, De Strycker, M, Van Houtte, P & Debruyne, D 2012, 'Investigation of the Uncertainty of DIC Under Heterogeneous Strain States with Numerical Tests', *Strain*, vol. 48, no. 6, pp. 453-462.

Ward, SR, Eng, CM, Smallwood, LH & Lieber, RL 2009, 'Are current measurements of lower extremity muscle architecture accurate?', *Clinical Orthopaedics and Related Research*, vol. 467, no. 4, pp. 1074-1082.

Wilharm, A, Hurschler, C, Dermitas, T & Bohnsack, M 2013, 'Use of Tekscan K-Scan Sensors for Retropatellar Pressure Measurement Avoiding Errors during Implantation and the Effects of Shear Forces on the Measurement Precision', *BioMed Research International*, vol. 2013, pp. 1-7.

Winby, CR, Lloyd, DG & Kirk, TB 2008, 'Evaluation of different analytical methods for subject-specific scaling of musculotendon parameters', *Journal of Biomechanics*, vol. 41, no. 8, pp. 1682-1688.

Wolff, J 1892, 'The law of bone remodeling. Maquet P, Furlong R, translators', Springer, New York, NY, USA, Hirschwald Berlin.

Wu, G, Siegler, S, Allard, P, Kirtley, C, Leardini, A, Rosenbaum, D, Whittle, M, D'Lima, DD, Cristofolini, L, Witte, H, Schmid, O & Stokes, I 2002, 'ISB recommendation on definitions of joint coordinate system of various joints for the reporting of human joint motion—part I: ankle, hip, and spine', *Journal of Biomechanics*, vol. 35, no. 4, pp. 543-548.

Zajac, FE 1989, 'Muscle and tendon: properties, models, scaling, and application to biomechanics and motor control', *Crit Rev Biomed Eng*, vol. 17, no. 4, pp. 359-411.

Zelik, KE & Adamczyk, PG 2016, 'A unified perspective on ankle push-off in human walking', *The Journal of Experimental Biology*, vol. 219, no. 23, pp. 3676-3683.

Zhang, J, Malcolm, D, Hislop-Jambrich, J, Thomas, CDL & Nielsen, PMF 2014, 'An anatomical region-based statistical shape model of the human femur', *Computer Methods in Biomechanics and Biomedical Engineering: Imaging & Visualization*, vol. 2, no. 3, 2014/07/03, pp. 176-185.

Zhang, J, Sorby, H, Clement, J, Thomas, CDL, Hunter, P, Nielsen, P, Lloyd, D, Taylor, M & Besier, T 2014, 'The MAP Client: User-Friendly Musculoskeletal Modelling Workflows', in F Bello & S Cotin (eds), *Biomedical Simulation*, Springer International Publishing, Cham, pp. 182-192.

Zhao, D, Banks, SA, D'Lima, DD, Colwell, CW, Jr. & Fregly, BJ 2007, 'In vivo medial and lateral tibial loads during dynamic and high flexion activities', *Journal of Orthopaedic Research*, vol. 25, no. 5, May, pp. 593-602.

Zhao, D, Banks, SA, Mitchell, KH, D'Lima, DD, Colwell Jr, CW & Fregly, BJ 2007, 'Correlation between the knee adduction torque and medial contact force for a variety of gait patterns', *Journal of Orthopaedic Research*, vol. 25, no. 6, 2007/06/01, pp. 789-797.

Zhao, R, Liu, Y & Tian, H 2021, 'Accuracy of soft tissue balancing in total knee arthroplasty using surgeon-defined assessment versus a gap-balancer or electronic sensor', *Journal of Orthopaedic Surgery and Research*, vol. 16, no. 1.

Zimmermann, EA, Busse, B & Ritchie, RO 2015, 'The fracture mechanics of human bone: influence of disease and treatment', *BoneKEy Rep*, vol. 4.

Appendices

Appendix A – Chapter Supplementary Material

Chapter 3 Supplementary Material

Supplementary Material 1 EMG Signals

For each challenge, 16 EMGs were positioned. The filtered and rectified signals are in Fig. 1-3. Muscles which were not used were either, weak (Maximum isometric force <500 N), noisy (as determined by a single operator, considering the raw EMG signals which were measured), or produced spurious results when running CEINMS.

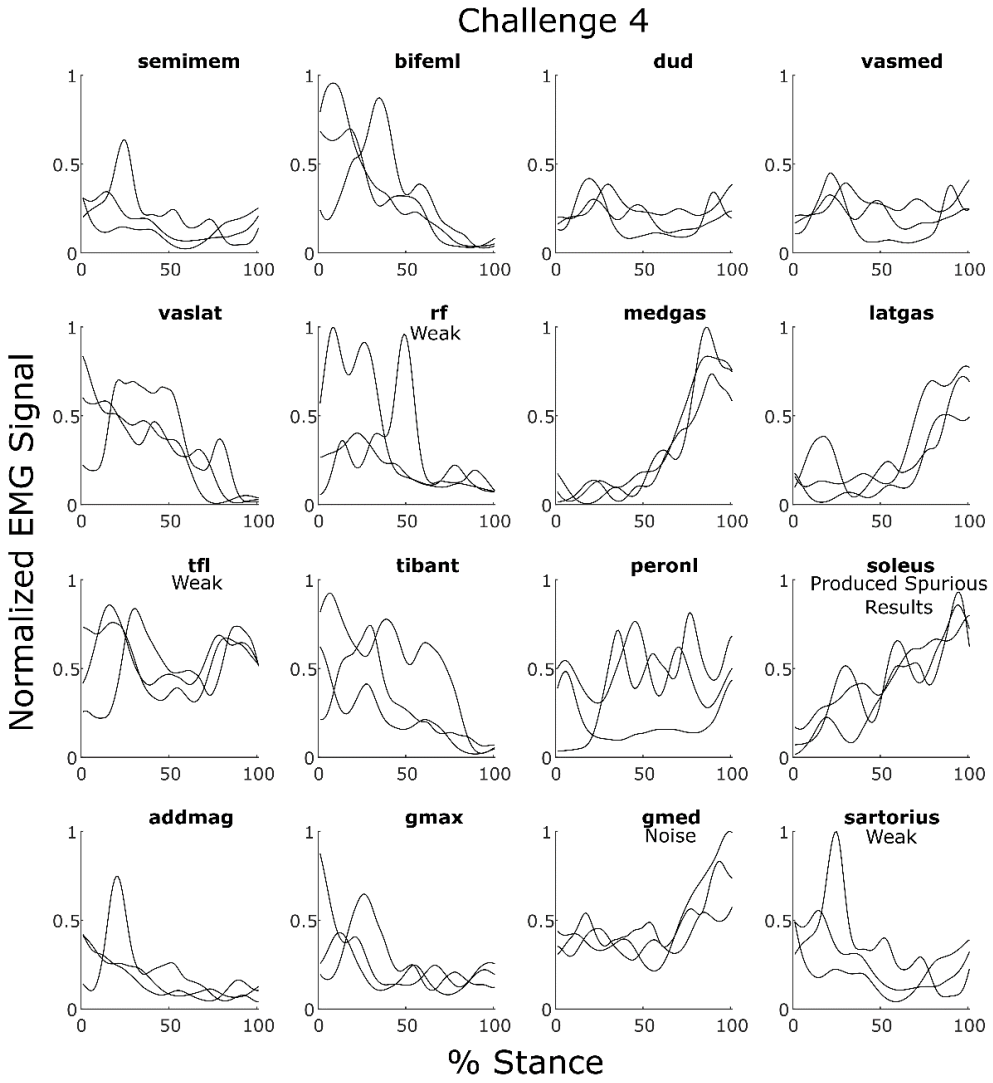

Figure 35 Normalized EMG signals recorded for Challenge 4 with their reasons for signals being excluded. Each line is an individual measurement.

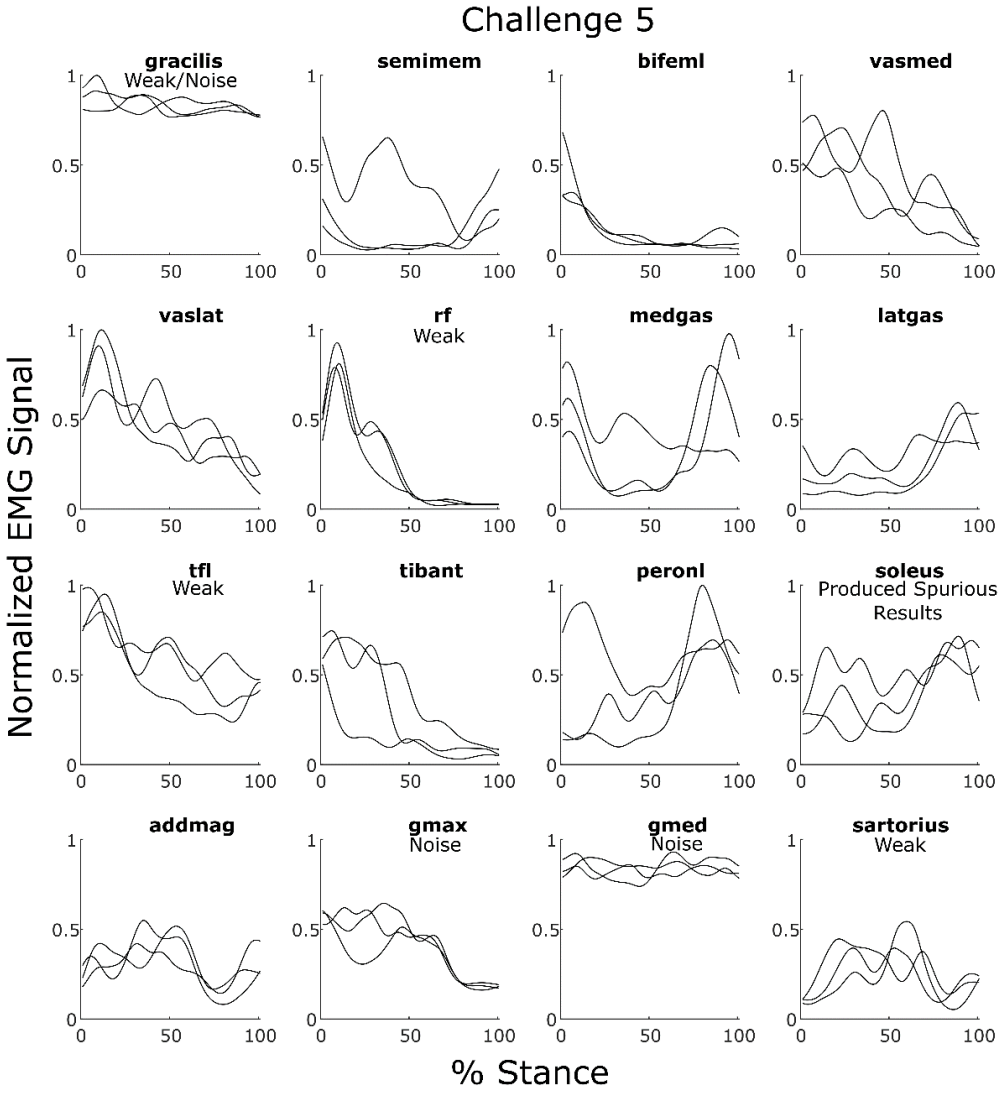

Figure 36 Normalized EMG signals recorded for Challenge 5 with their reasons for signals being excluded. Each line is an individual measurement.

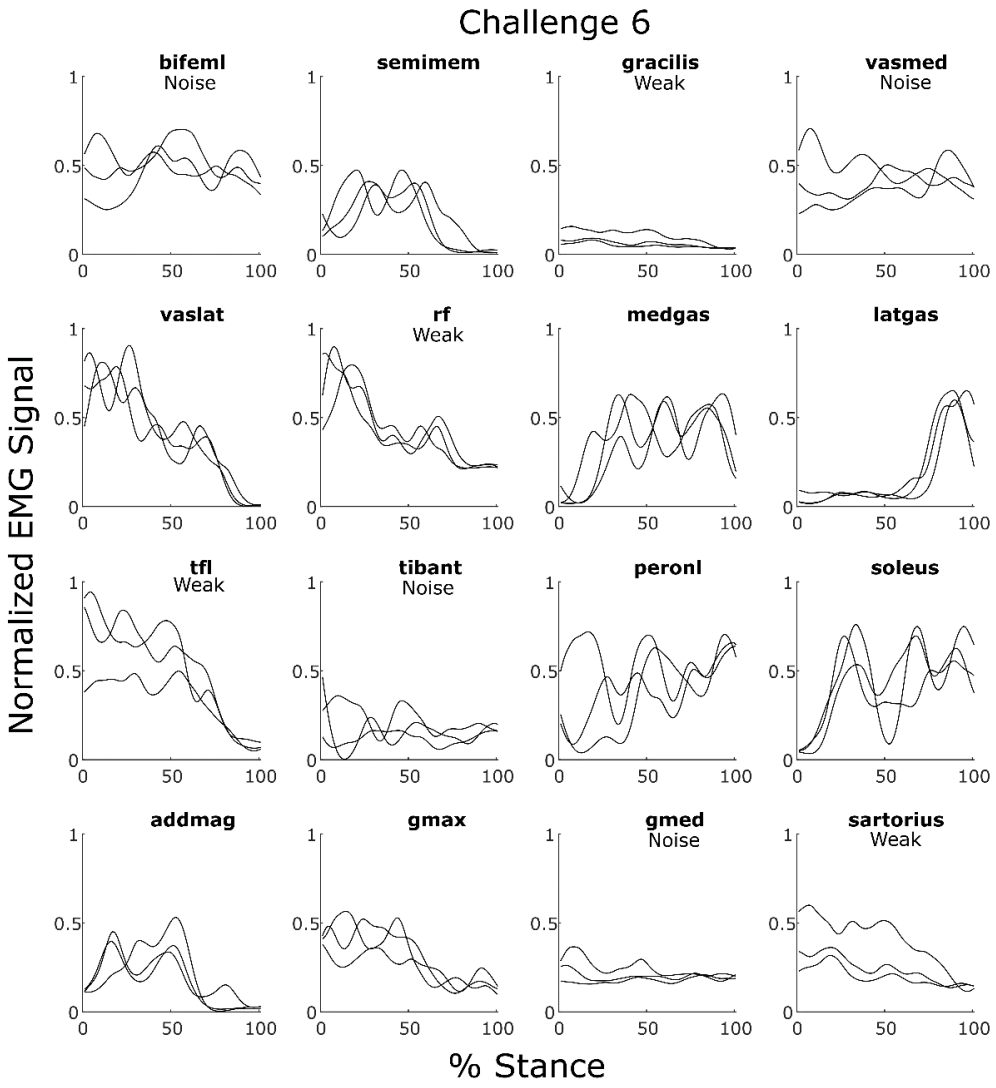

Figure 37 Normalized EMG signals recorded for Challenge 6 with their reasons for signals being excluded. Each line is an individual measurement.

Supplementary Material 2 CEINMS Calibration Functions

The general objective function (1) used in the calibration step was modified using the weighting and exponents in Table 1. The best performing objective functions based on root mean square error were functions: 2, 5, and 8. All joint loads for each of these calibration functions with the true measures overlaid are in Fig. 4-7. Functions 2 and 5 both show loading discontinuities around 35% of stance phase for at least one trial.

$$f_{obj} = w_1 NRMSE(\tau, \hat{\tau})^{k_1} + w_2 F_{hip}^{peak^{k_2}} + w_3 F_{knee}^{peak^{k_3}} + w_4 F_{ankle}^{peak^{k_4}} \quad (1)$$

Table 11 Summary of each calibration function tested.

	Normalised Torque RMSE		Hip		Knee		Ankle	
Objective Function	w	k	w	k	w	k	w	k
1	1	1	1	1	1	1	1	1
2	1	2	0	0	0.1667	1	0	0
3	2	2	0.01	1	0.01	1	0.01	1
4	2	2	0.05	1	0.05	1	0.05	1
5	2	2	0.1	1	0.1	1	0.05	1
6	2	2	0.1	1	0.1	1	0.01	1
7	1	2	0.01	1	0.01	1	0.01	1
8	1	2	0.05	1	0.05	1	0.05	1
9	1	2	0.1	1	0.1	1	0.05	1
10	1	2	0.1	1	0.1	1	0.01	1
11	2	2	0.001	2	0.001	2	0.001	2
12	2	2	0.005	2	0.005	2	0.001	2
13	2	2	0.01	2	0.01	2	0.01	2
14	2	2	0.01	2	0.01	2	0.001	2
15	2	2	0.05	2	0.05	2	0.05	2
16	2	2	0.05	2	0.05	2	0.01	2
17	1	2	0.001	2	0.001	2	0.001	2
18	1	2	0.005	2	0.005	2	0.001	2
19	1	2	0.01	2	0.01	2	0.01	2
20	1	2	0.01	2	0.01	2	0.001	2
21	1	2	0.05	2	0.05	2	0.05	2
22	1	2	0.05	2	0.05	2	0.01	2
23	2	3	0.001	2	0.001	2	0.001	2
24	2	3	0.5	1	0.5	1	0.5	1

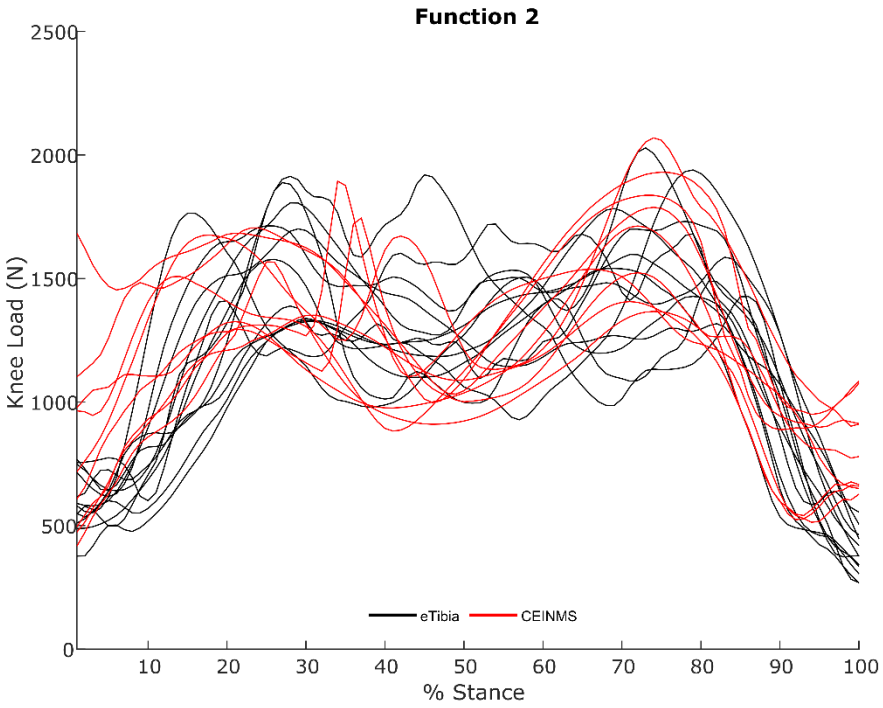

Figure 38 Knee load traces for all trials for both the eTibia and the CEINMS model calibrated with function 2.

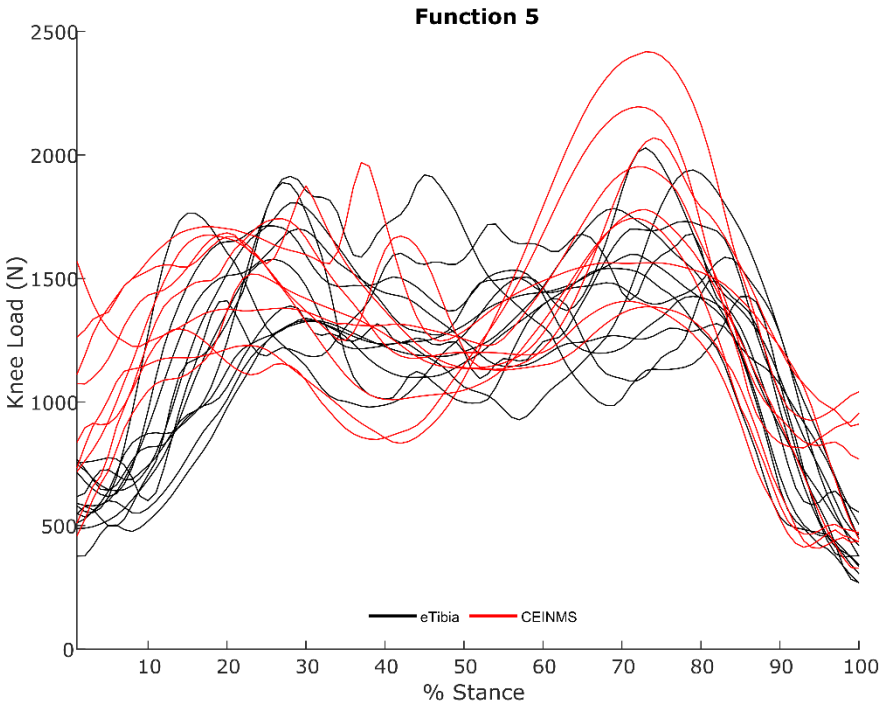

Figure 39 Knee load traces for all trials for both the eTibia and the CEINMS model calibrated with function 5.

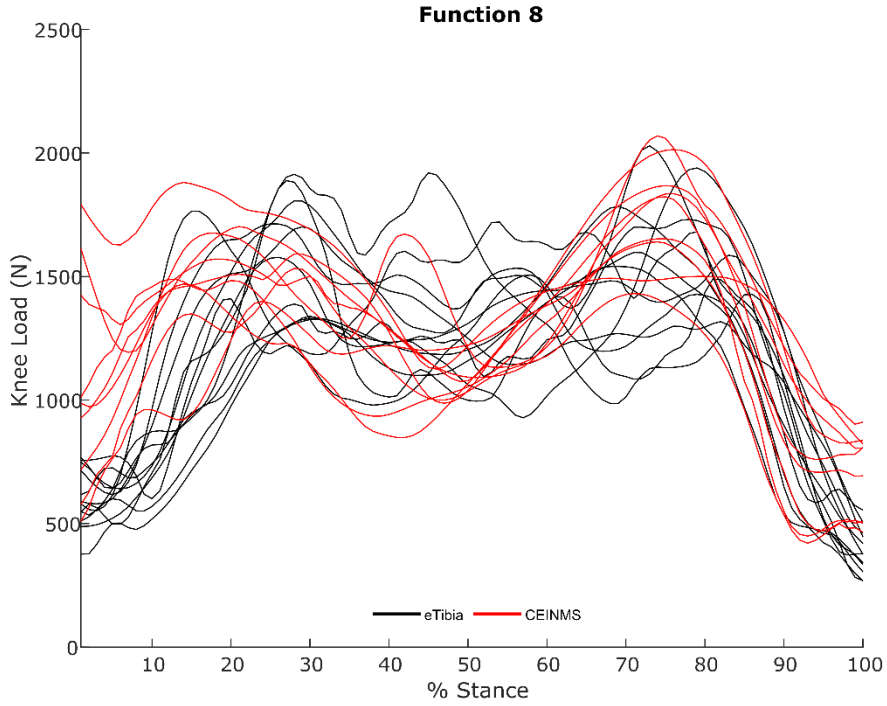

Figure 40 Knee load traces for all trials for both the eTibia and the CEINMS model calibrated with function 8.

Supplementary Material 3 Joint Moment Comparison

The joint moments calculated using inverse dynamics (used as the ground truth) and those calculated from CEINMS and SO are in Fig. 7, and the RMSE between inverse dynamics, and CEINMS and SO are in Fig. 8.

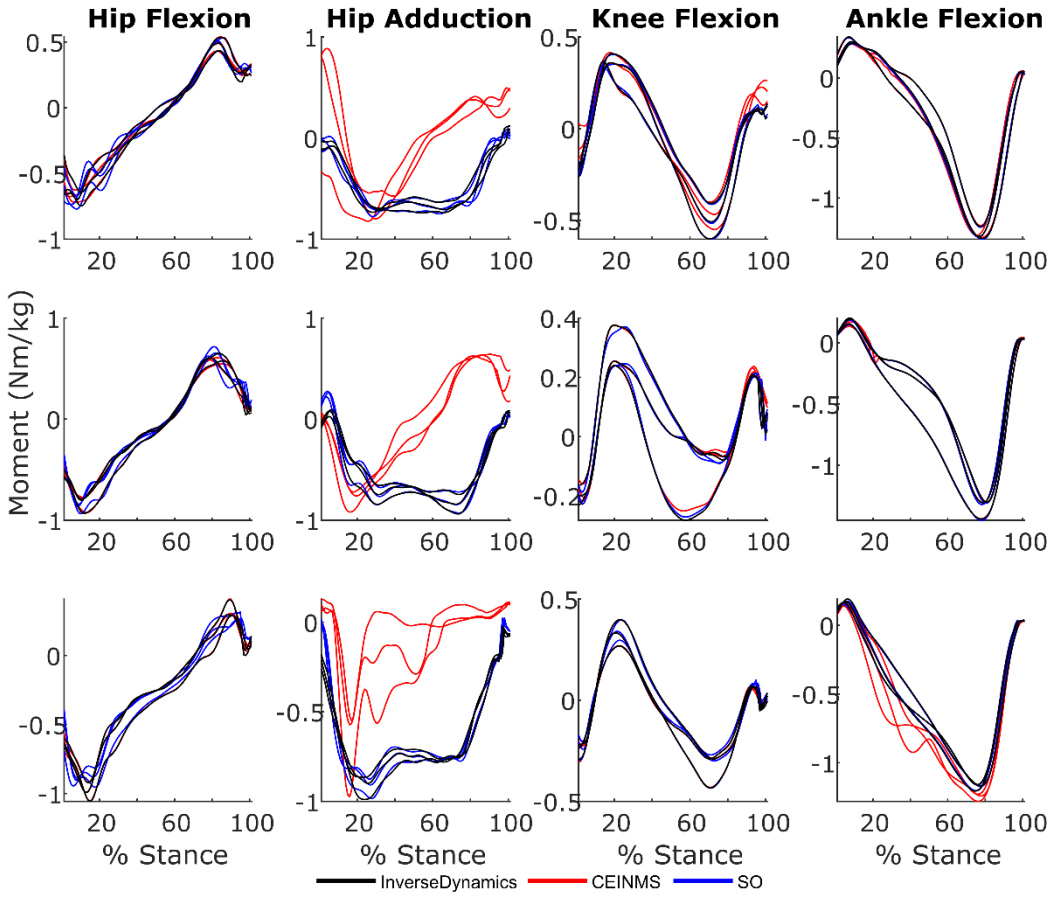

Figure 41 Joint moments normalized to body weight calculated using inverse dynamics (black), and the resultant joint moments from the muscle forces in CEINMS (red) and SO (blue).

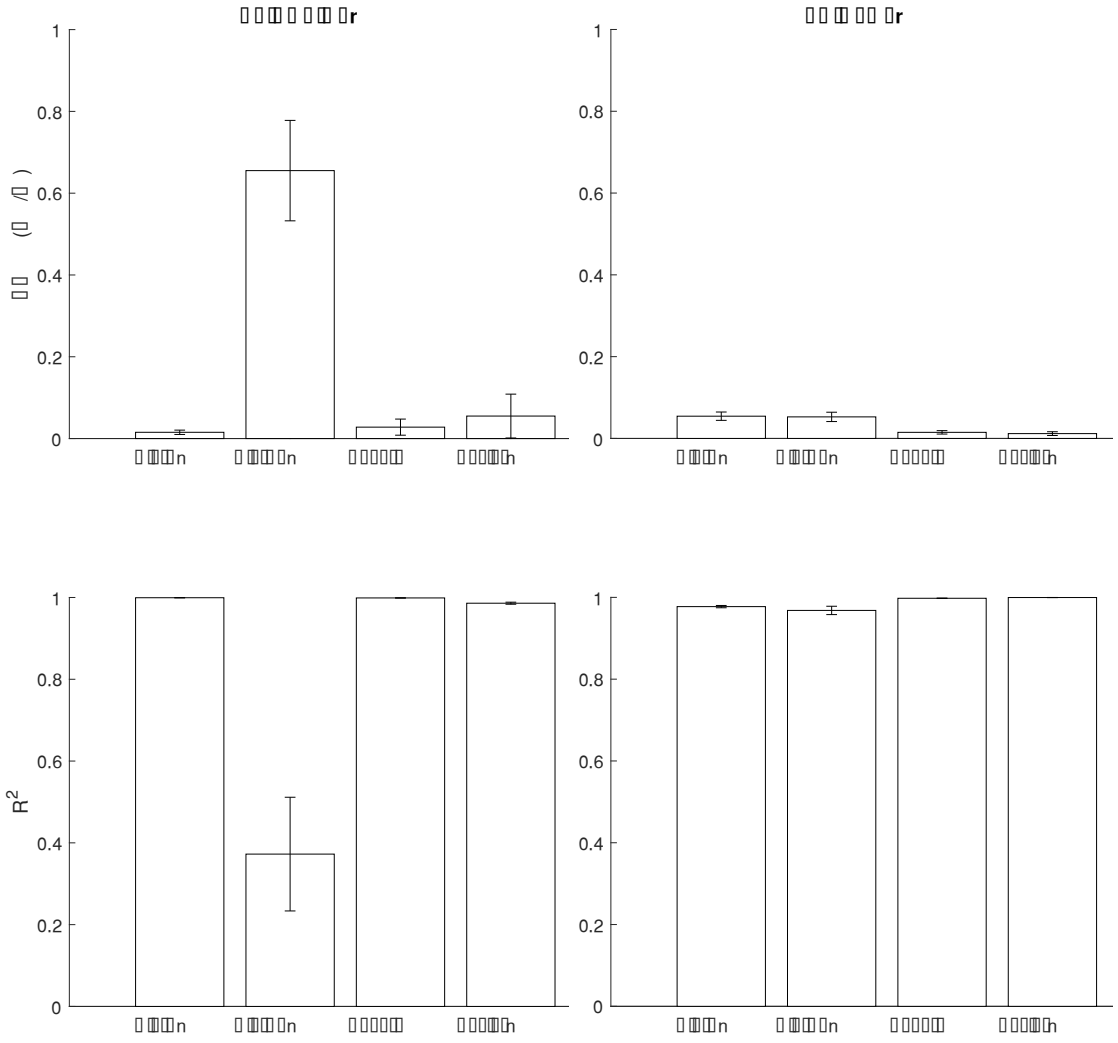

Figure 42 RMSE and R^2 between the inverse dynamics solution and the CEINMS and SO solutions.

Supplementary Material 4 Gluteal Muscle Force Comparison

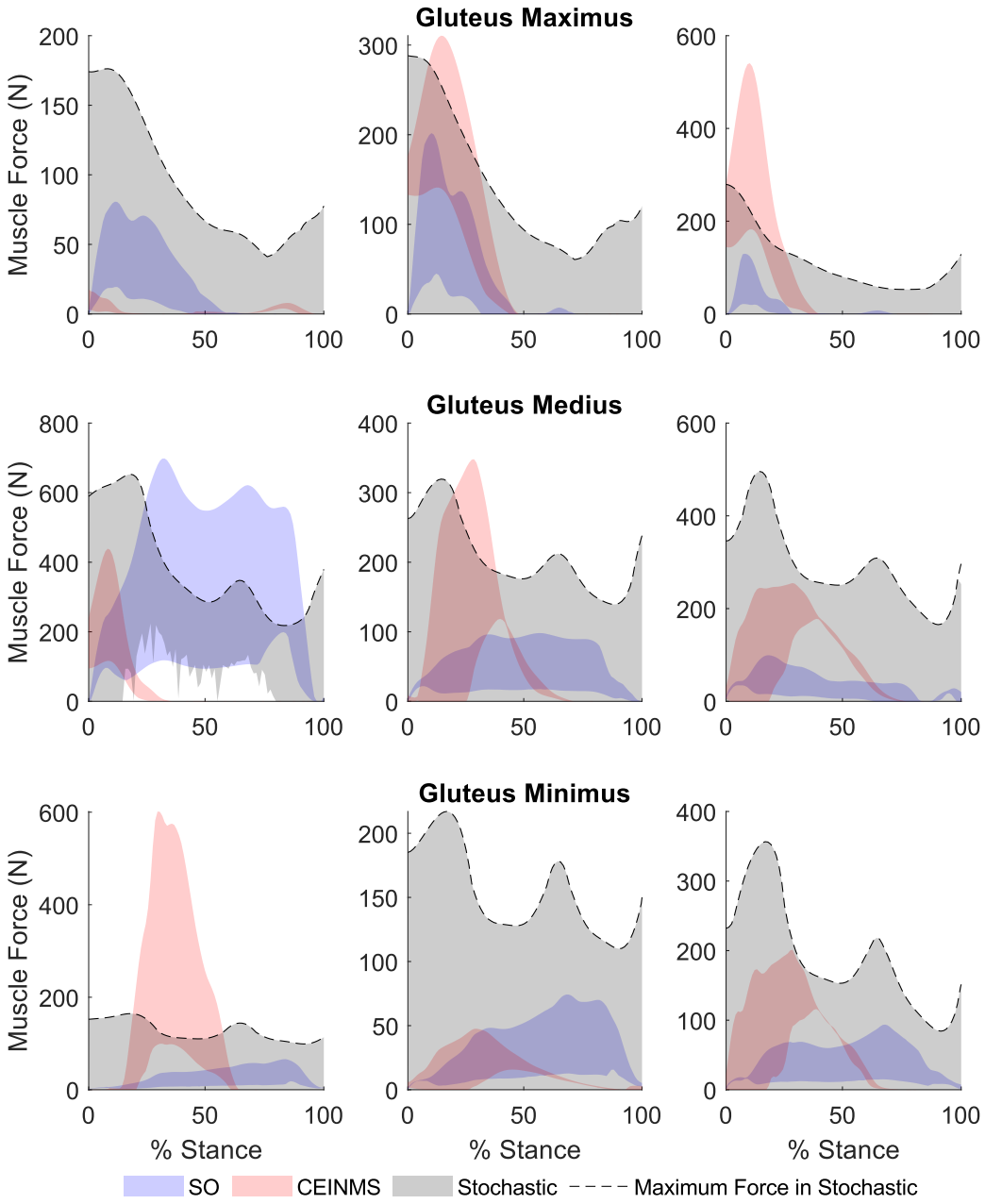

Figure 43 Standard deviation of gluteal muscle forces across stance for Challenge 4.

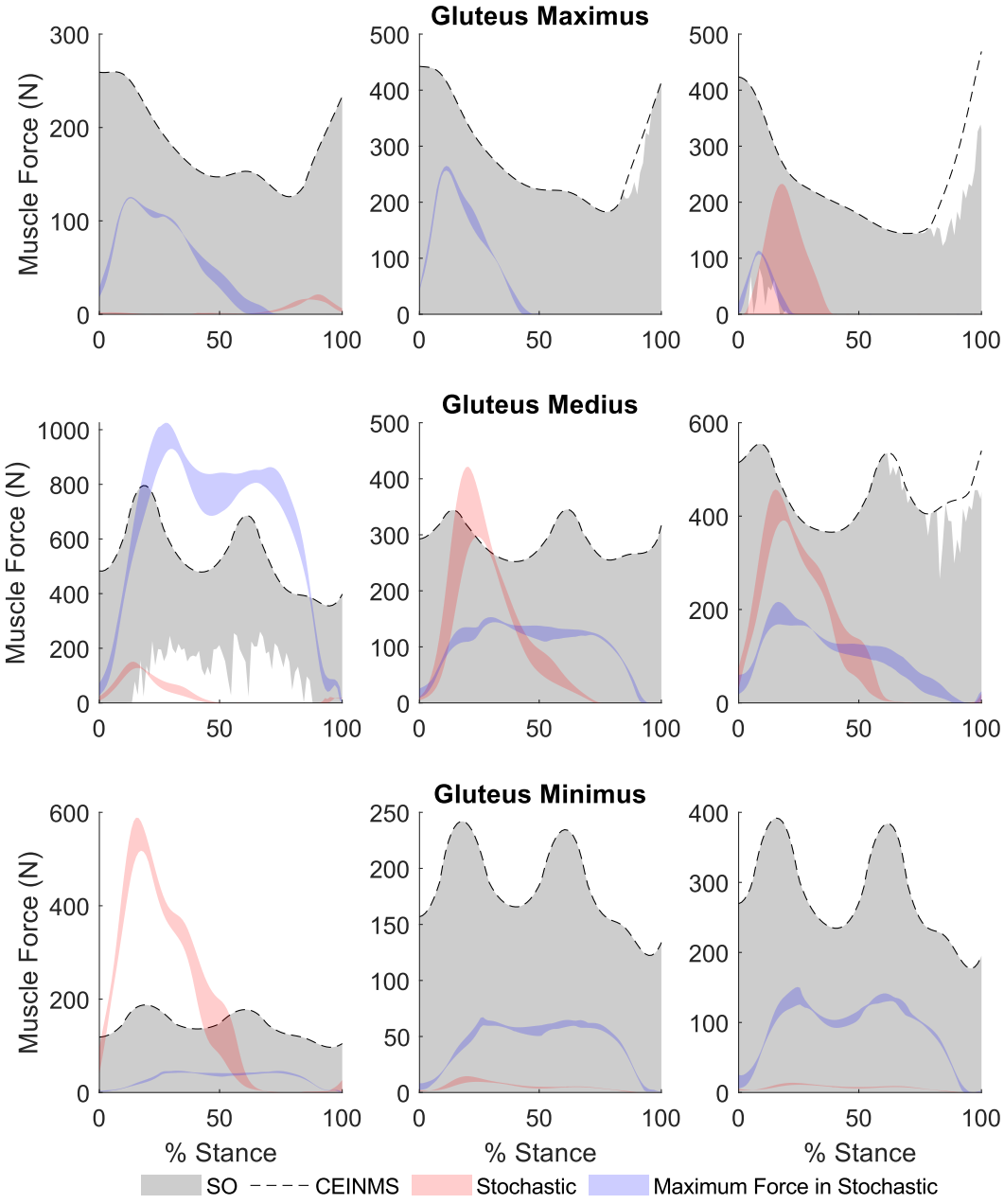

Figure 44 Standard deviation of gluteal muscle forces across stance for Challenge 5.

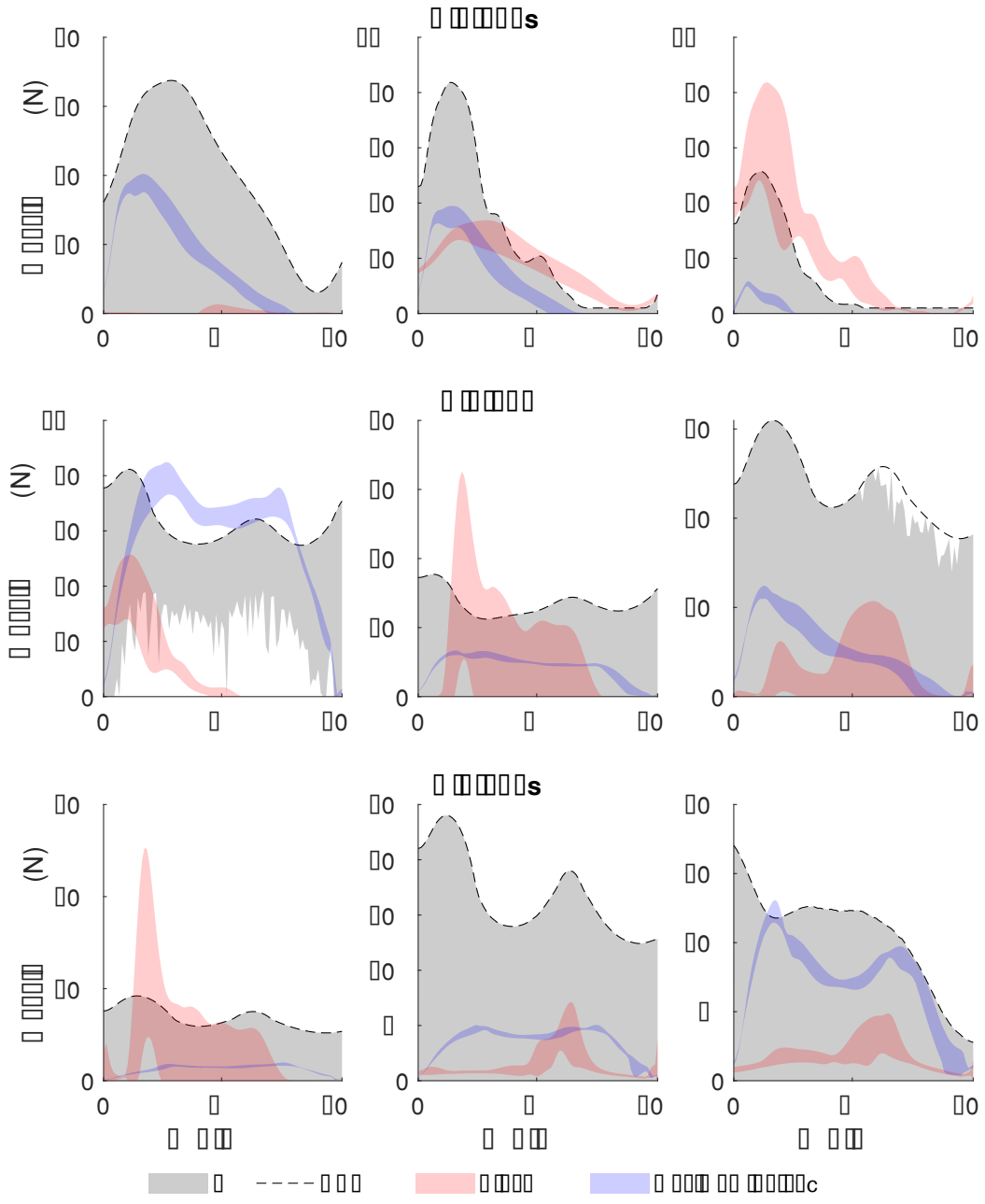

Figure 45 Standard deviation of gluteal muscle forces across stance for Challenge 4.

Chapter 4 Supplementary Material

Supp. 1 – Loading Profiles

During the experiment, the hand crank mechanism on the load cell was used to apply a uniaxial load which was measured continuously using a 6DOF load cell. The forces and moments recorded (Figure 46) show that, for both specimens, the target medial proportion (0.6) was overshot (specimen 1 medial proportion: 0.7; specimen 2 medial proportion 0.64).

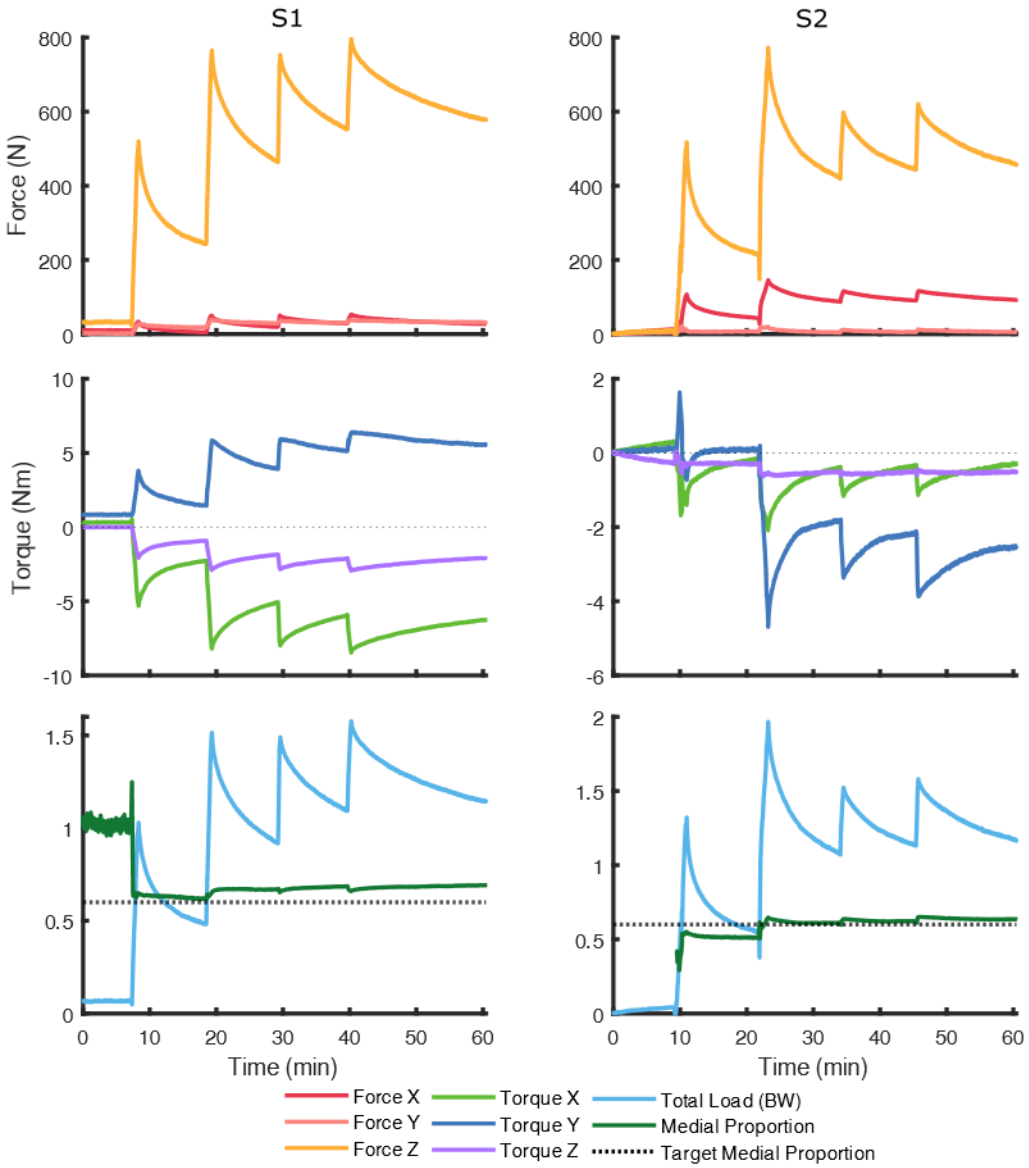

Figure 46. Load cell measurement during the loading experiment for specimens 1 (S1) and 2 (S2). The force in the Z direction has been normalized.

Supp. 2 – Zero Strain Analysis

The zero-strain analysis was conducted for four different sub-volume edge length procedures (Table 12) on unfiltered (Figure 47) and median filtered (Figure 48) images. The mean absolute error (MAER) and standard deviation of error (SDER) were calculated for each edge length, and a 34 voxel (1.56 mm) edge length was selected as a compromise between maximising error and minimising error.

Table 12. Sub volume edge length used for each of the multi-pass tests in DVC. The used sequence is in bold.

Step	Sub volume edge length in voxels			
1	320	160	**160**	128
2	160	128	**128**	92
3	128	92	**92**	46
4	92	46	**46**	34
Final	46	38	**34**	26

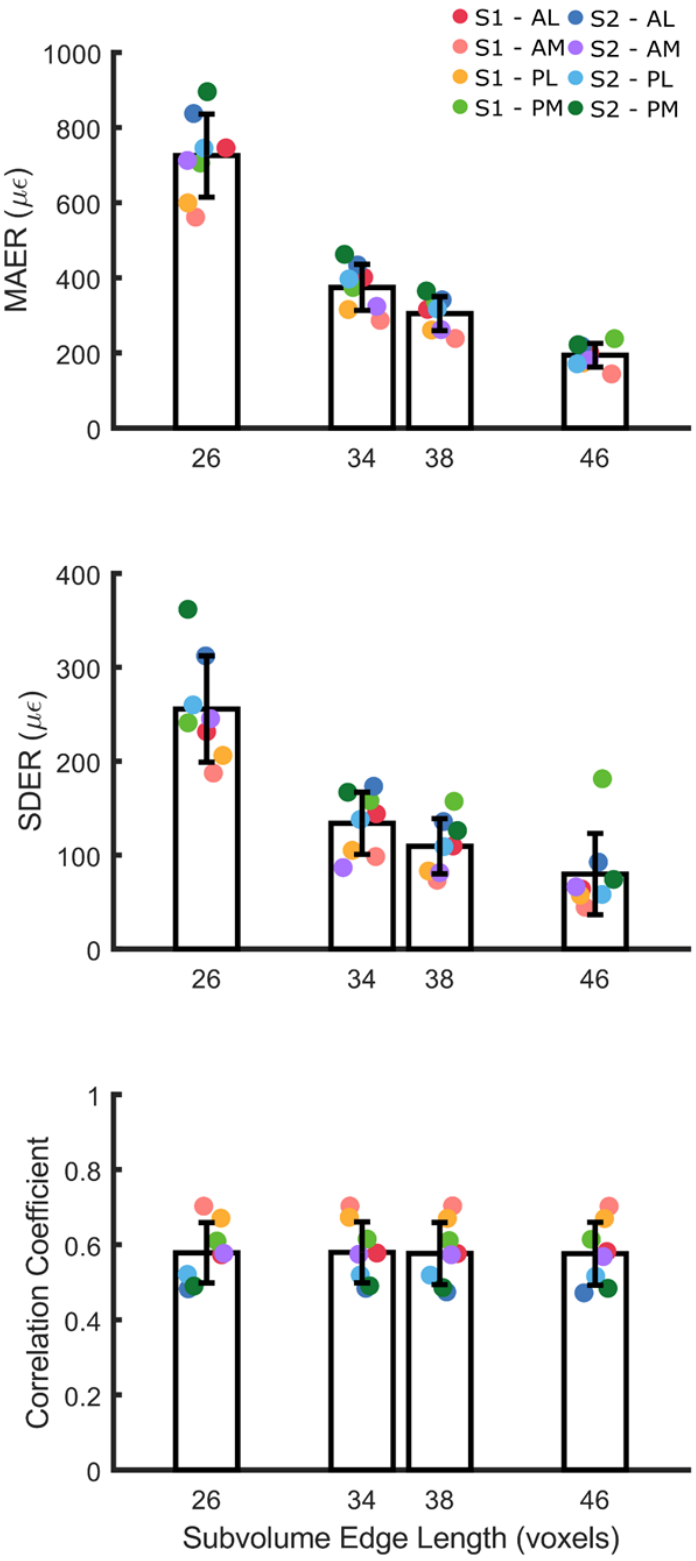

Figure 47 MAER, SDER, and Correlation coefficient for all tested sub volume edge lengths for each specimen and each VOI for the unfiltered image sets. S1 = specimen 1, S2 = specimen 2.

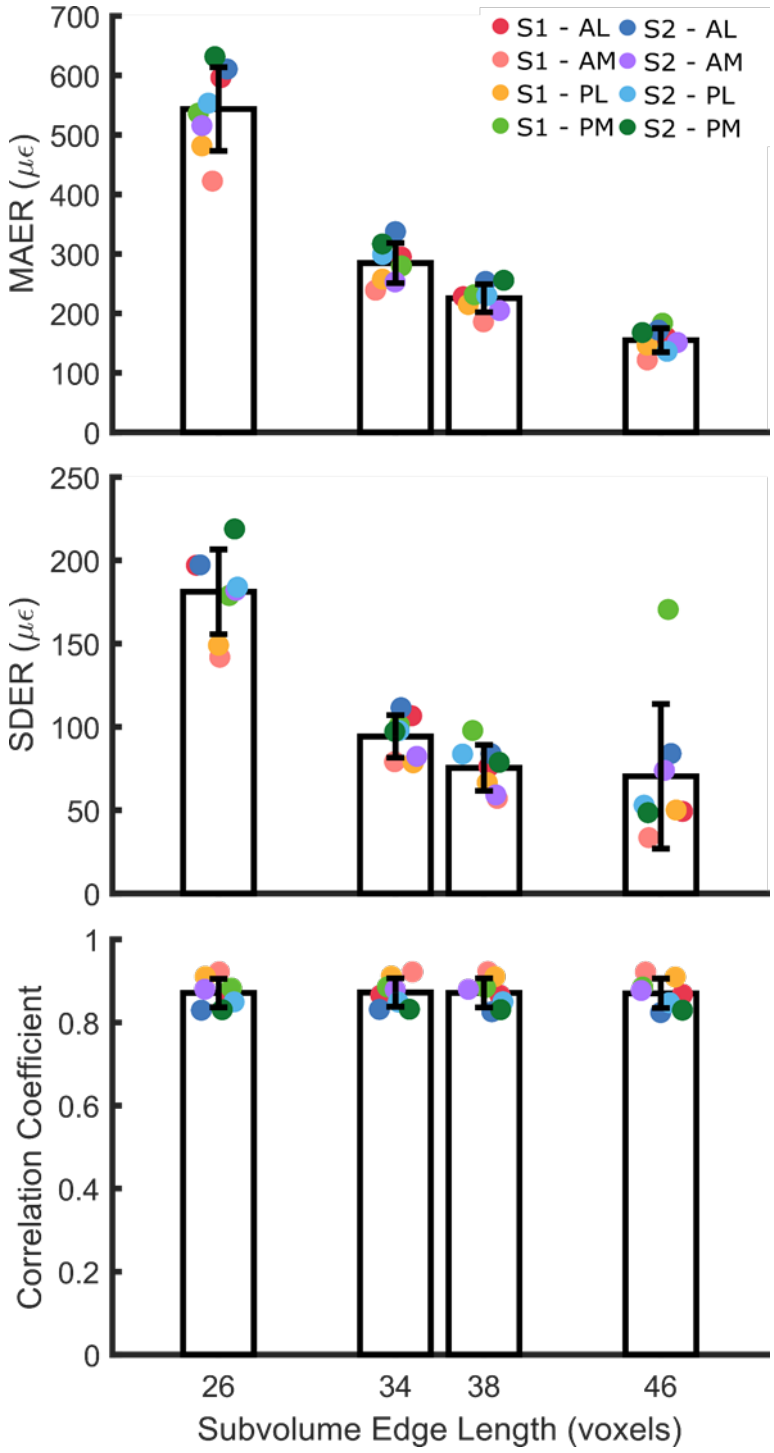

Figure 48 MAER, SDER, and Correlation coefficient for all tested sub volume edge lengths for each specimen and each VOI for the median filtered image sets. S1 = specimen 1, S2 = specimen 2.

Chapter 6 Supplementary Material

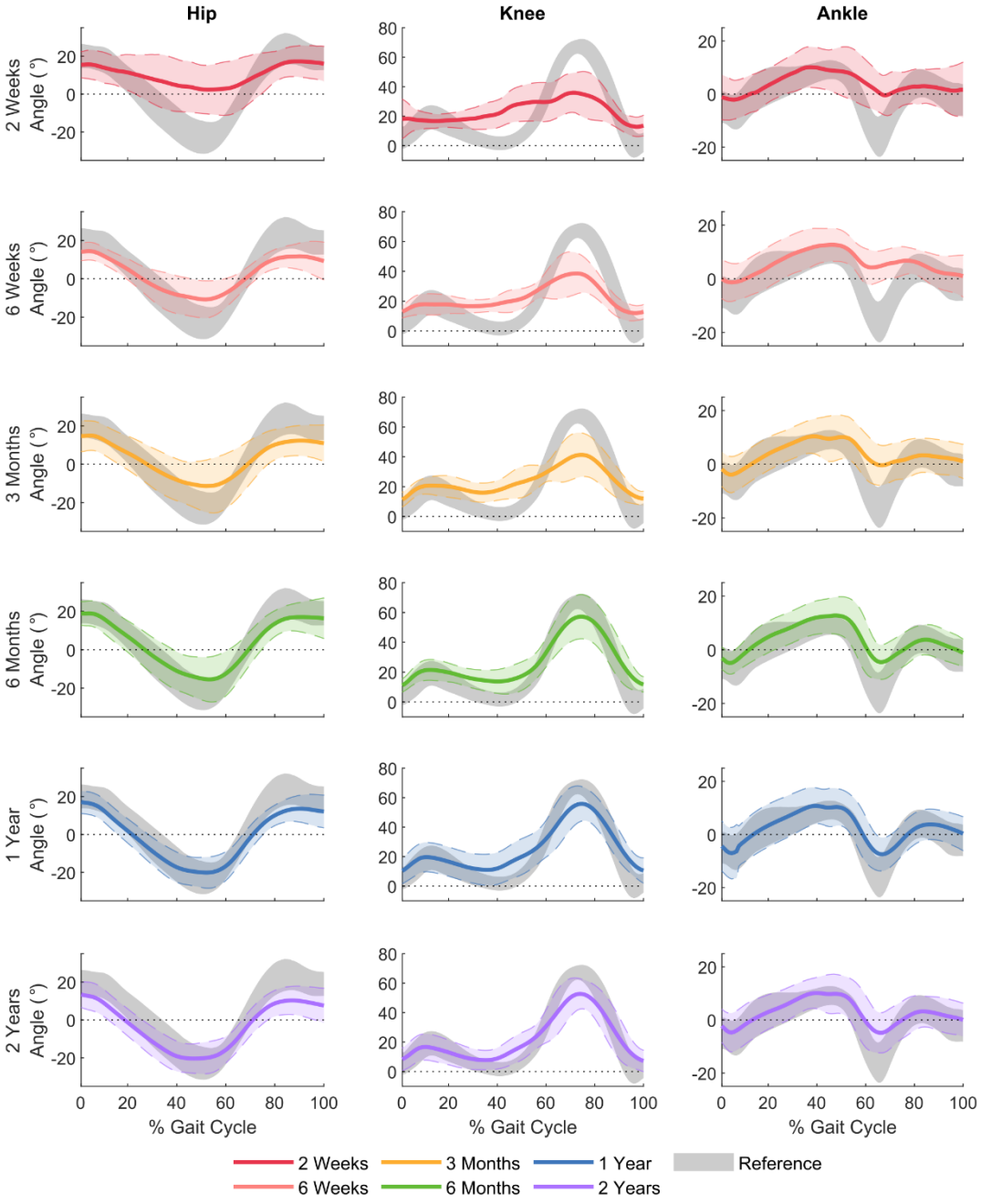

Figure 49 Mean and standard deviation of the hip, knee and ankle angles at each time point measured with healthy reference standard deviation superimposed.

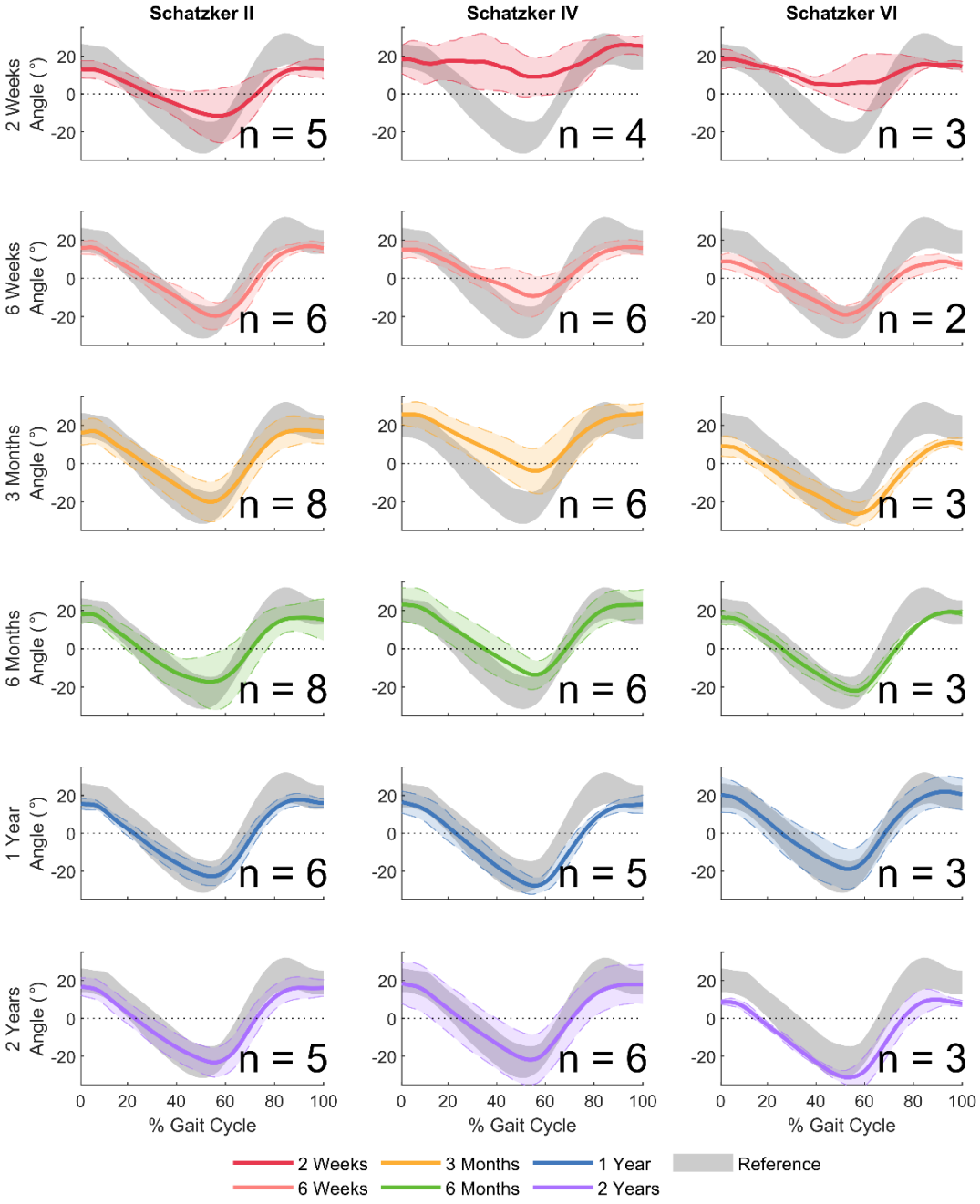

Figure 50 Mean and standard deviation of the hip angles by Schatzker fracture type at each time point measured with healthy reference standard deviation superimposed.

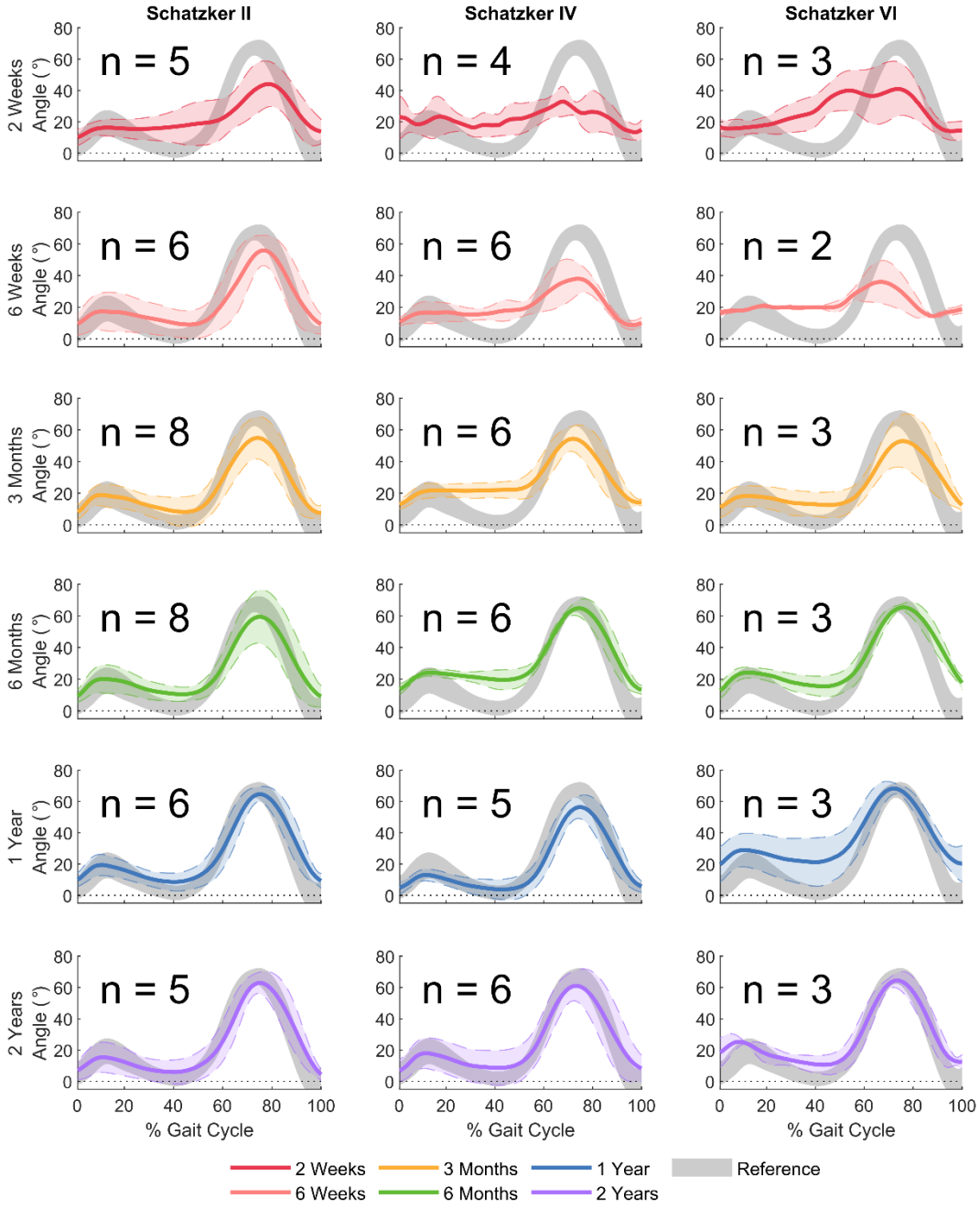

Figure 51 Mean and standard deviation of the knee angles by Schatzker fracture type at each time point measured with healthy reference standard deviation superimposed.

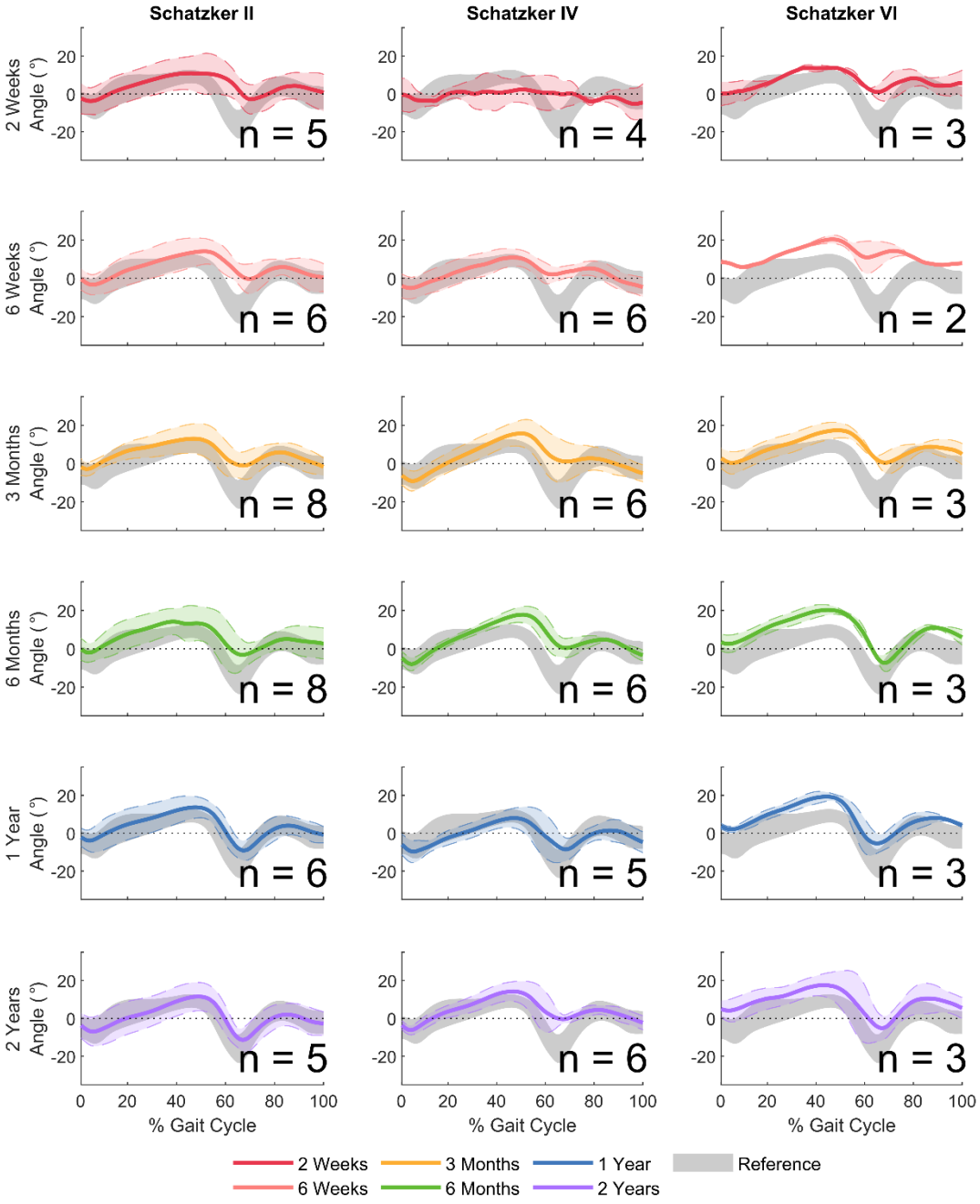

Figure 52 Mean and standard deviation of the ankle angles by Schatzker fracture type at each time point measured with healthy reference standard deviation superimposed.

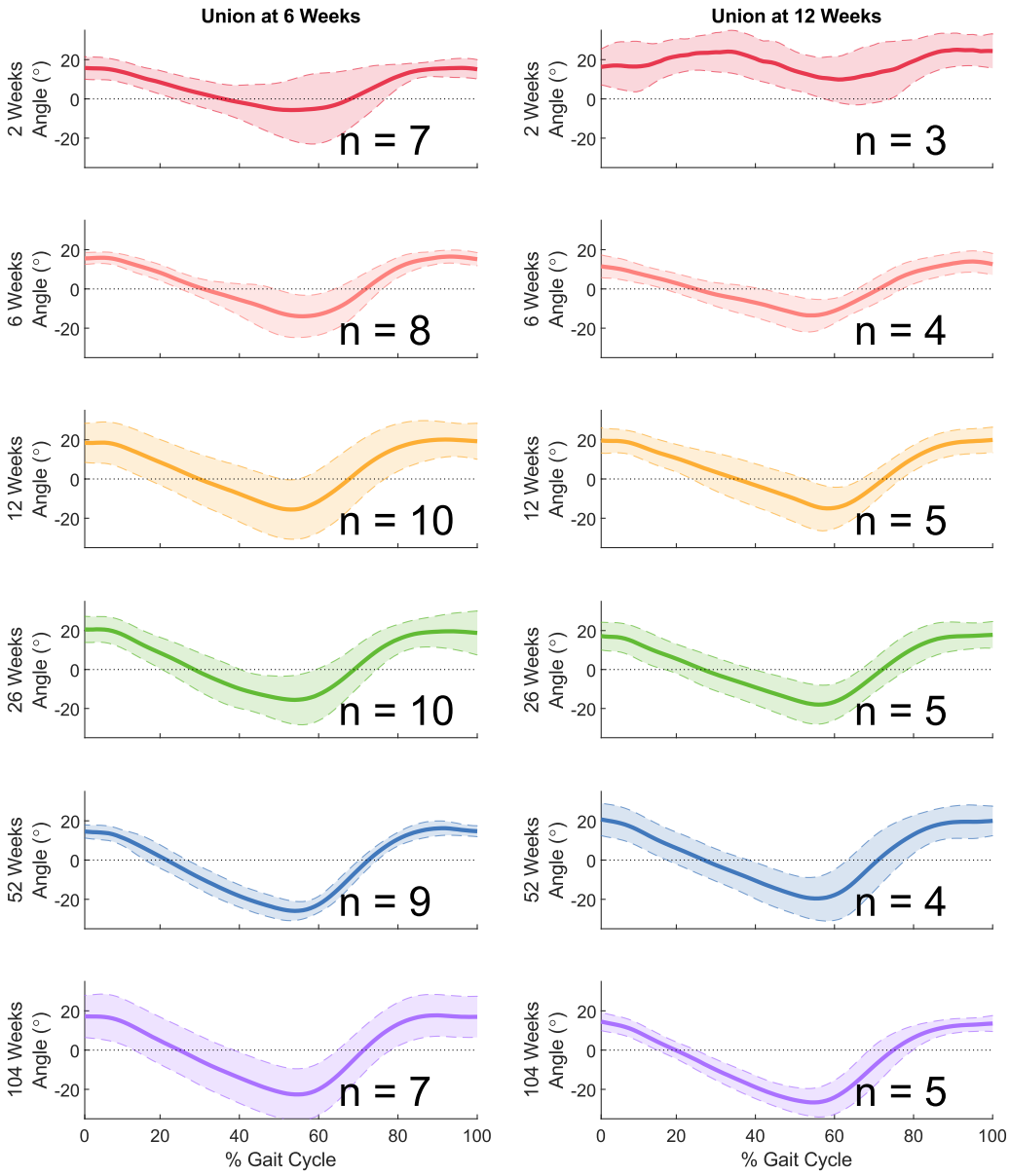

Figure 53 Mean and standard deviation of the hip angles by time to radiological evidence of fracture union at each time point measured.

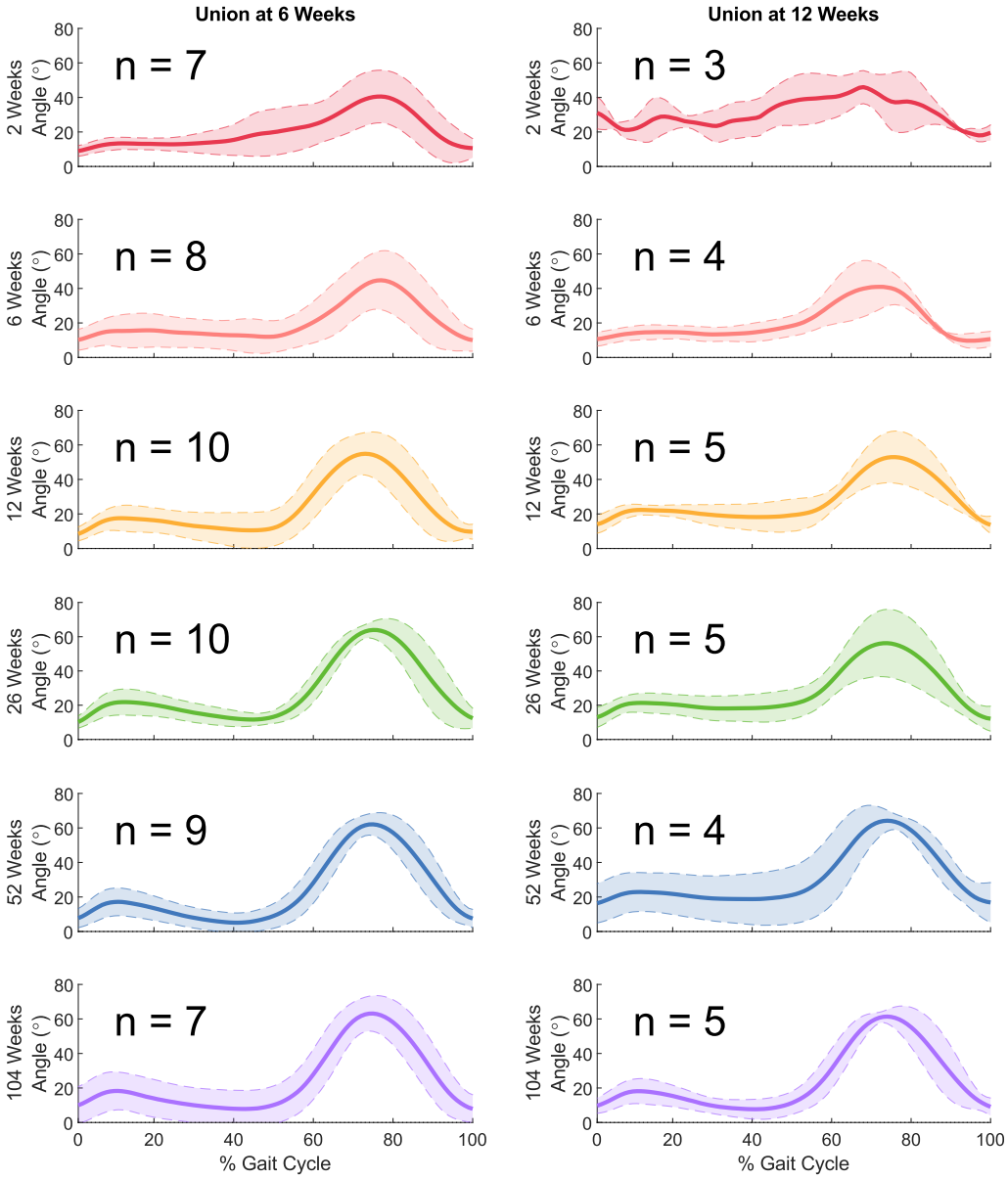

Figure 54 Mean and standard deviation of the knee angles by time to radiological evidence of fracture union at each time point measured.

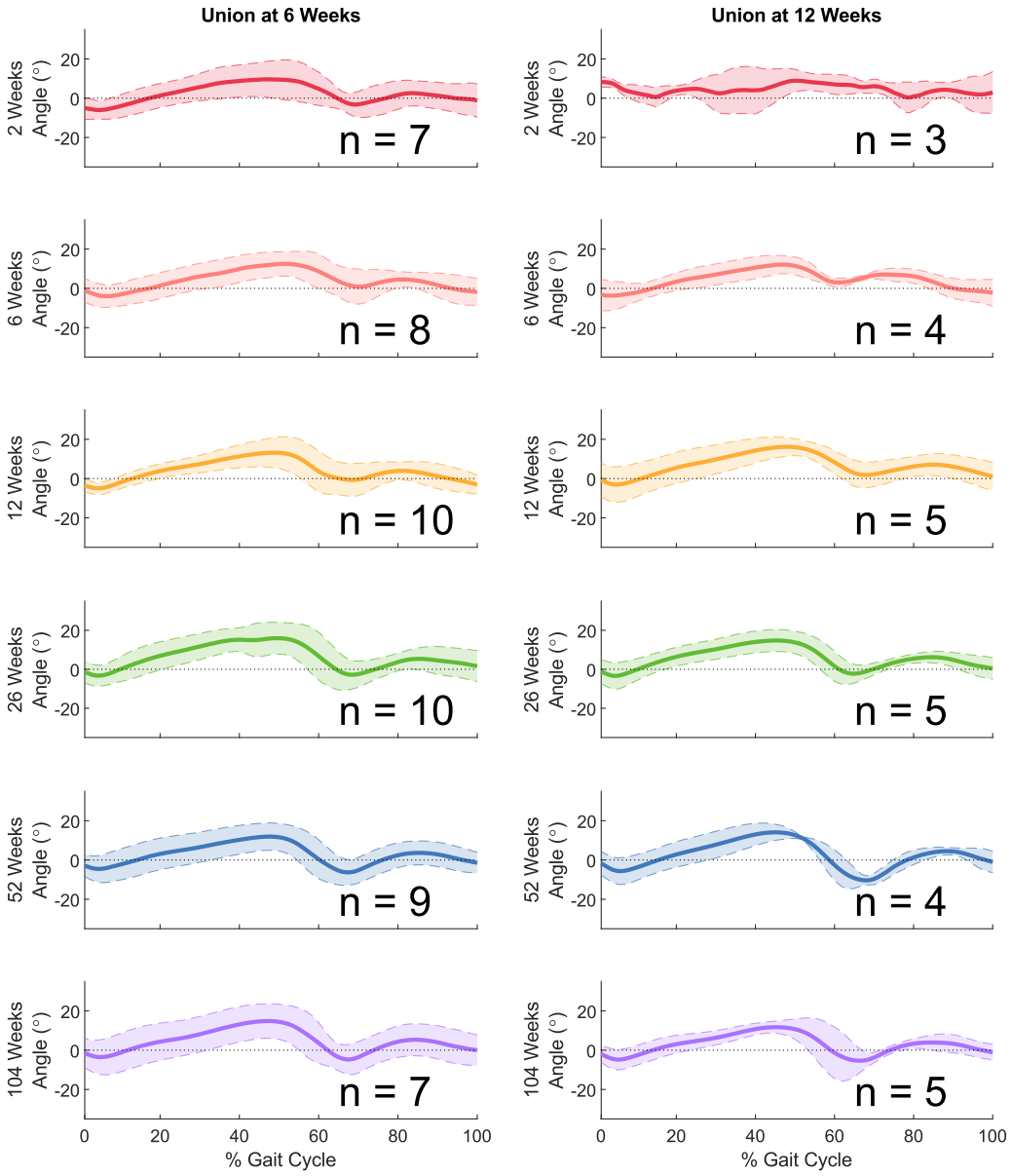

Figure 55 Mean and standard deviation of the ankle angles by time to radiological evidence of fracture union at each time point measured.

Appendix B – Ethical Approval Statements

Chapter 4, 5 Ethics: The University of Adelaide HREC reference number 34423

RESEARCH SERVICES
OFFICE OF RESEARCH ETHICS, COMPLIANCE AND INTEGRITY
THE UNIVERSITY OF ADELAIDE

LEVEL 4, RUNDLE MALL PLAZA
50 RUNDLE MALL
ADELAIDE SA 5000 AUSTRALIA

TELEPHONE +61 8 8313 5137
FACSIMILE +61 8 8313 3700
EMAIL hrec@adelaide.edu.au

CRICOS Provider Number 00123M

Our reference 34423

15 May 2020

Associate Professor Dominic Thewlis
Surgical Specialities - RAH

Dear Associate Professor Thewlis

ETHICS APPROVAL No: H-2020-076
PROJECT TITLE: MicroCT Imaging of the tibial plateau under loading

The ethics application for the above project has been reviewed by the Low Risk Human Research Ethics Review Group (Faculty of Health and Medical Sciences) and is deemed to meet the requirements of the *National Statement on Ethical Conduct in Human Research 2007 (Updated 2018)* involving no more than low risk for research participants.

You are authorised to commence your research on: 15/05/2020
The ethics expiry date for this project is: 31/05/2023

NAMED INVESTIGATORS:

Chief Investigator:	Associate Professor Dominic Thewlis
Student - Postgraduate Doctorate by Research (PhD):	Mr Kieran James Bennett
Associate Investigator:	Professor Bogdan Solomon
Associate Investigator:	Professor Gerald Atkins
Associate Investigator:	Dr Saulo Martelli
Associate Investigator:	Dr Egon Perilli

CONDITIONS OF APPROVAL: Thank you for addressing the feedback. The revised ethics application provided on the 14th of May 2020 has been approved.

Ethics approval is granted for three years and is subject to satisfactory annual reporting. The form titled Annual Report on Project Status is to be used when reporting annual progress and project completion and can be downloaded at http://www.adelaide.edu.au/research-services/oreci/human/reporting/. Prior to expiry, ethics approval may be extended for a further period.

Participants in the study are to be given a copy of the information sheet and the signed consent form to retain. It is also a condition of approval that you immediately report anything which might warrant review of ethical approval including:

- serious or unexpected adverse effects on participants,

- previously unforeseen events which might affect continued ethical acceptability of the project,
- proposed changes to the protocol or project investigators; and
- the project is discontinued before the expected date of completion.

Yours sincerely,

Ms Yvette Kim Clarissa Wijnandts
Secretary

The University of Adelaide

Chapter 6 Ethics: CALHN reference number R20160312

Kieran James Bennett

From: Health:CALHN Research Ethics <Health.CALHNResearchEthics@sa.gov.au>
Sent: Tuesday, 1 May 2018 1:28 PM
To: Kieran James Bennett
Cc: Dominic Thewlis; Bogdan Solomon
Subject: RE: Amended Study Protocol and Patient Information Consent Sheet

Importance: High

Dear Kieran,

Date: 1 May 2018

HREC reference number: HREC/16/RAH/74

CALHN Reference number: R20160312

Project title: Fracture fragment migration following articular fracture of the knee.

CPI: A/Prof Bogdan Solomon

Please accept this e-mail as **Acknowledgement of Receipt , Review and APPROVAL** of the document(s), on behalf of **Central Adelaide Local Health Network Human Research Ethics Committee (CALHN HREC) and CALHN Research Governance**, and retain a copy for your records.

For multi-centre studies a copy of this email must be forwarded to Principal Investigators at every site approved by the CALHN HREC for submission to the relevant Research Governance Officer along with a copy of the approved documents.

Document	*Version*	*Date*
Protocol	1.2	27 April 20
Patient Information Sheet and Consent Form	1.4	27 April 20
CV for Robyn Clothier	-	-
CV for Prof Gerald Atkins	-	-
CV for Saulo Martelli	-	-
CV for Kieran Bennett	-	-

Additional investigators covered by this approval:

- Robyn Clothier
- Prof Gerald Atkins
- Saulo Martelli
- Kieran Bennett

This approval is subject to the conditions outlined in the original ethics approval letter.

Should you have any queries about this matter please contact the Executive Officer of the HREC on 08 7117 2229 or 08 8222 6841 or Health.CALHNResearchEthics@sa.gov.au

Yours sincerely,

Eloise Spooner
Research Administration Officer
On behalf of:

1

Mr Ian Tindall
Chair,
Central Adelaide Local Health Network Human Research Ethics Committee (CALHN HREC)
CALHN Research Office
Phone: 08 7117 2229 or 08 8222 6841 | Email: Health.CALHNResearchEthics@sa.gov.au |

L3 Roma Mitchell House, North Terrace, Adelaide
https://www.rahresearchfund.com.au/rah-research-institute/for-researchers/human-research-ethics/

Ground Floor, Basil Hetzel Institute for Translational Health Research, 28 Woodville Road, Woodville South SA 5011 | DX: 465101
http://www.basilhetzelinstitute.com.au/research/information-for-researchers/human-research-ethics-committee/

Government of South Australia
SA Health
Central Adelaide Local Health Network Inc.

This email may contain confidential information, which also may be legally privileged. Only the intended recipient(s) may access, use, distribute or copy this e-mail. If this e-mail is received in error, please inform the sender by return e-mail and delete the original. If there are doubts about the validity of this message, please contact the sender by telephone. It is the recipient's responsibility to check the e-mail and any attached files for

Chapter 6 Ethics: The University of Adelaide HREC reference number 33506

Kieran James Bennett

From:	hrec_notification@adelaide.edu.au
Sent:	Monday, 18 February 2019 11:31 AM
To:	Dominic Thewlis; saulo.martelli@flinders.edu.au; Stuart Adam Callary; Bogdan Solomon; Kieran James Bennett; stuart.millar@mymail.unisa.edu.au
Cc:	hrec_notification@adelaide.edu.au
Subject:	33506 Notification of Human Research Ethics Approval - accepted

Application ID: 33506
Title: Fracture fragment migration following articular fracture of the knee Chief Investigator: Solomon, Lucian Bogdan Primary University of Adelaide Contact: Associate Professor Thewlis, Dominic Other Investigators: Thewlis, Dominic, Bennett, Kieran James, Callary, Stuart Adam, Saulo Martelli, Millar, Stuart, Solomon, Bogdan

This human research ethics approval notification has been reviewed by the Human Research Ethics Secretariat and Legal and Risk Office and has been accepted.

Please Login to ResearchMaster (https://rme6.adelaide.edu.au/RME6/) and locate the notification form via Ethics Applications, Amendments and Notifications> All Applications tab, and search for the Application ID. Refer to the user guide 'Searching for Ethics Applications in ResearchMaster'.

The Review Outcome page of the notification form will outline any conditions that apply to the acceptance of the notification and insurance details.

Office of Research Ethics, Compliance and Integrity Research Services The University of Adelaide

System Helpdesk: researchsystems@adelaide.edu.au User guides: ResearchMaster Home Page or https://www.adelaide.edu.au/research-services/systems-reporting/research-master/#ethics

This email was generated automatically; please do not reply to this email as this email address is not monitored.